

Sorption and Direct Speciation
of Neptunium(V) on Aluminium Oxide
and Montmorillonite

Thesis submitted for
obtaining the degree of

Doktor der Naturwissenschaften
doctor rerum naturalium

in Nuclear Chemistry

at the Department of Chemistry, Pharmacy, and Geosciences
of the Johannes Gutenberg - University Mainz

Sonja Wendt
born in Langenhagen, Germany

Mainz, 2009

Contents

Abbreviations and Terms	3
1 Introduction and Motivation	7
2 Fundamentals	11
2.1 Neptunium – History and Current Situation	11
2.1.1 Production and Global Inventory	12
2.1.2 Industrial Usage and Application	14
2.1.3 Releases into the Environment	15
2.2 Chemical and Radiochemical Characteristics of Neptunium . . .	16
2.2.1 Aqueous Chemistry	17
2.2.2 Radioactivity	21
2.2.3 Aspects of Toxicity – Health Effects	22
2.2.4 Neptunium in the Environment	24
2.3 Radioactive Waste	30
2.3.1 Waste Treatment	31
2.3.2 Disposal and Repository Safeguarding	33
2.3.3 Safety Assessment and Public Perception	36
2.4 Clay – Merits for Radionuclide Retention	36
2.4.1 Structure and Features of Montmorillonite	37
2.4.2 Aluminium Oxide as Reference Substance	43
2.5 Radionuclide Reactions with Natural Materials	47
2.5.1 Complexation	47
2.5.2 Sorption	49
2.5.3 Ion Exchange Processes	53
3 Practical Approach and Techniques	55
3.1 Laboratory System	56
3.1.1 Neptunium Concentration	57
3.1.2 pH-range	58
3.1.3 Ambient Air versus CO ₂ -free Conditions	59

3.1.4	Ionic Strength	60
3.1.5	Solid-to-liquid Ratio	61
3.1.6	Thermodynamics and Reaction Kinetics	63
3.2	Analytical Methods	64
3.2.1	γ Spectroscopy	64
3.2.2	Liquid Scintillation Counting	66
3.2.3	Direct Speciation via EXAFS	66
3.3	Modelling	80
3.3.1	The 2 SPNE SC/CE Model	81
4	Experimental	87
4.1	Radionuclides	87
4.1.1	Production of the Isotopes ^{237}Np and ^{239}Np	87
4.1.2	Separation and Purification	88
4.1.3	Assurance of the Fifth Oxidation State	90
4.2	Materials and Chemicals	90
4.2.1	Montmorillonite STx-1	90
4.2.2	Aluminium Oxide $\gamma\text{-Al}_2\text{O}_3$	91
4.2.3	Sodium Perchlorate NaClO_4 and its Purification	92
4.2.4	pH Adjustment and Buffer Solutions	93
4.2.5	Carbonate and Bicarbonate	94
4.3	Procedure of Batch Experiments	95
4.3.1	Preparation: Conditioning of Montmorillonite	95
4.3.2	Assemblage, Pre-conditioning and pH-adjustment	97
4.3.3	Addition of Np(V) and Contact Time	98
4.3.4	Centrifugation and γ Counting	100
4.3.5	Data Treatment	101
4.3.6	Batch Experiments	103
4.3.7	Sorption Isotherms	103
4.4	EXAFS Studies	105
4.4.1	Sample Preparation	106
4.4.2	Beamline Setup and Measurement	108
4.4.3	Data Processing	111
4.5	Surface Complexation Modelling	115
5	Results and Discussion	119
5.1	Np(V) Sorption on Montmorillonite and Aluminium Oxide	119
5.1.1	pH-Dependency: Edge and Maximum	119
5.1.2	Effect of Variations in Ionic Strength	124
5.1.3	Isotherms	127
5.1.4	Neptunium Complexation by Carbonates	132

5.1.5	Distribution Coefficients	134
5.2	Speciation	141
5.2.1	Theoretical Implications	141
5.2.2	Indications from the Sorption Behaviour	142
5.2.3	EXAFS-data and Curve-fitting	142
5.2.4	Structure of the Neptunium Carbonate Surface Complexes	149
5.2.5	Insights into the Sorption Mechanism	151
5.2.6	EXAFS on γ -Al ₂ O ₃ – Reliability Test of the Results . . .	151
5.2.7	Compilation of Speciation Results	157
5.3	Modelling Np(V) Sorption on Montmorillonite and γ -Al ₂ O ₃ . . .	158
5.3.1	Fixed Programme Parameters	158
5.3.2	Adjusted Constants	159
5.4	Consolidation of Results	165
6	Conclusion and Outlook	169
6.1	Summary of the Experiments	170
6.1.1	Sorption Processes	170
6.1.2	Surface Species	171
6.2	Evaluation and Usability of the Results	172
6.3	Future Progression	173
	Bibliography	175
 APPENDIX		
A	Chronology of Nuclear Research and Development	191
B	Nuclear Properties of Np	199
B.1	Electronic Configuration of ⁹³ Np	199
B.2	Isotopes and Decay Modes	200
B.3	Colour of Np-Ions in Aqueous Solution	201
C	Radioactivity	203
C.1	Types of Radioactive Decay	203
C.2	Nuclear Data Sources	204
C.3	Decay Series	205
D	Disposal of Radioactive Material	207
D.1	Treatment of Nuclear Waste	207

E	Definition and Classification of Clay Minerals	209
E.1	Definition by Particle Size	209
E.2	Classification According to Mineral Composition and Structure .	210
F	Instructions for Experimentation	211
F.1	The $^{237}\text{Np(V)}$ Stock Solution	211
F.2	The $^{239}\text{Np(V)}$ Stock Solution	213
F.3	Conditioning of Montmorillonite	215
F.3.1	Adjustment of Ionic Strength from 0.1 to 0.01 M NaClO_4	218
G	Experimental Overview	219
H	Periodic Table of the Elements	221
I	Curriculum Vitae	225
J	Declaration	227

List of Tables

3.1	2 SPNE SC/CE model – fixed parameters	84
4.1	Characteristics of the montmorillonite STx-1	91
4.2	Buffer substances	93
4.3	Volumes of NaHCO ₃ and Na ₂ CO ₃	94
4.4	Experimental conditions for the EXAFS samples	107
4.5	Specifications of the beamlines at ANKA and ESRF	109
5.1	Bond distances determined for montmorillonite	146
5.2	Literature data on bond distances	147
5.3	Reproducibility of EXAFS analysis – example γ -Al ₂ O ₃	153
5.4	Bond distances determined for γ -Al ₂ O ₃	154
5.5	Fit parameter for the soddyite model	154
5.6	Model parameters for Np(V) sorption on STx-1 and γ -Al ₂ O ₃	162
G.1	Batch experiments of this study	219
G.2	pH and Np(V) concentration range of the sorption isotherms	220
G.3	Summary of the EXAFS samples prepared	220

List of Figures

2.1	Edwin Mattison McMillan and Philip Hauge Abelson	13
2.2	Solubility of Np(V)	21
2.3	Radiotoxicity based on ingestion	23
2.4	Redox diagram	25
2.5	Eh/pH-diagram	27
2.6	Activity of nuclear waste	31
2.7	Multiple-barrier waste disposal concept	32
2.8	Sheet silicate layers	38
2.9	Illustration of triple-layered silicates	39
2.10	Empirical dissolution rate of montmorillonite	40
2.11	Silicon and aluminium release from montmorillonite	41
2.12	Cubic models of γ -Al ₂ O ₃	45
2.13	Dissolution of γ -Al ₂ O ₃	47
2.14	Molecular structure of surface complexes	51
2.15	Electric double layer model	54
3.1	Carbonate equilibrium	60
3.2	Solid-to-liquid ratio and curve shape	62
3.3	Interactions between X-rays and atom	68
3.4	EXAFS – probability of absorption	69
3.5	Possible scattering paths	70
3.6	Actinide XANES spectra	73
3.7	L _{III} -edge XANES spectra of neptunium	74
4.1	Research reactor TRIGA Mark II, Mainz	88
4.2	Cation exchange column and sand bath with infrared lamp	89
4.3	Fuming of the acid	90
4.4	Purification of NaClO ₄	92
4.5	Collection of the particle size fraction <0.5 μ m	96
4.6	Adjustment of ionic strength	96
4.7	Scales and rotator	98
4.8	pH adjustment	99

4.9	Centrifuges used for phase separation	100
4.10	γ detector	101
4.11	Aerial view of the ESRF	105
4.12	Glove box experiments	106
4.13	Preparation of the EXAFS samples	108
4.14	Rossendorf Beamline at the ESRF	109
4.15	Experimental hutch of the INE-beamline at ANKA	110
4.16	Pre-edge subtraction	112
4.17	Spline removal	112
4.18	EXAFS data	112
4.19	Fourier transform	113
4.20	Fitting of 1 st and 2 nd coordination sphere	114
4.21	Influence of neptunium concentration on modelling	115
4.22	Components of the modelled sorption curves	116
4.23	Extrapolation of the maximum capacity of γ -Al ₂ O ₃	117
5.1	Percentage sorption of Np(V) on STx-1 and γ -Al ₂ O ₃	121
5.2	Effect of neptunium concentration on sorption	122
5.3	Influence of ionic strength (γ -Al ₂ O ₃)	124
5.4	Sorption of Np(V) on kaolinite	125
5.5	Influence of ionic strength (STx-1)	126
5.6	Precipitation of neptunium carbonate complexes	128
5.7	Influence of CO ₂ on the absolute sorption	129
5.8	Np(V) sorption on montmorillonite and kaolinite	130
5.9	Np(V) sorption on γ -Al ₂ O ₃ and α -Al(OH) ₃	131
5.10	Aqueous speciation of neptunium	133
5.11	Solubility of NaNpO ₂ CO ₃	134
5.12	Measured and modelled sorption data	135
5.13	K _d -values for montmorillonite from literature and this study	136
5.14	K _d -values of the γ -Al ₂ O ₃ sorption isotherm	137
5.15	K _d -values for γ -Al ₂ O ₃ from literature and this study	138
5.16	K _a -values for pM and μ M Np(V)	140
5.17	EXAFS raw data and fit (STx-1)	143
5.18	Fourier transforms (STx-1)	145
5.19	Molecular structure of neptunyl aquoion and bi-carbonate	149
5.20	Fractional aqueous neptunium speciation	150
5.21	Influence of carbonate concentration on neptunium speciation	150
5.22	EXAFS raw data, fit, and Fourier transforms (γ -Al ₂ O ₃)	152
5.23	Comparison of two models for γ -Al ₂ O ₃	155
5.24	Saturation indices for Np ₂ O ₅	155
5.25	Effect of different neptunium loading on the EXAFS spectra	156

5.26	Possible binding modes of Np(V)-dimers	157
5.27	Comparative visualisation of the atomic distances	158
5.28	Modelled Np(V) sorption on montmorillonite – literature	160
5.29	Modelled Np(V) sorption on montmorillonite – best fit parameters	161
5.30	Modelled Np(V) sorption on γ -Al ₂ O ₃ – A	162
5.31	Modelled Np(V) sorption on γ -Al ₂ O ₃ – B	163
B.1	Electronic configuration of ⁹³ Np	199
B.2	Nuclear Wallet Card for neptunium	200
B.3	Colour of Np-ions in aqueous solution	201
C.1	Major decay paths for some actinides	205
C.2	Illustration of the decay chains	205
D.1	Swiss container for highly radioactive waste	208
H.1	Alternative periodic table	222
H.2	IUPAC periodic table of the elements	223

Abstract

This study comprised batch experiments, direct speciation studies via EXAFS, and modelling with the 2SPNE SC/CE model to elucidate the mechanisms of Np(V) sorption on montmorillonite and, for reference, on γ -Al₂O₃.

The sorption of pM ²³⁹Np(V) and μ M ²³⁷Np(V) on montmorillonite (STx-1, 4 g/L) and γ -Al₂O₃ (0.5 g/L) was studied at room temperature in the presence and absence of ambient CO₂ covering a pH-range from 2.5 (STx-1) or 5 (γ -Al₂O₃) to 10.5 with 0.01 or 0.1 M NaClO₄ as background electrolyte. The Np(V) uptake was determined by γ spectroscopy of the supernatants and calculated as percentage as well as distribution coefficient K_d . Sorption starts from pH \sim 6 and, under exclusion of CO₂, increases continuously, while, in the presence of ambient air, it reaches a maximum at pH \sim 8.5 (γ -Al₂O₃: $\log K_{dmax} \approx 4$ mL/g; STx-1: $\log K_{dmax} \approx 2.7$ mL/g). Beyond that it decreases again due to the formation of aqueous neptunium carbonate complexes. Furthermore, neptunium sorption on montmorillonite is influenced by ionic strength at pH $<$ 6 through ion exchange processes pointing towards the formation of outer-sphere surface complexes there. Isotherms measured at the sorption maximum showed the precipitation of presumably neptunium carbonate complexes above $3 \cdot 10^{-5}$ M under ambient air conditions. Additionally, they indicated progressive saturation of the sorption sites of γ -Al₂O₃. At selected pH (STx-1: 5.0, 7.0, 8.0, 8.5, 9.0, 9.5; γ -Al₂O₃: 8.5, 9.5) EXAFS samples were prepared as wet pastes with μ M ²³⁷Np and measured at room temperature in fluorescence mode at ANKA and ESRF. Several spectra were averaged and analysed with EXAFSPAK and FEFF 8.20 employing models of NaNpO₂(CO₃) or soddyite, (UO₂)₂SiO₄·2(H₂O). The shorter atomic distances of the neptunyl ion at pH 5 compared to the others hinted at the retention of the hydration shell and, thus, at outer-sphere sorption. On average the bond lengths for Np(V) sorbed on STx-1 at high pH were $O_{ax} \approx 1.84$ Å and $O_{eq} \approx 2.53$ Å. At high pH, ternary neptunyl carbonate surface complexes could be identified for montmorillonite ($C \approx 3.00$ Å), but not for γ -Al₂O₃, where an interaction of neptunium with the aluminium surface atoms according to the soddyite model gave better agreement with the experimental data. However, neither structure as suggested by the two models could be excluded for both systems rendering a combination most likely. Modelling of the sorption data provided further evidence for the existence of ternary neptunium carbonate surface complexes in both cases.

The results of this study can aid environmental risk assessment for clay-based nuclear waste repositories by providing valuable input data for simulations of radionuclide migration from a final disposal site.

Abbreviations and Terms

2 SPNE SC/CE:	Two Site Protolysis Non-Electrostatic Surface Complexation and Cation Exchange Model;
Actinide:	Member of the series comprising the 15 chemical elements between actinium and lawrencium with the atomic numbers 89 to 103;
Aluminium oxide:	Al_2O_3 , amphoteric oxide of aluminium existing in different crystalline modifications, e.g. as cubic $\gamma\text{-Al}_2\text{O}_3$;
Aquoion:	A hydrated ion; an ion containing one or more water molecules;
Batch:	Series of experiments in which only one parameter is varied, while all others are identical;
Bentonite:	Clayey rock consisting of a mixture of different minerals with smectite (usually montmorillonite) accounting for the main fraction (50-80 %) and impurities of quartz, glimmer, feldspar, pyrite, and calcite; it usually forms from weathering of volcanic ash;
Bidentate:	A ligand binding through two sites to the central metal atom or ion;
Brine:	Water (nearly) saturated with salt (>50 % NaCl);
CEC:	Cation exchange capacity;
Coordination sphere:	also: coordination shell; a set of same ligands attached to a metal ion or complex in similar distance; in EXAFS analyses specifically a group of atoms with identical properties like bond distance and chemical species;
EXAFS:	Extended X-ray Absorption Fine Structure;

Exotic nuclides:	Elemental isotopes, which are short-lived or at least have decayed on earth since it was formed and are not found in nature any more;
Functional group:	Sorption site; specific atoms within molecules that are responsible for their characteristic chemical reactions, e.g. the hydroxyl group $\equiv\text{S-OH}$ present on many mineral surfaces;
Inner-sphere complex:	The ion loses its hydration shell and binds directly to the mineral surface; mechanism of specific sorption to reactive surface sites through covalent binding;
Isotope:	Different nuclides of the same element; they have a different number of neutrons and, thus, differ in atomic mass and mass number (A), while their atomic number (Z) is the same; isotopes of the same element exhibit almost identical chemical behaviour;
Ligand:	Atom, ion, molecule, or (surface) functional group binding to a central atom or ion of a metal through a coordinate covalent bond;
Modelling:	Mathematical attempt to describe a (natural) system based on scientific theory; validated models can be used to predict certain scenarios;
Monodentate:	A monodentate ligand forms only one bond with the central atom, usually a metal ion;
Montmorillonite:	A clay mineral; dioctahedral triple-layered phyllosilicate of the smectite group;
Outer-sphere complex:	The ion is electrostatically bound to the surface retaining its hydration shell (unspecific sorption);
Neptunium:	First transuranic element with mass number 93, hence belonging to the actinide series; primordial, existing quantities are purely man-made;
Neptunyl ion:	The aqueous pentagonal bipyramidal neptunium(V) ion $\text{NpO}_2(\text{OH}_2)_5^+$;
Neptunyl unit:	The linear $\text{O}=\text{Np}=\text{O}$ unit of the neptunyl ion;
Sorbate:	Solute; substance in solution becoming sorbed;
Sorbent:	(Suspended) solid to which the sorbate is sorbed;

Speciation:	Analysis of the elemental species;
Species:	Chemical and physicochemical form of an element, i.e. isotopic composition, electronic or oxidation state, and/or complex or molecular structure; sometimes defined as an ensemble of chemically identical molecular entities, which are subject to a chemical process or to a measurement, such as atoms, molecules, molecular fragments, or ions;
Synchrotron radiation:	Electromagnetic radiation generated by the acceleration of ultrarelativistic (i.e. moving near the speed of light) charged particles through magnetic fields providing ultra-bright ultraviolet light and X-rays;
Ternary complex:	A three component complex comprising a metal cation and two different ligands other than water; those consisting of (actinide) ion, ligand, and coordinated (inner-sphere) water molecules are termed binary;
XANES:	X-ray Absorption Near Edge Structure;
X-rays:	Electromagnetic waves with energies ranging from ~ 500 eV to 500 keV, respective wavelength from ~ 25 to 0.25 Å; by far higher energetic than light.

1

Introduction and Motivation

The modern natural sciences have brought about great technical progress for mankind. In the beginning of the 19th century, Ernest Rutherford predicted and experimentally demonstrated the process of stimulated nuclear fission, induced by bombardment with accelerated particles. A few years later, Otto Hahn and Fritz Strassmann discovered natural spontaneous fission of uranium through identification of radioactive barium isotopes as fission fragments, later explained theoretically by their former colleague Lise Meitner. These findings stimulated great efforts within the scientific community, mainly driven by the search for new energy sources. Additional to the aforementioned contributors, many famous names are related to the intense research into this direction, like James Chadwick, Niels Bohr, or Albert Einstein, to mention just a few. Finally, it was Enrico Fermi who developed the first controlled nuclear fission reactor in 1942. For a more detailed chronology of the development of the nuclear industry refer to Appendix A of this thesis.

Unavoidably, the exploration of nuclear fission as an energy source went along with extensive military research into new weapons within the Manhattan Programme, which was dramatically concluded with the nuclear bombing of Hiroshima and Nagasaki in 1945 intended to end the Second World War. In spite of the horrible consequences of this event, the 1950th and '60th were characterised by an unparalleled arms race between the leading world powers connected with numerous nuclear tests in remote areas and corresponding significant radiotoxic contamination of the whole globe.

After the first flush of enthusiasm, the awareness of the dangers associated with nuclear fission, that was growing during the following decades, revealed the drawbacks of this technique. In particular, facing long term effects, further political activities focussed on international regulation for nuclear power usage as well as on concepts for final disposal of nuclear waste. Nowadays, the composition of burnt fuel from nuclear reactors is well known, but many questions are still open

concerning the environmental behaviour of the individual elements produced, of which several are purely man-made. The long-lived neptunium isotope ^{237}Np , for example, is not only created by irradiating uranium (^{235}U or ^{238}U) in a nuclear reactor, but also emerges from the slow decay of americium (^{235}Am) and, thus, will increase significantly during storage. After approximately one million years this element will dominate the radiotoxicity of nuclear waste and exceed today's safety limits. Furthermore, neptunium is quite soluble, poorly sorbed, and readily mobile under environmental conditions making it highly relevant for research within nuclear safety aspects.

By using nuclear fission as an energy source all industrialised nations are – ethically as well as legally – obliged to minimise the negative effects on future generations. Therefore, concepts have been developed on how to store the radioactive waste as safely as possible. While in the early times of nuclear activities it was simply dropped into oceans or landfills, deep geological repositories are favoured nowadays. The specifications vary according to regional availability and, of course, political climate. The main criteria considered are stability of the formation over geological timescales and low permeability for water. In Germany salt domes were the means of choice for a long time, but meanwhile investigations focus on granite formations influenced by recent trends e.g. in the U.S., in Switzerland, and in Scandinavia. Basically, the concepts employ vitrification of the waste and its welding in steel containers, which are stored in the rock and backfilled with concrete or clay. The latter material has been chosen due to its high sorption capacity for cations combined with a large surface area. Furthermore, clay can swell and shrink according to the water content, in this way closing any possibly emerging cracks immediately.

This work attempts to cover one particular aspect of the still large field of the unknown. Investigations concern the interaction of neptunium with the clay mineral montmorillonite, which is the major component of the clay of discussion, the abundant bentonite, under simplified but environmentally relevant conditions. For the initial experiments the montmorillonite was replaced by $\gamma\text{-Al}_2\text{O}_3$ in order to study the aluminol surface sites of the clay, which govern the sorption process. The neptunium concentration was chosen to be picomolar, representing the situation assumed for a possible release from the repository. Substitutional for the groundwater with its dissolved ions, NaClO_4 0.1 and 0.01 M was used as ionic background. Accordingly, the montmorillonite was purified and conditioned, and all exchangeable cations replaced by sodium. Batch experiments were conducted varying the pH, both under ambient air conditions as well as under exclusion of CO_2 , since dissolved aerial carbon forms aqueous neptunyl-carbonate complexes at high pH, in this way preventing neptunium from being sorbed.

The stability and, hence, the reversibility of sorption is dependent on the type of complex formed. If the neptunium keeps its hydration shell forming outer-sphere complexes, it will be readily removed from the surface again by cation exchange processes. Specific sorption instead involves inner-sphere complexation, where the neptunium ion is bound to the surface directly through mono- or bidentate bonds. To distinguish between these, speciation experiments were conducted applying EXAFS analyses. By this means, the bond distances between neptunium and its neighbours are measured using high energy synchrotron radiation. The samples had to be prepared with higher neptunium concentration in order to achieve a sufficiently high surface load. Merging the results, a consistent hypothesis was developed, describing the sorption behaviour of neptunium under the given conditions and elucidating its mobility in case of release.

The first chapter seeks to give an overview about this study and its intention. It brings together important properties of neptunium, its ions and environmentally relevant compounds including their aqueous speciation. Furthermore, it discusses the past and present production and use of neptunium as well as the current disposal concepts of nuclear waste. As part of most of these approaches, the use and benefit of clay minerals in repository sealing is discussed. Their structure and chemical behaviour regarding radionuclide retention is explained, pointing out the need of simplification when studying natural systems. In this case, montmorillonite was replaced by aluminium oxide during the first experiments. Subsequently, the reactions of radionuclides with clay minerals are elaborated to provide the reader with the necessary theoretical background information to understand the onset, proceeding, and results of this work.

The second chapter is dedicated to the technical aspects of this study, outlining the experimental frame, identifying the parameters of influence, and expounding their preset values and ranges, respectively. Afterwards, the analytical methods applied are introduced, together with some remarks on modelling. The detailed description of the experimental work, including chemical and technical specifications is given in a separate chapter, the third of this work.

The experimental outcome is shown, explained, and discussed in chapter four. It begins with the studies on the sorption behaviour of neptunium on montmorillonite and γ -Al₂O₃ as a function of pH, CO₂, ionic strength and sorbate concentration. Thereafter, the results of the direct speciation studies are presented. During this part, all findings are immediately compared to literature data in order to preserve the logical structure of the study. To complement the practical work, the results are processed by theoretical modelling, and the chapter concludes with a synthesis of the separate findings of sorption batch experiments, speciation analyses, and modelling.

The final chapter provides an integration of the present results into the scientific as well as the environmental context outlined before. The consequences for current safeguarding measures are discussed, the implications for further studies are emphasised, and some ideas for future research projects are provided.

The appendix comprises additional information for the interested reader as well as fundamental background knowledge, e.g. on radioactivity, for people who are laypersons in nuclear chemistry. Altogether, this work attempts to provide access to its contents not only for other disciplines, but also for ambitious non-scientists – motivated by the still large deficiencies in public awareness as well as in unambiguous perception of nuclear energy with its impact on nature and society.

2

Fundamentals

For comprehending context and aim of this study, some facts must be pointed out to emphasise the relevance of this topic. First, the nuclide in question must be known in its (radio-) chemical characteristics as well as environmental behaviour, including its physiological and radiotoxic properties. Second, its origin, abundance, present status of worldwide distribution, and possible fate need to be analysed to estimate current and future hazards evolving from its production and disposal. And finally, the relevant international covenants must be consulted to evaluate today's measures of mitigation.

2.1 Neptunium – History and Current Situation

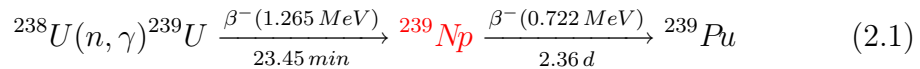
The periodic table developed by L. Meyer and independently by D. Mendeleev in 1869 initiated a search for those yet undiscovered elements that it predicted to exist. All elements with stable isotopes had been identified by 1925, and the investigation of radioactive decay of the already known elements uranium and thorium by Marie and Pierre Curie had led to the discovery of the naturally occurring elements with exclusively unstable isotopes such as protactinium, radon, or technetium. Stimulated by these findings, the scientific effort concentrated on the search for artificial elements which can only be produced through nuclear reactions. Special attention had been paid to the transuranic elements, since their discovery meant an extension of the periodic table to higher proton numbers $Z \geq 93$. E. Fermi started to work on this task in 1934, but his first products were identified as already known isotopes of uranium by O. Hahn and F. Strassmann, who in this way discovered the process of nuclear fission, rendering possible the development of the first nuclear reactor in 1942. The actual breakthrough in the synthesis of transuranic elements was made at Berkeley,

and within the following years to decades up to now main advances in the field were reached there, in Dubna, and in Darmstadt. The search still continues nowadays, reaching out towards the proclaimed superheavy elements within a predicted Island of Stability in the region around $Z = 120$.

2.1.1 Production and Global Inventory

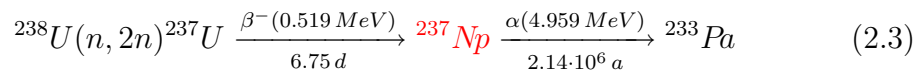
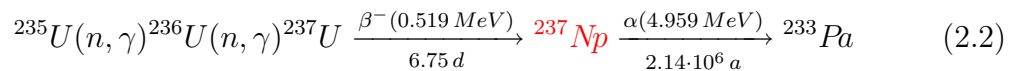
Neptunium ($Z = 93$) is the first of the transuranic elements and, hence, belongs to the actinide¹ series. It was initially synthesised by E.M. McMillan and P.H. Abelson at the Berkeley Radiation Laboratory of the University of California in 1940 (McMillan and Abelson, 1940) – Figure 2.1 shows historic photographs of these scientists at work –, for what the former of the two was awarded the Nobel Prize in chemistry together with G.T. Seaborg in 1951.

McMillan and Abelson produced the isotope ^{239}Np by exposing ^{238}U to slow cyclotron-produced neutrons (originating from beryllium bombarded with deuterium ions, McMillan, 1940):

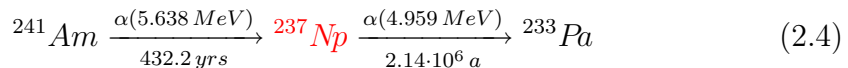


As indicated, ^{239}Np decays predominantly by β^- radiation with a half life of 2.36 d into ^{239}Pu .

Analogous to the element uranium the newly discovered elements were named after planets, Neptune and Pluto, according to their position “behind” uranium in the periodic table. The long-lived neptunium isotope present in nuclear waste, however, is ^{237}Np . It was discovered in 1942 by A.C. Wahl and G.T. Seaborg as a byproduct of plutonium production. ^{237}Np results from the irradiation of ^{235}U and ^{238}U , as well as from the decay of ^{241}Am in the reactions



and



¹As of recently, the term actinoides (in the style of metalloides for metal-like elements) is preferred by the International Union of Pure and Applied Chemistry (IUPAC), because the ending -id is reserved for binary salts such as hydride, chloride, or oxide. For reasons of convenience, however, the still tolerated old terminology is retained throughout this work.

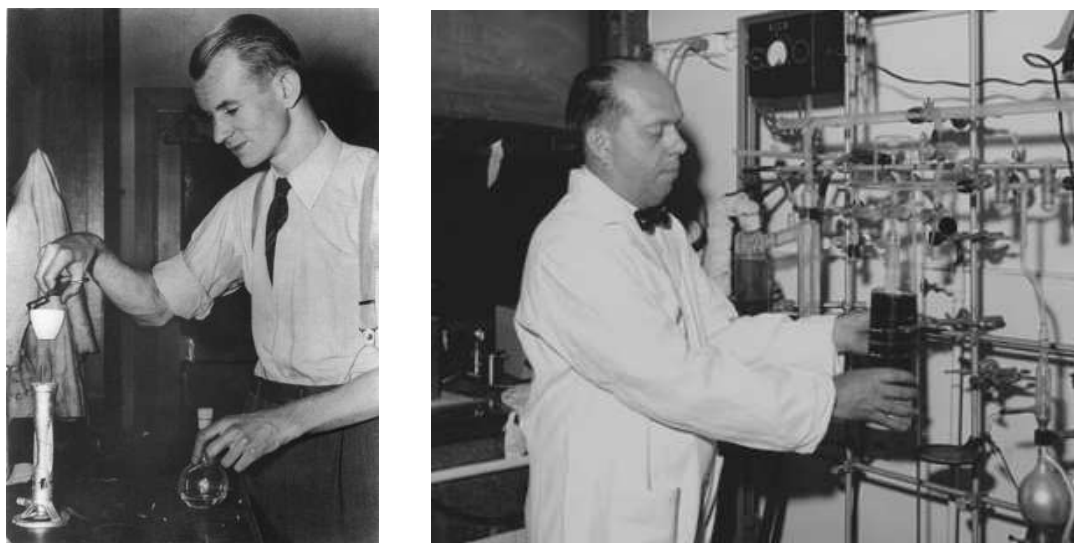


Figure 2.1: Edwin Mattison McMillan (September 18, 1907 - September 7, 1991), pictured 1940 (left) and Philip Hauge Abelson (April 27, 1913 - August 1, 2004) pictured 1947 (right).

Again as indicated, ^{237}Np decays predominantly by α radiation with a half life of $2.14 \cdot 10^6$ a into ^{233}Pa .

Until today 19 neptunium isotopes (plus three isomers) have been synthesised, of which all are radioactive (Yoshida, Johnson, Kimura and Krsul, 2006; Pfennig, Klewe-Nebenius and Seelmann-Eggebert, 1998). Among them, ^{237}Np has the longest half life (refer to Appendix B.2) and is the mother nuclide of the neptunium decay series (see Appendix C.3). However, since the age of the Earth is considerably larger (ca. $4.5 \cdot 10^9$ a), primordial neptunium no longer exists.

In nature only minuscule amounts of ^{237}Np are present in uranium ores ($^{237}\text{Np}/^{238}\text{U} \approx 10^{-12}$) produced by capture of neutrons originating from uranium decay and other processes. These include spontaneous fission of ^{238}U , neutron induced fission of ^{235}U , (α, n) -reactions on elements of low atomic number, and fission or spallation induced by cosmic rays (Yoshida et al., 2006; Lieser, 2001). These reactions are continuously taking place resulting in a dynamic equilibrium between the rates of formation and decay.

The total amount of ^{237}Np present on earth is not known precisely. The upper continental crust is said to contain approximately 2.8 ppm ^{238}U on average (Lawrence Berkeley National Laboratory, 2000). With an earth mass of $5.97 \cdot 10^{24}$ kg, of which 0.374 % account for the continental crust, and a ^{237}Np -to- ^{238}U ratio of $\sim 10^{-12}$, the total amount of natural ^{237}Np would be $6.3 \cdot 10^4$ kg. Holleman and Wiberg (2007) instead give an abundance of $4 \cdot 10^{-17}$ % for ^{237}Np

in the earth's crust which equals $2.4 \cdot 10^5$ kg. This high total amount is seemingly due to the authors basing their calculations on a much lower weight of the earth's crust, namely $5 \cdot 10^{17}$ kg (quantified from backwards calculations of values given for uranium). Using this specification, the amount of neptunium in the earth's crust would amount to $2 \cdot 10^4$ kg according to these authors.

The natural background of most radioactive isotopes has been significantly increased by anthropogenic activities, particularly the atmospheric and underground nuclear weapon tests, as well as by satellites containing ^{238}Pu , which burned up in the atmosphere (Holleman and Wiberg, 2007). The resulting global fallout is estimated at 2 500 kg of ^{237}Np (Yoshida et al., 2006). By far the largest amount of neptunium released into the environment, however, can be attributed to the operation of nuclear power plants. The total amount of ^{237}Np produced by the nuclear industry was estimated to be $5.4 \cdot 10^4$ kg at the end of 2003, annually increasing by about 3 000 kg (Albright and Kramer, 2005). Thus, any threat resulting from neptunium, that mankind is exposed to, can be regarded as originating from a predominantly artificial element.

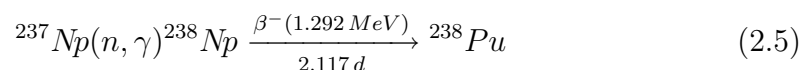
2.1.2 Industrial Usage and Application

In conventional nuclear reactors, ^{237}Np is generated as a byproduct according to reactions 2.2 and 2.3, whereby the former prevails in fuels of enriched ^{235}U (Yoshida et al., 2006). A typical 1 000 MW light-water reactor generates about 10 kg of neptunium per year (Albright and Barbour, 1999). Its decay products will remain a radiotoxic hazard long after plutonium, americium, and curium will have decayed (Albright and Kramer, 2005).

Partitioning and transmutation programs, that have been developed for transferring long-lived actinides into isotopes with shorter half lives or stable elements by fission or neutron capture, also focus on ^{237}Np . It is most efficiently separated from nuclear fission products through the PUREX (plutonium and uranium recovery by extraction) process (Albright and Kramer, 2005). Except for neutron detection instruments, there are only limited commercial uses for neptunium. One argument for its purification is the production of ^{238}Pu by bombardment of ^{237}Np with neutrons (Equation 2.5), which is used in nuclear batteries – precisely radioisotope thermoelectric generators (RTGs) and radioisotope heater units (RHUs) – for the energy supply of e.g. spacecrafts, satellites, cardiac pacemakers, or deep sea diving suits.

Comparably much more important for industrial application is the spontaneous fission isotope ^{239}Pu , which is produced through irradiation of ^{238}U followed by β^- decay of ^{239}Np (see Equation 2.1). After oxidation and extrac-

tion, it is used as fuel for plutonium reactors and for nuclear weapons (Yoshida et al., 2006; Holleman and Wiberg, 2007; Argonne National Laboratory, 2005).



Use of neptunium in weapons

Theoretically, ${}^{237}\text{Np}$ is also considered to be useable in nuclear weapons, but no country has declared so far to have applied it as material for a nuclear explosive device. Having a critical mass of 56 kg (IAEA, cited in Albright and Kramer, 2005) to 73 kg (Yoshida et al., 2006), and, when in metal form, being easier to compress than highly enriched uranium, about 30 kg of ${}^{237}\text{Np}$ or even less would be sufficient to create an explosive device. Due to its long half life no heat or radiation properties would complicate its use, and because of a low neutron background it could, in principle, also be used in a gun-type device (Albright and Barbour, 1999).

In response to the globally growing interest in separating particularly neptunium and a few other nuclides from fission products to ease radioactive waste disposal, the International Atomic Energy Agency (IAEA) has initiated a monitoring programme to track the current stocks of purified neptunium (Albright and Kramer, 2005). In contrast to the different americium isotopes, which are considered neglectable in terms of terroristic utilisation, a limited but increasing risk of proliferation for ${}^{237}\text{Np}$ is existent (Filges, 2002) requiring persisting awareness on this issue.

2.1.3 Releases into the Environment

As already mentioned, the main source of radioactive material in the environment were atmospheric as well as underground nuclear weapon tests (Runde, 2000). Considerable amounts of fission products and radioelements have been released and distributed via the atmosphere as radioactive fallout over large areas, particularly in the northern hemisphere. Local concentrations, however, are generally low (Lieser, 2001).

In comparison to this accepted distribution through wilful activities, the total amount of radioactivity accidentally released from nuclear power plants and research sites has been relatively small and is limited to only few severely contaminated locations, e.g. at Oak Ridge, Los Alamos, Rocky Flats, the Irish Sea, and, of course, Chernobyl (Allard, Olufsson and Torstenfelt, 1984). Apart from these unintended contaminations – which might be locally severe but which

are globally of rather low relevance – the far majority of radioactive waste is currently stored in well guarded aboveground temporal storage facilities. Final disposal is planned in deep geological formations to isolate the radioactive waste, which might pose a risk to ecosystems as well as to public health, from the living environment for thousands of years.

Neptunium, being also a byproduct of plutonium production, is present in all stages of the nuclear fuel cycle: in high-level radioactive waste from the processing of spent nuclear fuel as well as in radioactive waste associated with the operation of reactors and from fuel processing plants (Argonne National Laboratory, 2005). As ^{237}Np is the daughter nuclide of ^{241}Am and the granddaughter of ^{241}Pu , it emerges through radioactive decay in nuclear waste containing these isotopes, and can then, due to its suspected, comparably poor sorption properties, escape from the repository more easily than the initial parent elements. Within large timescales it is possible that water may infiltrate the repository and corrode the containers, releasing the fission products and their decay products into the environment. For such a scenario, the concentration of actinides in natural waters, generally and of ^{237}Np in particular, is anticipated to be 10^{-6} M or less (Runde, 2000).

Depending on the site-specific chemical conditions determined by the mineral composition of the repository, the actinides will behave differently (see Section 2.2.1 below). While in extremely salty brines of geological salt domes plutonium is the most mobile element, neptunium becomes the one of concern in granite formations, where it is over a thousand times more mobile compared to the former (Runde, 2000). Thus, two key natural barriers to actinide spreading are their solubility and their sorption; this work will concentrate on the latter aspect. In this way it will contribute to evaluating and ensuring the long-term safety of permanent geological repositories.

2.2 Chemical and Radiochemical Characteristics of Neptunium

As a member of the actinide series (see periodic table on page 223), which is located within the 6d transition elements in the seventh period next to actinium, neptunium behaves as a metal. The actinide series is characterised by step-wise occupation of the atomic 5f orbitals. Since these electrons extend farther out from the atomic core and, hence, are relatively easy accessible, most of the actinides, including neptunium, exhibit multiple oxidation states and form numerous molecular species of distinct chemical behaviour.

On the basis of decay properties, availability, and distribution, only six of the fourteen actinide elements are of long-term environmental concern, namely Th, U, Np, Pu, Am, and Cm (Clark, Hobart and Neu, 1995). Metallic neptunium belongs to the orthorhombic crystal system (α -phase), which is stable up to ca. 280°C where it transforms into a tetragonal crystal system (β -phase). Above 576°C, neptunium is present in a bcc crystal system (γ -phase) until it melts at 639°C (Gutowski, Bridges and Rogers, 2006).

Free actinides reveal a base character and a high chemical activity; when heated they react with most nonmetals (Holleman and Wiberg, 2007). Resulting from the effective charges of the ions, those of the third oxidation state form the strongest and those of the fifth the weakest complexes (Runde, 2000). Neptunium can exist in the oxidation states III to VII, most of which are only formed under rather unusual conditions such as extreme redox potentials, radiolysis, or elevated temperatures (Clark et al., 1995). Under a wide range of (environmental) conditions neptunium speciation is dominated by the pentavalent cation NpO_2^+ (Lieser, 2001).

Generally, the actinides form non-stoichiometric oxides as well as hydrous oxides, hydroxides, and peroxides. In the case of neptunium these are $\text{NpO}_3 \cdot \text{H}_2\text{O}$, Np_2O_5 , and NpO_2 (Holleman and Wiberg, 2007). In spite of the five oxidation states, there are only two known anhydrous oxides, NpO_2 and Np_2O_5 ; the former is synthesised by thermal decomposition of different neptunium compounds of any oxidation state. It is extremely stable over a wide range of temperatures and pressures, while Np_2O_5 decomposes to NpO_2 and O_2 above $\sim 400^\circ\text{C}$ (Yoshida et al., 2006). Anhydrous neptunium oxides beyond Np_2O_5 are not known. NpO_2 is isostructural adopting the face-centered cubic (fcc) structure, where the cations occupy the closest packing sites and the anions fill the tetrahedral holes resulting in a coordination number of eight. Due to the high formal charge on the neptunium atom, the binding is strongly covalent, so that any compounds formed reveal unusually high melting points (Gutowski et al., 2006).

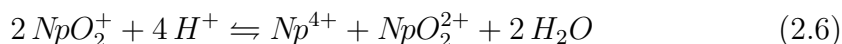
Since hydroxides and hydrated oxides, particularly those of Np(V), play an important role in the context of disposition of nuclear waste, the following section gives an overview of their reactions and behaviour in aqueous media.

2.2.1 Aqueous Chemistry

All stability studies of ionic compounds are based on the enthalpy of formation of the corresponding aqueous ion, as this property represents the fundamental parameter (Konings, Morss and Fuger, 2006). The thermodynamic properties of the lighter actinide elements U to Cm are fairly well established, although

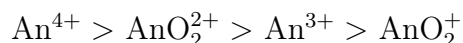
for actinide ions in aqueous solution the data are far from being complete or even satisfactory. Especially the hydroxides have hardly been studied at all, and the few experimental results available so far are not consistent (Konings et al., 2006). Data of the chemical thermodynamics for Np(V) oxides, hydrates, and hydroxides have been extensively reviewed by Lemire et al. (2001), page 105-129 (updated by Guillaumont et al., 2003) and shall not be discussed here in detail; emphasis is rather put on the qualitative and comprehensive description of the aqueous speciation of neptunium in the context of a possible release into the environment. As stated above, all processes related to the escape from a repository and subsequent transport through the environment will primarily take place via (subsurface) water. General information on the coordination chemistry of actinides in aqueous solution is readily available in literature, e.g. in the review by Szabó, Toraishi, Vallet and Grenthe (2006). The following paragraphs summarise the most important features in the context of the present study.

In aqueous media, Np(V) and Np(VI) hydrate instantaneously forming the linear *trans*-dioxo cations NpO_2^+ and NpO_2^{2+} , which are often referred to as the neptunyl ions (Runde, 2000) that are linear and symmetric (Gutowski et al., 2006). The latter is stable in acidic solutions predominating at pH 3-5, but is rather easily reduced to NpO_2^+ (Lemire et al., 2001). At high neptunium concentration and acidity, the two species are additionally connected via disproportionation, for which the reaction rate is extremely slow, though (Choppin and Jensen, 2006):



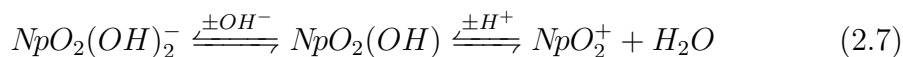
The simple pentavalent aquoion comprises about 95 % of the total soluble neptunium concentration (Choppin, 2006a), so that Np(V) is the most stable oxidation state in aqueous solutions. Due to the strong ion-dipole interactions of actinyl ions with water, the binding of H_2O -molecules in the first hydration sphere may cause the development of further layers attached by dipole-dipole bonds (Choppin and Wong, 1998).

Hydrolysis of elements in the oxidation states III, IV, and VI occurs in weakly acidic to alkaline solutions and often prevails over complexation reactions in neutral to basic solutions (Choppin and Jensen, 2006). Because of the positive charge of the metal ions, water molecules are polarised sufficiently to release protons, whereby the strength of hydrolysis reflects the effective charges of the actinide atoms following the order



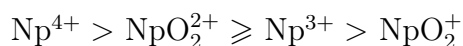
All actinides except for the pentavalent ions are significantly subject to hydrolysis at pH-values encountered in natural waters; the fifth is the most stable

oxidation state in water and does not hydrolyse significantly below pH 7 (Lemire et al., 2001). The products of hydrolysis can be monomeric, polynuclear, or colloidal (Loveland, Morrissey and Seaborg, 2006). Only at high pH, Np(V) forms the hydrolysis products $\text{NpO}_2(\text{OH})$ and $\text{NpO}_2(\text{OH})_2^-$ (Clark et al., 1995, see Figure 5.10 on page 133). Under such conditions, Np(V), and similarly Np(VI), exist as hydroxides and hydrated oxides (Konings et al., 2006). Noteworthy is the amphoteric character of Np(V):



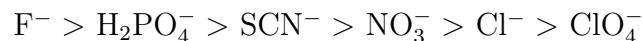
Regarding their reaction chemistry, actinide ions in all common solution oxidation states are hard Lewis acids. Their bonding with ligands is of mainly ionic character resulting in kinetically labile, non-directional bonds, and a profound preference for ligands with hard Lewis base donor atoms. The degree of covalence in actinide-ligand bonds is very small, if existent at all, so that the coordination geometry is not determined by the directionality of the overlap of the binding orbitals. The most distinct covalent effect becomes apparent in the short $\text{O}=\text{An}=\text{O}$ bonds in the linear dioxo actinyl ions. The bond strengths are determined primarily by electrostatic attraction and steric constraints, too, leading to large and variable coordination numbers. In the actinyl ions, the two oxo groups on a linear axis provide an inherent limitation to the number of ligand donor groups that can bind with the actinyl cations (Choppin and Jensen, 2006). Hence, the ligand binding is restricted to the equatorial plane perpendicular to the dioxo structure.

The actinyl ions behave like large singly charged alkali metal cations without any noteworthy tendency for precipitation and complexing reactions (Holleman and Wiberg, 2007). Thereby, compared to its analogues as well as to its other oxidation states, Np(V) is even more noncomplexing and, likewise, resistant to precipitation. Correspondingly, the stability constants of Np(V) complexes are relatively low compared to Np(III, IV, and VI) (Lieser and Mühlenweg, 1988). Like the hydrolysis reactions, the tendency of neptunium ions for complex formation is determined by their ionic potential, i.e. formal charge divided by ionic radius, giving an ordering of



(Lemire et al., 2001). Thereby, the hydration of the cations themselves is a critical factor in structural and chemical behaviour of their complexes, because the formation of inner-sphere complexes (see Section 2.5.1 below) involves the displacement of one or more water molecules by each ligand (Choppin and Jensen, 2006).

The exact character of the bonds formed within a complex, however, is determined by the oxidation state of the actinide and the hard or soft properties of the ligand(s). The stability sequence of neptunium complexes with monovalent inorganic ligands is



and with divalent ligands



as expected from the strength of the corresponding acids² (Lemire et al., 2001). Generally, divalent ligands are more strongly complexing than monovalent ligands, and hydrated compounds and higher order complexes are more stable than anhydrous binary compounds (Gutowski et al., 2006). The latter fact is due to the release of water molecules during complexation into the bulk solution, which contributes to entropy – although this effect might partly be offset by an increase of enthalpy (Choppin and Jensen, 2006). Nevertheless, the neptunium complexes with carbonate ligands studied within the scope of this thesis are the most significant among those present in nature, as discussed in more detail below.

Interestingly, pentavalent actinyl ions are even able to form cation-cation complexes, because their axial oxygen atoms have a residual negative charge that allows them to form weak electrostatic bonds with other cations. Such polymeric structures of NpO_2^+ molecules, however, are not important in solutions as long as the neptunium concentrations are small, and the actinyl ions are fully hydrated (Choppin and Jensen, 2006).

Solubility of Neptunium

Theoretical calculations of neptunium solubility often give wrong, too low results. Especially predictions using thermodynamic data only (compare Section 3.3), e.g. for the dissolution of stable crystalline solids, are usually significantly lower than experimental data. This finding is caused by the fact that solubility is controlled by the surface properties of the substance in question, which vary between natural and synthetic particles (Fanghänel and Neck, 2002). Since the stability of solids normally increases with their ageing, laboratory values can generally be regarded as conservative upper limits for environmental actinide concentrations.

²Concerning this work, it should be noted that the perchlorate media used is the least complexing counterion available.

Experiments studying the influence of pH on the solubility of NpO_2^+ observed a decrease with increasing pH, which was connected to the elevated formation of CO_3^{2-} , and identified a sodium neptunium carbonate hydrate as solubility limiting solid (Nitsche, 1991). However, under CO_2 -free conditions, too, the solubility of Np(V) decreases with pH, as shown in Figure 2.2. In both cases, a minimum is traversed at pH 9 and 12, respectively, beyond which the solubility increases again. No significant temperature dependency was observed between 25 and 90°C.

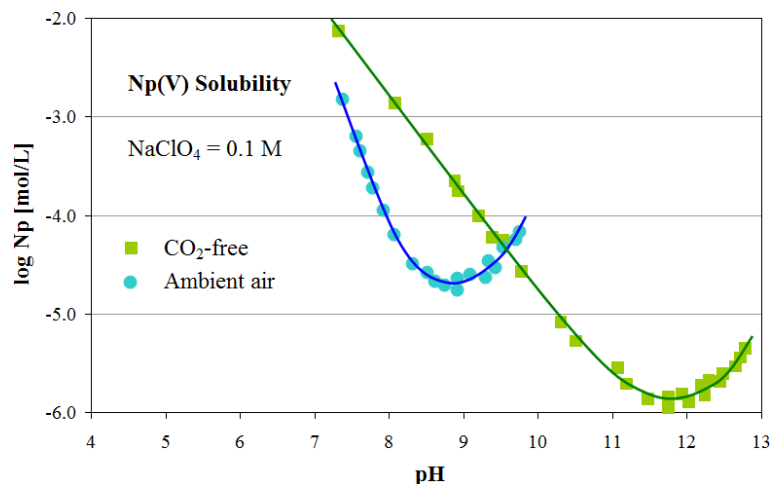


Figure 2.2: Solubility of Np(V) as function of pH under exclusion and atmospheric pressure of CO_2 . Increasing CO_2 concentration shifts the curve further towards more acidic pH (not explicitly shown; Meinrath, 1994).

2.2.2 Radioactivity

Only certain combinations of neutron (N) and proton numbers (Z) form stable nuclei. At low atomic numbers ($Z < 20$), isotopes with N/Z -ratios around one are stable, whereas a progressively larger proportion of neutrons is necessary to ensure stability at higher atomic numbers (Siegel and Bryan, 2003). All nuclei with N/Z -ratios differing from this restriction, which defines the so-called valley of β -stability, are unstable and, correspondingly, subject to radioactive decay. The latter results in changes in proton and neutron number, with the nucleus undergoing a transformation into another element. Appendix C.1 gives an overview of the different types of radioactive decay, of which α decay (i.e. emission of a ${}^4\text{He}$ nucleus) and β^- decay ($n \rightarrow p + e^- + \bar{\nu}$) are of relevance here.

Often a daughter nuclide again is unstable and even a whole series of unstable intermediate nuclides – as for many actinide isotopes – might be passed until

the final stable nuclide is reached. The few possible α decay chains are shown in Appendix C.3. Apart from fission products and their daughter nuclides, the radioactive inventory of nuclear waste is formed by those often short-lived decay chain nuclides in spite of their relatively low concentrations (Siegel and Bryan, 2003). After several half lives, the radioactive parent is in secular equilibrium with its daughter nuclide(s), wherein the relative contribution of each nuclide to the total radioactivity stays constant.

Neptunium is the dominant decay product of ^{237}Pu and ^{241}Am (see Section 2.1.1). With a considerable half life of $2.14 \cdot 10^6$ years, it decays via several transient daughters to the stable ^{209}Bi , thereby emitting seven α and four β^- particles aside of numerous γ rays (cf. Appendix C.3).

2.2.3 Aspects of Toxicity – Health Effects

In general, ionising radiation passing through tissue excites or ionises the component atoms through breaking up their molecular bonds. In this way, the genetic material (DNA) is damaged, altering the functional and/or reproductive behaviour of the cell. Radiation-induced injury can thereby be differentiated into deterministic and stochastic effects. The former are usually related with high doses causing acute symptoms of radiation disease and are characterised by a threshold. The latter represent the opposite dose risk, which appears without a threshold and might lead to the development of radiation induced cancer types (Magill and Galy, 2005). The dose itself is determined by the intensity, energy, and type of the radiation, exposure time, disposed energy, and affected organ or part of body.

Figure 2.3 shows the biological risk arising from spent fuel and corresponding high-level nuclear waste through a comparison of the emitted radioactivity. The fission products are comparably short-lived and dominate for only ~ 100 a, with their contribution to the total radiation hazard becoming completely neglectable after 1 000 a. Up to 10 000 a, americium and plutonium decay accounts for the greatest share, while later on – due to its extraordinary long half life and additional feeding through ^{241}Am decay – the radioactivity of ^{237}Np and the decay chains will dominate the risk.

To address the environmental hazard of the individual radioactive isotopes, however, further aspects must be considered: The elements and corresponding radioactive isotopes of relevance will exist in different oxidation states and, thus, exhibit significant differences in their mobility, which will even undergo alterations depending on extraneous influences. This fact is a central part of the motivation for this work. In general, neptunium is more environmentally mobile than other transuranic elements and is more readily absorbed by living

organisms. This property may easily enhance its radiation hazard in case of an escape into the environment by a considerable factor of up to a few orders of magnitude and, thus, will require consideration notwithstanding its longevity.

In animal studies, furthermore, the ratio of neptunium deposition in bone and liver is significantly greater than that of other transuranic elements (Thompson, 1982). In plants, the assimilation usually declines in an order reverse to that of hydrolysis, namely $\text{Np(V)} > \text{U(VI)} > \text{Am(III)} > \text{Pu(IV)}, \text{Np(IV)}$ (Loveland et al., 2006). The accumulation of actinides from water to food, however, generally “appears to be fairly well compensated for by metabolic discriminations against these elements” (Allard et al., 1984). Correspondingly, compared to other heavy metals, the ratio of 0.05 % absorbed into the blood from ingested neptunium is fairly small. Thus, lifetime cancer mortality risk coefficients are much higher for the inhalation path. Of ingested amounts, typically 35 % are excreted directly via the kidneys, while 15 % are accumulated in liver and skeleton with biological half lives of about 20 and 50 years, respectively (Argonne National Laboratory, 2005). The major health risk for human safety is, therefore, addressed to the development of cancer resulting from the ionising radiation emitted by the

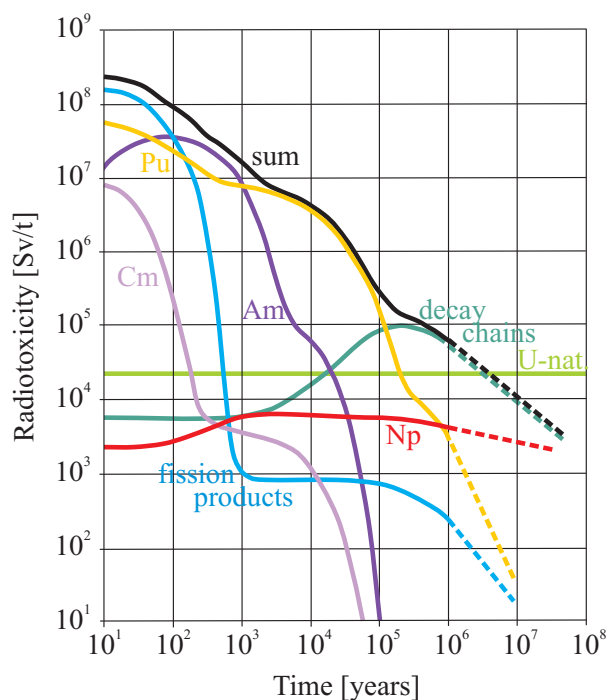


Figure 2.3: Estimated contributions to radiotoxicity based on ingestion by radioactive nuclides disposed with nuclear reactor waste and their daughter nuclides (enrichment: 4 % ^{235}U ; burn-up: 50 GWd/t; based on Kim, 2006).

deposited percentage of radioactivity including that of the daughter nuclides. In case of ^{237}Np , for example, it is dominantly caused by the high specific activity of its daughter ^{233}Pa (Argonne National Laboratory, 2005). In contrast to the radiotoxicity, the acute toxicity of neptunium as a typical heavy metal is negligible due to its minuscule concentration and low ingestion danger.

As an environmental pollutant, the potential risk arising from neptunium is, of course, strongly related to its chemical properties, dispersion and distribution, as well as to biological availability.

2.2.4 Neptunium in the Environment

The prominent hazard of any nuclear waste disposal is the potential dissolution and escape of radioactive nuclides from the repository along with subsurface waters into the biosphere. Similarly, the widespread usage of radioactive material in connection with the nuclear fuel cycle has increased the risk of accidental releases into the environment during handling or transport. Additionally, an intentional distribution by terrorists or maniacs must be considered. The fate of radionuclides in the biosphere – i.e., their solubility, migration potential, and effect on biota – is governed by interdependent processes determining chemical speciation, oxidation state, redox reactions, and sorption characteristics. These control transport mechanisms, bioavailability, and interactions with omnipresent carbonates as well as with humic substances and other ligands.

Kinetic patterns of the aforementioned processes largely depend on the origin and initial form of the actinide. Therefore, radionuclides released into the environment are divided into source dependent and source independent elements. In the vicinity of a repository, usually source dependent species are found, which normally do not attain thermodynamic equilibrium for long time periods (Choppin, 2006b). Especially their migration behaviour is strongly related to the chemical form, in which the contaminants are introduced into the aquatic systems surrounding the repository. The latter, so-called source independent elements, instead, reflect the environmental conditions much faster – they e.g. dissolve more readily soon after their release. They exhibit much more rapid kinetics than the former. Over time, however, the source specific species are modified to become source independent with their behaviour depending on the environmental conditions.

The Environmental Behaviour of Actinides

Nowadays, the environmental geochemistry of the actinides is considered of high relevance owing to their radiotoxicity and ongoing integration of anthro-

pogenic contributions into different (bio-) geochemical compartments and cycles (Misaelides and Godelitsas, 1999). The upper limit of the actinide concentration in environmental aquatic pathways is determined by precipitation and dissolution of their solids, while redox reactions and complex formation govern distribution and stability of their individual species. Figure 2.4 depicts the speciation of neptunium and other actinides as a function of the redox potential. The interaction of a dissolved species with mineral surfaces and/or colloids, in return, controls if and how the actinide will migrate through the environmental structures in question.

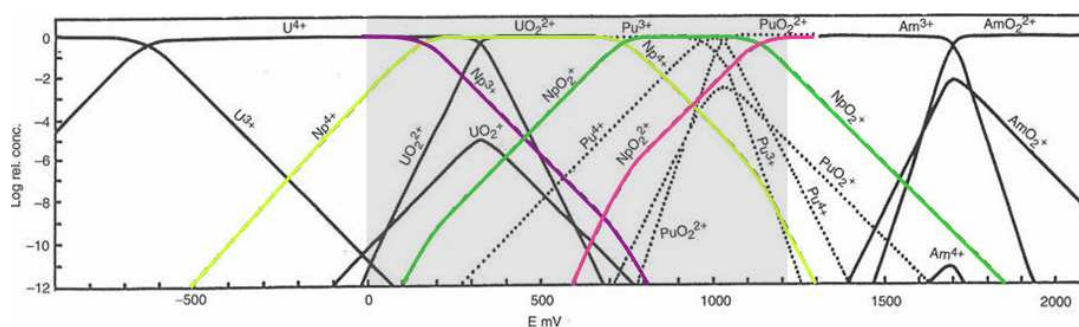


Figure 2.4: Redox diagram for U, Np, Pu, and Am in 1 M NaClO₄ (25°C); grey area – stability field of water (Choppin et al., 2002, cited in Loveland et al., 2006, modified).

When developing a scenario of radionuclide release from a repository, a possibly elevated temperature in the vicinity of the high-level waste must be considered. Studies have shown, for example, that neptunium solubility will rise with increasing temperature in oxidising solutions, while under reducing conditions it is widely temperature independent (Lemire 1984, cited in Dozol and Hagemann, 1993).

Favoured Oxidation States

As pointed out in Section 2.2.1, neptunium is stable in its fifth oxidation state under usual environmental conditions; Np(IV) is only occurring in the absence of oxygen, while Np(III) and Np(VI) can just exist under extremely reducing or oxidising conditions or under the influence of radiation (Choppin and Jensen, 2006). Hence, the redox reactions encountered in the far field of nuclear repositories as well as in most groundwater or ocean environments do not induce considerable changes in neptunium speciation.

Under less severely reducing conditions (e.g. in the presence of Fe²⁺) found in some natural groundwaters, the tetravalent species, mainly Np(OH)₄ or NpO₂ ·

n H₂O (Lieser and Mühlenweg, 1988), could possibly dominate the aqueous speciation for concentrations not above 10^{-10} to 10^{-9} M and NpO₂(s) being the solubility-limiting phase (Allard et al., 1984). Such reducing conditions might be promoted by the release of Fe²⁺ and H⁺ from corrosion in the vicinity of the disposed waste canisters, but according to Dozol and Hagemann (1993) an oxidising environment will, nevertheless, be established due to radiation and elevated temperatures. Thus again, as well as in oxic natural waters, Np(V) is expected to be by far the most commonly appearing oxidation state.

A detailed study delivers further possibilities for an occurrence of neptunium also in other oxidation states: Bentonite pore water has reduction properties with a redox potential (Eh) below -100 mV caused by mineral impurities of α -Fe₂O₃ and γ -Fe₃O₄, which would favour the fourth oxidation state (Sabodina, Kalmykow, Artem'eva, Zakharova and Sapozhnikov, 2006). Similarly, Np(V) can be reduced to the fourth oxidation state directly on the surface of a mineral like observed, e.g., for pyrite (Allard et al., 1984). The Eh range of most natural aquifers, however, starts from -300 or -200 mV and extends to +500 or even +700 mV (Loveland et al., 2006; Runde, 2000) promoting the possible simultaneous existence of several oxidation states of neptunium at certain pH values. This relationship can conveniently be illustrated in an Eh/pH-diagram, as presented in Figure 2.5. As indicated, all natural waters experimentally analysed by Loveland et al. (2006) exhibit conditions, which clearly promote Np(V), either dissolved or in crystalline form. As unavoidable simplification the diagram does not consider kinetic aspects. It only includes thermodynamically feasible reaction products and just shows the predominant compound, while coexisting species in lower concentrations do not appear.

Concerning a possible temperature dependency, there is little difference in neptunium speciation over the range of 25-150°C, only the field of NpO₂CO₃⁻ predominance increases with temperature (Dozol and Hagemann, 1993). Nevertheless, neptunium speciation could be affected by sunlight, as shown by Shilov and Yusov (2001). Photochemical reactions include oxidation of Np(IV) to Np(V) and reduction of Np(VI) to Np(V). After several hours of exposure to light, an equilibrium different from the initial oxidation state composition will be reached in solution. These processes are also controlled by the HCO₃⁻-to-CO₃²⁻ ratio (i.e. pH), but they are independent from the oxygen concentration. The fraction of Np(VI) increases with pH to, e.g., 95 % in 1 M Na₂CO₃ and 70 % in 1 M NaHCO₃. However, such light-induced processes can occur only in shallow surface waters and can be regarded negligible in a general safety assessment of a radionuclide release scenario. Hence in conclusion, aspects of changes in oxidation state within the given system are neglected in the present study and the focus is given to investigation of the fifth oxidation state.

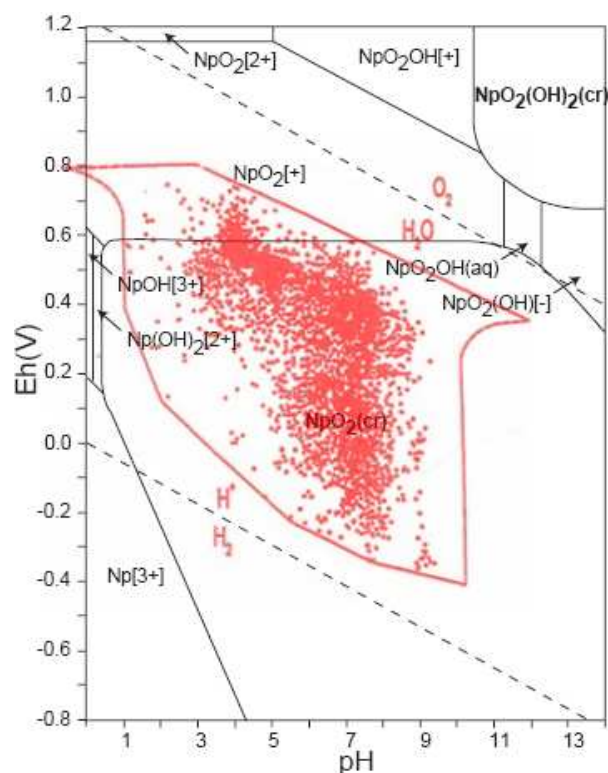


Figure 2.5: Eh/pH-diagram of the system Np-O-H ($c_{\text{Np}} = 10^{-10}$ M; 25°C; 10^5 Pa), calculated from thermodynamic data published by OECD/NEA (Takeno, 2005); dashed lines – stability field of water. The red area shows the range of pH and Eh in natural waters, the red dots represent empirical measurements (Loveland et al., 2006).

Complexation with Natural Ligands

Complexation with different ligands, preferably with oxygen-containing hard bases, reveals a great influence on neptunium behaviour in solution. Ligands often stabilise the aqueous phase and, in this way, enhance neptunium mobility. Under certain circumstances, however, such complexes might move from solution to mineral surfaces by coprecipitation.

The most important inorganic complexing components in natural systems are carbonate, chloride, phosphate, sulfate, fluoride, and silicate. Since fluoride, sulfate, and phosphate ions are generally present in much lower concentrations and, furthermore, are suppressed by the formation of sparingly soluble compounds with calcium, their influence on neptunium complexation can be neglected. Also, the chloro complex is much less stable than the hydroxo complex, even in high

salinity groundwaters and brines (Lieser and Mühlenweg, 1988) excluding chloride from the list of potentially important complexing agents. Silicate is soluble to a significant extent only above pH 9, ruling out its ions as likely complexing ligands in the vast majority of natural systems. This leaves carbonate as the most important inorganic ligand in solution, which is further supported by the lower stability constants of complexes with the other ions (see Section 2.2.1). Since the solubility of CO_2 is limited to alkaline environments and increases with pH, it becomes relevant for neptunium complexation beyond pH ~ 8 .

In typical groundwaters, $\text{NpO}_2(\text{CO}_3)^-$ will, therefore, be the predominant solution species aside of NpO_2^+ (Eckhardt, 2000). At both high pH and elevated carbonate concentration, bishydroxo- and hydroxy-carbonate species are the important solution species, exhibiting neptunium solubilities, which are two to three orders of magnitude higher than those encountered for, e.g., Np_2O_5 (Siegel and Bryan, 2003). Additionally, neptunium carbonate complexes are environmentally relevant due to the high abundance not only of CO_2 itself, but also of carbonate-containing minerals such as calcite, CaCO_3 , and dolomite, $\text{CaMg}(\text{CO}_3)_2$, which are estimated to contain more than 80 % of all carbon on earth (Clark et al., 1995).

Expected Mobility

Neptunium is perhaps the only actinide favouring the fifth oxidation state under a wide range of environmental conditions. Therefore, it is predicted to be the most highly soluble and mobile actinide in the environment, considering similarly the repository surroundings as well as most natural waters (Runde, 2000). The apparent diffusivity for $\text{Np}(\text{V})$ in, e.g., compacted bentonite is ten to 100 times higher compared to low-valent actinides like $\text{Am}(\text{III})$ or $\text{Pu}(\text{IV})$ (Allard et al., 1984). Since $\text{Np}(\text{V})$ forms the weakest complexes among the actinides (see Section 2.2.1), the corresponding solids $\text{Np}_2\text{O}_5(\text{s})$ and $\text{MNpO}_2(\text{CO}_3) \cdot n\text{H}_2\text{O}(\text{s})$ ($\text{M} = \text{alkali metal cation}$) are the most soluble³. As pointed out by Eckhardt (2000), solid $\text{Np}(\text{V})$ -carbonates, however, are not likely to be stable in most natural environments, so that oxides and hydroxides determine the solubility of neptunium.

At those rather low neptunium concentrations, that can be expected after a possible release from a repository, sorption onto particulates or rock is the main factor influencing the environmental fate of neptunium and, thus, is the most important geochemical mechanism for limiting its migration. Once sorbed,

³The thermodynamically stable solid $\text{NpO}_2(\text{s})$ has never been observed; instead $\text{Np}_2\text{O}_5(\text{s})$ and $\text{Np}(\text{OH})_4(\text{s})$ precipitate (Siegel and Bryan, 2003).

neptunium might even diffuse into the mineral and become incorporated permanently.

Necessary to mention, although beyond the scope of this study, is the interaction of actinides with microorganisms. These can affect radionuclide mobility in the same manner as they affect that of other heavy metals by surface binding or metabolic uptake, thereby acting as mobile or even self-propelled colloidal transport media. Such interactions usually enhance, or, in few exceptional cases, reduce the mobility of the actinides and make them subject to coprecipitation, mineralisation, and diffusion processes. Furthermore, microorganisms are known to mediate redox processes, which, as shown above, can dramatically influence radionuclide behaviour (Runde, 2000).

Similarly, the complexity of interactions between actinides and the vast variety of organic substances will not be addressed in this study, although these are known to be ubiquitous in the environment and of high relevance. The interested reader is referred to, e.g., Choppin and Wong (1998) for a detailed review and further literature on this topic. Nevertheless, the influence of interactions with organic material must be taken into account when transferring experimental findings to the natural system. In an anaerobic microbiological system, for example, Np(IV) is expected to be the dominant oxidation state having significantly lower solubility and mobility than Np(V) (Reed, Sherman and Hermes, 2000). The strong affinity of organic substances to mineral surfaces might imply a lower effective radionuclide solubility than established in the laboratory experiment.

Concluding Remarks

Generally, actinide solubilities are comparably low in most natural environments with values of $<10^{-6}$ M⁴. Only those elements present in the fifth oxidation state, like neptunium, reveal a significantly higher solubility with NpO_2^+ of up to 10^{-4} M. Actinide migration is dominated by a variety of interdependent processes such as complexation, sorption, colloidal transport, diffusion into rock interfaces, coprecipitation, mineralisation, and microbiological activities, which are greatly influenced by pH, p_{CO_2} , and the existence of ligands as well as competing ions. A huge set of thermodynamic and kinetic data is required to quantify these processes and to predict the fate of neptunium and, similarly, of other actinides in the environment.

⁴The solubility of plutonium, for comparison, is around 10^{-8} - 10^{-7} M.

2.3 Radioactive Waste

High-level nuclear waste raises the greatest concern in all considerations of long term storage. It consists of spent fuel rods from military and commercial nuclear reactors, as well as of highly radioactive nuclides in primarily liquid form originating from fuel reprocessing facilities. Apart from the remaining uranium, such waste contains all fission products along with the long-lived isotopes of numerous actinides, neptunium and transplutonium nuclei, including $^{238-241}\text{Pu}$, ^{241}Am and ^{237}Np . In addition to the radiological hazard due to the extraordinary activity level and the corresponding high heat output, liquid wastes are very corrosive with acidities of up to 7 M HNO_3 and a salt content of ~ 250 g/L (Loveland et al., 2006).

Since many of the nuclides present in spent fuel are members of decay chains (see Appendix C.3), some of the developing isotopes further increase the activity of the nuclear waste with time after discharge. During the first 100 years, the initial activity of the waste will be primarily due to short-lived fission products (Eckhardt, 2000). As visualised in Figure 2.6, over time the radioactivity hazard arising from a repository will be dominated by ^{241}Am during the first 1 000 years, thereafter by $^{239,240}\text{Pu}/^{242}\text{Am}$ (up to 10^5 years), and later on by ^{237}Np until 10^6 - 10^7 years following final deposition (Allard et al., 1984).

With the exception of ^{244}Pu and ^{247}Cm – which are produced in very small amounts only –, the half life of ^{237}Np is longer than that of all other transuranium isotopes (Lieser and Mühlenweg, 1988). Among the entire radionuclides present in spent nuclear fuel (several hundreds) only six are sufficiently long-lived, soluble, mobile, and hazardous to contribute to the considered long-term radioactivity significantly: ^{239}Pu , ^{242}Pu , ^{99}Tc , ^{129}I , ^{234}U , and ^{237}Np (Eckhardt, 2000). Regarding their presumed environmental fate, plutonium, even though produced in highest doses, will strongly sorb to minerals and colloids, and only the remaining four radionuclides might considerably undergo transport by groundwater. ^{99}Tc and ^{129}I will contribute little to the overall radiation inventory, in spite of their relatively high concentrations in spent nuclear fuel during the first 10^4 years. ^{237}Np , however, will become the radionuclide of major environmental relevance because of its radiotoxicity, long half life, high solubility, and low sorption affinity, particularly since its concentration will even increase over time through the decay of ^{241}Am . Thus, neptunium has been identified as the “worst-case” (Eckhardt, 2000) radionuclide regarding both likelihood and long-term consequences of environmental migration.

Theoretically, disposed burnt fuel should be isolated from the living environment for the entire period of its potential hazard, i.e., virtually over an infinite period of time. Obviously, the greatest difficulties are faced with the eternal

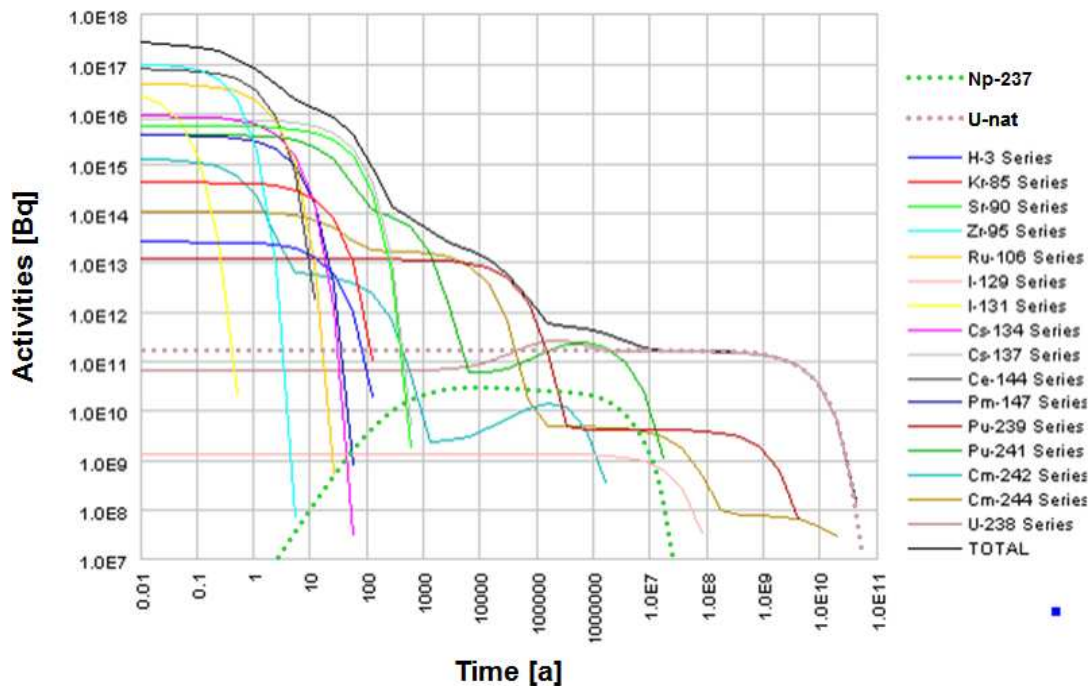


Figure 2.6: Activity of nuclear waste calculated with the Universal Decay Calculator (Vers. B) (Radiation Safety Information Computational Center (RSICC), 2006) starting from one metric tonne of heavy metal contained in spent fuel (= 88% of total weight) from a light water reactor after burn-up of 33 GWd/t at time of unload (short-lived nuclides omitted). ^{237}Np belongs to the ^{241}Pu series and is added to the chart as dotted green line; at time of unload it accounts for an activity of $1 \cdot 10^4$ Bq increasing continuously until the time covered in the graph. For comparison, the purple dotted line shows the activity of natural uranium in secular equilibrium with its decay products.

safe storage of the long-lived actinides. Therefore, attempts have been made to separate these from the spent nuclear fuel to reduce the amount of high-level long-lived waste that requires special treatment. Apart from technical and environmental issues, also political and economic considerations affect that discussion as well as corresponding research and development activities; within this work, however, only the technical aspects are regarded.

2.3.1 Waste Treatment

Between 1946 and 1983, low- and medium-level radioactive wastes were dumped into oceans or landfills (RÖMPP Online, 2007a), but this practise was abandoned due to increasing amounts of waste and growing environmental concern. Accord-

ing to an internationally agreed set of principles and criteria, the International Atomic Energy Agency has established the so-called multiple-barrier concept combining engineered and natural impediments (IAEA Safety Standards, 1989). Thereby, the radionuclides are immobilised in a waste matrix, which is enclosed in a non-corrosive canister (technical or engineered barriers), and are dumped into a geological host formation (natural barrier), see Figure 2.7. An approved practise of radioactive waste treatment is vitrification followed by disposal in deep clayey or crystalline rock or salt domes. Upon final closure, the caverns will additionally be backfilled with usually clay.

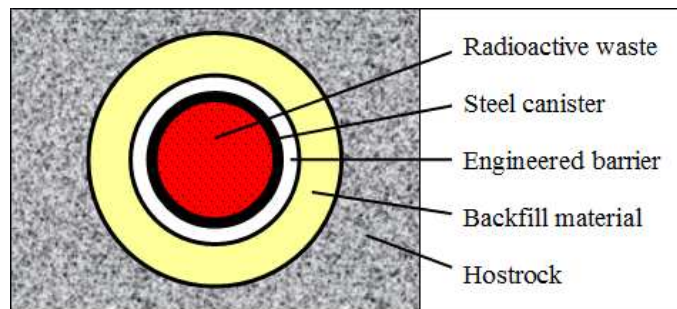


Figure 2.7: Schematic sketch of the multiple-barrier waste disposal concept.

Nevertheless, groundwater is predicted to ultimately seep back into the repository, to slowly corrode the canisters and leach the glass matrix. Based on theoretical estimations of the time required for this process storage times should exceed at least ten half lives of the longest-lived component; this is the time span deemed necessary to ensure environmental safety. The main criteria to assure such a delay through the choice of appropriate materials are chemical inertness, non-dispersibility, and insolubility, as well as radiolytical, mechanical/structural and thermal stability, plus good heat conductance of the whole barrier structure (Choppin and Wong, 1996). The individual steps of current radioactive waste treatment are summarised in Appendix D.1.

Presently, there are 439 nuclear power plants under operation worldwide (World Nuclear Association, 2008). Counting only the estimated volume of heat developing waste generated by the 17 reactors situated in Germany yields $9\,300\text{ m}^3$ until 2010 and up to $51\,300\text{ m}^3$ until 2080 (Brenneke and Hollmann (Bundesamt für Strahlenschutz (BfA) 1997, BFS-ET-29/97), cited in RÖMPP Online, 2007b). A commercial 1 GW nuclear power reactor plant annually produces 10 to 20 m^3 of solidified high-level waste, which can be reduced to less than 3 m^3 via reprocessing (IEA Energy Technology Essentials, 2007).

Several efforts have been made to reduce the volume and the radioactivity of nuclear waste prior to geological storage. One concept is partitioning, i.e. chem-

ical separation, and subsequent transmutation of the actinides by bombardment with high-energy protons of ~ 800 MeV. This process induces fission and/or neutron capture followed by β decay leading to transformation of a great part of the waste into short-lived or even stable products. Considering the required effort and the risk through the necessary further handling of radioactive materials, these methods are discussed highly controversial in their benefit (Loveland et al., 2006; Lieser, 2001).

A recent approach suggests the chemical conversion of long-lived actinides into a rigid solid (Omel'yanenko, Livshits, Yudintsev and Nikonov, 2007). Thereby, neptunium can, together with other actinides of concern, be incorporated into the lattice of artificial uraninite, commonly known as pitchblende, because of the similar dimension of the uranyl, UO_2^{2+} , and neptunyl, NpO_2^+ , molecular ions (Burns et al., 1997, cited in Omel'yanenko et al., 2007). Owing to the stability of UO_2 towards chemical weathering, leakage of the radioactive isotopes into subsurface water could be prevented in this way. Similarly, synthetic matrices of comparable properties but without natural analogues can be designed for reliable isolation of hazardous radionuclides. The authors assert that, in spite of secondary phase formation and considerable amorphisation, these minerals remain virtually unaltered over geological timescales and will be much more durable than vitrified materials. The capacity of 1 t of ,e.g., a murataite ceramic can be as high as 350 kg of elements derived from nuclear waste (Laverov, Yudintsev, Stefanovsky, Omel'yanenko and Nikonov, 2006).

2.3.2 Disposal and Repository Safeguarding

It is presently believed that the safest way to isolate radioactive waste from the biosphere is the storage in deep underground repositories. Nevertheless, future releases must be anticipated and the consequences be estimated, while such an event must be prevented as well as possible. Therefore, geologically stable host rock must be identified and the backfill material must be chosen to possess highest buffer properties regarding the spread of eventually released radionuclides by impeding their mobility.

Host Rock

The precise concept for the final disposal of high-level radioactive waste varies among countries according to the types of rock formations available. Granite, basalt, gneiss, salt, clay, and tuff are equally discussed (Loveland et al., 2006; RÖMPP Online, 2007a).

The choice of a geologic host formation and, especially, the definitive location for a storage site are controversial issues in radioactive waste disposal. The final repository should not only have low water permeability, high heat conductivity, and thermal stability, but also be remote from any human activities including deposits of valuable natural resources, and at a sufficient depth regarding any forces of nature or terrorists. Ideally, the disposal site should be impermeable to surface waters, void of any seismic, tectonic, or volcanic activity, and shielded with a substantial margin of host rock to isolate the dangerous content to all sides.

The main rock formations evaluated for final disposal of radioactive waste are granite, salt, and clay. The former represents the most abundant type of rock in the continental crust, but its local suitability as a host for nuclear waste depends on the site-specific amount of fractures and fissures. The main virtue of granite is the exponential decrease of the hydraulic gradient, inducing a downward pattern of groundwater flow before it moves up towards the biosphere (Choppin and Wong, 1996). In the 1990's, granite formations were favoured by France, Switzerland, Canada, Finland, Japan, Sweden, and the UK (Choppin and Wong, 1996), but that situation has somewhat changed by now. Switzerland, for example, is presently concentrating on clay formations.

Salt formations excel in plasticity, thermal conductivity, and water permeability. They reveal little corrosion or fracturing, have not experienced tectonic or volcanic activity for millions of years, and, like clay, salt self-seal cavities or fissures. The little water content exists as brines, though, which are highly corrosive to the canister material. Nevertheless, salt formations were considered by the US (Choppin and Wong, 1996) and still are under discussion in Germany to date. The US have decided to construct their final repository in welded volcanic tuff (Loveland et al., 2006).

Clay is favoured as host rock as well as backfill material owing to its characteristics described below. Clay minerals are the major component of many argillaceous formations proposed as host rocks for repositories, for example Opalinus clay in Switzerland, Boom and Ypresian clays in Belgium, Callovo-Oxfordian and Toarcian clays in France, and Horonobe sediments in Japan. Additionally, bentonite based backfill barrier materials are considered in most disposal concepts worldwide (Bradbury and Baeyens, 2006b).

The time spans needed for the deposited nuclides to reach the biosphere are estimated to be several million years from a salt dome and 10^{13} years from a granite repository (for clay no estimates are given), which is deemed sufficient for the radioactivity to decrease to insignificant levels (Choppin and Wong, 1996). Such approximations are based on the retardation factor R , which is the ratio of groundwater velocity (0.1-10 m/a) to radionuclide veloc-

ity (Loveland et al., 2006). R is derived from the distribution coefficient K_d (explained in Section 4.3.5) of the radionuclide in the groundwater-rock-system as

$$R \approx 1 + 10 K_d \quad (2.8)$$

Also from this point, concern is raised at the long-lived, poorly sorbed radionuclides ^{99}Tc and ^{237}Np (Loveland et al., 2006).

Backfill Material: Clay

The radioecological safety of a repository is ensured by high sorption capacities of host rock and engineered barriers. Bentonite clay has been chosen for this purpose⁵ due to its ubiquitous occurrence and distinguished physicochemical properties like high swelling capacity and plasticity closing any fractures immediately upon the intrusion of water, low water permeability, and high ion exchange capacity. Its structure is characterised by intracrystal micropores, i.e., interlayer void spaces, providing a high surface area (Misaelides and Godelitsas, 1999).

Clay particles (as well as Fe-, Al-, and Mn-oxides) are so-called secondary minerals emerging from weathering of, e.g., quartz or feldspars. During decomposition of the primary minerals and subsequent crystal growth, aliovalent isomorphic lattice substitution (e.g. Mn^{2+} instead of Al^{3+}) results in a net negative surface charge. An additional variable charge is caused by functional groups located at the mineral surface, which are connected to the H^+/OH^- concentration of the aqueous phase.

Together with iron oxides, clay minerals are the major constituent of soils and sediments, which represent the interface between geo-, atmo-, bio-, and hydrosphere, and are the most important sink for metals once introduced into the environment. Migration through the backfill clay occurs via diffusion.

Bentonite contains 50 to 80% montmorillonite, which is the mineral of concern in this work; its structure and properties are described in Section 2.4.1. The global inventory of bentonite clay is estimated at $6.67 \cdot 10^9$ t (Störr, 1993). It originates either from synsedimentary submarine conversion of volcanic ashes, from fluvial or lacustrine sedimentation in the vicinity of volcanic regions, or from weathering or hydrothermal conversion of alkaline rocks like basaltic tuffs or basalts. While maritime bentonites are often loaded with Na^+ , those of fluvial or limnic origins are mostly covered with Ca^{2+} . Exploitable deposits

⁵Other backfill materials under investigation are asphalt, corundum, copper, and crushed salt (Choppin and Wong, 1996). While these have a better heat resistance, they lack quite a few of the advantages of clay.

are located in northern America, Europe (Bavaria, Scotland, Sardinia, Slovakia, Greece), Asia (Iraq, Yemen, Cyprus, Azerbaijan, Syria, China, Japan), and Africa (Egypt) (Störr, 1993).

Different Concepts

In the 1980's, further options for the final disposal of high-level radioactive waste were discussed such as deep sea sediments, Greenland and Antarctic ice, as well as the transport into space (RÖMPP Online, 2007a). By today, these have been abandoned following environmental, political, and economical concerns.

2.3.3 Safety Assessment and Public Perception

Current estimates assume that it will take about 10^4 years for disposed radionuclides to escape from the repository, and that 10^6 years will pass until significant amounts of them reach the living environment (Eckhardt, 2000). However, there is often a considerable difference between the actual chance of environmental contamination and the perceived hypothetical risk.

Compliance with the international safety objectives “shall be demonstrated by means of safety assessment based on models that are validated as far as possible” (IAEA Safety Standards, 1989). It is recognised, though, that this cannot be done directly, but requires predictive analyses based on technical and scientific data.

Nevertheless, the public fear of risks associated with nuclear power and eventual radioactive contamination has been a recurrent topic in the media, and, furthermore, a readily abused issue in political power struggles. In this way, the apparent and presumed dangers have had, together with the still (kept) very low understanding of the true hazards, important effects on policy as well as on commercial decisions over decades. Thus, it is important for both the general public and the scientific community to have access to validated information to identify the true areas of uncertainty and to understand their importance for profound risk assessment.

2.4 Clay – Merits for Radionuclide Retention

The surfaces of most natural particles contain functional groups, which can interact with ions present in the surrounding aqueous phase including H^+ and OH^- ; if Lewis acid sites are present at the surface (e.g. coordinatively unsaturated aluminium atoms written as $\equiv Al$), these can even interact with ligands

(Stumm, 1992). The functional surface groups are involved in many processes relevant for surface-solute interactions. They are particularly important when considering radionuclide immobilisation through sorption. Therefore, this section is dedicated to the properties of clay minerals, chiefly montmorillonite, and their interactions with dissolved actinide species.

2.4.1 Structure and Features of Montmorillonite

Clay minerals form basically during weathering of silicate rocks, together with oxides and hydroxides of silicon, aluminium, and iron. The conditions for the formation of secondary minerals are provided through the interaction of dissolved H^+ , CO_2 , OH^- , and other ions with the surfaces of rocks and primary minerals. Thereby, the type of (clay) mineral formed is determined by the chemical composition of the primary material and influenced by the climatic situation.

Crystalline Composition

After their mineral composition and shape, clay minerals are classified into kaolinite (double-layered), smectite (triple-layered), and common (mixed) clays as summarised in Appendix E.2. Montmorillonite belongs to the class of smectites. Their structure is formed by $[SiO_4]$ -tetrahedrons and $[M(O,OH)_6]$ -octahedrons (M stands for a metal; in the case of montmorillonite this is primarily aluminium). The former connect via shared oxygen atoms forming a tetrahedral sheet with all tops pointing to the same side. In the plain, the tetrahedrons establish a network of ring structures as shown in Figure 2.8. This layer is condensed to an octahedral sheet, in which the octahedrons are connected via their edges with two of their triangular sides parallel to the tetrahedral plain. Thus, the oxygen atoms at the tetrahedral tops are simultaneously part of the oxygen octahedrons. All octahedral oxygen atoms not belonging to a $[SiO_4]$ -tetrahedron bind a proton, in this way constituting OH^- -groups.

In many clay minerals, a second tetrahedral sheet is connected to the octahedral layer, mirror-symmetrically to the first; an idealised structure is displayed in Figure 2.9. During mineral growth, however, the centre ions may be replaced by those of similar size but lower valency (isomorphic substitution, Al^{3+} instead of Si^{4+} , Mg^{2+} or Fe^{2+} instead of Al^{3+}), which results in a permanent negative charge of the clay mineral. In montmorillonite the total charge is mainly caused by octahedral substitution (Lagaly and Köster, 1993). For electrostatic reasons, the excess negative charge is compensated by accretion of counterions, typically Ca^{2+} , Mg^{2+} , or Na^+ , in the interlayer space. These cations can be exchanged

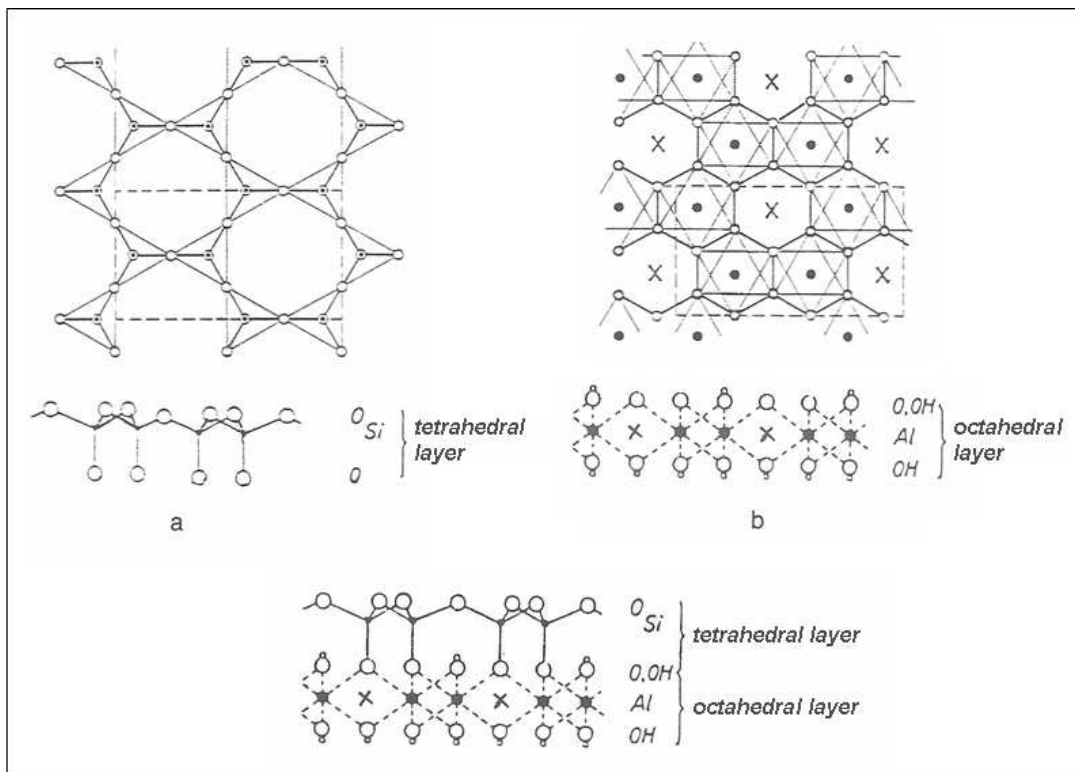


Figure 2.8: Tetrahedral (a) and octahedral (b) layers in sheet silicates. The dashed lines contour the unit cell. Depending on the type of clay mineral, the octahedral positions indicated by X can be occupied; in the case of montmorillonite they are vacant (Lagaly and Köster, 1993).

for others. This property, together with the pH of the surrounding liquid phase, which influences the $\equiv\text{SOH}$ functional groups of the clay, governs the sorption capacity for cations like NpO_2^+ . Montmorillonite typically has a cation exchange capacity (CEC) of ~ 1 eq/kg⁶ (Manceau, Marcus and Tamura, 2002).

Montmorillonite forms thin crystals (platelets) with frayed edges, which appear as uneven confined, twisted, sometimes folded, and rolled up pieces of foil (Lagaly and Köster, 1993). In regions of low overlapping, these layered packages can easily break apart. Because of their structure, clay minerals are referred to as phyllosilicates. Their diameter is typically below $2\ \mu\text{m}$, whereby a single sheet is normally composed of five to 80 layers (Tadjerpisheh and Kohler, 1998), which are connected by dipole interactions, hydrogen bonds, and van-der-Waals forces.

⁶eq – equivalent, for monovalent ions = 1 mole ($6.022 \cdot 10^{23}$), for divalent = 0.5 mole, etc.

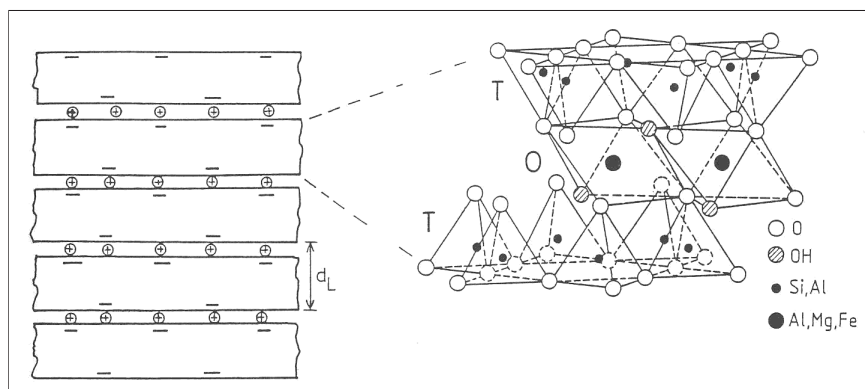


Figure 2.9: Three-dimensional illustration of triple-layered silicates (T – tetrahedral sheet, O – octahedral sheet, d_L – sheet distance (Lagaly and Köster, 1993).

With respect to sorption processes, it is important to note that the mineral surface carries a constant negative charge, while the functional surface groups, especially at the edges, readily interact with H^+ and OH^- ions; hence, the effective sorption potential depends on the pH of the surrounding solution (Nagasaki, Tanaka and Suzuki, 1997). The ions present in the interlayer space can become hydrated by water molecules, in this way increasing the sheet distance from 10 \AA to more than 20 \AA (Köster and Schwertmann, 1993). In water and low-salt solutions, the silicate layers can even completely disintegrate into colloidal dispersions (delamination).

Stability of Montmorillonite

In aqueous solution, clay minerals are – similar to other solids – subject to dissolution effects. Depending on proton concentration and temperature, the mineral dissolves at a certain pace until equilibrium is reached by saturation of the solution. The rate of mineral dissolution r is defined as the number of moles passing into solution per unit initial surface area (usually measured by the adsorption BET method) and time, having the dimension of $[\text{mol m}^{-2} \text{ s}^{-1}]$ (Alekseyev, 2007). Thereby, the normalisation to surface area poses the problem of accurate determination of that parameter. Alterations may occur during the experiment following disintegration of particles and increase in porosity due to the removal of interlayer cations (Alekseyev, 2007). r is derived from the amounts of aluminium or aluminium and silicon extracted into solution. Their concentrations were found to increase linearly with time (Zysset and Schindler, 1996).

Dissolution occurs mainly on the edge surfaces of crystals (Metz et al., 2005, cited in Alekseyev, 2007; Zysset and Schindler, 1996), as was derived from observations of the silicon-to-aluminium ratio in solution. A value close to the mineral stoichiometry was measured indicating congruent dissolution of the solid phase and supporting the hypothesis that (at pH 1-5) the contribution of the basal planes, which would supply silicon only, is negligibly small. Additionally, it was found that stirring the suspension has no effect on dissolution (Alekseyev, 2007). The rate is linearly dependent on the concentration of H^+ , i.e. the pH (Zysset and Schindler, 1996). Alekseyev (2007) developed the following equation for the dissolution rate of montmorillonite from an empirically derived relationship at constant temperature combined with the Arrhenius equation including a U-shaped dependency on pH:

$$r = \exp\left(\frac{-E_a}{RT}\right) (A_{H^+} a_{H^+}^m + A_{OH^-} a_{OH^-}^n) \left\{ 1 - \exp\left[-p \left(\frac{\Delta G}{RT}\right)^q\right] \right\} \quad (2.9)$$

where $E_A = 9.34 \text{ kcal/mol}$, $A_{H^+} = 8.30 \cdot 10^{-5}$, $m = 0.739$, $A_{OH^-} = 8.78 \cdot 10^{-6}$, $n = 0.385$, $p = -6 \cdot 10^{-10}$, $q = 6$; ΔG is the free energy of the reaction, R the gas constant, and T the absolute temperature. a_{H^+} and a_{OH^-} are the activities of H^+ and OH^- in the solution. This equation is valid for temperatures of 20-80°C and pH values of 1-14. Figure 2.10 shows the fit of dissolution rates of montmorillonite as function of pH and temperature performed by Alekseyev (2007) using own experimental and several sets of literature data.

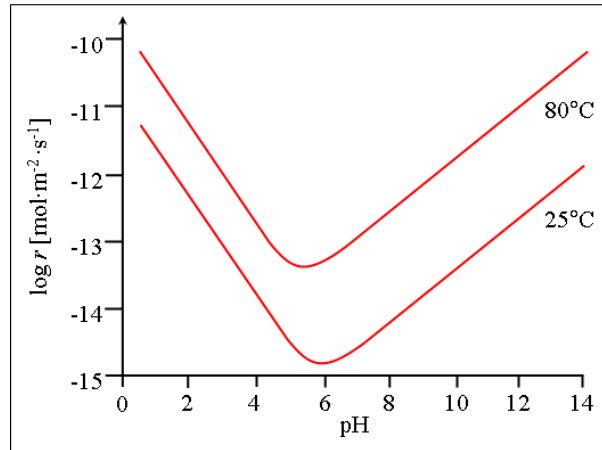


Figure 2.10: Dissolution rate of montmorillonite as function of temperature and pH. Mathematically processed data applying Equation 2.9 (by Alekseyev, 2007, modified).

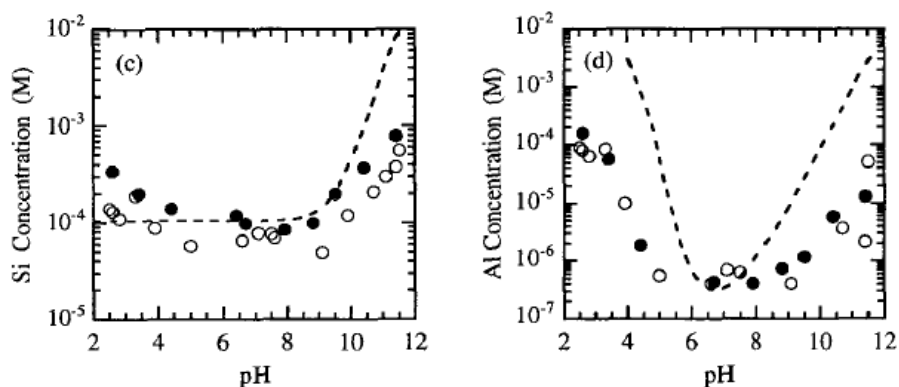


Figure 2.11: Silicon and aluminium concentrations in batch experiments with montmorillonite determined after one (\circ) and seven (\bullet) days, dashed lines – calculated solubilities for quartz, SiO_2 (left), and gibbsite, $\alpha\text{-Al}(\text{OH})_3$ (right); $\text{NaClO}_4 = 0.5 \text{ M}$ (Baeyens and Bradbury, 1997).

Applying this graph, the dissolution of montmorillonite in the present study (STx-1; $83.4 \text{ m}^2/\text{g}$; 4 g/L) after three days at 25°C would be $2.6 \cdot 10^{-6} \text{ mol/L}$ at pH 3 or 10.5, which equals 0.05% of the initial mass assuming a molecular weight of 713.7 g/mol (refer to Table 4.1 on page 91). These values are roughly consistent with silicon and aluminium concentrations measured in experiments with montmorillonite by Baeyens and Bradbury (1997) as shown in Figure 2.11. Based on these findings, the authors attest a great uncertainty in experimental sorption data at $\text{pH} > 11$ resulting from dissolution effects.

An effect of Na^+ was found to be very small if any (Amram and Ganor, 2005, cited in Alekseyev, 2007). Also the influences of aluminium, silicon, and other inorganic ligands present in solution on the dissolution rate are negligible; it appears as a sole function of temperature, pH, and degree of solution saturation (ΔG) only (Alekseyev, 2007). Köhler, Dufaud and Oelkers (2003), in contrast, detected dissolution rates decreasing with time for the clay mineral illite⁷, which they attributed (amongst other factors) to a significant change in surface area during the experiments due to initial decomposition of fine particles and disturbed surfaces. In natural systems, however, the weathering rates are generally one to three orders of magnitude smaller than those observed in laboratory experiments, which has been explained by the readsorption of dissolved aluminium on the crystal edge faces, in this way inhibiting further dissolution (Zysset and Schindler, 1996). Hence, once again, studies on the isolated system provide a conservative upper limit for extrapolations to the natural environment.

⁷Illite is a triple-layered phyllosilicate belonging to the smectite group; it is similar to montmorillonite but non-swelling due to poorly hydrated potassium cations in the interlayer.

Sorption Sites

As soon as an ion is not only attracted to the mineral surface by electrostatic forces, but forms bonds with surface atoms this requires certain amphoteric binding structures. Often natural minerals contain different types of such sorption sites, which reveal different affinities for the sorption of protons and metal ions. Furthermore, their distribution over the mineral surface is not uniform. Together with the irregular shape of natural clay platelets, this causes secondary effects on sorption kinetics and complex stability through steric and electronic variability (Nagasaki and Tanaka, 2000).

Montmorillonite has experimentally been attested a strongly heterogeneous surface. Nagasaki and Tanaka (2000) measured the kinetics of Np(V) sorption to finely dispersed montmorillonite in very short time intervals and, in this way, identified two main ion exchange processes (at pH 6) that they attributed to quick Np(V) sorption to the easily accessible outer surface of montmorillonite particles and to slower sorption on the interlayer surface. The authors conclude that, instead of describing such a system with one definite affinity, rather a spectrum of those should be assumed, and that the classical treatment with one or two discrete exchange coefficients is only approximately valid. Nevertheless, this is the general practice to date for modelling Np(V) sorption on complex (clay) minerals (see Section 3.3.1).

The sorption of metals on clays often occurs via complex formation with singly coordinated OH-groups, such as aluminol or silanol groups (Stumm, 1992). The latter, however, show only very weak interaction with Np(V), if any, and are hardly significant under real conditions (Yusov, Fedoseev, Isakova and Dele-gard, 2005)⁸; therefore, the focus is on the aluminol groups. Singly coordinated, reactive hydroxyl groups are present on the mineral edges, while aluminol groups formed by Al atoms that are substituted for Si in the tetrahedral lattice constitute a trace amount only; both are high-affinity sites for neptunyl ions (Del Nero, Assada, Madé, Barillon and Duplâtre, 2004). According to the available total number of sites, the ions are bound with different strength. Apparently, the binding constant declines with increasing ion concentration when the stronger sorption sites become limited due to increasing occupation.

Since clay minerals interact with metal ions in a similar manner as oxides (Stumm, 1992), these can serve as reference substances through analysing the sorption behaviour of metal oxides chosen with regard to a certain type of surface sites. In this study γ -Al₂O₃ is used to represent aluminol groups.

⁸This finding is also supported by comparative sorption experiments on alumina and silica, e.g. by Li and Tao (2003).

2.4.2 Aluminium Oxide as Reference Substance

Montmorillonite, like other clay minerals, contains aluminol and silanol groups as crucial binding sites. Hence, aluminium oxides and hydroxides can serve as reference substrates for examining the influence of the chemical environment on the interaction between NpO_2^+ and the $\equiv\text{AlOH}$ functional groups of clay minerals.

Oxides and hydroxides are typical products of rock weathering. In the presence of water, siliceous compounds are oxidised, whereby the SiO_4 -ligands of the metals are replaced by oxygen atoms and hydroxyl groups (Schwertmann, 1993). Together with silicon and iron oxides, aluminium oxides are abundant components of the earth's crust. Furthermore, most solids present in natural waters, soil, and sediments contain oxides, which are generally covered with surface hydroxyl groups ($\equiv\text{S-OH}$) in the presence of water. Although these are not exactly equal⁹, they are usually considered similar in their chemical behaviour. When deprotonated to $\equiv\text{S-O}^-$ such surface groups behave as Lewis bases, on which the sorption of protons and metal ions follows competitive complex formation. Similarly, the whole structural hydroxyl group can be exchanged against other ligands (Stumm, 1992). Like on clay minerals (see Section 2.4.1 above) sorption on aluminium oxides and hydroxides proceeds in a two stage process. A rapid initial uptake within the first hour of contact occurs through the interaction between the neptunyl ions and surface sites and already reaches close to maximum, while a secondary mechanism involves slow diffusion of the ions into interior regions of the sorbent particle (Tochiyama, Yamazaki and Mikami, 1996).

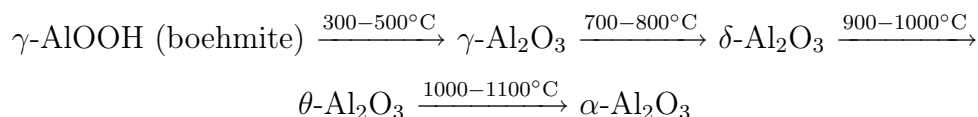
Since the several types of binding sites on, for example, clay minerals differ both in chemical structure and crystallographic plane, the investigation of neptunium sorption to aluminol and silanol groups in simpler model substances such as oxides or hydroxides is helpful and allows for generalisations concerning the interpretation of sorption experiments with more complex minerals.

Mineral structure of Aluminium Oxide

For assessing the suitability of a substance as reference for another one not only the atomic composition is of relevance, but also the spatial ordinance of the constituting atoms. The mineral structure determines the amount and position of available binding sites and, thus, has a strong influence on the sorption behaviour of the substance. Aluminium oxide exists in a variety of solid polymorphs with

⁹possible surface groups of clay minerals are $\begin{matrix} \text{S} \\ \diagdown \\ \text{OH} \end{matrix}$; S-OH ; $\begin{matrix} \text{OH}_2 \\ \diagdown \\ \text{S} \\ \diagup \\ \text{OH} \end{matrix}$; $\begin{matrix} \text{OH} \\ \diagdown \\ \text{S} \\ \diagup \\ \text{OH} \end{matrix}$ (Schindler 1985, cited in Stumm, 1992).

α -Al₂O₃ (corundum or sapphire, respectively ruby) being the most stable. It is created from bauxite ore via a series of metastable so-called transition alumina phases, e.g.



(Pinto, Nieminen and Elliot, 2004). Interestingly, McHale et al. (1997, cited in Brown et al., 1999) discovered that nanocrystalline aluminium oxide attracts water, which could not be completely removed without particle coarsening. They showed that when the surface area of nanocrystalline alumina exceeds about 125 m²/g, the γ -Al₂O₃ form of alumina is stabilised relative to the α -Al₂O₃ form. When particles of α -Al₂O₃ reach this size, the surface energy becomes a dominant contribution to the free energy and the structure rearranges to form γ -Al₂O₃.

In the present study, γ -Al₂O₃ was chosen as a reference substance, because it reveals the octahedral crystal structure, which is typical for the central layer in montmorillonite and other clay minerals. Furthermore, γ -Al₂O₃ has the unique properties of a high surface area combined with mechanical strength, for which it is often used as a catalyst (Gutiérrez, Taga and Johansson, 2001). It is an important synthetic substance used in heterogeneous catalysis and a model material commonly used as a surrogate for more complex aluminosilicate substrates of importance in interfacial geochemistry and soil chemistry. As of 1999, γ -Al₂O₃ has not been prepared in single-crystal form (Brown et al., 1999).

Most insight into the mineral structure of aluminium oxide has been gained through the aid of theoretical calculations identifying the energetically favourable structures. The precise mineral composition and configuration, however, is still a controversially discussed issue. By X-ray diffraction studies a defect spinel¹⁰ structure of 24 cations and 32 anions in a cubic unit cell has been established, with aluminium occupying tetrahedral and octahedral positions among the cubic close-packed oxygen atoms. To satisfy the stoichiometry of γ -Al₂O₃, 2²/₃ out of the 24 cation sites must be vacant, whereby the distribution of these vacancies remains unclear (Sohlberg, Pennycook and Pantelides, 1999). Even theoretical calculations provide no conclusive answer whether these are located at octahedral or tetrahedral positions or if they are spread among both (Gutiérrez et al., 2001).

¹⁰cubic minerals of A²⁺B₂³⁺O₄²⁻ with the oxygen atoms arranged in a close-packed lattice where A and B occupy the octahedral and tetrahedral positions. If some sites are vacant, the structure is called a defect spinel.

Doubts on the theory of a defect spinel arise from chemical analyses indicating the presence of varying amounts of hydrogen in the crystal composition ($\text{Al}_2\text{O}_3 \cdot n\text{H}_2\text{O}$), which associate more closely with one of the nearest neighbour oxygen atoms forming OH-groups within the bulk. Again contradicting, other experiments showed the presence of hydrogen in the crystalline bulk to be rather unlikely (Paglia, Rohl, Buckley and Gale, 2005).

In general, the spatial distribution of atoms in a unit cell is given by an individual space group. $\gamma\text{-Al}_2\text{O}_3$ has the space group $Fd\bar{3}m$, but viewed locally, it deviates from a cubic spinel and is better represented by a $C2m$ space group (Pinto et al., 2004). Paglia et al. (2005) even consider it as a dual phase material consisting of both cubic and tetragonal domains, because in their study they found over 40% of the cations occupying nonspinel positions. Therefore, the authors recommend the $I4_1/amd$ space group for the best representation of the distorted structure of the cubic lattice. Figure 2.12 shows two different structural models drawn from data by Verwey (1935, given in the structural database Retrieve 2.01, Gmelin Institute, 1997) and Gutiérrez et al. (2001).

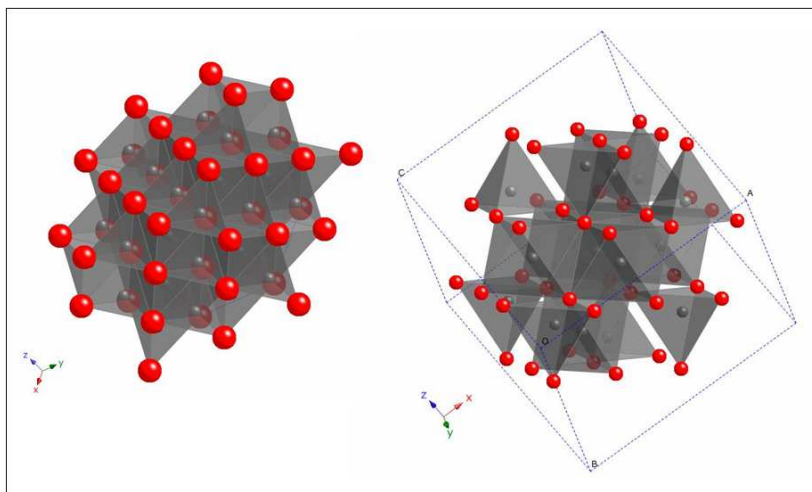


Figure 2.12: Cubic models of $\gamma\text{-Al}_2\text{O}_3$. The left one is based on a $Fm\bar{3}m$ space group, showing aluminium atoms in tetrahedral positions, while the right one represents a $Fd\bar{3}m$ space group with aluminium in both tetrahedral (top and bottom layer) and octahedral (central layer) sites.

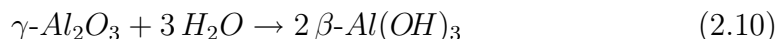
Environmental Occurrence of Aluminium Oxides

$\gamma\text{-Al}_2\text{O}_3$ does not occur naturally and, in soils, aluminium hydroxide $\text{Al}(\text{OH})_3$ (gibbsite) dominates instead. There, the Al^{3+} -ions form octahedra with six OH^- -ions, which are linked by shared OH^- -ions to form hexagonal layered

platelets. The solubility product of $\text{Al}(\text{OH})_3$ is rather small under environmental conditions (at pH 5: $K_{sp} \approx 10^{-34}$ equalling ca. 3 mg/L Al^{3+}), but with decreasing pH it rises by three orders of magnitude per unit. Apart from $\text{Al}(\text{OH})_3$, AlOOH (diaspore, α -, and boehmite, γ -) is formed during weathering processes, but its appearance is rare in soils. α - Al_2O_3 (corundum) mostly is of lithogenic origin or arises from tropical fires (Scheffer, Schachtschabel and Blume, 2002; Schwertmann, 1993).

Surface Chemistry and Solubility

Although often high stability of γ - Al_2O_3 is assumed, there is the possibility of transformations leading to oxi-hydroxide, AlOOH , or trihydroxide, $\text{Al}(\text{OH})_3$; thermodynamical calculations predict the hydration to a more stable phase like bayerite, gibbsite, or boehmite, already at the water vapour pressure in ambient atmosphere (Lefèvre, Duc, Lepeut, Caplain and Fédoroff, 2002). Bulk hydroxylation of α - and γ - Al_2O_3 powders may result in the formation of $\text{Al}(\text{OH})_3$ phases, as also Brown et al. (1999) conclude from their literature review. Lefèvre et al. (2002) observed a progressive transformation of γ - Al_2O_3 into β - $\text{Al}(\text{OH})_3$ within a few weeks according to



The first crystalline bayerite phase was detected following four days of hydration. As well, the authors could identify a transient amorphous phase with a maximum after ca. 10 days, being a precursor of bayerite. While after two weeks the surface appeared unchanged, its reactivity was totally controlled by the hydroxide phase. In their experiments the density of reactive surface sites decreased dramatically with hydration time. Simultaneously, the specific surface area increased by 6 % within two weeks and by 9 % within six months of hydration. Hence, the new phase is probably mainly non-reactive. However, the authors state that it is not possible to determine whether the surface is completely hydroxylated. Even after several months, no steady state was achieved suggesting another process, since bayerite is not the thermodynamically stable phase.

The solubility of aluminium oxide is negligibly small. Rates determined for δ - Al_2O_3 , which has a defect spinel structure like γ - Al_2O_3 , in 0.1 M NaNO_3 range from 10^{-8} (pH 2) to 10^{-9} (pH 6) $\text{mol m}^{-2} \text{h}^{-1}$, corresponding to a half life of functional groups of $5 \cdot 10^3$ to $5 \cdot 10^4$ h (Furrer and Stumm 1986, cited in Sigg and Stumm, 1996). Calculated for the specifications of the γ - Al_2O_3 used in this study ($\sim 100 \text{ m}^2/\text{g}$, 0.5 g/L, 102 g/mol) the maximum dissolution amounts to $2.8 \cdot 10^{-12}$ mol/L or $2.9 \cdot 10^{-10}$ g/L, corresponding to $5.7 \cdot 10^{-8}$ % within three days. Figure 2.13 presents the dissolution of finely ground γ - Al_2O_3 as a function of pH measured by Horst and Höll (1997), revealing that the sorbent is stable in the pH-range 5 to 10.

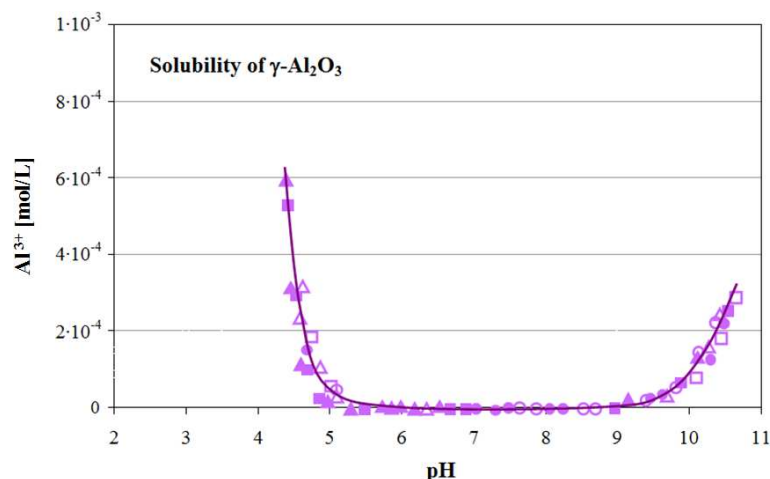


Figure 2.13: Dissolution of $\gamma\text{-Al}_2\text{O}_3$ (Horst and Höll, 1997). The individual symbols represent different ionic backgrounds.

2.5 Radionuclide Reactions with Natural Materials

As discussed above, the major chemical parameters influencing actinide sorption are redox conditions (oxidation state), pH (degree of hydrolysis), and complexing agents (e.g. carbonate) (Allard et al. 1983, cited in Dozol and Hagemann, 1993). The following section elucidates the physical aspects of complex formation and the mechanisms of sorption as well as ion exchange processes with respect to the molecular structure of sorbate and solid phase.

2.5.1 Complexation

Since actinide ions are non-polarisable and their bonding is strongly ionic, they act as hard Pearson acids and, therefore, form complexes with highly anionic ligands, preferably with hard base complexants containing oxygen and fluorine donors (Choppin, 2006b; Choppin and Wong, 1998). In ionic compounds, the bond strength is roughly proportional to the effective charge density (Konings et al., 2006). The coordination number (i.e., the number of bound ligands) is primarily determined by steric and electrostatic principles; for actinyl ions it is 4 or 5 for An(V)O_2^+ and 5 or 6 for An(VI)O_2^{2+} (Runde, 2000; Choppin and Wong, 1998). These high numbers are due to the ability of most ligands to act in both mono- and bidentate modes, whereby the latter is more common because of the small oxygen distances of the ligands. Carbonates, for example, can develop

monodentate bridging even though they typically bind in a bidentate fashion (Gutowski et al., 2006).

Both hydroxide and carbonate strongly complex actinide ions, thereby significantly affecting their mobility in natural waters. The interaction of actinides with hydroxides results in the formation of monomeric solution species – whereas solid hydroxides as well as oxides can limit the solubility of Np(V) complexes (Runde, 2000). Carbonate is in effective competition with hydroxides, because it typically shares two of its three oxygen atoms with the actinyl ion, in this way forming strong and very stable bidentate bonds (Choppin and Jensen, 2006). In solutions with carbonate concentrations below 10^{-4} M, 95 % of the neptunium are comprised of NpO_2^+ , while above that concentration $\text{NpO}_2(\text{CO}_3)^-$, $\text{NpO}_2(\text{CO}_3)_2^{3-}$, and $\text{NpO}_2(\text{CO}_3)_3^{5-}$ may be present (Choppin, 2005; Choppin and Wong, 1998). In natural waters of neutral or alkaline pH, only these complexes exist in solution, and even at very high pH (i.e., near pH 11) they are not subject to hydrolysis (to form $\text{NpO}_2(\text{OH})$, cf. Figure 5.10, page 133) (Clark et al., 1995).

Generally, the stabilities of An(V) complexes are about 13 orders of magnitude smaller than those of the corresponding An(VI) complexes (Choppin and Jensen, 2006). Yet, in comparison to other actinides, neptunium reveals the lowest effective charge of the AnO_2^+ ion, causing it to form the weakest complexes and, in this way, being the most soluble and mobile actinide (Runde, 2000).

Complexation has a crucial influence on the environmental behaviour of the actinides, including neptunium. The penta- and hexavalent actinyl hydroxycarbonates exhibit some solubility, but the neutral hydroxycarbonates, $\text{An}(\text{OH})(\text{CO}_3)$, represent the solubility limiting species in near neutral solutions that are in equilibrium with atmospheric carbon (Choppin and Jensen, 2006). As solids Np(V)-carbonates form ternary complexes with monovalent metal cations compensating the overall charge. Their solubilities depend, apart from the carbonate concentration, on the ionic strength (i.e. mainly the sodium concentration), which is typically rather low in most natural waters. A much higher ionic strength than encountered in most environments would be necessary to precipitate a ternary Np(V) carbonate solid (Runde, 2000).

The complexes formed by actinides can be differentiated into inner-sphere complexes, in which anion and cation are in direct contact (with, e.g., (bi-) carbonate and carboxylate ligands), and weaker outer-sphere complexes, in which the actinide retains its hydration shell separating anion and cation by a bridging water molecule (with, e.g., chloride and perchlorate ions) (Choppin and Wong, 1998). Actinide cations form inner-sphere complexes with strongly negative anions like (bi-) carbonate, whereas they form outer-sphere complexes with weakly basic ligands (Choppin, 2005). For some ligands, however, both types of complexes may even be present simultaneously (Choppin and Jensen, 2006).

The mechanism of complex formation comprises a first rapid step of outer-sphere ion pair binding followed by a subsequent rate-determining step, in which the ligand replaces one or more water molecules. Thereby the upper limit to the formation rate is given by the velocity of solvent-water exchange. Generally, because of changes in the ligand structural characteristics during the reactions, the kinetics of multidentate ligands are slower than those of monodentate ones (Choppin and Jensen, 2006).

The understanding of complex formation and structure is central to the comprehension of the environmental chemistry of the actinides. As the utility of thermodynamic and kinetic measurements diminishes with increasing difference between the natural and laboratory systems (cf. Section 2.2.1), advanced techniques for studying the structure – such as EXAFS (see Section 3.2.3) – become important sources for extra-thermodynamic information on dissolved actinide complexes.

2.5.2 Sorption

The various physical and chemical processes between an element and environmental components that are responsible for retardation along the migration path have received the generic name of sorption in nuclear waste literature and elsewhere (Dozol and Hagemann, 1993). In this study, the mechanism of ion exchange will be treated separately (as opposed to adsorption), because the focus of this work is on the speciation of the bound neptunium ion. As will be discussed below, ion exchange leads to retention of the hydration shell (so-called outer-sphere sorption), while during adsorption this is at least partly lost and the ion is bound directly to the surface (inner-sphere sorption); both processes occur in different pH-regions. They are also referred to as non-specific and specific sorption (International Union of Pure and Applied Chemistry (IUPAC), 2008).

Sorption processes govern the intermolecular interactions between solute and sorbent, thereby determining the distribution of substances between aqueous phase and particulate matter, which in turn affects their mobility in and transport through the environment. There is a huge number of different solids present in nature sorbing ions from solution, this study in particular focusses only on clay minerals. Their surfaces can be regarded as formed by extending structures bearing functional groups, which provide a diversity of interactions through the formation of coordinative bonds (Stumm, 1992). As demonstrated above already, oxides are of great importance at the mineral-water interface, too.

Since neptunium sorption is determined by the equilibrium of NpO_2^+ , respectively that of the Np(V) carbonate complexes, between aqueous and solid phase,

this process is in principle reversible (Lieser and Mühlenweg, 1988). Most sorption theories differentiate between sorption on a charged surface and the binding of aqueous ions to special sorption sites. In a surface complexation model it is assumed that ions of the opposite sign are sorbed on the respective functional groups, thereby compensating the mineral surface charge. In this way, ion pairs of surface groups and counterions are formed, which are designated as surface complexes, and constitute an ordered double (or so-called Stern) layer. Each kind of those counterions is located at a characteristic distance from the sorbent (Horst and Höll, 1997). The remaining excess charge of the mineral surface is balanced by counterions in a diffuse layer, which also contains coions but in a lower concentration.

Mechanisms of Sorption

Depending on pH and ionic strength, an either negative or positive surface potential is generated by protonation or dissociation of the functional $\equiv\text{SOH}$ groups. The relevant sorption mechanisms can basically be divided into physical, electrostatic, and chemical sorption (Allard et al., 1984). Physical sorption arises from non-specific forces of attraction between sorbate and sorbent. Thereby, sorption takes place on non-specific positions, so that the composition of the solid phase is of minor importance. This process is rapid, reversible, and independent from solute concentration. Electrostatic sorption results from coulombic attraction between a charged surface and an aqueous ion or charged dissolved species. This process is rapid and largely reversible like the former, but depends on solute concentration and competing ions (i.e., ionic strength), as well as on some properties of the solid, e.g. its ion exchange capacity. Chemical sorption, instead, is fairly slow, partly irreversible, and concentration-dependent. Since it is caused by chemical forces, this process requires a certain composition of the sorbent facilitating the formation of strong complexes with the solute species.

Investigating the principal uptake mechanisms for metals in the geosphere, it is expedient to even further differentiate the process of sorption according to Manceau et al. (2002):

- **Outer-sphere surface complexation** (physical, respectively electrostatic, sorption) is defined as that form of sorption at which the sorbate ion retains its hydration shell; it is caused by electrostatic interactions at a charged surface within a diffuse ion swarm (Figure 2.15). This frequently occurs in the interlayer space of clay minerals. Near the charged surface an electric double layer is formed, which is influenced by the ionic strength of the solution (see Section 3.1.4). Elements sorbed in this way are only

loosely bound and easily replaced by ion exchange mechanisms. Thus, they may easily be leached and are highly mobile.

- **Isolated inner-sphere complexes** (chemical sorption) distinguish themselves by sharing one or several ligands (mostly oxygen atoms) with one or several sorbent cations. This type of sorption is much less reversible compared to the former and represents the primary form of metal uptake by most minerals. Both constituents usually share edges and corners, since dangling chemical bonds on particle edges generate a macroscopic variable, pH-dependent charge.
- **Multinuclear surface complexation** occurs when sorbate cations polymerise on the substrate, whose surface is acting as a structural template. In this way, the supersaturation needed for precipitation is reduced, because the energy barrier for crystal formation decreases due to the provision of a sterically similar surface for nucleation. The chemically foreign but coherently oriented lattices attach by electrostatic interactions, hydrogen bonds, or van-der-Waals forces. Elements incorporated into such structures are largely immobilised.
- **Homogeneous precipitation** differs from the former in that the dissolved cationic species polymerise and precipitate in solution without a structural link to the surface. These complexes may as well deposit on the substrate forming a surface coating.
- **Lattice diffusion** is a kinetically controlled process causing sorbed single ions to be incorporated into the sorbent to fill vacancies or replace lattice atoms.

A graphical overview of the main sorption mechanisms is given in Figure 2.14.

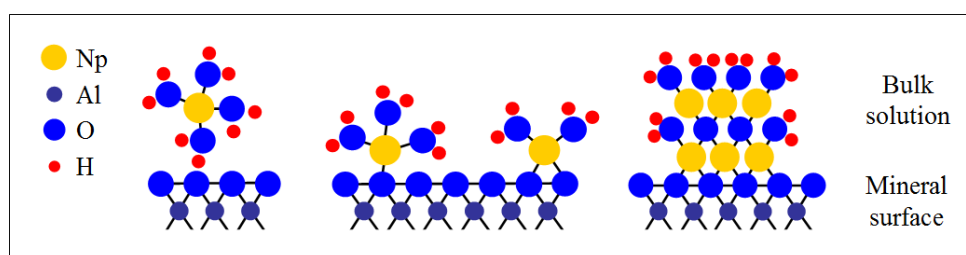


Figure 2.14: Molecular structure of outer-sphere and inner-sphere complexes, and surface precipitates (left to right). It should be noted, however, that the distinction between outer-sphere and inner-sphere complexes is a continuous transition (Stumm, 1992).

Once a radionuclide has been released from the repository, sorption processes represent an effective natural barrier to its mobility in the environment. Immobilisation on rock or mineral surfaces, however, depends on many factors which determine the mechanisms involved, such as elemental speciation, radionuclide concentration, flow rate and chemistry of the pore water, and mineral composition of the surrounding rock. Depending on the prevailing conditions, the radionuclide is bound by ion exchange, physical sorption, chemical sorption, or – when present in sufficiently high concentrations – as surface precipitate (Runde, 2000).

Like complexation, sorption is influenced by steric effects and the net charge of the ion, and thus follows the same trend with similar binding strengths (Choppin, 2006b; Choppin and Wong, 1998). Thereby, a small charge-to-radius ratio as in the case of neptunium, its large size, and the corresponding low tendency for complexation, causes a low affinity to sorption on mineral surfaces (Eckhardt, 2000). Especially the comparably low charge of the NpO_2^+ ion (see Section 2.2.1) results in poor sorption affinity (Runde, 2000). Furthermore, other dissolved ions compete for the available surface sites and may interfere with neptunium sorption (Choppin and Wong, 1998).

In addition to the properties of the mineral acting as sorbent, the total salt concentration of the aqueous phase has an influence on the magnitude of sorption. Only when non-hydrolysed species are dominant and cause electrostatic interactions, or when the solid phase exhibits specific complexing properties relevant for chemical sorption, the ionic background is of comparably low relevance. While at low pH ion exchange processes dominate the sorption process, this situation applies to the higher pH-region above $\text{pH} \sim 5$, where hydrolysis reactions of the aqueous phase become relevant. Then, specific sorption starts and, generally, reaches a maximum at a pH favouring neutral hydroxy species, while the formation of anionic complexes such as $\text{NpO}_2(\text{CO}_3)^-$ hampers the immobilisation on a generally negatively charged mineral or rock surface (Allard et al., 1984; Runde, 2000). Additionally, the extent and type of sorption depends on the particle net charge (see Section 2.4.1), surface area, and nature of the individual surface sites (Stumm, 1992). NpO_2^+ sorbs, for example, much stronger on carbonates and organics than on other minerals (Choppin, 2005).

Ternary Complexes

In certain cases, also ions that are bound by one or more ligands become attracted by a mineral surface. Even the sorption of negatively charged aqueous molecules like neptunium carbonate complexes might, although being small, well exceed negligibility. Such surface species have already been observed on

e.g. hematite (Arai, Moran, Honeyman and Davis, 2007). The finding that similar complexes form on the surface of clay minerals as well would be of major importance for the assessment of nuclear repositories and the estimation of radionuclide mobility in the environment. Their consideration in the underlying models would significantly improve any predictions concerning eventual release scenarios.

Relevance of Colloids

Colloids are ubiquitous in the natural environment with typical concentrations around 10^6 cm^{-3} . They are usually defined on the basis of size, having dimensions of 1 nm to $1 \mu\text{m}$ in at least one direction (Lyklema, 1991, cited in Stumm, 1992). According to their composition, intrinsic colloids, which exclusively consist of the element considered, are differentiated from carrier colloids that are minerals on which the element of concern is sorbed (Dozol and Hagemann, 1993).

In environmental systems, colloids can arise from mineral or organic natural material, as well as from engineered repository structures such as canister steel or cement. The extent of colloid formation is dependent on pH as well as on ionic strength (Nagasaki et al., 1997). Their presence causes major difficulties in distinguishing between dissolved and particulate matter. When their formation is neglected, apparent radionuclide solubilities might be largely overestimated, leading to severe errors if thermodynamic data are derived (Dozol and Hagemann, 1993).

Neptunyl ions sorb only scarcely onto colloids (Choppin and Wong, 1998). While Np(IV) is known to form intrinsic colloids, Np(V) only sorbs on colloidal carriers already present in the system (Sabodina et al., 2006). Although particulate transport constitutes a significant migration mechanisms in the aqueous environment, and physical rather than chemical processes dominate the transport of actinides in flowing water systems (Allard et al., 1984), these aspects are outside the scope of this study and will not further be discussed.

2.5.3 Ion Exchange Processes

This specific type of sorption denotes the mechanism of an ion sorbed in an outer-sphere complex or in the diffuse ion swarm being reversibly replaced by another similarly charged ion following the law of competition. Based on the extent of this reaction, respectively the amount of ions bound to the surface in this manner, a cation exchange capacity (CEC) can be defined for the sorbent as charge per mass of solid [eq/kg].

Since the functional surface groups are positively charged in the acidic pH region, specific sorption of the neptunyl cation is impeded by electric repulsion. Therefore, on clay minerals, sorption below pH ~ 5 is governed by the competing processes of complex formation and ion exchange, while only above pH ~ 5 , reactions with surface hydroxyl groups of the clay prevail (Sabodina et al., 2006). The region of ion exchange is characterised by a marked dependency of the neptunium sorption on competing dissolved ions, i.e. ionic strength. Figure 2.15 shows the process of cation sorption on a negatively charged surface.

Here it is worth mentioning that the penetration of cations into the interlayer of clay platelets via ion exchange results in swelling and shrinking of the mineral caused by their hydration. Hence, differences in the osmotic pressure between solution and interlayer space cause water to enter there inducing different interlayer spacings (Stumm, 1992). This characteristic feature of smectite minerals was utilised in the cleansing process of the montmorillonite used in this study (cf. Section 4.3.1 and Appendix F.3).

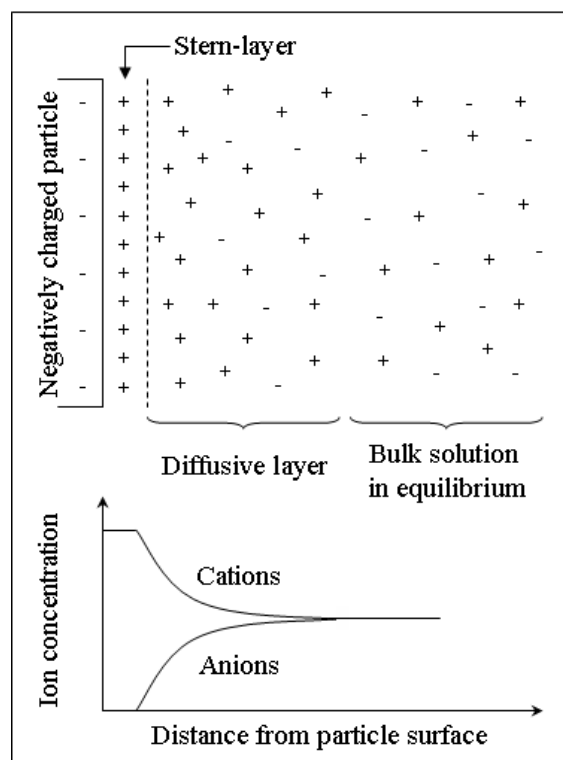


Figure 2.15: Distribution of ions in the vicinity of a charged surface after the electric double layer model by Gouy and Stern (adapted from Scheffer et al., 2002).

3

Practical Approach and Techniques

After a possible release of radionuclides from a repository, transport by groundwater will most likely be the major mechanism of radioactivity spreading in the environment. Consequently, studies related to waste disposal safety assessment must cover aqueous radionuclide chemistry, geochemical behaviour, site-specific geology, hydrology, and physical parameters, as well as modelling. Thereby, reasonable approximations taking into account the slow water fluxes expected in the vicinity of a nuclear repository are made by assuming steady state conditions (Dozol and Hagemann, 1993), which allows for a thermodynamic approach. Nevertheless, knowledge on the kinetics is also required in order to examine the transport processes with respect to radionuclide interactions between aqueous phase and mineral surfaces. Hence, safety evaluations must comprise studies aiming to understand those systems, which necessarily require thermodynamic as well as basic sorption data. The influence of colloid formation and humic complexation should additionally be addressed, and analytical spectroscopic techniques be used to determine radionuclide speciation in aquatic systems for filling gaps in the current scientific knowledge. The three main fields of research interest are solubility, sorption behaviour, and transport mechanisms.

Natural systems, however, are characterised by a vast complexity, making it necessary to abstract and simplify the encountered conditions for the laboratory setup. In this process, nature is approximated by an idealised counterpart to determine the various influencing parameters. As a first approach, well-defined systems are required, which usually contain a single solid phase and an ionic medium of known composition.

Since the chemical interactions of actinides in the environment are dynamic and exceedingly complex, all local conditions must be analysed to predict their escape and spreading velocity. This includes the nature of site-specific minerals,

temperature and pressure profiles, pH, redox potential (Eh), and ligand concentrations, as well as thermodynamic variables like stability constants and activity coefficients. Furthermore, a quantitative understanding of the competing geochemical processes, i.e., complexation, sorption, precipitation, and few others is necessary¹.

In order to obtain the most profound insight, radionuclide mobility is studied by laboratory experiments (see below), *in situ* investigations (taking into account repository site-specific parameters), computer modelling (predicting migration over a long time period), and natural analogues (unveiling slow processes by analysing geologically old deposits of radioactive isotopes). Because of their particular environmental hazard, studies of actinide geochemistry must almost exclusively be conducted remotely in the laboratory. Hence, the applying conditions must be simulated as best as possible. As one important aspect of the complex natural system, the analytical part of this work concentrates on the interactions of Np(V) with hydroxide (OH^-) and carbonate (CO_3^{2-}) ions, which are the two most relevant environmental ligands, and herein focusses on its specific sorption behaviour.

Another factor of known but not yet quantified impact on neptunium transport, that presently is gaining more and more attention, is seen in the possible uptake by or interaction with microorganisms. This aspect will not be covered in the present study; similarly, reactions with organic substances will not be addressed – but should be considered for future work on the topic of environmental behaviour of neptunium and other radionuclides.

3.1 Laboratory System

For ensuring reliable, high quality results some criteria are mandatory concerning the performance of laboratory experiments. These are the establishment of equilibrium conditions, accurate adjustment and determination of concentrations, complete phase separation, usage of a well defined solid phase, and knowledge of the oxidation state (Nitsche, 1989, cited in Dozol and Hagemann, 1993).

Laboratory *in vitro* experiments are able to identify mechanisms and individual model parameters (Choppin and Wong, 1996), thereby establishing the

¹Further processes that actinides in general are subject to, which primarily influence their aqueous speciation and, hence, are of minor importance within the scope of this study, are precipitation/dissolution and redox equilibria, solubility, radiolysis, hydrolysis, humic acid complexation, colloid generation, and the effects of other metal ions and potential ligands (Clark et al., 1995).

basis for numerical modelling. It is important to keep in mind, however, that such experimental data can reflect short-term processes only, limited by the time span of the laboratory work, and must be treated with care when extrapolating them to repository, i.e., geological timescales.

In the present study, batch sorption experiments have been chosen to investigate the behaviour of Np(V) in the environment. Aqueous solutions containing ^{237}Np or – in cases where a lower concentration and, therefore, a higher specific activity was required – the shorter-lived ^{239}Np were brought into contact with either $\gamma\text{-Al}_2\text{O}_3$ or montmorillonite (STx-1). The drawbacks of such rather simple experiments, though, are their static character that does not allow for any conclusions on dynamic non-equilibrium processes of radionuclide interactions in the natural environment. Thus, they provide only partial insight into the different conditions found throughout a repository and within its vicinity. Batch experiments alone cannot explain sorption processes completely. In general, all results must be scrutinised within the context of the multi-component natural system. Furthermore, laboratory experiments can only predict radionuclide migration on a human timescale, but forecasts must cover geological periods. All results obtained must, therefore, be interpreted with these limitations kept in mind. But still, in spite of all these limitations, batch experiments represent a valuable first approach to comprehending actinide behaviour under real conditions.

The following subsections summarise the experimental design and setup and explain why these particular conditions were chosen for this work.

3.1.1 Neptunium Concentration

The concentration of actinides in natural waters is predicted to be 10^{-6} M at the highest (see Section 2.1.3) being limited by the solubility of the corresponding solids. Nevertheless, this value will, if at all, not be reached immediately in a release scenario. It can rather be anticipated that slow seepage will generally result in quite low trace concentrations of radionuclides leaving the repository.

Therefore, the neptunium concentration was aimed to be as low as possible, while still accounting for manageable and measurable amounts. In these considerations, the lucky situation of having the research reactor TRIGA Mainz readily available for generating the short-lived ^{239}Np facilitated the realisation of sorption experiments at neptunium trace level. The lower limit was given by the reliable determinability within reasonable time via γ spectroscopy of the neptunium content in 1 mL of solution even after sorption of $\sim 80\%$ of the incident concentration. The compromise was found to be within the picomolar ($1\text{ pM} = 10^{-12}$ mol/L) concentration range, conveniently 7-8 pM.

For the preparation of EXAFS samples, however, such a low neptunium content would not provide a sufficient load on the montmorillonite or aluminium oxide surfaces to allow for the acquisition of analysable spectra. Therefore, the neptunium concentration was chosen to be in the micromolar ($1 \mu\text{M} = 10^{-6} \text{ mol/L}$) range. Additional batch experiments ensured the preservation of the same sorption regime as encountered for picomolar concentrations and supported the selection of the precise experimental conditions (i.e., pH, ionic strength, presence/absence of CO_2) for each EXAFS sample.

Since the formation of solid neptunium phases would falsify the sorption results and mislead the analysis and interpretation of the experimental data, the precipitation limit was determined via isotherms at a pH-value around the sorption maximum (i.e., pH 8.0-9.5) for a neptunium concentration of up to 10^{-4} M in presence as well as in absence of ambient CO_2 . Nevertheless, the data obtained from such studies provide only an upper limit to potential aqueous concentrations in a release scenario, because actinides precipitate as an amorphous, rather soluble phase during laboratory experiments. Thus, the precipitate found may not represent the thermodynamically most stable – hence, least soluble – solid possible, which might form over longer time periods (Runde, 2000).

3.1.2 pH-range

Cations are sorbed electrostatically on clay minerals not only because of their permanent structural charge due to isomorphic substitution (see Section 2.3.2), but also because of the charge caused by the binding or dissolution of protons. Thus, the effective ion exchange capacity is pH-dependent. To account for this fact, experiments were planned as to examine the relationship between solution pH and neptunium sorption in the given system.

The definition of an appropriate pH-range must consider several aspects: First, it must be wide enough to allow for a clear identification of the expected dependency (e.g. sorption edge or ion exchange); second, adverse and falsifying conditions such as dissolution effects must be avoided as best as possible; third, the natural system upon which the studies are based must be represented.

Most natural waters are relatively mild with near neutral pH, ranging from 5 to 9, and low salinities of $<1 \text{ M}$ (Runde, 2000). Under repository conditions and in the near field, the pH might be more extreme, in either acidic or alkaline terms. In designing laboratory experiments that properly reflect these conditions, certain limitations arise from the stability of clay minerals. The closer both extremes of the pH-scale are approached, the faster is the dissolution of montmorillonite as well as of $\gamma\text{-Al}_2\text{O}_3$ (see Sections 2.4.1 and 2.4.2). Hence,

to preclude dissolution processes to a great extent, the batch experiments conducted covered a limited pH-range from 3 (montmorillonite) or even 5 (γ - Al_2O_3) up to 10.5 only.

3.1.3 Ambient Air versus CO_2 -free Conditions

As already discussed in the previous chapter (Sections 2.2.4 and 2.5.1), the absence or presence of CO_2 has an outstanding impact on the sorption behaviour of actinides. Correspondingly, for the present study, two contrary situations were examined regarding their influence on neptunium sorption, the presence of ambient CO_2 and its complete absence. Experiments were either conducted in the laboratory exhaust hood or alternatively in a sealed glove box flooded with argon.

Experimentally, it is extremely difficult to distinguish between $\text{CO}_2(\text{aq})$ and H_2CO_3 , and in nearly closed systems like in deep groundwaters or in oceans, the exchange of dissolved CO_2 with the atmosphere is very slow. Thus, the total carbonate concentration is expressed as the sum of $[\text{CO}_2(\text{aq})]$, $[\text{HCO}_3^-]$, and $[\text{CO}_3^{2-}]$ (Clark et al., 1995). At constant CO_2 pressure, however, an equilibrium is maintained, so that the specific condition is conveniently expressed in terms of gaseous p_{CO_2} .

The partial pressure of CO_2 in natural waters extends over almost three orders of magnitude ranging from ca. $7 \cdot 10^{-4}$ to $1 \cdot 10^{-1}$ M. This results in a carbonate concentration of 10^{-5} to 10^{-3} M in surface waters and up to 10^{-2} M in groundwater aquifers (Runde, 2000). Sabodina et al. (2006), for example, measured 50 mg/L, respectively $8 \cdot 10^{-4}$ M, for bentonite pore water. Thereby, the equilibrium between gaseous and dissolved CO_2 is directly linked to pH: the more alkaline the solution, the more carbonate dissolves, as illustrated in Figure 3.1.

Although the samples in this study were allowed to equilibrate with the respective atmosphere over several days, problems occurred at high pH under ambient air (see Section 5.1.4). The experimental results gave rise to the suspicion that the samples at high pH had still not reached satisfactory equilibrium with the aerial CO_2 . To accelerate the process of increasing carbonate dissolution with pH, the corresponding concentrations of HCO_3^- and CO_3^{2-} were calculated theoretically with the programme Visual MINTEQ (Gustafsson, 2007) and added to the samples as solutions of NaHCO_3 and Na_2CO_3 . The error resulting for the ionic strength (through the simultaneous increase of Na^+) was regarded minor in comparison to the benefit from this procedure.

It must be noted that, in addition to HCO_3^- and CO_3^{2-} , also OH^- is present as a ligand in carbonate solutions and that hydrolysis and carbonate equilibria

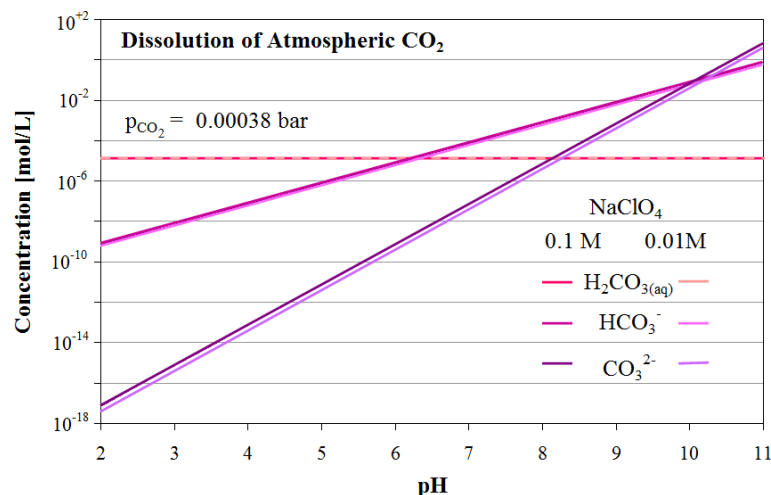


Figure 3.1: Dissolution of atmospheric CO_2 in aqueous media, calculated with Visual MINTEQ (ionic strength fixed). While the concentration of carbonic acid is constant, the formation of hydrogen carbonate (also called bicarbonate) and carbonate increases significantly with pH. The influence of the ionic strength is comparably small.

are closely connected in that CO_3 species suppress the former under ambient air conditions (compare Figure 5.10, page 133). In this work, however, only the overall effect on the sorption of neptunium is studied.

3.1.4 Ionic Strength

Equilibria involving ionic species – in the present case NpO_2^+ – are always affected by all ions present in solution, which together comprise the ionic strength (Clark et al., 1995). For a 1:1 electrolyte (such as $\text{NaClO}_4 \rightleftharpoons \text{Na}^+ + \text{ClO}_4^-$) the ionic strength equals the concentration, but for salts dissociating in multivalent components (such as $\text{Na}_2\text{SO}_4 \rightleftharpoons 2\text{Na}^+ + \text{SO}_4^{2-}$) the ionic strength is correspondingly higher (for the given example by three times). According to this, the ionic strength is calculated as

$$I_c = \frac{1}{2} \sum_{B=1}^n c_B z_B^2 \quad (3.1)$$

where c_B is the molar concentration of ion B and z_B is its charge; the sum is taken over all ions in solution (International Union of Pure and Applied Chemistry (IUPAC), 2008).

Thus, the ionic strength of natural waters depends on its salt content. While saltwater of 35 ‰ salinity has an ionic strength of about 0.7 M, that of freshwater is usually less than 0.02 M (Appelo and Postma, 2005). The ionic strength of groundwater is even lower (up to ten times). Characteristic bentonite pore water with a solid-to-liquid ratio of 100 g/L has a Na^+ content of 310 mg/L (Sabodina et al., 2006), which equals 0.013 M. Taking into account all other ions present (F^- , Cl^- , NO_3^- , SO_4^{2-} , Br^- , $\text{CO}_3^{2-}/\text{HCO}_3^-$, Na^+ , K^+ , Ca^{2+}) the total ionic strength comes to 0.009 M applying the equation given above. Compacted bentonite instead reveals a much higher ionic strength, which is correlated with its dry density. At 1500 kg/m³, for example, the ionic strength is 0.31 M (Bradbury and Baeyens, 2003). Commercial compacted Na-bentonite with 70–90% montmorillonite typically has an ionic strength of 0.2 to 0.3 M (Bradbury and Baeyens, 2006b).

Neptunium sorption is influenced by ionic strength in that the electric double layer (see page 50) forming in the vicinity of a charged surface is compressed with increasing concentration or valence of the counterions. Changes in ionic strength affect the competition with other ions under investigation, whose concentration is not varied; in the present study, that is the case for NpO_2^+ .

For laboratory experiments, the natural system must largely be simplified. However, one important factor in radionuclide environmental behaviour is the composition of the groundwater. In order not to neglect the influence of competing ions, sodium perchlorate², NaClO_4 , has been chosen as background electrolyte. In respect to other substances, the ClO_4^- ion has the advantage of being non-complexing, as outlined in Section 2.2.1 (Runde, 2000). The central chlorine is a closed-shell atom well protected by the four surrounding oxygen atoms and, therefore, it reacts very slowly unless heated. In this study, the ionic strength was chosen to be either 0.01 or 0.1 M to give some idea about its effect on neptunium sorption, reflecting the main range assumingly encountered by actinides after a possible release from the repository.

3.1.5 Solid-to-liquid Ratio

The sorption behaviour of different elements can be compared through the distribution coefficient K_d (see Section 4.3.5 for its definition). Although this quantity is independent from the solid-to-liquid ratio, it is an important parameter in the design of sorption experiments. Since the neptunium uptake by the solid phase

²The ionic structure of NaClO_4 is $\text{Na}^+ \text{O}=\overset{\text{O}}{\underset{\text{O}}{\text{Cl}}}-\text{O}^-$.

is determined in this study indirectly from the alteration in neptunium concentration of the aqueous phase, a distinct difference between initial and final state is essential for practical reasons. Thus, the solid-to-liquid ratio must be sufficiently high to provide an adequately large surface area, respectively enough sorption sites. Conversely, the solid-to-liquid ratio must not be too high, so that never all neptunium is sorbed from solution. Otherwise, the shape of the (e.g. pH-dependent) sorption curve will not be sound showing a sharp and sudden cutoff at 100 %, which is demonstrated in Figure 3.2.

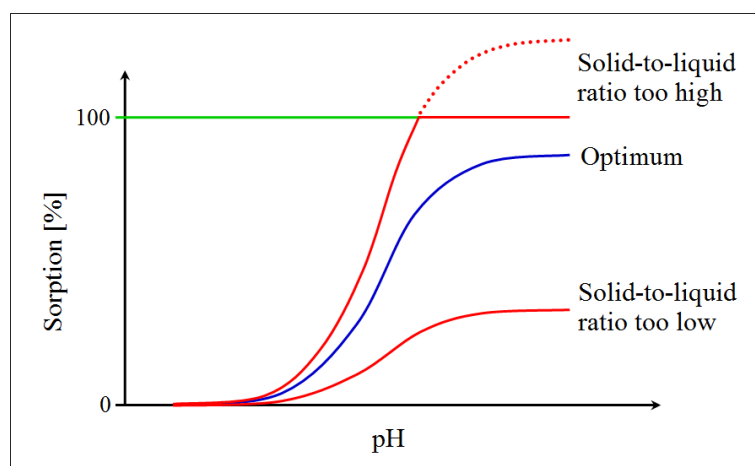


Figure 3.2: The influence of the solid-to-liquid ratio on the shape of the sorption curve. An excess of sites in relation to the number of ions causes a quick achieving of 100 % sorption, whereas too few sites compared to the dissolved ions result in a limitedly structured curve; in both cases an optimal interpretation is hardly possible.

The optimum situation is 50 % sorption. Then, the neptunium concentration in solution has decreased significantly during the experiment, while the remaining share is still well measurable. For convenience as well as to allow for data presentation on a percentage basis, the solid-to-liquid ratio was kept constant during the batch experiments. To take account of the shape of the sorption curve, i.e., the regime over the entire pH-range, sorption was aimed to be 80 % at maximum what enabled the determination of low neptunium uptake in the acidic pH-region, as well. Since for calculating the distribution coefficient K_d the ratio of sorbed to dissolved neptunium is normalised by multiplication with the solid-to-liquid ratio (see also Section 4.3.5), the desired neptunium uptake can be calculated when the K_d is known. If the initial neptunium concentration is given and the ratio of final to initial concentration shall equal e.g. 0.8, the

only unknown variable is the mass of solid, m , because the sample volume is determined by the experimental setup. Hence, m can be calculated via

$$K_d = \frac{Np_s}{Np_d} \cdot \frac{V}{m} = \frac{c_f - c_i}{c_f} \cdot \frac{V}{m} \quad (3.2)$$

$$\Leftrightarrow c_f = \frac{c_i}{1 + K_d \cdot \frac{m}{V}} \quad \wedge \quad c_f \stackrel{!}{=} 0.8 c_i \quad (3.3)$$

where K_d is the sorption coefficient [mL/g], Np_s and Np_d are the sorbed and the dissolved amounts of neptunium [mol or g] in the equilibrated sample, c_i and c_f are the initial and final neptunium concentrations [M] in solution, V is the volume of the sample [L], and m is the mass of sorbent in the sample [g] (Baeyens and Bradbury, 1995b).

For this calculation, K_d -values were inserted from published data of similar experiments, e.g. by Li and Tao (2003), or by Righetto, Bidoglio, Marcandalli and Bellobono (1988) for aluminium oxide and Baeyens and Bradbury (1995b) for montmorillonite. Together with results from previous studies (Dierking, Vicente Vilas, Baeyens and Reich, 2006) solid-to-liquid ratios of 0.5 g/L for γ -Al₂O₃ and 4 g/L for montmorillonite were determined.

3.1.6 Thermodynamics and Reaction Kinetics

As pointed out before, due to the complexity of the natural system and the lack of a consistent description, sorption studies are commonly based on thermodynamic data, assuming steady state conditions within the considered timescale. A virtually complete collection of these data sets for neptunium can be found in Lemire et al., 2001 (OECD Nuclear Energy Agency) including computerised data bases.

Many sorption processes, however, are rate-controlled at the surface and not determined by the transport velocity of the sorbate. Thus, surface structure and properties – i.e., speciation and microtopography – determine the kinetics of the sorption process (Stumm, 1992). On clay platelets, sorption is time-dependent, suggesting a more complex mechanism than encountered for processes on oxide minerals (Runde, 2000). In addition to the various steps generally involved in the transfer of the dissolved ion to the sorbing surface of the solid, such as molecular convection, attachment, dehydration, and bond formation (Stumm, 1992), the diffusion into the interlayer space of clay minerals prolongates the establishment of equilibrium. Furthermore, sorption kinetics are influenced by the experimental conditions. For example, steady state is reached faster in acidic than in neutral or alkaline media (Sabodina et al., 2006).

To estimate the contact time required to ensure equilibrium between the sorbed and dissolved neptunium phases in the experiments, literature data were consulted. For a sorption experiment with γ - Al_2O_3 in 1 M NaClO_4 , Yamaguchi, Nakayama and Yoshida (2004) determined the attainment of equilibrium within 24 hours. Also for radionuclide sorption on Na-montmorillonite no kinetic effects were observed after 1 day end-over-end shaking (Baeyens and Bradbury, 1997). This is consistent with the observation that the sorption of Np(V) on the double-layered clay mineral kaolinite is fairly quick; equilibrium is attained within less than two hours (Jermolajev, Kasbohm, Amayri and Reich, 2005). Therefore, to be on the safe side in this study, the suspensions were separated not before three days of contact between Np(V) and the sorbents.

3.2 Analytical Methods

3.2.1 γ Spectroscopy

For all investigations within this work, the overall amount of neptunium present in solution was quantified via γ spectroscopy. This method allows for straightforward, reliable and easy determination of the γ dose rate and thus the radioactivity content in a sample, while the well developed technology facilitates safe handling of radioactive liquids, minimising the risk of contamination or spill. In brief the experimental approach is the following:

Nuclear radiation in general has ionising properties, since the energy released in nuclear processes is by far larger than the binding energies of atomic electrons. This fact enables the observation of nuclear decay processes through detection of the interaction of the emitted radiation with matter. Even though the total number of ion pairs created by γ rays is considerable (e.g. $\sim 10^5$ by a 1 MeV decay, corresponding to a charge of $\sim 10^{-14}$ C; Loveland et al., 2006), amplification processes must be embedded for observation. Suitable methods of γ decay detection thus involve ionisation and charge collection in a gas or in a solid crystal, secondary atomic excitation and optical emission in a liquid or solid scintillator material, or specific changes induced within sensitive emulsions. In all cases the individual detector has to provide sufficient detection efficiency as well as energy and time resolution, to ensure reasonable selectivity and sensitivity in the radioisotope determination.

A typical detection system for γ rays consists of an energy sensitive radiation detector head, an electronic pulse discriminator with associated amplifiers, and a data readout device, usually a multichannel analyser. Most suitable are semiconductor Ge or Ge(Li) detectors, since they offer the best energy resolution

of about 0.2 to 0.4 keV (Lieser, 2001). Within the semiconductor volume the incident radiation creates hole-electron pairs, of which the latter are collected by electrodes. Intensity, shape and duration of the electrical pulse created encodes information on the type and energy of a single particle or on the number of particles, which arrived per time unit.

The detection process is entirely passive in a sense that the γ interaction within the crystal volume (via photoelectric effect, Compton effect, and pair production) by itself produces a voltage pulse, which is directly converted into a corresponding digital signal. Subsequent peak search routines, calculations of peak and net peak area, energy calibration, determination of resolution, and final radionuclide identification and quantification were performed by the experimenter using GenieTM 2000 Gamma Analysis Software (Canberra Industries, Inc.).

Since the γ spectrum is characteristic for each emitting radionuclide, the composition of a sample can clearly be identified. Due to limited counting statistics, however, thorough calibration of the energy scale through the pulse height is necessary. To allow for proper geometry factor consideration, always 1 mL of neptunium containing solution was measured at the same position in the detector arrangement.

The nuclear decay of ^{239}Np emits predominantly γ rays with energies of 103.76 keV (24.2%), attributed to the metastable state of ^{239}Pu ($K_{\alpha 1}$), and 106.12 keV (27.2%); ^{237}Np is characterised by γ energies of 29.40 keV (15.0%) and 86.48 keV (12.4%) (Ekström and Firestone, 2004). For ^{239}Np the counting rates at the two close-lying peaks were averaged to determine the content in the sample. For ^{237}Np , however, only the counting rate at 29.40 keV was used, because γ rays around 86 keV are also emitted by its decay product ^{233}Pa .

The duration of measurement of the respective sample was fixed according to the counting rate. Assuming pure statistical uncertainties following a normal Gaussian distribution, at least 10 000 events are necessary to achieve an error of less than 1% according to

$$\Delta n = \frac{\sqrt{n}}{n} \quad (3.4)$$

where n is the counting rate and Δn its error.

Depending on the final concentration of neptunium in solution and the time elapsed since phase separation, the counting time was set between 20 min and 12 h.

3.2.2 Liquid Scintillation Counting

In samples with very low ^{237}Np content, the γ measurements were verified by liquid scintillation counting (LSC). In this detection method, the energy of the ionising radiation is transferred to optically active molecules dissolved in an usually nonpolar solvent. These emit luminescent light in the visible to near-ultraviolet region (so-called scintillation) during their atomic deexcitation, which is detected by means of a photomultiplier. There, the photons are converted to photoelectrons on a photocathode and afterwards amplified by secondary electron emission on a series of dynodes to create a sizable electronic pulse for further processing. As the number of photons produced is proportional to the energy of the incoming radiation and each primary photoelectron is multiplied to deliver a pulse of 10^5 - 10^6 electrons (Loveland et al., 2006) a linear relationship of the output signal to the energy of the incident γ ray is assumed.

For these measurements, 1 mL of supernatant was mixed with 20 mL Ultima GoldTM AB scintillator cocktail. Due to the high quantum efficiency of the photomultiplier, the efficiency of this method is much better than that of the conventional γ detector, which is further limited by its geometry. Nevertheless, LSC is less feasible than γ counting because of the large quantity of liquid waste produced and was, therefore, only applied when necessary.

For LSC the counting time was again fixed on the basis of a statistically relevant counting rate of 10 000 (see Equation 3.4 above), what amounted to ~ 150 to 3 750 s per sample ($8 \mu\text{M}$ ^{237}Np , 4 g/L sorbent).

3.2.3 Direct Speciation via EXAFS

In order to better understand the binding of neptunium to mineral surfaces, the structural identity as well as the geometry of the coordination spheres of surface sites and sorbed ions need to be known. Most mechanisms of surface controlled processes depend on the molecular coordination at the solid-water interface (Stumm, 1992), so that speciation analyses are mandatory for a thorough interpretation of batch experimental results.

Advanced X-ray techniques at synchrotron facilities can be beneficial to speciation research in that the information obtained helps in understanding the transformation between species. This, in turn, facilitates the prediction of likely consequences following physico-chemical perturbation of the system (Manceau et al., 2002). In particular, the application of Extended X-ray Absorption Fine Structure (EXAFS) analysis may contribute to yield precise information about the local environment of the absorbing central actinide atom. This includes the identity of the surrounding atomic species, coordination numbers, bond lengths,

and thermal disorder. Thus, by the EXAFS technique the molecular structure can be derived as well as the spatial distribution of atoms around the selected central site. The following paragraphs give a brief introduction to the underlying theory of this technique.

EXAFS Theory

To obtain an EXAFS spectrum, basically, photons from an energy-tunable synchrotron X-ray source are sent onto a sample and the energy dependence of the absorption is monitored. When the incident X-ray energy crosses the binding energy of an atomic core electron this is excited, resulting in a strongly increased absorption.

At a certain energy, the incident photons excite one of the deep core electrons into a high-lying, unoccupied state or into continuum for ionisation. The fact that the atoms of every element reveal characteristic electron binding energies enables the analysis of individual elements in a mixed or heterogeneous matrix by selecting a corresponding incident X-ray energy range. The energy dependence of the absorption probability is sensitive to oxidation state, coordination chemistry, and the distances, coordination numbers, and atomic species surrounding the atoms of the selected element (see below). Thus, the EXAFS spectrum provides a practical way to determine chemical state and local atomic structure for practically any element of interest. The eminent strength of this method is that crystallinity of the sample is not required and that measurements can be performed on elements of minority or even at trace level. For non-crystalline material EXAFS delivers structural data that are not available to any other technique (Ravel, 2000).

The detailed phenomenology of EXAFS has been known since the 1930's and is investigated and analysed in terms of quantum mechanical interference effects. Nevertheless, it took 40 more years until routine applications became possible through the construction and availability of tunable, high flux, high energy-resolution synchrotron radiation facilities and corresponding beamlines. This advance was supported by the development of the EXAFS equation by Sayers, Stern and Lytle (1971) and their finding that a meaningful analysis can be given through application of a Fourier transformation – this approach will be discussed in detail below. Today the EXAFS technique is employed for numerous applications in chemistry, physics, biology, as well as in materials and environmental sciences.

Precisely, X-rays with an energy E greater than the binding energy E_0 of a given electron shell are absorbed and lead to ionisation. The excess energy ($E - E_0$) is transferred to the photoelectron, which is ejected from the atomic

shell, as shown in Figure 3.3. Characteristic for this photo-electric effect is the dependency of $\lambda^{-1} \sim (E - E_0)$, where λ is the wavelength of the emitted photoelectron, which propagates outward from the centre. It can be described as a spherical wave with initial core ($|i\rangle$) and final, unbound ($\langle f|$) state being inter-related by Fermi's Golden Rule to give the transition probability:

$$P(E) = \langle f|H_{int}|i\rangle^2 \cdot g_f \quad (3.5)$$

Here $\langle f|H_{int}|i\rangle^2$ is the matrix element between initial and final state, which is induced by the perturbing interaction. The latter is expressed quantum mechanically correct by the interaction Hamiltonian H_{int} . g_f is the density of final states.

In the realistic case of an atom embedded in the environment of a solid or liquid phase, single scattering processes and – in more complex cases – even multiple scattering with the surrounding atoms must be considered. A mathematical Green's function must be used as solution for the corresponding inhomogeneous differential equation, which replaces Equation 3.5 to precisely describe the propagation of a photoelectron of given energy, respectively wavelength λ , in such a system under consideration of neighbouring atoms. These scattering atoms are located at different distances along the path from the absorber's core, thus contributing with different intensity and phase to the backscattered wave, which must be taken into account, too. The final state wavefunction ψ_f thus includes both outgoing and backscattered parts, which interfere either constructively or

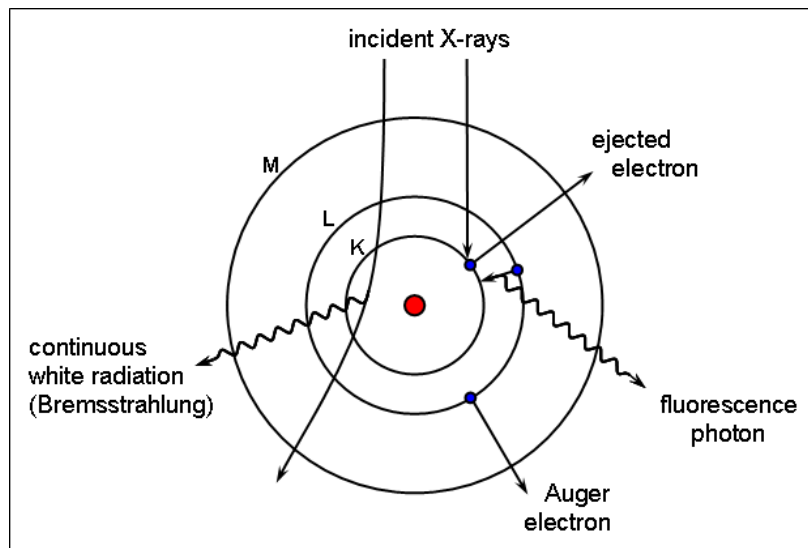


Figure 3.3: Interactions of incident X-rays with an atom (after Teo, 1996, modified), for details see text.

destructively in a complex dependence on the electron wavelength and the displacements between the central and each backscattering atom. The effect of this distinctive phenomenon on the EXAFS spectrum is outlined in Figure 3.4. Here, the constructive and negative interferences at $\lambda = R/3$, $R/3.5$, and $R/4$, respectively, are shown; the superposition of outgoing and scattered wave contributes to the absorption cross section.

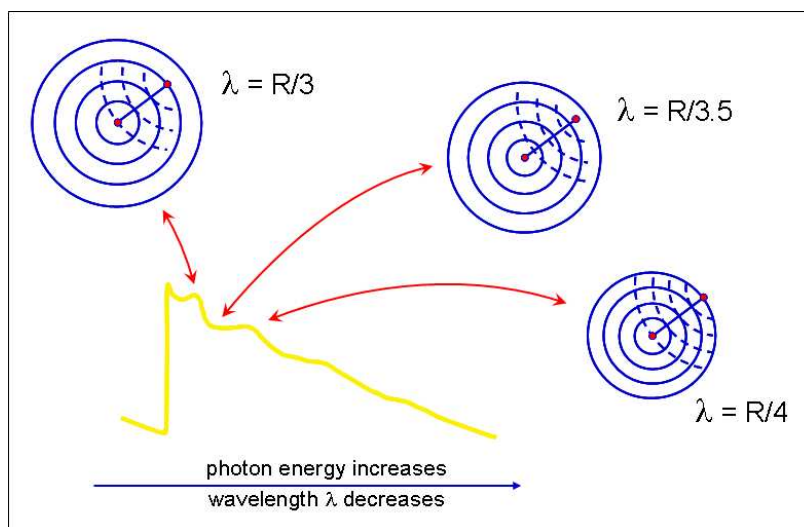


Figure 3.4: Obtaining structural information by EXAFS. The probability of absorption oscillates due to constructive and destructive interference of initial and scattered wave (Sakura Pascarelli, ESRF Grenoble, France; Science on Stage, Apr. 2nd, 2007).

Both formulae, Fermi's Golden Rule as well as the more precise Green's function, are difficult to solve exactly as this involves large matrices, whereas an intuitive interpretation focussing on individual scattering pathways can be derived rather easily. When the photoelectron is scattered only once off a given neighbouring atom, this process is denoted a single scattering path. Any other case is termed multiple scattering path, including events which involve two surrounding atoms (double scattering), located in a single or two neighbouring coordination spheres around the central atom, as well as scattering of the photoelectron from still more atoms. Accordingly, there is an almost infinite number of scattering paths possible even within a single molecule, for which fortunately some rules of thumb help determine their relevance: Single scattering, short double scattering and so-called linear³ multiple scattering pathways – sketched in Figure 3.5 – generally contribute most strongly to the spectrum, while any others can largely be ignored (Ravel, 2001).

³scattering angle close to 180° – usually denoted as focussing path

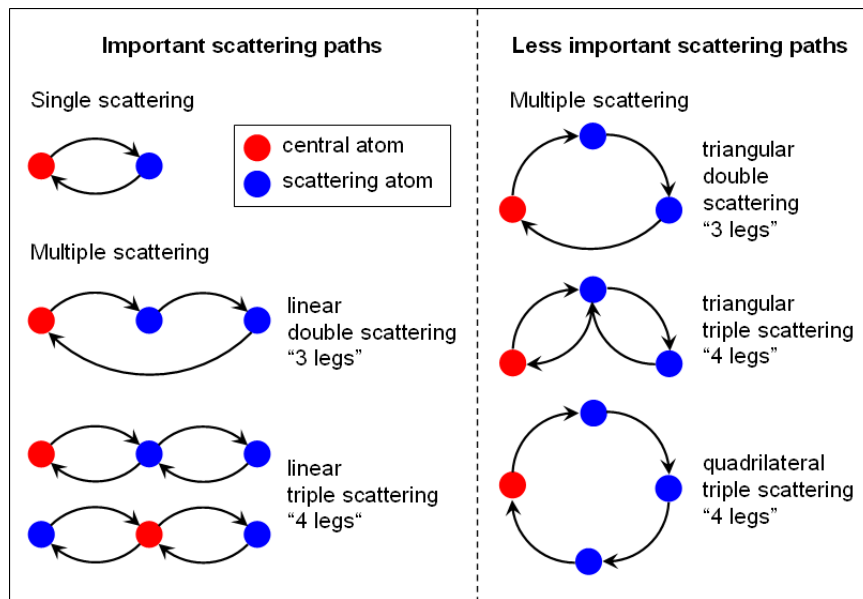


Figure 3.5: Possible scattering paths between the central atom and surrounding neighbours (after Ravel, 2000, modified).

The contributions from all individual paths Γ , which can be parameterised as $\chi_{\Gamma}(E)$, are summed to give the total $\chi(Ek)$, i.e. the EXAFS signal. Filtering by amplitude with consideration of single, double, and linear multiple scattering paths only and by path length (contributions to the fitting region in R -space⁴ only) helps to reduce the extent of the required data processing.

The lifetime of the final atomic state, i.e. with a hole in the electronic K- or L-shell, is well below a few femtoseconds, $<10^{-15}$ s, which is about 10^3 times shorter than periods of interatomic vibration (Bunker, 1997). The distance that the photoelectron can travel within this time, called its mean free path, is rather limited. Thus, EXAFS acts as a local probe only, which cannot reach further than typically $\sim 5 \text{ \AA}$ from the absorbing atom's site (Newville, 2004b).

The core-hole is filled by an electron from a higher-lying level, accompanied by the emission of a fluorescent photon with the well-defined energy difference of these two levels (Ravel, 2001), which is illustrated in the top right part of Figure 3.3. This process can be used to clearly identify the atoms in the system and to quantify their concentrations (Newville, 2004b). As also shown, an alternative process for deexcitation is the emission of an Auger electron together with the electron dropping down from the higher level to fill the core-hole. Within the

⁴real space (\mathbb{R}^3), as contrasted with reciprocal space (k -space, also called Fourier space, see below)

hard X-ray region above 2 keV encountered for synchrotron radiation, however, fluorescence is more likely to occur (Newville, 2004b).

For a further detailed discussion of the EXAFS technique, outlining the underlying physical principles and providing a full mathematical derivation of the corresponding equations, the interested reader is referred to e.g. Koningsberger and Prins, 1988, or Teo, 1986. A brief description is given below.

EXAFS Analysis

Synchrotron radiation is emitted tangentially when fast moving electrons are forced by bending magnets to leave their linear path. From the resulting spectrum of polychromatic X-rays, an energy band of ca. 1 eV bandwidth is selected by diffraction from a silicon double-crystal monochromator, and allowed to pass through the sample. All elements with $Z > 18$ have either a K- or L-shell binding energy between 3 and 35 keV and, thus, are accessible at state-of-the-art synchrotron facilities (Newville, 2004a). For measurement the incident (I_0) and transmitted (I) X-ray fluxes are monitored via gas ionisation chambers; alternatively, EXAFS can make use of a fluorescence geometry.

Fluorescence measurements are preferred for thick samples or low concentrations. The detected spectrum will, however, not only contain the fluorescence line of interest, but also those from other elements, plus both elastically (coherent Rayleigh scattering) and inelastically (incoherent Compton scattering) scattered X-rays. The latter can effectively be reduced by taking account of the fact that the incoming radiation is polarised in the plane of the synchrotron. While the fluorescence X-rays are emitted isotropically, scattering mainly occurs in forward direction and is least at right angle with respect to the polarisation direction. Therefore, the fluorescence detector is placed at an angle of 90° to the incident beam to suppress the scatter signal. Further energy discrimination is either accomplished physically by filtering out unwanted emission before detection or electronically afterwards (Newville, 2004b). In the latter case, usage of a solid Si or Ge detector is helpful, as it provides an energy resolution better than 200 eV, but has the drawbacks of dead time effects and required liquid nitrogen cooling.

The monitored X-ray intensities directly provide the absorption probability according to the Lambert-Beer law by

$$I = I_0 \cdot e^{-\mu d} \quad (3.6)$$

where I_0 is the incident X-ray intensity, I the transmitted intensity, and d the sample thickness. From the X-ray intensities incident onto the sample as well as

after passing through, the energy dependence of the absorption coefficient $\mu(E)$ is calculated either in transmission with

$$\mu(E) = \log \left(\frac{I_0}{I} \right) \quad (3.7)$$

or in fluorescence with

$$\mu(E) \propto \frac{I_f}{I_0} \quad (3.8)$$

where I_f is the intensity monitored for a fluorescence line. The total absorption coefficient $\mu(E)$ is typically expressed as that of the isolated atom $\mu_0(E)$ times a correction factor, which accounts for the fractional change induced by neighbouring atoms. Thereby, $\mu_0(E)$ depends on sample density ρ , atomic number Z and mass A , as well as on the X-ray energy E according to Newville (2004b):

$$\mu_0(E) \approx \frac{\rho Z^4}{AE^3} \quad (3.9)$$

The strong dependency of X-ray absorption on Z and A , especially the Z^4 correlation, gives good contrast between different elements and is the basis for the elemental specificity of the EXAFS technique.

The absorption coefficient $\mu_0(E)$ decreases as the energy (E) increases with $\sim 1/E^3$, but when an incident X-ray photon provides just sufficient energy (the absorption threshold E_0) to excite an electron from any filled bound level, i.e. the 1s-state, up to an unoccupied configuration, i.e. a p-state, a sudden rise in absorption occurs, the so-called corresponding absorption edge (for $n=1$ the K-edge). In addition, transitions from less deeply bound levels, such as 2s, 2p_{1/2}, 2p_{3/2}, 3s, etc. occur at lower X-ray energies. The corresponding absorption edges are designated L_I, L_{II}, L_{III}, M_I, etc. Since for elements of higher atomic number the energy required to excite a 1s-electron is particularly large, the latter are preferred for their EXAFS studies.

At energies close to the absorption edge, i.e. in the near edge region, all kinds of transition may occur, i.e. into unfilled bound, nearly-bound (resonance), or into continuum states lying close to the binding energy E_0 . In case of a solid sample this is given by the Fermi energy. These processes yield the X-ray Absorption Near Edge Structure (XANES) (Rehr and Albers, 2000). At energies sufficiently high above (≥ 30 eV) the absorption edge, transition always leads into continuum. In this region, the Extended X-ray Absorption Fine Structure (EXAFS) is detected as a signal, which is strongly modulated by the existence of neighbouring atoms as a function of energy. Both XANES and EXAFS yield extremely valuable structural information of a solid or liquid sample:

- The pre-edge region and the rising part of the edge (the XANES) is very sensitive to formal oxidation state and coordination (e.g. octahedral or tetrahedral) of a chosen central atom, revealing details of its local site symmetry. In addition, bond length, charge state, and orbital occupancy are probed (Bunker, 1997), which together provide valuable insight into the chemical state of the sample.
- In the EXAFS region, distances to the neighbouring atoms, coordination number, and species become observable (Newville, 2004b). The valence state of the central atom can be determined from the absolute position of the absorption edge (E_0) using both techniques.

The XANES-analysis, however, is a rather qualitative approach lacking suitable quantitative descriptions and equations for calculation, and it is used predominantly as a fingerprint of known phases (Newville, 2004a). The exact physical and chemical interpretation of spectral features is difficult, if not impossible. For demonstration, examples for absorption edge shapes and positions corresponding to different oxidation states are given in Figure 3.6 in a general overview for actinides. Figure 3.7 shows a detailed comparison for the specific cases of the oxidation states IV to VII for neptunium.

For EXAFS analysis (i.e., to facilitate data interpretation in terms of wave behaviour) the initial X-ray energy is related to the wavenumber k [in m^{-1} or \AA^{-1} ,

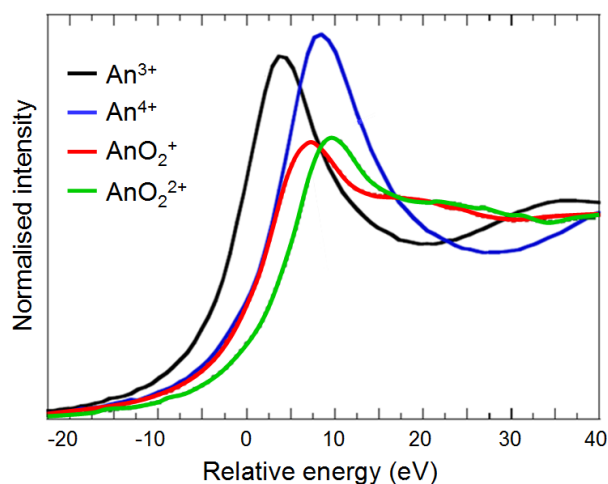


Figure 3.6: Representative actinide XANES spectra as function of oxidation state and coordination (Hudson et al., 1995, cited in Antonio and Soderholm, 2006).

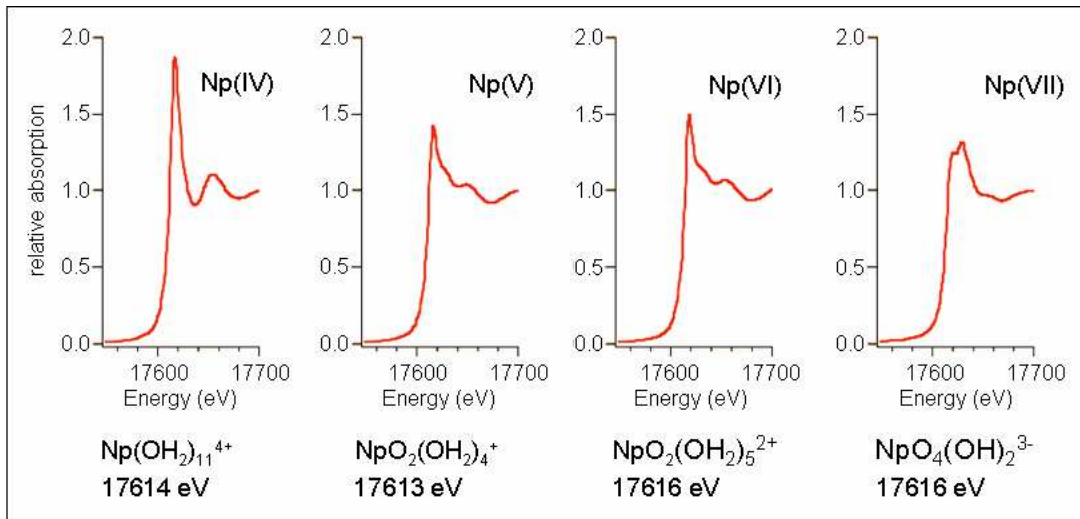


Figure 3.7: L_{III} -edge XANES spectra of certain neptunium compounds with their inflection point energy, i.e. their absorption edge position (T. Reich, GRK-lecture, Mainz, Jan. 16th, 2008).

respectively] of the outgoing photoelectron via its momentum, the DeBroglie wavelength

$$p = \hbar|k| \quad (3.10)$$

using the non-relativistic momentum-energy relation

$$E = \frac{p^2}{2m} \quad (3.11)$$

as

$$|k| = \sqrt{\frac{2m_e(E - E_0)}{\hbar^2}} = \sqrt{0.2624(E - E_0)} \quad (3.12)$$

with E_0 being the absorption edge energy, \hbar the Planck's constant over 2π , and m_e the electron mass.

As the energy E of the incident X-rays is varied, the kinetic energy of the photoelectron ($E - E_0$), and consequently its momentum and wavelength, changes and the absorption probability $\mu(E)$ is altered. In addition, the outgoing and backscattered waves interfere. This gives rise to oscillations in the absorption coefficient, which are periodic in the wavenumber k , as illustrated in Figure 3.4.

These oscillations, denominated $\chi(k)$, are calculated as function of photoelectron wavenumber. Different frequencies present in the signal can be assigned to separate neighbouring coordination spheres (also called shells). $\chi(k)$ is proportional to the amplitude of the scattered photoelectron at the central absorbing atom.

The classical EXAFS equation taking account of all influencing variables and parameters explained above is

$$\chi(k) = - \sum_j \frac{N_j}{kR_j^2} \cdot S_0^2(k) \cdot |f_j(k)| \cdot e^{\frac{-2R_j}{\lambda_e}} \cdot e^{-2k^2\sigma_j^2} \cdot \sin(2kR_j + 2\delta_l(k) + \varphi_j(k)) \quad (3.13)$$

where $\chi(k)$ is the normalised oscillatory part of the X-ray absorption, N_j is the number of atoms of element j in the coordination sphere (i.e., the number of equivalent scatterers) and σ_j^2 the temperature-dependent root mean square fluctuation about the average interatomic distances R_j in the j^{th} sphere, which also includes effects due to structural disorder; $|f_j(k)|$ and $\varphi_j(k)$ are the magnitude and phase of the complex scattering amplitudes for each atom.

The individual parts can be analysed as follows: The term $\frac{N_j}{kR_j^2}$ accounts for the proportionality of the sum of contributions from backscattering atoms of a certain sphere and their number, as well as for the fact that their contribution decreases linearly with wavenumber and squared with the distance to the central atom. $f_j(k)$ is the amplitude function describing the scattering probability of atom j depending on the scattering angle, which is characteristic for each element. $e^{\frac{-2R_j}{\lambda_e}}$ considers the limited lifetime of the photoelectron represented by the mean free path length λ_e , which depends on the wavenumber of the electron. The Debye-Waller-factor $e^{-2k^2\sigma_j^2}$ specifies the thermal disorder of the backscattering atoms based on a Gauss-distribution. The last term, $\sin(2kR_j + 2\delta_l(k) + \varphi_j(k))$, and in particular the first summand therein, represents the oscillatory part of $\chi(k)$ as function of k due to superposition of outgoing and backscattered wave. The second and third addends are the central-atom partial-wave phase shift of the final state $2\delta_l(k)$ and the phase factor $\varphi_j(k) = \arg(f_j(k))$. The latter can be identified with the so-called phase function, which describes the phase shift of the electron wave as a result of passing through different atomic potentials.

The factor $S_0^2(k)$ incorporates many-body effects, namely indirect excitations of the so-called passive electrons of the absorbing atom. When the so-called active core electron is removed from the atom by the incident X-rays, all other electrons experience a sudden change in the binding potential – into that of the atom with Z increased by 1 – and herein relax to lower energy levels. Still they can be affected by Coulomb interactions with the active electron, in this way changing the overall X-ray absorption coefficient. Thus, $S_0^2(k)$ is an amplitude reduction or scaling factor, decreasing from unity at low k to values between 0.7 and 0.8 for $k \geq 7 \text{ \AA}^{-1}$ (Carlson et al., 1968, cited in Koningsberger and Prins, 1988).

Structural information is contained in the parameters N_j , R , and σ^2 , as well as in the scattering amplitude $f_j(k)$ for each element considered, the partial phase shift of the absorbing atom $\delta_l(k)$, and the photoelectron mean free path $\lambda(k)$. Details concerning the derivation of the equation and the relevance of these individual quantities are discussed in e.g. Sayers, Stern and Lytle, 1971. By inserting the scattering factor (which depends on the Z of the neighbouring atom(s)) into the measured spectrum, these structural parameters can be determined from the EXAFS equation.

Data Processing

Although the principles of fitting the EXAFS are well understood, the correct interpretation of the measured data is neither straightforward nor trivial. The required use of simulations for estimating the contributions from multiple scattering and best-fit procedures sometimes provides ambiguous or unreliable results, so that the choice of a correct model system as well as profound expert scrutiny is essential to extract valuable structural information from the EXAFS.

The analysis of experimental spectra can be divided into multiple steps of data reduction. First, the measured absorption or fluorescence intensity as function of X-ray energy is converted to the absorption coefficient $\mu(E)$ (Equation 3.7 or 3.8, see above). Instrumental effects such as detector dead time losses as well as absorption from other edges are corrected by fitting a smooth pre-edge function. The spectra are averaged for each sample and artefacts from measurement such as monochromator glitches are removed. Then the data are normalised to an unit edge step to compensate for variations in sample thickness or concentration. The energy threshold E_0 is selected, usually assuming its value at the maximum derivative of $\mu(E)$ corresponding to the sharpest rise of the absorption edge. Since the Fermi energy E_0 is somewhat imprecise, slightly depending on the particular environment of the central atom, this value must be refined later on (Newville, 2004a).

The oscillatory part of the signal $\chi(E)$ is extracted from the processed data by subtraction of a smooth background function $\mu_0(E)$ and division by the edge step $\Delta\mu_0(E_0)$, which normalises the oscillations to one absorption event:

$$\chi(E) = \frac{\mu(E) - \mu_0(E)}{\Delta\mu_0(E_0)} \quad (3.14)$$

Since the absorption of an isolated atom cannot be measured, the value $\mu_0(E)$ is estimated by empirical fitting of a polynomial (typically a cubic spline) to the background, which resembles a sawtooth function closely approximating

the overall trend of $\mu_0(E)$. The determination of the spline function for post-edge background removal is the most error-prone step in EXAFS data analysis, because the flexibility of the spline must be chosen properly as to match the low frequency components of $\mu_0(E)$, but in parallel to avoid extinction of the EXAFS with a too flexible function. The subtraction of the spline leaves $\chi(E)$ isolated. Traditionally, χ is given as function of the photoelectron wave number k using Equation 3.12.

Subsequently, $\chi(k)$ is k -weighted⁵ to emphasise oscillations in the high k -region, which are suppressed due to the increasing displacement from the absorption edge. Since $\chi(k)$ is a (damped) oscillatory function composed of sine waves, a Fourier transformation is used for analysis, converting from the reciprocal wavenumber space of k into the real distance space of R [in m, resp. Å], whereby proper filtering produces single sphere amplitudes and phases. The EXAFS signal is disentangled into its separate contributions in this transformation by conversion of each sinusoidal component into a Fourier modulus peak (i.e., frequency separation). As the scattering amplitudes $f(k)$ of neighbouring atoms exhibit individual maxima at different k -values, each peak in the Fourier plot relates to a coordination sphere. The corresponding distance given on the abscissa, however, does not directly reveal the real distance between the central absorbing atom and this particular backscatterer, because it includes the phase factors $2\delta_l(k)$ and $\varphi_j(k)$, which typically contribute ~ 0.5 Å (Newville, 2004b). Since both terms are negatively correlated with k , peaks are generally shifted to lower R values (Vlaic and Olivi, 2004).

The fit is further improved by introducing the energy shift of the edge, ΔE_0 . As already mentioned, the Fermi energy cannot be precisely determined from experiment and the measured value differs marginally from theory. Thus, E_0 is determined individually for each spectrum as the inflection point of the absorption edge; hence, the k -scale is not absolute⁶.

The Fourier transformation from the complete k - to R -space would assume that all damped sinusoidal oscillations of the EXAFS continue infinitely. However, such extrapolation of the spectrum towards infinity could introduce artefacts. To avoid misinterpretation or false identification, in particular for large oscillations with large k , the spectrum is multiplied by a window-function. Hence, the data are correspondingly also restricted in R -space. For analysis, they are inversely transformed back to the space of photoelectron wavenumber and finally analysed there by curve fitting methods.

Ideally the resulting function $\chi(R)$ exhibits well separated peaks, $\chi_j(R_j)$, which correspond to each coordination sphere. These can be isolated by sub-

⁵Typically $\chi(k)$ is multiplied by a factor of k to k^3 .

⁶For consideration, a parameter k' is calculated via $k' = \sqrt{k^2 + 0.2624 \cdot \Delta E_0}$

traction from the spectrum and filtered back-transform to facilitate the identification of the remaining structure. In reality, the peaks often overlap significantly, and sometimes a peak is made up completely by superposition of separate oscillations. Furthermore, as discussed before, multiple scattering must not be ignored, because it could add larger amplitudes than the competing single scattering path, i.e. focussed paths might contribute stronger than single scattering paths of the same length (Ravel, 2000). In certain cases, even non-collinear, triangle multiple scattering paths between near neighbouring atoms must be considered, too, especially when they appear frequently. Hence, to concentrate on short scattering paths, it is convenient to set an upper limit on the extent in R -space, over which the EXAFS is analysed.

Finally, model parameters are determined by nonlinear least squares fitting of known experimental or theoretical phase and amplitude functions. As explained in Section 3.2.3, accurate values for scattering amplitudes $f(k)$ and phase shifts $\delta_l(k)$ and $\varphi_j(k)$ are required to extract the structural information from the measured data. In the technique of applying so-called empirical standards – which are roughly equivalent to single scattering paths (see Figure 3.5, page 70) – for this step, the experimental data on a sample of unknown structure are compared with data collected on a chemically similar sample of well-known, well-ordered structure. From the differences in these two data sets, information about additional disorder can be acquired (Ravel, 2001). For exotic compounds like transuranic elements chemical transferability from other substances must be assumed to bridge remaining gaps in the availability of corresponding standards. In this way, a reasonably good approximation of scattering amplitudes and phases is most often obtained for solving the EXAFS equation.

Alternatively, theoretical standard methods provide comparative data sets based purely on calculations by *ab initio* procedures. In contrast to the empirically derived scattering factors, such calculated parameters are not restricted to the first coordination sphere. Single and multiple scattering paths are handled equivalently and transparently. One major theory code making complicated problems tractable – including the analysis of higher coordination spheres, multiple scattering contributions, or mixed spheres – is the FEFF Project. This name is derived from $f_{eff}(k, R)$, which replaces $f(k)$ in the EXAFS equation to include spherical wave effects with a dependency on the distance R between absorbing and backscattering atoms. As input data the program requires a list of atomic x, y, z coordinates for a given physical structure and a selected central atom only. A molecule that is sufficiently similar to the expected structure can be used to generate a reasonable FEFF model, which can be applied to refine distances and coordination numbers of the real compound. Practically, the structural parameters are determined by an automatic computer-based minimisation

procedure such as EXAFSPAK described in detail in Section 4.4.3 (George and Pickering, 1995).

With such a computer program, scattering amplitudes, phase shifts, and mean free paths are calculated theoretically for each coordination sphere and stored in separate files, which are then used to derive the structural parameters from the experimental data. This process is conducted iteratively allowing R , N , and σ^2 to float and refining the value for E_0 , until the best fit is obtained. Thereby, proper restriction in k -space helps to selectively disregard higher coordination spheres, which contribute only weakly to the total spectrum.

The maximum number of free variables that can be effectively fit depends on the range of R as well as of k . Applying the general Nyquist criterion⁷ for sampling processes N_{max} is estimated as

$$N_{max} \approx \frac{2 \cdot \Delta k \cdot \Delta R}{\pi} \quad (3.15)$$

(Ravel, 2008). Since the fit statistics is necessarily limited by the amount of input data at hand, it is important to constrain the structural parameters for different paths according to chemical plausibility. For example, previous knowledge about the local coordination of the compound in question is incorporated artificially.

As the final excited state in EXAFS is very short lived (see Section 3.2.3), essentially snapshots of the instantaneous atomic configuration are taken. Even for neighbouring atoms of the same type, thermal and static disorder in the bond lengths result in a distribution of distances, which is represented by σ^2 , the mean square displacement in bond length R . Contributions from atoms of the same atomic number and at similar distances may not be resolvable from each other and are grouped conceptually into so-called coordination spheres (Bunker, 1997).

Real systems usually have more than one type of neighbouring atoms of which the measured EXAFS is the sum of contributions. Coordination spheres of similar Z become difficult to distinguish when their distances are close together, i.e. within 0.05 Å of each other (Newville, 2004b). Consequently, an unknown contributor cannot be identified more accurately than $Z \pm \sim 5$.

However, care must be taken to avoid over-fitting or over-interpretation of the data. The information content is limited through the finite ranges both in k -space Δk and in R -space ΔR , the latter primarily because of the short photoelectron mean free path and the limited lifetime of the excited state (Bunker, 1997).

⁷This assumes an ideal signal, a normally distributed error, understanding of all error sources and their quantifiability, as well as knowledge of the theoretical curve shape. Since none of these conditions can really be met with EXAFS, N_{max} determined in this way represents an upper limit to the actual information content.

Generally, at least some initial knowledge of the molecular structure is required for a successful designation of separate coordination spheres and a sensible selection of starting values for the iteratively calculated fitting parameters. Still, without complementary techniques a complete disentanglement of the three dimensional structure of a compound from EXAFS data alone is not possible.

3.3 Modelling

To meet safety regulations, the consequences of an eventual leaching from a nuclear waste repository must be estimated. Experimental data are combined with simulations to forecast the barrier efficiency through detailed modelling. As sorption is a function of aqueous and mineral surface chemistry, distribution ratios like the K_d (see Section 4.3.5) or Freundlich isotherms (see Section 4.3.7) are commonly used in performance assessments to describe the partitioning of dissolved (radio-) nuclides between the aqueous phase and immobile solid surfaces (Bradbury and Baeyens, 2006b). Both approaches are strictly empirical and, therefore, only applicable for the experimental conditions under which they were measured. Consequently, large amounts of data and fitting parameters are required to describe sorption under the full range of realistically conceivable conditions, and only interpolation procedures are reliable while extrapolations to other conditions are highly questionable.

The prediction of actinide behaviour in the environment requires the application of conceptual and numerical migration models combining features, events, and processes into likely scenarios (Turner, Bertetti and Pabalan, 2006). These, however, demand much input data for calculation. The need for numerous thermodynamic and kinetic variables to appropriately describe the multitude of possible processes including their interdependencies is the major drawback of numerical modelling (Choppin, 2006b). The analysis of solubilities and speciation should be related to a system at equilibrium on the basis of thermodynamic data, but also combined with kinetic information describing non-equilibrium conditions (Allard et al., 1984). However, commonly kinetic aspects are neglected, leading to rather steady state than equilibrium conditions. Consequently, there is the general consensus that such chemical models should better serve as guides for planning further research than as prediction devices (Choppin, 2006b).

Mechanistic sorption models instead help understand and quantify the processes controlling uptake and release of aqueous species on solid surfaces with much less effort by identifying relevant sub-processes and merging their contributions (see below). This approach requires mineral specific characteristics such as site types and capacities, protolysis constants, selectivity coefficients,

and surface complexation constants for the relevant nuclides to complement the groundwater specific parameters and allow sorption to be calculated under any possible condition (Bradbury and Baeyens, 2006b). For Np(V) three different types of thermodynamic data are well established: activity coefficients of aqueous species, formation constants of aqueous complexes, and solubility constants of isostructural solids (Fanghänel and Neck, 2002). A database for relevant sorbents is not yet existing, and modelling efforts have concentrated on few well-homogenised substances so far.

Modelling limitations arise from the complexity of natural systems. While the mentioned data are appropriate for modelling separate sub-systems, entirely describing natural conditions in their intricacy would require so much, partly still vague input data and large computing capacity, that modelling can never claim to achieve truly predictive status. Furthermore, water flow and diffusion must be considered simultaneously with the sorption mechanisms to properly describe environmental conditions. In any case, the validity of such predictive models, as well as all extrapolations from laboratory data to environmental systems must be checked rigorously before final conclusions are drawn.

3.3.1 The 2 SPNE SC/CE Model

The quasi-mechanistic Two Site Protolysis Non-Electrostatic Surface Complexation and Cation Exchange Model, abbreviated 2 SPNE SC/CE, was developed by scientists from the Paul Scherrer Institut (PSI) in Villigen, Switzerland (Bradbury and Baeyens, 2006b), to predict the partitioning of dissolved radionuclides between the aqueous phase and immobile solid surfaces. It combines thermodynamic models based on cation exchange and on surface complexation to cover a broad range of pH, background electrolyte, and sorbate concentration. The model is capable of quantitatively describing the sorption behaviour for a wide variety of metals on montmorillonite. In order to investigate the simplified system first before increasing the complexity in a stepwise systematic manner, the emphasis was placed on this clay mineral as the major component of bentonite. Additionally, the material was purified and conditioned to the homo-ionic Na-form (see Section 4.3.1).

Sorption Site Types

Modelling of metal sorption (in the present case that of actinides) on mineral surfaces is based on the assumption of amphoteric hydroxyl groups, which are protonated and deprotonated according to the pH of the surrounding solution (Turner et al., 2006). As explained in section 2.4.1, the surface of clay minerals carries a permanent negative charge due to isomorphic substitution, which

is compensated by an excess of solution cations held electrostatically in close proximity. These constitute the electrical double layer that can stoichiometrically exchange with cations in solution. The total permanent charge is defined as the cation exchange capacity (CEC, see section 2.5.3). In the case of montmorillonite, approximately 10 % of the CEC (Bradbury and Baeyens, 2006b) are contributed to the total sorption capacity by surface hydroxyl groups ($\equiv\text{SOH}$). These are reactive sites situated along the edges of the clay platelets that can become $\equiv\text{SOH}_2^+$ and $\equiv\text{SO}^-$ as a function of pH (so-called variable charge, see section 2.3.2) and interact with the ions present in solution.

The 2 SPNE SC/CE Model combines cation exchange and surface complexation in a multi-site approach. Strong sites having the greatest affinity towards the actinides are present only in a limited number. They saturate first when the radionuclide concentration is increased. As long as the availability of free sites exceeds the amount of ions in solution, sorption is characterised by a linear proportionality between sorption density and sorbate concentration. A flattening in slope at higher actinide supply is explained by sorption on weak sites after all strong sites are occupied. These are present in sufficient concentration to account for the sorption maxima observed (Turner et al., 2006).

Cation Exchange and Surface Complexation

Laboratory experiments reveal that cation exchange dominates sorption at low pH and/or high sorbate concentrations and low ionic strength, being stoichiometric and independent of pH, but sensitive to background electrolyte concentration. In moderate to high ionic strength solutions and above $\text{pH} \sim 5$, in contrast, the uptake process is dominated by surface complexation, which is strongly dependent on pH, little related to background electrolyte concentration, and generally non-stoichiometric. The former process is normally expressed by a mass action law applying selectivity coefficients, since the protolytic reactions at the surface can be considered as local equilibria (Horst and Höll, 1997). The latter is best described by the well-established diffuse double layer model (cf. Section 2.5.2) simplified through elimination of the electrostatic term⁸.

Selectivity coefficients, ${}^B_A K_C$, can be derived from experimental data acquired at trace B concentrations with the fractional occupancy of A (N_A , equivalents of A sorbed per kg of sorbent divided by the CEC) being ~ 1 :

$${}^B_A K_C = ({}^B K_d)^{z_A} \cdot \frac{(z_B)^{z_A}}{\text{CEC}^{z_A}} \cdot [A]^{z_B} \cdot \frac{(\gamma_A)^{z_B}}{(\gamma_B)^{z_A}} \quad (3.16)$$

⁸The electrostatic term proved to be of secondary importance since experiments showed that apparently the chemical part dominates over the electrostatic contribution.

$[A]$ and $[B]$ are the aqueous concentrations [mol/kg] of the metals A and B, which have the valencies z_A and z_B ; γ_a and γ_B are the respective aqueous phase activity coefficients.

The measure for the resistance of a complex to dissociate in solution are stability constants. Since it is often difficult to quantify the chemical activities for their calculation, concentrations are commonly used instead (Choppin and Jensen, 2006). The stability constant β_{nq} for the reaction of an actinide (An) with a ligand (L) according to



is

$$\beta_{nq} = \frac{[An_n L_q]}{[An]^n [L]^q} \quad (3.18)$$

For surface complexation, the experimental data are best described using a two site approach with equal capacities but individual protolysis constants. Two types of weak sorption sites were derived from titration curves, while in addition strong sites were necessary to describe the sorption edges⁹ and isotherms observed. They are assumed to have the same protolysis constants but differ considerably in the strength of the complexes formed with metals. Although strong sites reveal a much lesser capacity than weak sites, they dominate the sorption process at trace level. Generally, the following equation is applied to model surface complexation on them:



where Me is a metal with the valency z , and y is an integer.

Calculations of the aqueous radionuclide speciation are used to guide the choice of surface complexes in different pH regions. For numerical processing, any computer code containing subroutines for simultaneous calculation of cation exchange and surface complexation can be employed. In the present case, the modelling programme Visual MINTEQ version 2.53 (Gustafsson, 2007) was utilised.

Modelling Procedure

Model parameters are determined by fitting a set of one or more surface reactions to experimental sorption data, even though, in theory, some of them are measurable directly. In this approach extrapolations are rather uncertain;

⁹the pH at which 50% of the maximum sorption is reached

the transferability of results is limited, and an intercomparison among different models is impeded. To reduce these disadvantages as well as to minimise the computational effort, some parameters are fixed during the whole modelling process, such as sorption site density or surface area.

The first experimental step in acquisition of the required modelling parameters for the present study were acid/base-titration measurements, which yielded weak site capacities and protolysis constants. These experiments were performed by PSI scientists at an earlier stage (Bradbury and Baeyens, 1997), giving fixed values for all subsequent modelling. These are shown in Table 3.1.

Table 3.1: Fixed modelling parameters of strong and two weak sorption site types for conditioned Na-montmorillonite as used in this study (Bradbury and Baeyens, 1997).

Site type	Site capacity	Surface complexation reaction	log K
$\equiv S^S OH$	$2 \cdot 10^{-3}$ mol/kg	$\equiv S^S OH + H^+ \rightleftharpoons \equiv S^S OH_2^+$	4.5
		$\equiv S^S OH \rightleftharpoons \equiv S^S O^- + H^+$	-7.9
$\equiv S^{W_1} OH$	$4 \cdot 10^{-2}$ mol/kg	$\equiv S^{W_1} OH + H^+ \rightleftharpoons \equiv S^{W_1} OH_2^+$	4.5
		$\equiv S^{W_1} OH \rightleftharpoons \equiv S^{W_1} O^- + H^+$	-7.9
$\equiv S^{W_2} OH$	$4 \cdot 10^{-2}$ mol/kg	$\equiv S^{W_2} OH + H^+ \rightleftharpoons \equiv S^{W_2} OH_2^+$	6.0
		$\equiv S^{W_2} OH \rightleftharpoons \equiv S^{W_2} O^- + H^+$	-10.5

Second, batch sorption experiments – like conducted in this study – at trace radionuclide concentration as function of pH at fixed ionic strength (sorption edges) and as function of radionuclide concentration at constant pH and ionic strength (isotherms) provided binding constants and the strong site capacity. Finally, cation exchange capacities and selectivity coefficients were obtained from sorption measurements in the low pH region.

The overall aim was to develop a self consistent data set with a minimum number of parameters describing all available experimental results. Apart from the values being entered into the modelling process directly, certain supplementary information is necessary to assure comparability of the underlying experiments. These are cation exchange capacity, ionic strength, solid-to-liquid ratio, and radionuclide concentration.

In contrast to the so far mentioned parameters, there are no theoretical approaches to derive surface complexation constants causing them to be frequently determined by trial and error methods (Turner et al., 2006). One way

to overcome this problem is the application of so-called linear free energy relations. These are systematic dependencies between free energies of complex formation and thermodynamic properties of the metal ions or ligands. For the 2SPNE SC/CE modelling approach similar relationships are established between the experimentally determined surface complexation constants and their corresponding hydrolysis constants. Thus, this method is regarded as a useful tool for estimating surface complexation constants for metals, for which there are no measured data. If these are determined for both site types, they can be used together with the surface protolysis constants, site capacities, and selectivity coefficients to calculate sorption under various conditions.

Nevertheless, difficulties may arise by implying more than one surface complex, multidentate sorption, or consideration of polynuclear species, as well as from competition effects in complex, multi-element systems. Since most radionuclides will be present at trace concentrations under the anticipated repository release scenario, the dominant sorption mechanism will be surface complexation on the strong sites, which could possibly become saturated. However, investigations showed that all metals are not necessarily competitive, but rather selectively sorbed; only chemically similar elements compete with one another. While competition can successfully be modelled with the 2SPNE SC/CE approach, modifications in terms of multiple sets of strong sites are required to render the model capable of selectivity effects.

Further problems result from the quality of aqueous phase thermodynamic data. They are a critical factor in predicting sorption in real systems where complex water chemistry comes into play. For example, carbonate, hydroxycarbonate, sulfate complexes, etc. will be present simultaneously and possibly interact with the clay mineral surface. These processes still need closer elucidation and quantification for correct consideration in the 2SPNE SC/CE model.

Contribution of this Study

The 2SPNE SC/CE model can calculate sorption values specific to different geochemical scenarios including competitive effects, but still is confined to a relatively simple system of a single, purified clay mineral, ordinary background electrolytes (NaClO_4), and carbonate free conditions. At PSI all experiments were conducted under inert gas atmosphere; the present study complements these investigations by contributing experimental data gathered under ambient air conditions.

The model by itself is not capable of identifying the nature of the surface sites or the surface complexes formed. For its application, their stoichiometry was linked to the aqueous speciation of neptunium, and monodentate surface

species were assumed. Since there has been no independent evidence of the postulated structure so far, the 2 SPNE SC/CE model had to be termed quasi-mechanistic. The advanced surface analytical technique of EXAFS performed in this study provides the necessary information on identity and structure of the surface species, thereby yielding further insight into the underlying sorption process. The formation of outer-sphere complexes indicates cation exchange, while inner-sphere complexes are typical for surface complexation reactions, so that the detection of these different species will support the modelling theory.

4

Experimental

4.1 Radionuclides

As chemical isotope effects regarding reaction equilibria and rates can generally be neglected for all elements with an atomic number greater than 10 due to the diminishing mass difference with increasing Z (Loveland et al., 2006), both neptunium isotopes used in this study, ^{237}Np ($t_{1/2} = 2.14 \cdot 10^6$ a) and ^{239}Np ($t_{1/2} = 2.36$ d), were considered identical except for their radioactive properties.

4.1.1 Production of the Isotopes ^{237}Np and ^{239}Np

Resulting from their base character, metallic actinides reveal a relatively high chemical activity and dissolve in acids like hydrochloric acid with formation of H_2 and the actinide ion in its most stable oxidation state (Holleman and Wiberg, 2007). Making use of this property, solid NpO_2 , comprised of the long-lived isotope ^{237}Np , was dissolved in hot aqua regia. This process needed much time (several weeks) and the procedure of repeatedly adding a few millilitres of HCl and HNO_3 in a ratio of 3:1 followed by heating until almost dryness.

For the $^{239}\text{Np(V)}$ stock solution ^{238}U (uranyl nitrate $\text{UO}_2(\text{NO}_3)_2 \cdot 6 \text{H}_2\text{O}$) was irradiated in the Research Reactor TRIGA Mainz (Figure 4.1) with a neutron flux of $7 \cdot 10^{11} \text{ n cm}^{-2} \text{ s}^{-1}$ for 6 h according to Eberhardt and Kronenberg (2000)¹. An amount of approximately 30 mg dissolved in 1 mL ultrapure water was generated and provided sufficient neptunium for an ordinary batch experiment with twelve samples, which were complemented by two blanks of 10 mL each.

Both these crude neptunium solutions also contained many other heavy elements apart from the desired isotopes. Therefore, they had to be cleaned from fission products and daughter nuclides with due diligence as described below.

¹The nuclear reaction leading to the production of ^{239}Np is given on page 12.



Figure 4.1: The research reactor TRIGA MarkII, Institute for Nuclear Chemistry, University of Mainz.

4.1.2 Separation and Purification

For both neptunium isotopes ion exchange chromatography was applied to separate the desired radionuclide from other fission products present in the stock solutions. This process is described by Seibert, Mansel, Marquardt, Keller, Kratz and Trautmann (2001). The solutions obtained in the previous steps were brought into contact with a synthetic organic resin containing specific functional groups that selectively bind the ions in question. This procedure, however, is

only suitable for small amount of radionuclides, because the exchange resin is decomposed by intense radiation (Holleman and Wiberg, 2007).

Practically, the solutions were run through a column, pictured in Figure 4.2, filled with the cation exchanger Dowex 50, which consists of crosslinked polystyrenes with attached sulfonic acid functional groups (SO_3H) where the ions present in solution replace the hydrogen ion (Loveland et al., 2006). From the group of ions adsorbed on the column material the individual elements are selectively eluted by complexing agents that form complexes of different solubility with them. Thus, they can be collected separately, discarded or further used.



Figure 4.2: Cation exchange column and sand bath with infrared lamp.

In this way, ^{239}Np was separated from uranium and its fission products and ^{237}Np was purified from traces of ^{239}Pu and ^{233}Pa . In both cases neptunium was stripped off using a mixture of hydrochloric and hydrofluoric acid, after the contaminants had been washed from the column. Through a treatment with fluoride the passivation of Th, U, and Pu is avoided, which ensures that these elements dissolve well in concentrated acid containing F^- (Holleman and Wiberg, 2007).

Afterwards, both solutions were evaporated to dryness, fumed with concentrated HClO_4 as shown in Figure 4.3 to remove the acid from the sample, and the remains were taken up in 0.1 M NaClO_4 .

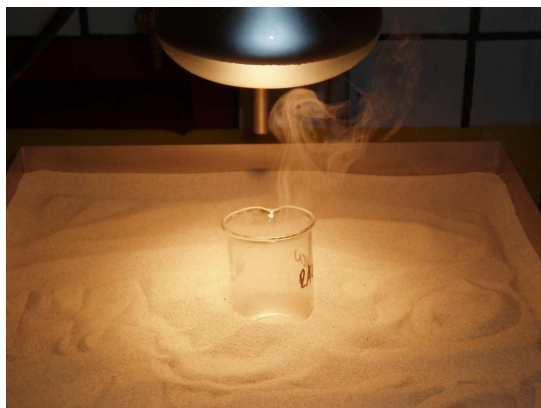


Figure 4.3: Fuming of the acid under the infrared lamp on the hot sand bath.

4.1.3 Assurance of the Fifth Oxidation State

After purification the neptunium was present in the sixth oxidation state, apparent from the pink colour of the solution (cf. Appendix B.3). To reduce Np(VI) to Np(V) a small amount of NaNO_2 was added. The production of the pentavalent oxidation state of neptunium was verified in millimolar concentration range by UV/vis spectroscopy (980 nm, $\epsilon = 395 \text{ M}^{-1}\text{cm}^{-1}$).

The neptunium concentrations in the stock solutions of ^{239}Np and ^{237}Np were approximately 10^{-9} and $5 \cdot 10^{-3}$ M, respectively, as determined by γ spectroscopy (^{239}Np : 103.8 and 106.1 keV; ^{237}Np : 29.4 keV). The pH of the stock solutions was adjusted to approximately 5 by addition of NaOH.

The precise procedure for the preparation of the ^{237}Np and ^{239}Np stock solutions is given as a step-by-step instruction in Appendices F.1 and F.2.

4.2 Materials and Chemicals

4.2.1 Montmorillonite STx-1

Information on reference clays is provided in the Data Handbook for Clay Materials and Non-metallic Minerals prepared under the auspices of the OECD and the Clay Minerals Society (van Olphen and Fripiat, 1979). The most important features of the montmorillonite used in the present study are summarised in Table 4.1.

Table 4.1: Characteristics and properties of the reference substance Texas Montmorillonite STx-1 provided by the Clay Minerals Society and used in this study.

Texas Montmorillonite STx-1						
Origin	Manning formation, Jackson Group (eocene) County of Gonzales, State of Texas, USA					
Location	29°30' N, 97°22' W; collected October 17 th , 1972					
Structure	$(\text{Ca}_{0.27}\text{Na}_{0.04}\text{K}_{0.01})[\text{Al}_{2.41}\text{Fe(III)}_{0.09}\text{Mn}_{tr}\text{Mg}_{0.71}\text{Ti}_{0.03}][\text{Si}_8]\text{O}_{20}(\text{OH})_4$					
CEC	84.4 meq/100 g, major exchange cation: Ca octahedral charge: -0.68 interlayer charge: -0.68 tetrahedral charge: 0.0 unbalanced charge: -0.08 extra Si: 0.59					
Surface area	83.79±0.22 m ² /g (N ₂)					
Chemical composition	SiO ₂	70.1 %	MnO	0.009 %	F	0.084 %
	Al ₂ O ₃	16.0 %	MgO	3.69 %	P ₂ O ₅	0.026 %
	TiO ₂	0.22 %	CaO	1.59 %	S	0.04 %
	Fe ₂ O ₃	0.65 %	Na ₂ O	0.27 %	CO ₂	0.16 %
	FeO	0.15 %	K ₂ O	0.078 %		

The montmorillonite found in Texas belongs to the Southern Bentonites, which are Ca²⁺-covered, converted volcanic tuffs or rearranged weathering products of the upper cretaceous and tertiary ages (Störr, 1993). A clay mineral of this type was chosen under the aspect of a low iron distribution in the octahedral sheet, because a high iron content – as encountered in many other montmorillonites – might interfere with EXAFS analyses by modification of the interference fingerprint. While other montmorillonites exhibit a random or even ordered distribution, the STx-1 displays an extensive clustering at a comparably low total iron concentration in the range well below 1 % (Vantelon, Montarges-Pelletier, Michot, Briois, Pelletier and Thomas, 2003).

4.2.2 Aluminium Oxide $\gamma\text{-Al}_2\text{O}_3$

For the experiments with $\gamma\text{-Al}_2\text{O}_3$ as a sorbent, being representative for the aluminol groups of clay minerals, a pure powder (99.97 %) with a high surface area (similar to the clay) was obtained from AlfaAesar. Its specifications were given as 80-120 m²/g by the manufacturer, while BET measurements conducted at the Research Centre Dresden Rossendorf yielded 68.4±0.5 m²/g only. Since

the determination of the surface area is known to be subject to uncertainty depending on the approach (Turner et al., 2006), this discrepancy was ascribed to a probably different method applied by AlfaAesar for characterisation. Because of the inconsistent result, normalisation of the sorption to surface area would involve an uncertainty of up to 150 % and, thus, was avoided during this study.

The high surface area, however, implies a small grain size, which unexpectedly introduced the problem of weighing small aliquots: Compared to montmorillonite providing sorption sites on the mineral edges only, aluminium oxide offers aluminol groups all over its surface. Therefore, the solid-to-liquid ratio had to be chosen small in order to produce reasonable results (see Section 3.1.5). Since it turned out a great source of error to weigh in only 5 mg per sample, while additionally facing electrostatic charging of tube and scales, a different method had to be developed to minimise variations within the batches. Hence, a homogeneous suspension of γ - Al_2O_3 in 0.01 or 0.1 M NaClO_4 was produced first, of which, while stirring thoroughly, corresponding aliquots were pipetted into the sample tubes to give the desired solid-to-liquid ratio.

4.2.3 Sodium Perchlorate NaClO_4 and its Purification

The perchlorate ion is the least complexing monovalent inorganic ligand (see Section 2.2.1, page 20) and, therefore, best suited as a counterion for Na^+ , which was chosen to provide the ionic background in this study. All experiments were conducted with NaClO_4 concentrations of 0.01 or 0.1 M.

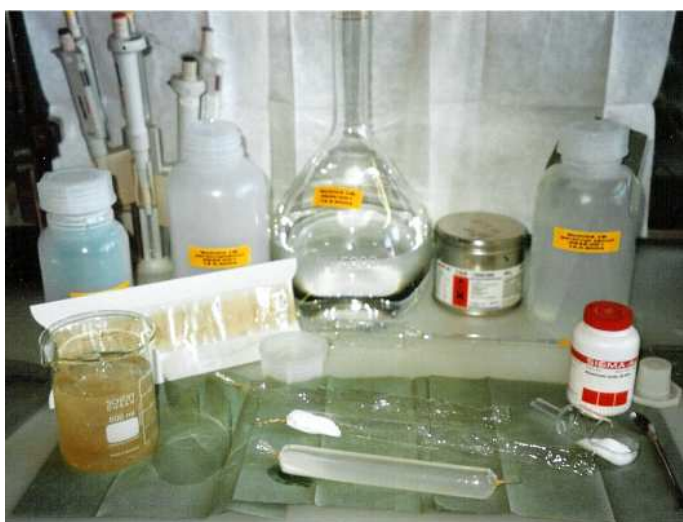


Figure 4.4: Purification of NaClO_4 with Al_2O_3 . The powder was given into dialysis bags, which were shaken in the solution for at least one day.

Since neptunium was applied in trace concentrations, contamination by other cations had to be kept as low as possible. Thus, although very pure NaClO_4 had been obtained to prepare the background solution, it was further cleaned with aluminium oxide. For this purpose, the insoluble powder was added in dialysis bags as a scavenger for any unwanted ions, which is displayed in Figure 4.4; the precise procedure is explained in Appendix F.3.

4.2.4 pH Adjustment and Buffer Solutions

To produce reliable results, it was essential to keep the pH constant during the whole experiment with a duration of usually three days. Therefore, the batch experiments with montmorillonite were conducted with buffer solutions; the substances used are listed in Table 4.2. Their use facilitates pH stabilisation, especially in the near-neutral region, which proved particularly difficult to adjust due to a considerable buffering ability of the clay causing prolonged drifting of the data. Tests conducted by Baeyens and Bradbury (1995b) demonstrated that the individual buffer materials chosen do not influence the sorption behaviour to any significant extent.

Table 4.2: Buffer substances used in the sorption experiments with montmorillonite (data from Perrin and Dempsey, 1974, cited in Baeyens and Bradbury, 1995b). pK_a values and suitable pH ranges are given.

Buffer	pK_a^*	pH range
AA (acetic acid)	4.76	4.3-5.3
MES (2-(N-Morpholino)ethanesulphonic acid)	6.15	5.7-6.7
MOPS (3-(N-Morpholino)propanesulphonic acid)	7.20	6.8-7.7
TRIS (Tris(hydroxymethyl)aminomethane)	8.06	7.5-8.5
CHES (3-(cyclohexylamino)ethanesulphonic acid)	9.55	9.0-10.0

* negative decadic logarithm of the dissociation constant K_a of an acid

During the experiments with $\gamma\text{-Al}_2\text{O}_3$ as well as in the preparation of the EXAFS-samples the pH was adjusted manually by addition of aliquots of NaOH and HClO_4 in different molarities. The standard equilibrium solution contained in the pH-electrode, KCl, had been exchanged against 3 M NaCl to avoid precipitation of the relatively low soluble KClO_4 in the contact zone with the perchlorate ions. Prior to measurement of each batch, the pH-meter was calibrated over three points according to its specifications at pH 4.01, 6.87, and 9.41.

In the first experiments, a slight memory effect of the pH measurements was observed. Therefore, always the same order from lowest to highest pH

was followed. Before plunging the electrode into the suspension the sample was shaken thoroughly. The reading was taken after the drifting had largely stopped, typically after three to five minutes, whereby shaking the sample at least once during this time accelerated the equilibration process. Most critical were the readings in the near-neutral region; here specific attention was paid to treat all samples in the same way. Nevertheless, some measurements – especially those conducted under exclusion of atmospheric CO_2 – still proved critical, wherefore some of the pH values obtained might be slightly too low. This is particularly regrettable in respect of the sorption edge being situated in this region; any findings must, therefore, be scrutinised carefully.

4.2.5 Carbonate and Bicarbonate

One part of the experiments was conducted under ambient air conditions to examine the influence of CO_2 on the sorption of neptunium. Since the pH strongly influences its solubility, attention must be paid on the complete equilibration of the sample solution with air. During the first experiments, however, it turned out that the air volume with which the solution is in contact within the sample tubes is too small to ensure sufficient dissolution of CO_2 especially at higher pH. On the other hand, it was not possible to leave their caps open, first because of large volume losses due to evaporation and its unforeseeable effects, second because of the required continuous mixing of the suspensions that would otherwise settle.

Therefore, the appropriate concentrations of carbonate and bicarbonate – according to the aqueous speciation of CO_3 shown in Figure 3.1 on page 60 –

Table 4.3: Addition of sodium carbonate and sodium bicarbonate per 10 mL sample in the air equilibrated system.

NaClO ₄ M	pH	NaHCO ₃ μL	Na ₂ CO ₃ μL
0.01	8.5	17.0	0.2
0.01	9.0	54.8	2.1
0.01	9.5	185.4	30.8
0.01	10.0	715.5	1176.7
0.1	8.5	20.1	0.5
0.1	9.0	64.1	5.3
0.1	9.5	210.0	63.0
0.1	10.0	898.3	2527.0

were calculated theoretically with the geochemical speciation software Visual MINTEQ (Gustafsson, 2007) for each pH value. The corresponding amounts, given in Table 4.3, were added as 1 M NaHCO₃ and 2 M Na₂CO₃. With the increasingly high volumes required in the alkaline pH region, the ionic strength of the samples was unavoidably altered, too. In order to keep this effect as small as possible, any additional dilutions of the affected samples were made with water instead of NaClO₄. Nevertheless, the pH range was limited to pH 10 as the highest due to the volume of NaHCO₃/Na₂CO₃ becoming larger than the samples themselves.

4.3 Procedure of Batch Experiments

4.3.1 Preparation: Conditioning of Montmorillonite

To ensure the most simplified system (see Section 3.3.1 above), the montmorillonite was purified in accordance with Baeyens and Bradbury (1997) before it was used in the experiments; all steps required in this process are particularised in Appendix F.3.

First, the reference material was transferred to the homo-ionic sodium form using purified 1 M NaClO₄, whereby all interlayer cations were exchanged against Na⁺. In the second step, the fraction <0.5 μm was selected. For this purpose pure water was used to disperse all flocculations². To sediment all particles larger than the desired fraction, the suspension was then repeatedly centrifuged at a defined speed to generate 614 *g* for a duration of 7 min calculated after Stokes' Law:

$$v_s = \frac{2r^2g(\rho_p - \rho_f)}{9\eta} \quad (4.1)$$

where v_s is the settling velocity [m/s] of the particles with radius r , g is the gravitational acceleration (9.81 m/s²; in the present case, 6 023 m/s² must be entered for centrifugation at 614 *g*), ρ_p is the mass density of the particles [kg/m³] (montmorillonite: 2 350 kg/m³ on average), ρ_f is the mass density of the fluid [kg/m³], and η is the dynamic viscosity [Pa s] resp. [kg/(m·s)]. The supernatant with the remaining smaller particles was collected as depicted in Figure 4.5. To reduce the volume the ionic strength was increased again forcing flocculation of the clay.

Then, to remove all salts and soluble minerals including hydroxy-aluminium compounds that had perhaps formed via hydrolysis during the treatment with

²This water had been brought in contact with an old batch in advance for equilibration with the mineral, in this way preventing dissolution of the montmorillonite during conditioning.



Figure 4.5: Collection of the particle size fraction $<0.5 \mu\text{m}$. Impurities of iron and manganese oxides, visible through their dark colour, and others are removed by centrifugation as well.

de-ionised water, the clay suspension was acidified to pH 3.5 for one hour. After centrifugation, the supernatant was decanted off and the montmorillonite re-suspended in 0.1 M NaClO_4 and neutralised.

Finally, the suspension was filled into dialysis bags and equilibrated with 0.1 M NaClO_4 , which is shown in Figure 4.6. When needed, the stock suspension obtained in this way was further conditioned to 0.01 M; the success of this procedure was checked by comparison of the conductivity in the equilibrium and the original solution. Below ca. 1 mol/L the conductivity is directly pro-

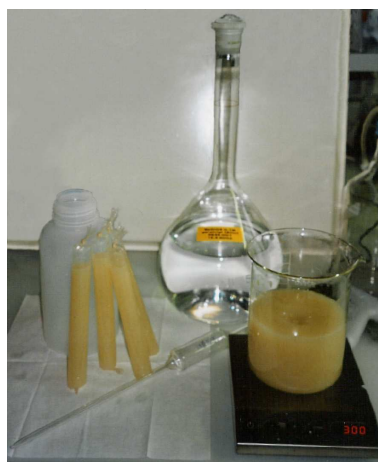


Figure 4.6: Adjustment of ionic strength. The clay suspension is pipetted into dialysis bags and equilibrated with the corresponding NaClO_4 solution.

portional to the salt content providing a convenient measure for controlling the experimental performance ($1\,040\ \mu\text{S} \hat{=} 0.01\ \text{M NaClO}_4$).

The clay content of the stock suspension, i.e. the solid-to-liquid ratio, was determined via dry weight obtained at 105°C . Until use the stock suspension was stored in the refrigerator; it was kept for no longer than six months.

A daily schedule for the conditioning of montmorillonite is provided in Appendix F.3 dividing the procedure into eight subsequent steps.

4.3.2 Assemblage, Pre-conditioning and pH-adjustment

All experiments were conducted at room temperature either under ambient air ($p_{\text{CO}_2}=10^{-3.5}\ \text{bar}$) or in a glove box under exclusion of CO_2 (argon atmosphere in Mainz, nitrogen at the PSI). In the latter case all solutions except for the montmorillonite stock suspension were prepared within the glove box with water that had been boiled for several hours to degas.

The sample volume was 10 mL for batch experiments and sorption isotherms; for the preparation of the EXAFS samples more solid material was required, wherefore the volume of these sorption samples was increased to 40 mL. Before the experiments were started the tare weights of the sample tubes were determined (Figure 4.7).

The montmorillonite was pipetted into the 15, respectively 50 mL polypropylene centrifuge tubes, while mixing the stock suspension continuously with a magnetic stirrer to ensure its homogeneity. The required volume was calculated from the clay content of the stock suspension to give an overall solid-to-liquid ratio of 4 g/L. Next, for the batch experiments the buffer solutions (1.25 mL per 10 mL sample), as well as in all ambient air samples beyond pH 8 NaHCO_3 and Na_2CO_3 corresponding to the intended pH were added. The samples were then diluted with 0.01 or 0.1 M NaClO_4 to 9 or 38 mL leaving enough space for the neptunium stock solution and the subsequent pH adjustment of the EXAFS samples. Exceptionally, the samples at pH 9.5 and above were diluted with ultrapure water in order to minimise alterations of the ionic strength following the addition of relatively large amounts of NaHCO_3 and Na_2CO_3 (see Table 4.3).

Since the solid-to-liquid ratio of $\gamma\text{-Al}_2\text{O}_3$ was set to 0.5 g/L due to its high sorption capacity, only a quite small quantity was needed per sample tube – i.e. 5 mg/10 mL – for the batch experiments. As already mentioned in Section 4.2.2, the very fine powder caused troubles on the scales because of electrostatic charging. Hence, a suspension was prepared giving the desired ratio when diluted from

8 to 10 mL, i.e. 156 mg γ -Al₂O₃ in 250 mL NaClO₄. Only for the larger EXAFS samples, which were all conducted with 4 g/L, the required quantity of solid (160 mg per 40 mL) was large enough to be weighed directly into the sample tubes.

When a buffer substance was used, no pre-conditioning was done expecting a quick equilibration of the system. In all other cases, the mixtures of solid sorbent, NaClO₄, and, if applicable, NaHCO₃ and Na₂CO₃ were placed into an end-over-end rotator, shown in Figure 4.7, for three days. After this time, the pH of each sample except for the blanks was adjusted manually by adding NaOH or HClO₄ as pictured in Figure 4.8 until the desired value was reached with a precision of ± 0.03 units. The rotating was continued and the pH checked daily and, if necessary, readjusted until it had stabilised indicating that the sample had reached equilibrium with the respective atmosphere, what usually took three to five days.

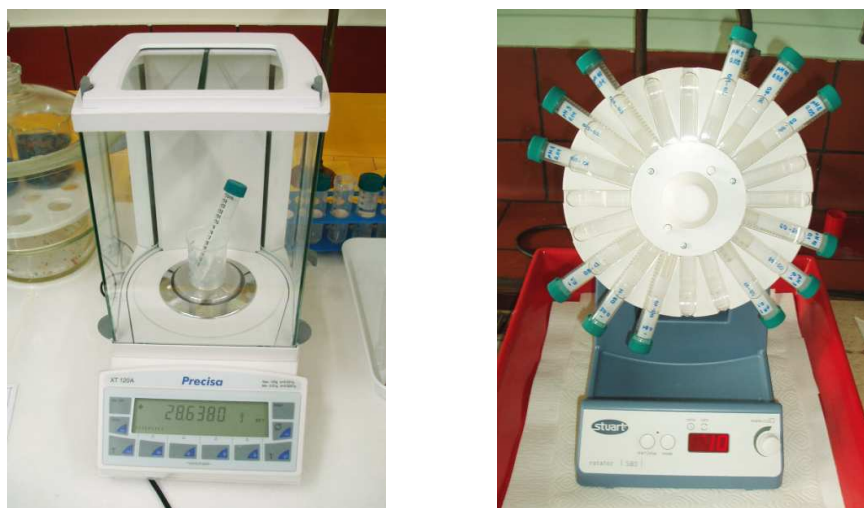


Figure 4.7: Weighing of the tubes (left) and mixing of the samples in an end-over-end rotator (right).

4.3.3 Addition of Np(V) and Contact Time

When the pH had stabilised, the samples were weighed to determine their precise volumes from their respective mass, because the individual effort needed for pH readjustment had led to dissimilar rates of evaporation. The difference from the desired 10 or 40 mL minus the volume of the neptunium stock solution was calculated and the respective gap filled up with NaClO₄. After the initial pH adjustment described in the previous section, usually only a few μ L of further



Figure 4.8: Manual pH adjustment of the γ - Al_2O_3 samples behind a lead brick. Suspension samples are kept in the green-capped vessels; for γ spectroscopy the supernatant is pipetted into the capsules placed in front.

acid or base addition were required to readjust the pH to the desired value ± 0.03 during the actual experiment, significantly reducing the time needed for this procedure, so that the sample volume was assumed to stay constant from here onwards.

Then, the neptunium was added. The required volume was calculated from the concentration of the stock solutions determined via γ counting (see above). In case of the short-lived isotope ^{239}Np the time elapsed between concentration measurement and addition was accounted for by applying the radioactive decay law

$$N(t) = N_0 \cdot e^{-\lambda t} \quad \wedge \quad \lambda = \frac{\ln 2}{t_{1/2}} \quad (4.2)$$

with $N(t)$ being the number of atoms after time t [mol/L], N_0 the initial number of atoms [mol/L], λ the decay constant [h^{-1}], and $t_{1/2}$ the half life [h] (^{239}Np : 56.52 h).

For the micromolar concentration range, ^{237}Np was used with ^{239}Np as tracer, whereas the experiments at picomolar concentrations were conducted solely with ^{239}Np . In the EXAFS samples only the long-lived isotope was allowed due to transport restrictions and exemption limits of the synchrotron facilities, wherefore these were prepared exclusively with ^{237}Np .

Since the stock solutions were prepared at $\text{pH} \sim 5$, the pH of the samples had immediately to be checked again, before the samples were put back into the end-over-end rotator. To keep the conditions constant, the pH was controlled and readjusted daily during the whole experiment. After a contact time of 72 h the solid and liquid phases were separated by centrifugation.

4.3.4 Centrifugation and γ Counting

The $\gamma\text{-Al}_2\text{O}_3$ samples were centrifuged at $4025 g$ for 20 min, the clay needed 1 h at $100\,000 g$ (Figure 4.9). Of each sample 1 mL of the supernatant was pipetted into PE capsules for subsequent γ spectroscopy (for details on this method see Section 3.2.1). These were put into an acrylic glass holder and adjusted in the closest position to the detector. Figure 4.10 shows the detector setup used for this study.



Figure 4.9: The table centrifuge used for $\gamma\text{-Al}_2\text{O}_3$ (left) and the ultra-centrifuge used for montmorillonite (right).

The duration of the measurement was kept flexible according to the activity of the sample. Thereby, attention was paid to receive at least 10 000 counts (compare Equation 3.4, page 65) for the largest peak area.

The readings were taken at the 103.76 and 106.12 keV lines for ^{239}Np and at the 29.40 keV line for ^{237}Np , with the counting rate being averaged over both values for the former. Owing to efficiency calibration of the detector, the γ energy and counting rate can be directly related to the individual radionuclides present in the sample and their precise amounts. Thus, the neptunium content

in each sample was determined, based on the specific activities of $8.58 \cdot 10^{15}$ bq/g of ^{239}Np and $2.61 \cdot 10^7$ bq/g of ^{237}Np , and projected to concentration [mol/L].



Figure 4.10: The γ detector at the Institute for Nuclear Chemistry, University of Mainz. For cosmogenic and laboratory background suppression, lead absorbers are placed around the apparatus. Left: general view; right: sample holder (front) and detector crystal with shielding (back).

4.3.5 Data Treatment

The amount remaining in solution after equilibration of the system compared to the initial concentration quantifies the amount of neptunium sorbed to the substrate. For a first check, the neptunium uptake was related to the total starting concentration and expressed as percentage. This manner of representation constituted a quick tool for verifying the success of the experiment and, furthermore, proved useful in e.g. determining the sorption edge (see Section 5.1.1).

Furthermore, such a depiction is helpful in cases where there is no sorption or where the numerical calculation yielded even negative results that can be ascribed to the typical variation of analytical measurements and the unavoidable imprecision of the practical experimental performance. Since, by convention, the distribution (or sorption) coefficient K_d is presented on a logarithmic scale³, values of zero and below are not defined and can therefore not be shown. Percentage scales instead provide a better impression of the sorption behaviour in the low pH region.

For reasons of comparison among different substrates or with literature data, however, the results must essentially be transferred to K_d -values to cancel out the effect of various solid-to-liquid ratios as well as to obtain absolute, comparable characteristics. The K_d can be calculated from the initial and equilibrium

³By convention, the unit [mL/g] is omitted with the logarithmic K_d values.

concentrations. It is defined as the moles of sorbed ions – in this case neptunium – per gram of solid phase divided by the moles of neptunium per millilitre of solution, normalised by the inverse solid-to-liquid ratio, and reported as millilitres per gram:

$$K_d = \frac{Np_s}{Np_d} \cdot \frac{V}{m} \quad (4.3)$$

where the K_d is given in [mL/g], Np_s and Np_d are the sorbed and the dissolved amounts of neptunium in either [mol] or [g] in the equilibrated sample, V is the volume of the sample [mL], and m is the mass of sorbent in the sample [g]. For easier use the equation can be simplified to concentrations:

$$K_d = \frac{c(Np_i) - c(Np_f)}{c(Np_f)} \cdot \frac{V}{m} \quad (4.4)$$

with $c(Np_i)$ and $c(Np_f)$ being the initial and final neptunium concentrations measured in the experiment.

Thereby, low K_d -values signify ineffective sorption and high values imply efficient immobilisation of neptunium due to sorption to the mineral surface. The K_d is by definition independent of the concentration of suspended solids (i.e., the solid-to-liquid ratio) and, as long as the ion concentration is small compared to the number of available surface sites, also of the concentration of dissolved ions (Stumm, 1992). The K_d depends on pH, number of surface sites per mass of solid, and the extend of complexation in solution. Hence, it is strictly valid for certain, well-defined conditions only.

Yet, even in a relatively simple system, the K_d combines a range of retention phenomena and is derived from empirical measurements. To extend its interpretation beyond simple fitting efforts, the underlying physical and chemical mechanisms must be investigated, understood, and related to the distribution coefficient. It is assumed that the amount of the radionuclide sorbed is directly proportional to the amount dissolved, but changes in the system chemistry or variations in mineral surface properties affecting sorption are not considered (Turner et al., 2006).

Attention must be paid to the interpretation of the K_d at high neptunium concentrations, because then it might reflect the solubility product instead of the sorption process. The distribution coefficient is not a thermodynamic or even an element specific quantity, but depends highly on system inherent parameters as well as on the experimental methodology (Allard et al., 1984).

Even the distribution coefficients determined in homogenised systems reveal a certain range due to experimental variability. In numerous studies Baeyens and Bradbury (1995b) and Bradbury and Baeyens (2006a) determined a typical uncertainty of $\pm 0.2 \log K_d$ units.

4.3.6 Batch Experiments

To study the impact of the pH on the sorption behaviour of neptunium, experimental series – i.e. batches – of identical samples were conducted, in which only this parameter was varied. All other influencing factors, such as ionic strength, solid-to-liquid ratio, or presence/absence of CO₂, were kept constant within the same series.

Typically, samples for the batch sorption studies with γ -Al₂O₃ were prepared in the range pH 5 to 10 with increments of 0.5 units covering the sorption edge region; for montmorillonite the series were started already at pH 2.5 to detect the effect of cation exchange processes in the acidic region as well (compare page 82*f*).

Batch experiments were prepared with 7 to 8·10⁻⁶ M ²³⁷Np or 7·10⁻¹² M ²³⁹Np, under ambient air as well as CO₂-free conditions. The ionic strength was set either to 0.01 or 0.1 M NaClO₄, while the solid-to-liquid ratio was always the same, 4 g/L for montmorillonite and 0.5 g/L for γ -Al₂O₃.

The percentage of neptunium sorbed was calculated from the concentration of neptunium in the supernatants and in blank samples without sorbent. These blanks were treated in the same way as the suspensions, but without adjustment of pH. From this the sorption edge was identified as the pH of 50% of the total sorption in the respective experiment. In the ambient air batches, the pH of the sorption maximum was recorded as well. This relative approach also proved useful in comparing the sorption behaviour at the different neptunium concentrations.

4.3.7 Sorption Isotherms

Batch experiments can also be conducted with varying neptunium concentration at constant pH. Such plots show the relationship between the sorbate activity and the amount sorbed to the mineral surface. The shape of the corresponding graphs can be described mathematically allowing for conclusions on the mechanism of sorption under the applied conditions. A so-called Langmuir isotherm is defined as

$$\frac{x}{m} = \frac{a \cdot C}{1 + b \cdot C} = \frac{b \cdot C \cdot N_{max}}{1 + b \cdot C} \quad (4.5)$$

where $\frac{x}{m}$ is the weight of sorbate divided by the weight of sorbent [$\mu\text{g/g}$], a and b are constants, C the aqueous sorbate concentration [g/L], $a = b \cdot N_{max}$, and N_{max} the maximum sorption possible [$\mu\text{g/g}$] usually assuming a monolayer surface coverage. Often this equation is found in different forms and/or with different nomenclature, e.g. with b exchanged against K_L , the concentrations

named q , respectively q_{max} , and their fraction expressed as θ representing the share of sorption sites occupied. The ability to depict the asymptotic maximum coverage of the surface as the sorbate concentration increases is the most outstanding feature of the Langmuir isotherm, which is conveniently plotted double-logarithmically.

In general, each surface complex formation equilibrium can be converted into a Langmuir sorption constant. Nevertheless, the approach requires the assumptions that sorption occurs in a single molecular layer, all sorption sites are equal and the surface uniform. Furthermore, there must be no interactions between neighbouring sorption sites and the sorbed ions. These facts are not truly valid for montmorillonite.

In the case of a very small or very high sorbate concentration C causing a log-normal distribution of b – i.e. no saturation of the sorption sites indicated by a decrease in slope is present – the Langmuir equation reduces to a simplified so-called Freundlich isotherm with $n = 1$, respectively $n = 0$. The corresponding equation is typically written as

$$\frac{x}{m} = K_F \cdot C^n \quad (4.6)$$

with K_F and n being constants. In the extreme of $C \rightarrow 0$ ($n = 1$), a of the Langmuir equation equals K_F , which in turn equals the distribution coefficient K_d . Typical values of n range from 0.9 to 1.4 (Lyman et al., 1982, cited in Langmuir, 1997). Again, the nomenclature is often changed, e.g. Γ for $\frac{x}{m}$ or m for K_F . The Freundlich isotherm works well for solids with heterogeneous surface properties. When depicted in a Langmuir plot, i.e. double-logarithmically, a Freundlich isotherm reveals a straight line. Its intercept equals $\log K$ and its slope is n . Thereby values of $n < 1$ indicate decreasing sorption with increasing surface coverage due to progressive saturation of binding sites.

According to Nagasaki and Tanaka (2000), the Langmuir equation cannot be used for heterogeneous surfaces, such as those being characteristic for complex natural minerals including clay minerals. Thus, based on the attested heterogeneity of montmorillonite (cf. Section 2.4.1), a Freundlich isotherm was anticipated for the present study. The experimental results were plotted as the logarithms of dissolved versus sorbed neptunium, expecting a linear fit of the data with a slope of ~ 1 . Any precipitation resulting from exceeding maximum solubility should become apparent in a vertical alignment of the data points at the respective critical concentration.

4.4 EXAFS Studies

Certain samples were prepared for EXAFS investigations to supplement the conventional wet-chemical and radiochemical methods described above. This combination technique contributes significantly to the understanding of the structure and composition of the sorbed complex, in this way facilitating the characterisation of the neptunium species and elucidating the processes taking place during the actinide-surface interaction (Misaelides and Godelitsas, 1999). Thus, EXAFS allows for the interpretation of macroscopic events in molecular terms. Within the scope of this study, beamtime was allocated at the INE (Institute for Nuclear Waste Disposal) beamline of the synchrotron light source at the Karlsruhe Research Centre (ANKA – Angströmquelle Karlsruhe GmbH) and at the beamline of the Research Centre Dresden Rossendorf (ROBL–BM20) at the European Synchrotron Radiation Facility (ESRF) in Grenoble (aerial view in Figure 4.11).

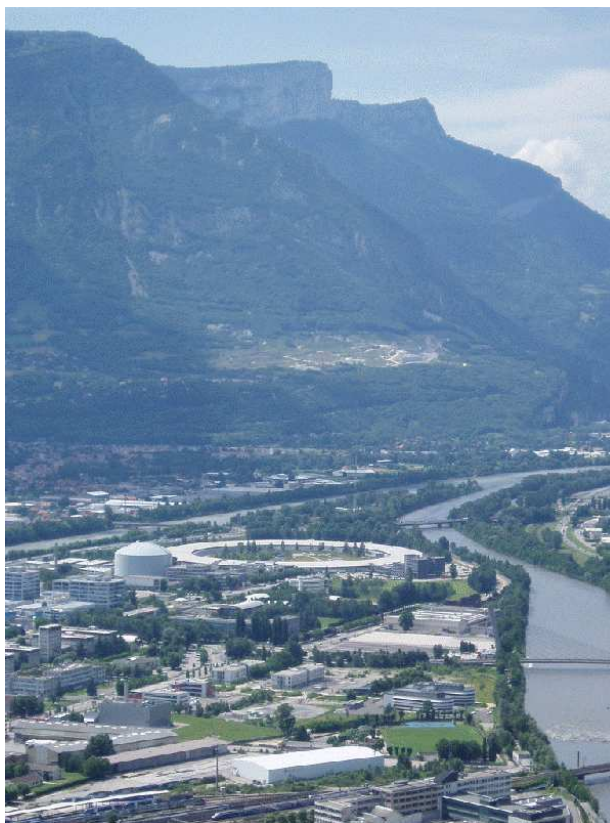


Figure 4.11: The European Synchrotron Radiation Facility (ESRF) in Grenoble. The storage ring is 270 m in diameter and the circulating electron beam has an energy of 6 GeV at 200 mA maximum beam current.

4.4.1 Sample Preparation

Since the EXAFS studies were aimed at gaining insight into the sorption regime of neptunium on a substrate of montmorillonite or $\gamma\text{-Al}_2\text{O}_3$, the samples were prepared as wet pastes with size and shape being predefined by the beamline setup, in particular by the dimensions and the 45° angle of the incident beam. Furthermore, the sample should absorb 50-90 % of the incident X-rays to give a good signal (Bunker, 1997). Based on these considerations, acrylic glass sample holders were manufactured in a thickness of 2 (ANKA) or 3 mm (ESRF) with an oval transfixion of 3×8 mm for ANKA and 3×12 or 3×16 mm for the ESRF. By experience, this volume had proved sufficient to receive well analysable data with the typically attainable neptunium loading.

To determine the required amount of solid a large preliminary sample was prepared without any neptunium (0.1 M NaClO_4 ; 4 g/L STx-1). The suspension was centrifuged at 100 000 g for 1 h and the $2\times 3\times 12$ mm sample holder was filled with the moist residue; the capacity for this paste was then calculated from the difference in weight. The remaining moist sorbent was placed in the oven at 105°C until complete dryness yielding the water content of the sample after centrifugation. With this procedure a capacity of 90 mg moist paste and a water content of 77.6 % were obtained. Extrapolated to the other sample holder sizes this equalled 60, 135, and 180 mg or a dry weight of 13, 30, and 40 mg.

For the preparation of the EXAFS samples sorption experiments with a solid-to-liquid ratio of 4 g/L and a volume of 40 mL, like shown in Figure 4.12, were conducted according to the procedure described in Section 4.3.2 *ff* to obtain enough material for the sample holders. The respective experimental conditions



Figure 4.12: A sorption sample for EXAFS studies prepared in the glove box.

Table 4.4: Experimental conditions of the samples prepared for EXAFS studies at ANKA and ESRF. The total concentration of Np(V) was 6 to 10 μM .

Date	Facility	Sorbent	CO ₂	pH	NaClO ₄ [M]	Np [ppm]
31 Oct–2 Nov 2006	ANKA	$\gamma\text{-Al}_2\text{O}_3$	no	8.5	0.1	314
		$\gamma\text{-Al}_2\text{O}_3$	yes	8.5	0.1	408
5–7 Mar 2007	ANKA	$\gamma\text{-Al}_2\text{O}_3$	no	8.5	0.1	437
		$\gamma\text{-Al}_2\text{O}_3$	yes	8.5	0.1	382
14–16 May 2007	ANKA	$\gamma\text{-Al}_2\text{O}_3$	no	8.5	0.1	418
		$\gamma\text{-Al}_2\text{O}_3$	yes	8.5	0.1	407
		STx-1	yes	8.5	0.1	72
15–19 Jun 2007	ESRF	$\gamma\text{-Al}_2\text{O}_3$	no	9.5	0.1	638
		$\gamma\text{-Al}_2\text{O}_3$	yes	9.5	0.1	583
		$\gamma\text{-Al}_2\text{O}_3$	no	8.5	0.1	556
		$\gamma\text{-Al}_2\text{O}_3$	yes	8.5	0.1	543
		STx-1	no	9.0	0.1	314
		STx-1	no	9.5	0.1	416
		STx-1	yes	9.0	0.1	166
		STx-1	yes	9.5	0.1	139
8–11 Mar 2008	ESRF	STx-1	no	5.0	0.01	81
		STx-1	no	7.0	0.01	408
		STx-1	no	8.0	0.01	70
		STx-1	no	8.0	0.01	165
		STx-1	no	8.0	0.01	340
		STx-1	no	8.0	0.01	453
		STx-1	yes	8.0	0.01	139

are given in Table 4.4. The supernatant was carefully decanted off and the ^{237}Np content determined via γ spectroscopy or LSC to verify the expected uptake by the solid sorbent.

Before the moist residue was filled into the sample holder as shown in Figure 4.13, the oval transfixion had been closed with Kapton[®] (polyimide) tape on one side. Great attention was paid to prepare a homogeneous sample free from bubbles or holes. Once the surface was smoothed the sample was immediately girded with Kapton[®] tape also on the second side to avoid desiccation. While the sample materials must be pure and well characterised, the sample environment is insignificant to the measurement (Ravel, 2000). Thus, for safety reasons as well as for protection of the paste, especially in the case of the CO₂-free

samples, they were further covered with two layers of heat-sealed PE foil (Figure 4.13). The transport of the samples to the respective facilities for EXAFS was conducted by an authorised company.



Figure 4.13: Preparation of the EXAFS samples. Insert: an EXAFS sample in an acrylic glass holder, girded with Kapton[®] tape and twice heat-sealed in PE foil.

4.4.2 Beamline Setup and Measurement

The two synchrotron facilities utilised during this study differ in size and, thus, in brilliance as well as in available energy range of the radiation produced. While both provide electron beam intensities of 200 mA maximum, the ANKA storage ring (35 m in diameter) is operated at 2.5 GeV, the ESRF at 6 GeV (270 m in diameter). An overview of the relevant beamline parameters is given in Table 4.5.

As they were designed to fulfil the same purpose, however, the construction of the INE-beamline and the ROBL is quite similar. The latter is depicted in a detailed sketch in Figure 4.14, while the INE beamline measuring station is shown in the photo of Figure 4.15. The horizontally polarised, broadband electromagnetic radiation of X-ray photons is emitted from the electrons in the storage ring as they are deflected by the bending magnets. At ROBL, for example, it enters the beamline through a first slit unit as a well collimated beam of 20×3 mm

Table 4.5: Comparison of the EXAFS-beamlines at ANKA and ESRF (source: facility homepages).

	INE-beamline ANKA	ROBL-BM20 ESRF	unit
Energy range	2.1-25	5-35	keV
Integrated photon flux	$3.5 \cdot 10^{11}$ (at 18 keV)	$6 \cdot 10^{11}$ (at 20 keV/200 mA)	photons/s
Standard beam size	?	20×3	mm^2 (w×h)
Focussed beam at sample		$\sim 0.5 \times 0.5$	mm^2

(w×h) with a divergence of 2.8 mrad. Downstream this beam is manipulated through multi-component X-ray optics. These include a vertically collimating mirror, a double-crystal monochromator (DCM), and a focussing mirror, as well as attenuators and beam position monitors. A final slit limits its spacial extent at the sample location. The main element, the fixed exit double crystal monochromator located between two bendable curved mirrors, selects the transmitted energy range according to Bragg's Law. In this way, a selected band of well defined spectral width is extracted from the full range of synchrotron X-ray energies.

The beam intensities incident and transmitted through the sample are quantified with ionisation chambers. The gas contained therein is ionised by the X-rays and the ions are collected at electrodes inducing a current pulse, which is amplified and counted. For measuring the fluorescence signal, solid state de-

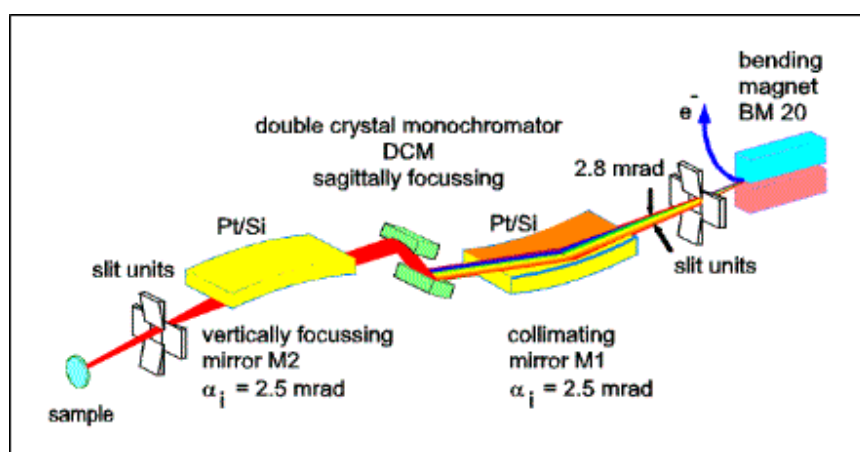


Figure 4.14: The optics of the Rossendorf Beamline (ROBL) at the ESRF in Grenoble.

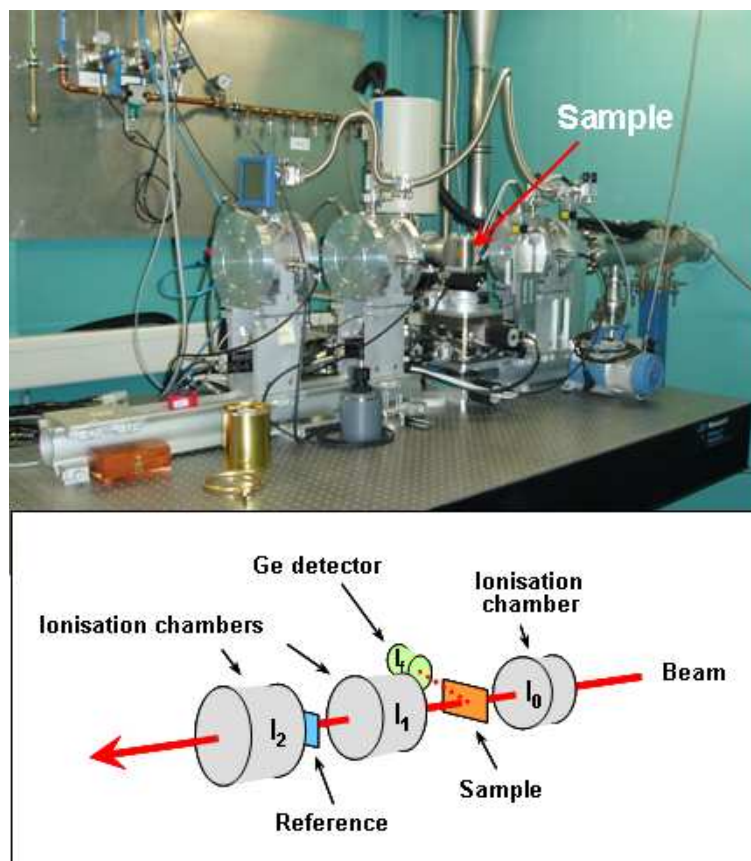


Figure 4.15: The INE-beamline measuring station in the experimental hutch with ionisation chambers, solid state detector, and sample mount. For clarity, the experimental setup is sketched schematically.

tectors (cf. Section 3.2.1) are used to provide reasonable energy discrimination. More detailed information on the beamlines can be found in Denecke et al. (2005) and Reich et al. (2000) as well as on the facility websites of ANKA, ESRF, and FZD (see bibliography). Figure 4.15, bottom, schematically gives the basic layout of the EXAFS experimental arrangement, showing both geometries with ionisation chambers for the primary beam and absorption as well as the Ge detector for fluorescence measurement.

EXAFS spectra of the neptunium L_{III} -edge at ~ 17610 eV were collected in fluorescence mode at room temperature using a Ge solid-state detector. Depending on the respective neptunium loading and the effective beamline performance, multiple scans were run on each sample. To enhance their quality, the time of measurement at the separate energy steps was prolonged according to the weakening of the signal for increasing displacements above the absorption edge. Some

samples were affected by the incident beam, resulting in a progressive alteration of consecutive scans that pointed towards reduction of Np(V) to Np(IV). In these cases, the sample position was varied so that every spectrum was measured on a fresh spot of the sample. The transmission signal of a zirconium foil reference was recorded simultaneously for calibration purposes. At the ESRF also a detector dead time profile was measured and considered later on during data processing.

4.4.3 Data Processing

EXAFS analysis was performed with the software packages EXAFSPAK (George and Pickering, 1995) and FEFF 8.20 (FEFF Project, 2002). Scattering phases and amplitudes were calculated using either the structure of soddyite, $(\text{UO}_2)_2\text{SiO}_4 \cdot 2(\text{H}_2\text{O})$ (Demartin, Gramaccioli and Pilati, 1992), replacing uranium with neptunium and assuming that silicon and aluminium have largely identical electron scattering properties.

Before fitting of the coordination spheres, the raw data was processed through various steps. Briefly, each scan was recalibrated on the basis of the zirconium reference (sub-routine MCALIB; Zr K-edge 17 996 eV, Np L_{III} -edge 17 608 eV) and corrected for the detector dead time (MDEAD). Then, all spectra corresponding to the same sample were averaged (MAVE) creating an *.ave*-file.

EXAFS data reduction was performed with the sub-routine PROCESS. First, a polynomial pre-edge function of order -1 was subtracted from the data as shown in Figure 4.16. Then, a spline function was fitted to the EXAFS region of the resulting graph applying the programme default settings in most cases. Only the order of the component polynomials and the number of individual polynomials, the so-called range, was slightly varied to obtain the best fit. A Victoreen⁴ was used with programme-internally tabulated coefficients to normalise the data (Figure 4.17). From this the oscillating EXAFS signal could be extracted and inspected together with the I_0 signal, which helps identify and, if necessary, remove crystal glitches in the data. An example of fully processed data is provided in Figure 4.18, showing a spike ascribed to a monochromator glitch at 8 \AA^{-1} . In the present study, however, the appearing glitches were found negligible and without influence on the subsequent fitting process.

In the next step, the Fourier transform was calculated from the unsmoothed data over a Gaussian k -window located roughly in the range 2.5 to 9.75 \AA^{-1} depending on the graph. Figure 4.18 shows the corresponding determination of

⁴This is the mathematical function $f(\lambda) = C\lambda^3 - D\lambda^4$, where λ is the X-ray wavelength and C and D are free parameters (Koningsberger and Prins, 1988).

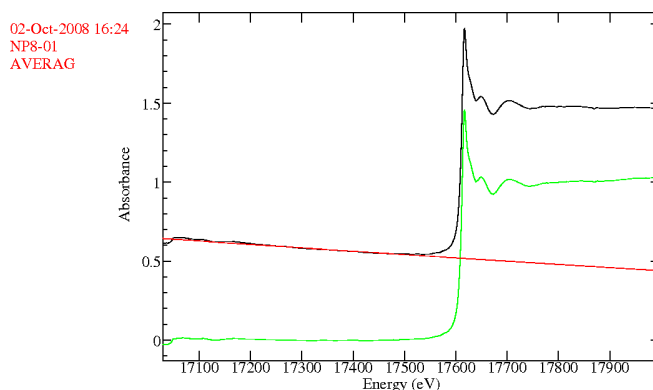


Figure 4.16: Plot of the pre-edge subtraction with raw data (black), polynomial function (red), and difference (green) superimposed.

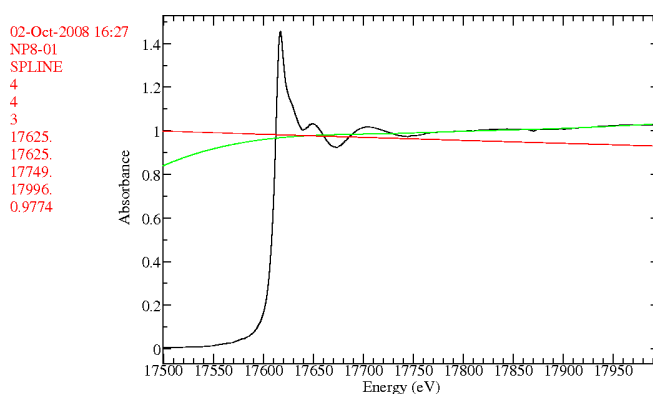


Figure 4.17: Removal of the spline (green) from the processed data (black); the Victoreen is also shown (red).

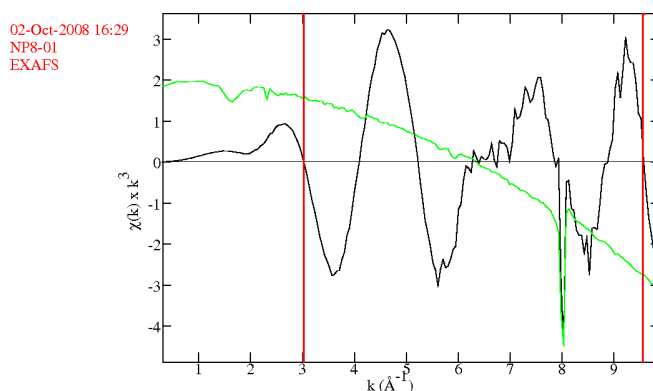


Figure 4.18: The resulting EXAFS data (black) plotted together with I_0 (green). A glitch is evident at $k = 8 \text{ \AA}^{-1}$. The determination of the k -window (red, here from 3.0 to 9.6) to reduce ringing effects in the transform is indicated.

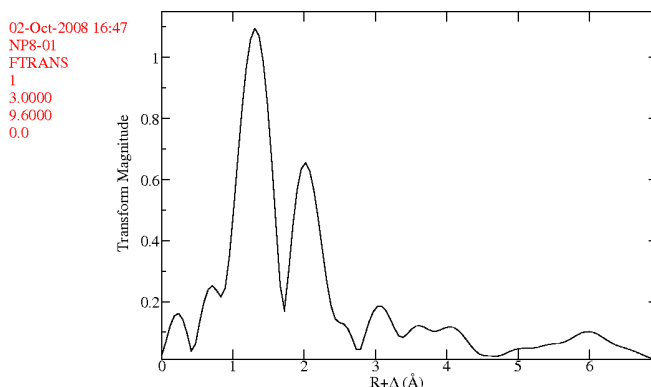


Figure 4.19: The Fourier transform in the range $R + \Delta = 0$ to 7 Å.

the k window of $3.0 < k < 9.6 \text{ \AA}^{-1}$, selected by the corresponding zero crossings. In Figure 4.19 the resulting Fourier transform is presented for the given range of relevance. No phase correction was done but the default settings were applied; neither any other tools for data processing such as edge manipulation or recalibration, or deglitching were used.

The curve-fitting analysis as well as FEFF phase and amplitude calculations were carried out with the sub-routine OPT. It takes the *.ave*-file as input and creates an *.hld*-file with the structural information of the fit. The k -range is individual for each sample and must be re-entered; the k -weighting applied in this step was always chosen to be k^3 .

As a neptunyl compound was expected, coordination numbers of 2 for the axial (O_{ax}) and 5 for the equatorial oxygen atoms (O_{eq}) were anticipated and fixed during the fitting. These spheres – both single scattering paths – were entered first, linked to the corresponding FEFF-file, which was derived from the soddyite model (Demartin et al., 1992). Approximate distances were given to provide a reasonable starting point for the subsequent iterations. Additionally, a multiple, namely triple, scattering path was included for the closest, i.e. the axial, oxygen atoms (O_{ax} MS). To fit surface aluminium (or silicon⁵) atoms in greater distance from the central absorbing neptunium, the signal-to-noise ratio was too low in the majority of the samples. So this option could be attempted only in few exceptional cases and, for reasons of consistency and comparability, was abandoned for final data evaluation.

Spectra of samples prepared under ambient air conditions that revealed notable contributions from further coordination spheres were analysed on the basis of a model of $\text{NaNpO}_2(\text{CO}_3)$ (Volkov, Visyashcheva, Tomilin, Kapshukov and

⁵Al and Si are adjacent in the periodic table and because of their similar atomic number indistinguishable to EXAFS (cf. Section Data Processing).

Rykov, 1981), accounting for a carbonate structure of the neptunyl. In the respective samples, a single scattering carbon sphere (C) was added as well as two linked spheres of double and triple scattering, respectively, for the associated distal oxygen atoms (O_{dist}). The overall scaling factor S_0^2 was 0.9, which is the EXAFSPAK program default, for all samples.

During the calculation process the Debye-Waller factors were allowed to level off individually, while the threshold ΔE_0 shift was coupled over all coordination spheres. The data were treated with the multiple scattering curved-wave theory. The interface for entering these parameters is shown in Figure 4.20 (top).

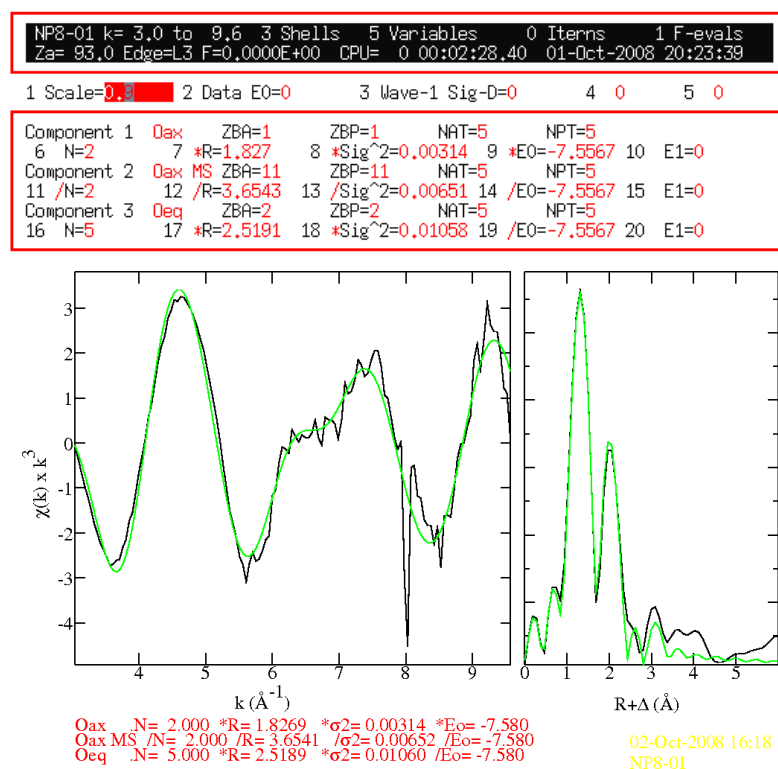


Figure 4.20: Input interface for fitting of the first and second coordination spheres, axial (including multiple scattering) and equatorial oxygen. ‘*’ denotes a floating, ‘/’ a parameter linked to the value of the previous sphere.

The curve-fitting was performed using the Marquardt algorithm yielding the variability of each floating parameter as well as some statistical information like the reduced error (χ^2) or the resolution in distance, which hint at the quality of the fit. The result can then be plotted (Figure 4.20, bottom). It is also possible to show the residual and the fit deconvolution to identify hidden oscillations, which can be extracted and reprocessed with other likely components of the anticipated compound.

4.5 Surface Complexation Modelling

A representation of the experimental data was attempted by modelling with the chemical equilibrium program Visual MINTEQ Version 2.53 (Gustafsson, 2007; thermodynamic data by NEA, 2005), employing the 2 SPNE SC/CE model (see Section 3.3.1). Sorption of the applied neptunium trace amounts was assumed to involve only the strong sites, $\equiv\text{S}^{\text{S}}\text{OH}$. The site capacities and protolysis constants were fixed as given in Table 3.1 on page 84, while the cation exchange selectivity coefficient ${}_{\text{Na}}^{\text{Np}}K_C$ and the surface complexation constants ($\log {}^{\text{S}}K_y$) were varied to obtain the best fit⁶. The site concentration relevant for ion exchange was taken from the certified properties of the montmorillonite STx-1 (Table 4.1, page 91). As initial modelling showed that the neptunium concentration (pM to μM) has hardly any influence on the results – confer Figure 4.21 – all calculations were executed with $1 \cdot 10^{-12} \text{ M NpO}_2^+$. Figure 4.22 depicts the separate components of the modelled graphs, i.e. cation exchange (specified via ${}_{\text{Na}}^{\text{Np}}K_C$), two surface complexation reactions (${}^{\text{S}}K_0$ and ${}^{\text{S}}K_1$) for $\equiv\text{SONpO}_2$ and $\equiv\text{SONpO}_2\text{OH}^-$, plus a third one (${}^{\text{S}}K_{\text{CO}_3}$) for a ternary carbonate complex that forms in the presence of ambient air.

Unlike all other procedures, the modelling could not be transferred to $\gamma\text{-Al}_2\text{O}_3$ directly, because the 2 SPNE SC/CE model was especially designed to study the sorption on clay minerals, which is jointly composed of cation exchange and surface complexation. Oxides instead lack a permanent charge as well as interlayer

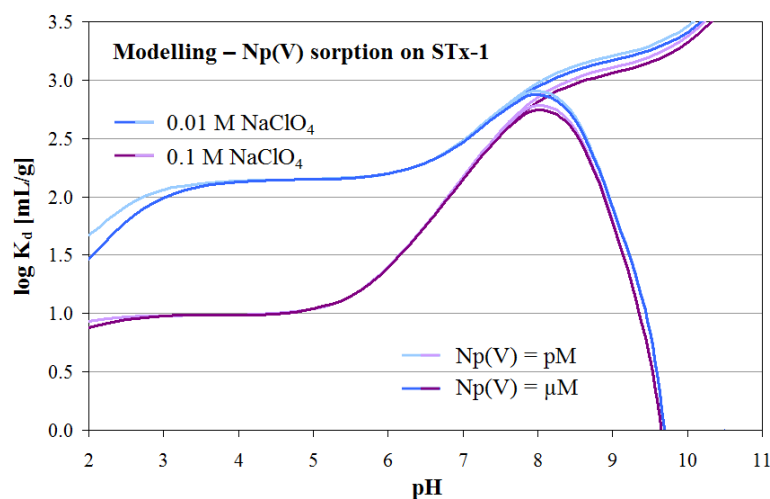


Figure 4.21: Influence of the Np(V) concentration on the modelling results (${}_{\text{Na}}^{\text{Np}}K_C = 1.1$; $\log {}^{\text{S}}K_0 = -2$; $\log {}^{\text{S}}K_1 = -12$).

⁶ y in ($\log {}^{\text{S}}K_y$) is an integer derived from the surface complex $\equiv\text{S}^{\text{S}}\text{ONpO}_2(\text{OH})_y^{2-(y+1)}$.

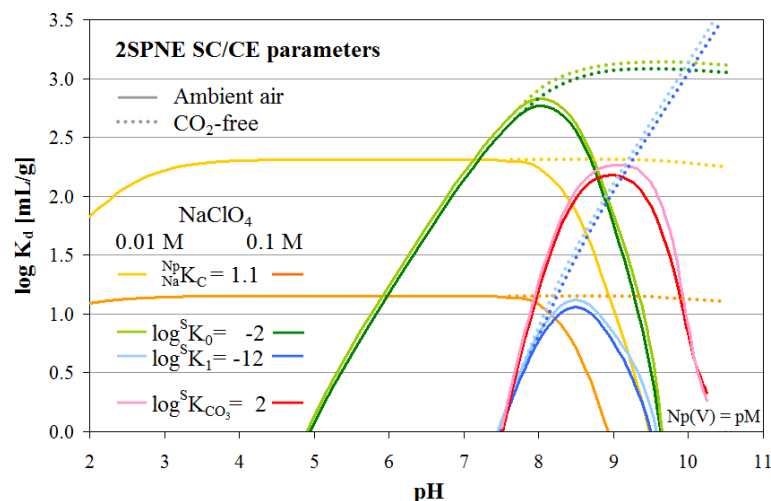


Figure 4.22: The separate components of the modelled sorption curves (here modelled for 4 g/L montmorillonite). The difference between solid and dashed lines reflect the influence of ambient CO_2 on the sorption of neptunium. Remarkably, only the ion exchange process is influenced by changes in ionic strength.

space, which together induce the cation exchange capacity of sheet silicates. Deleting this part of the model, strictly speaking, modifies the inherent approach.

Nevertheless, this transfer was attempted in order to obtain surface complexation constants for comparison with those determined for montmorillonite. The relevant modelling parameters were either kept (e.g. the protolysis constants) or adapted to the experimental conditions to treat $\gamma\text{-Al}_2\text{O}_3$ as similar to montmorillonite as possible. However, some quantities, from which required input values could be deduced, are not known; particulars on the number of exchangeable protons, for example, vary from 1.3 to 12.5 mol/g (Goldberg, Davis and Hem, 1996). Therefore, the sorption site capacity (Q_{max}) was extrapolated from data for activated $\gamma\text{-Al}_2\text{O}_3$ by Horst and Höll (1997) according to Figure 4.23. The extracted value for Q_{max} of the material used in this study is, depending on the surface area assumed, $1.5 \cdot 10^{-4}$ or $2.2 \cdot 10^{-4}$ mol/g, respectively⁷, giving $0.75 \cdot 10^{-4}$ or $1.1 \cdot 10^{-4}$ mol/L for suspensions of 0.5 g/L. This number agrees with the surface-site density recommended by Davis and Kent (1990). These often cited authors assign an universal amount of 2.31 sites per nm^2 to all natural materials, amounting to $1.91 \cdot 10^{-4}$ mol/L for the $\gamma\text{-Al}_2\text{O}_3$ used in this study with 100 g/m^2 and 0.5 g/L.

⁷Note: For the sorption of monovalent cations such as Na^+ and NpO_2^+ , the number of sorption sites [mol] equals the number of charges [eq].

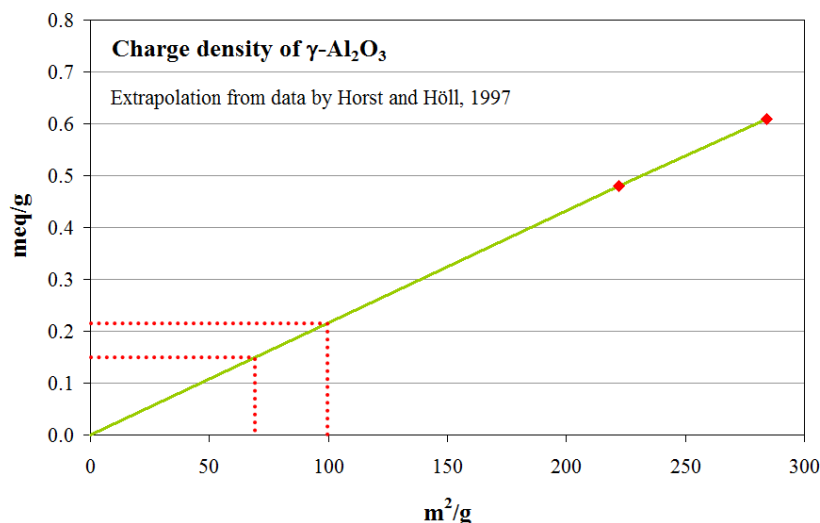


Figure 4.23: Extrapolation of the maximum capacity of $\gamma\text{-Al}_2\text{O}_3$ from the only two data points available in literature. The red dotted lines mark the two possible values for the surface area of the material used in this study, $100\text{ m}^2/\text{g}$ (average of manufacturer declaration) and $68.4\text{ m}^2/\text{g}$ (BET measurement; see Section 4.2.2).

For comparison, the number of strong sorption sites for complex formation was also derived from that of montmorillonite ($2 \cdot 10^{-3}\text{ mol/kg}$, Bradbury and Baeyens, 1997), assuming the same site density on the surface of $\gamma\text{-Al}_2\text{O}_3$. With $83.79\text{ m}^2/\text{g}$ for STx-1 (cf. Table 4.1, page 91) and approximately $100\text{ m}^2/\text{g}$ for $\gamma\text{-Al}_2\text{O}_3$, the batches of 0.5 g/L contained $1.2 \cdot 10^{-6}\text{ mol/L}$ of $\equiv\text{S}^{\text{S}}\text{OH}$. The total number of strong and weak sites, $0.5 \cdot 10^{-4}\text{ mol/L}$ is in the order of the site capacity calculated from Horst and Höll (1997), which was interpreted as supporting this approach.

For reasons of consistency within this study and since the $\gamma\text{-Al}_2\text{O}_3$ used was not activated, the value deduced from the clay was preferred for the modelling. Although, in contrast to montmorillonite, the isotherms of neptunium sorption on $\gamma\text{-Al}_2\text{O}_3$ point towards saturation of the available sorption sites (see Section 5.1.3), reactions of NpO_2^+ with weak sites, e.g. $\equiv\text{S}^{\text{W}_1}\text{OH}$ (Table 3.1, page 84), were not explicitly considered in the modelling process.

5

Results and Discussion

This chapter presents the outcome of the experiments described in the previous section and relates the findings to similar domains explored within the research group as well as to data published by others and to the general literature. First, the results of the batch experiments are presented including the sorption isotherms. Thereafter, the EXAFS studies are discussed, while the third part comprises the modelling approach. The chapter concludes with a synthesis of the separate findings, which are merged to establish a conclusive picture of the system studied. A compilation of all experiments conducted in the context of this study is provided in Appendix G; a detailed overview of the EXAFS samples is given in Table 4.4 on page 107.

5.1 Np(V) Sorption on Montmorillonite and Aluminium Oxide

The study of the sorption behaviour of Np(V) on montmorillonite and γ -Al₂O₃ constituted a great proportion of this work as it served as background and basis for decisions on the preparation of EXAFS samples and also as reference for modelling. The study of the sorption process, however, is largely empirical and sensitive to experimental errors. Facing the high temporal effort of approximately three weeks per batch, the capability for validation of the results by repetition of the studies was limited. Hence, some questionable or at least not fully conclusive findings occurred, which are pointed out and discussed as such.

5.1.1 pH-Dependency: Edge and Maximum

The sorption of actinides reveals a strong pH dependence due to the high charge of the aqueous species involving a large number of protons in surface reactions (Turner et al., 2006). This general statement was reconfirmed by the results of

this work. For more clarity the figure graphs¹ were drawn following a colour code. Within each subsection the similar shades were assigned to montmorillonite and γ -Al₂O₃, respectively.

In the acidic region, the sorption was observed to be constant and independent of pH. On γ -Al₂O₃ no neptunium at all was sorbed below pH ~6. On montmorillonite, however, a low constant sorption was detected, the extent of which correlated with the ionic strength (see Section 5.1.2). Some results of the batch experiments for Np(V) at μ M concentration and 0.1 M NaClO₄ with montmorillonite as well as for Np(V) at pM concentration and 0.01 M NaClO₄ with γ -Al₂O₃, respectively, are given in Figure 5.1. For a clear identification of the sorption edge, they are presented as percentage² indicating the extent of sorption in relation to the available neptunium concentration (cf. Section 4.3.5).

At a certain pH the uptake rises rather abruptly over a range of 2-3 pH units, which can be described in terms of beginning surface complexation processes on amphoteric surface hydroxyl groups (\equiv SOH) that are situated at the mineral edges (Bradbury and Baeyens, 2006b). This increase in sorption over a fairly narrow pH span is identified as the sorption edge, numerically defined as the point where 50% of the maximum sorption is reached. Its location is related to the hydrolysis behaviour of the sorbate – in this case to the formation of NpO₂OH(aq) (see Figure 5.10, page 133) – and for neptunium occurs at pH 7.0-8.5 (Turner et al., 2006). This general observation is again supported by this study.

In all cases the sorption of Np(V) increases significantly above pH 6. Mostly, 50% of the maximum sorption is reached between pH 7.0 and 7.5. Altogether, the initial neptunium concentration seems to influence the position of the sorption edge, because it shifts towards higher pH with increasing neptunium supply as visible in Figure 5.2 where pico- and micromolar concentrations are compared both for montmorillonite (upper) and γ -Al₂O₃ (lower plot). This finding is contrasted by Del Nero et al. (2004) who detected no such effect on neptunium sorption on silica. Nevertheless, also in the CO₂-free experiments with γ -Al₂O₃ and picomolar neptunium concentration at 0.01 and 0.1 M NaClO₄ the sorption edge apparently shows a clear dependency on the ionic strength, which is clearly recognisable in Figure 5.3. For a discussion of this particular finding see Section 5.1.2 below.

¹In Section 5 the experimental curves were fit by eye due to limited data.

²At the PSI the batches were conducted with variable solid-to-liquid ratios in order to create the best possible contrast between initial and final neptunium concentration (high in regions of low sorption and vice versa). For the percentage depiction, the theoretical uptake for 4 g/L montmorillonite was calculated from the K_d -values obtained using Equation 3.1.5 (page 61).

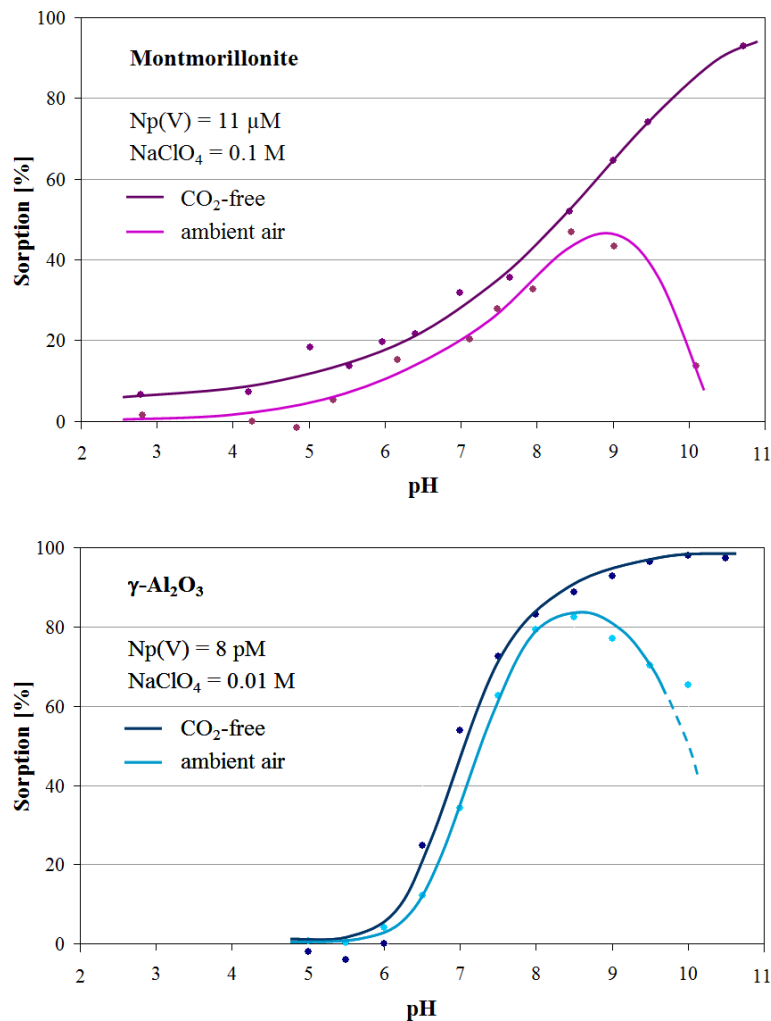


Figure 5.1: Examples of the sorption of Np(V) on montmorillonite (upper) and γ -Al₂O₃ (lower), expressed as percentage of the initial neptunium concentration (for a discussion of the dashed line see Section 5.1.4).

The reliability of the defined sorption edge, however, requires some general discussion. In the experiments with γ -Al₂O₃ serious difficulties were encountered with the measurement of the pH, especially under exclusion of CO₂. As Baeyens and Bradbury (1995b) state in their report (on montmorillonite), a large scatter together with poor and sometimes even time dependent results occurred between pH 5 and 9, which was caused mainly by the pH measurements. In this range they observed a drift towards neutral pH and noted that it took up to one hour to reach steady state. From their studies, the authors estimated an uncertainty of ± 0.5 units in pH leading them to test buffer substances (see

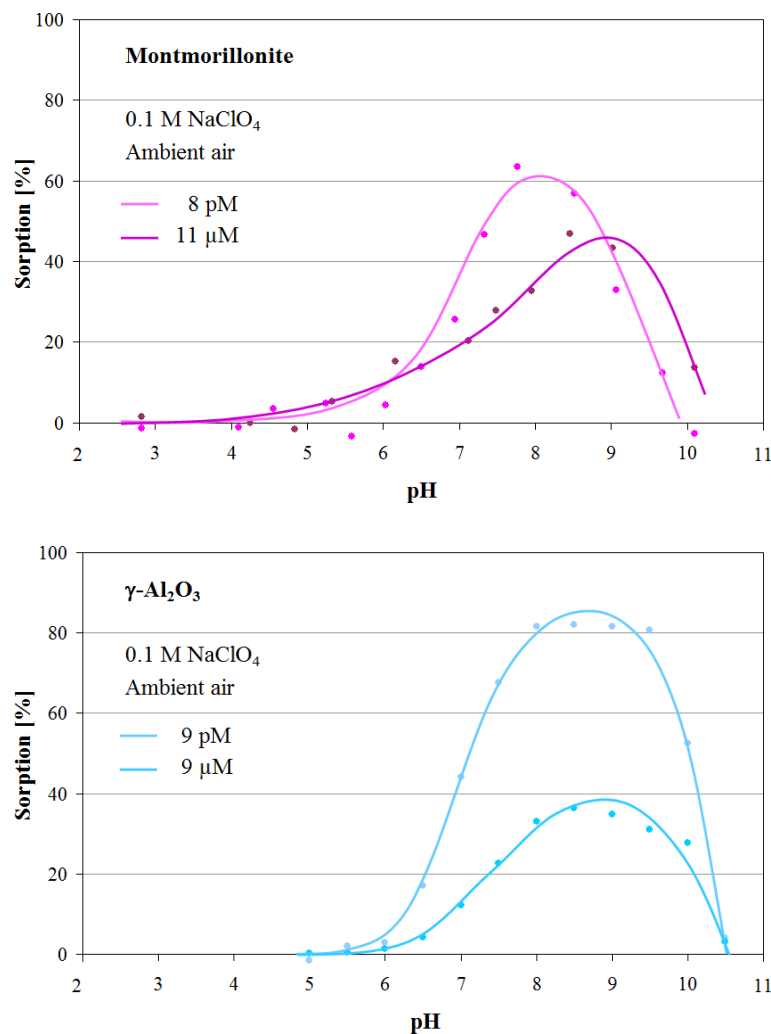


Figure 5.2: The effect of neptunium concentration on the extend of uptake and on the position of sorption edge and maximum for montmorillonite (top) and γ -Al₂O₃ (bottom).

Table 4.2, page 93) to obtain better results. They demonstrated that these do not influence the sorption behaviour. Unfortunately, such a study is quite ample and could not be conducted within the scope of this thesis for γ -Al₂O₃, resulting in the constraint of manual pH adjustment during these experiments with the above-mentioned consequences and possible errors. Hence, the corresponding sorption edges presented here must be considered with certain scrutiny.

In a CO₂-free environment, sorption increases continuously with pH. A maximum uptake followed by a decline in the far alkaline region is, in contrast, observed for the experiments conducted under ambient air. Here the neptunium is

kept in solution by carbonate complex formation (as pointed out in Section 2.2.4, for a more thorough discussion see Section 5.1.4). In the air-equilibrated system, maximum sorption of Np(V) on montmorillonite and γ -Al₂O₃ is reached at pH 8.0-8.5. Like the sorption edge the maximum is shifted to a slightly higher pH with micromolar neptunium concentration (Figure 5.2). A decrease of sorption with increasing carbonate concentration³ was also observed before and quoted in literature, as stated by e.g. Choppin and Wong (1998) in their topical overview. Sabodina et al. (2006), for example, observed a maximum of Np(V) sorbed on bentonite at pH 7-8, which is quite close to the observations of the present study.

As intended (cf. Section 3.1.5), at low neptunium concentration ($7 \cdot 10^{-12}$ M) approximately 80 % of the Np(V) are sorbed on γ -Al₂O₃ at a solid-to-liquid ratio of 0.5 g/L. This was similarly calculated for montmorillonite yielding an optimum solid-to-liquid ratio of 4 g/L, but the sorption stayed 20 % lower than expected during the picomolar experiments, for which no explanation was found. At $7 \cdot 8 \cdot 10^{-6}$ M, however, only 40 % of the Np(V) are sorbed on both substrates, because the solid-to-liquid ratios were kept constant for all experiments. Since they were optimised for 80 % sorption at picomolar neptunium concentration, an increase in sorbate results in a lower ratio of sorbed to dissolved ions when the number of sorption sites becomes limited. This is especially valid for γ -Al₂O₃ as will be discussed in connection with the sorption isotherms in Section 5.1.3 below.

The batch results were compared to similar studies conducted independently within the research group. With kaolinite, for example, which is a double-layered clay mineral⁴ that was subject of similar investigation within the working team, the sorption edge occurs slightly higher at pH 7.5-8.0, while the sorption maximum under ambient air is reached at pH 9.0.

Sorption to vial walls

A decrease in radionuclide concentration of the sample is not necessarily due to sorption to the surface of the suspended mineral phase. Competing interactions with components of the experimental setup must be considered, too, first of all with the walls of the vials. In the batch experiments, the radionuclide solution was in contact with ca. 47 cm² ($= 4.71 \cdot 10^{-3}$ m²) of polyethylene vial wall. For comparison, the mineral surface constituted 0.34 to 3.35 m² (γ -Al₂O₃: 0.5 g/L, 68 m²/g; STx-1: 4 g/L, 84 m²/g; in both cases 10 mL per sample), which is a factor of 100 to 1 000 larger. Nevertheless, different sorption affinities could

³The dissolution of CO₂ and, thus, the formation of carbonate species increases with pH, see Figure 3.1 on page 60.

⁴Kaolinite 'lacks' one of the two tetrahedral layers of montmorillonite, see Section 2.4.1.

result in large discrepancies regarding the amount of radionuclides sorbed per surface area.

For the applied experimental setup and material, however, a measurable effect of wall sorption has been ruled out in previous studies (by A. Jermolajev, working group member). This agrees with literature: Baeyens and Bradbury (1997), for example, quantified wall sorption as $\sim 0.1\text{--}0.5\%$ of the initial radionuclide activity over the pH range 4.5–8.2, and Nagasaki and Tanaka (2000) state that also in their study with a much lower solid-to-liquid ratio of montmorillonite (0.08 g/L) sorption of Np(V) to PE vial walls was negligible.

5.1.2 Effect of Variations in Ionic Strength

A shift of the sorption edge induced by alterations of the ionic strength as shown in Figure 5.3 was exclusively observed in the CO_2 -free batches with $\gamma\text{-Al}_2\text{O}_3$, but neither in the experiments under ambient air, nor with montmorillonite. This led to a repetition of the $\gamma\text{-Al}_2\text{O}_3$ series allowing for a more thorough analysis. The error bars in the graphs show the range of these two independent measurements. Although they are quite large for certain values around the sorption edge, the tendency is obvious: An increase in the ionic background causes the sorption edge to shift to higher pH under CO_2 -free conditions. This corresponds to a reduction in sorption. Interestingly, Del Nero et al. (2004) observed a slight effect of ionic strength on neptunium sorption even under ambient air conditions. Similar to the present study, the sorption edge was shifted towards the alkaline

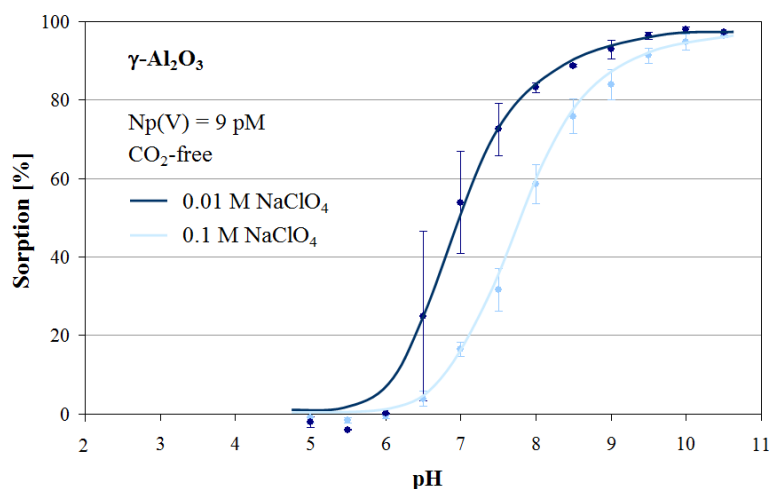


Figure 5.3: The influence of ionic strength on the position of the sorption edge. The error bars represent the range of measurements on two separate batches each.

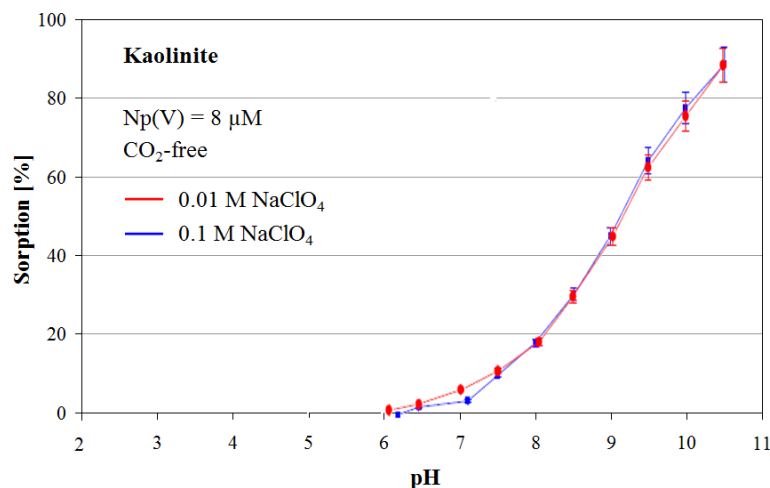


Figure 5.4: Sorption of Np(V) on kaolinite (Amayri et al., 2005). No influence of the ionic strength on the sorption edge is visible.

region with increasing NaClO₄ concentration. In synthetic groundwater (pH 8.3) the influence of ionic strength is clearly significant and sorption decreases with increasing ionic background (Lu et al., 2000).

The particularly large differences between the parallel experiments at 0.01 M NaClO₄ reflect the difficulties of pH measurement and adjustment in the glove box. Under exclusion of CO₂, the pH of the suspension drifted remarkably, in particular in the near-neutral region, where, because of the logarithmic definition, small changes in the proton concentration cause massive fluctuations in pH. In spite of the provisions taken to ensure reproducibility as described in Section 4.2.4 this could not be amended. It would have been desirable to use buffer solutions as with montmorillonite, but the compulsory assurance that these do not alter the sorption behaviour was beyond the scope of this study.

However, a comparison with kaolinite – its sorption behaviour with respect to ionic strength is shown in Figure 5.4 – bears no analogy to the present results: no dependence on the ionic strength is observed. One possible explanation might just be that the effect is cancelled out by the 10⁶ times higher neptunium concentration in this particular study compared to the present experiments with γ -Al₂O₃. Even in the presence of ambient CO₂, the situation seems to be reversed with kaolinite compared to γ -Al₂O₃. While for the latter no effect of changes in ionic strength is visible under such conditions, it is reported that higher ionic strength increases sorption on kaolinite (Amayri, Jermolajev and Reich, 2005). As an attempt for explanation, the shift observed in the present work under exclusion of CO₂ might have been caused by an overlaying effect of cation exchange processes over the whole pH-range leading to less sorption

with increasing ionic strength. However, such a pronounced occurrence should be limited to clay minerals with a correspondingly high CEC and should show up in the lower pH region only.

As mentioned above, the sorption edge of montmorillonite is not influenced by the ionic strength under ambient air at picomolar neptunium concentration; this is depicted in Figure 5.5. However, montmorillonite generally exhibits a different behaviour to $\gamma\text{-Al}_2\text{O}_3$ as well as to kaolinite due to cation exchange processes gaining in importance at low pH. With triple-layered clay minerals forming interlayer space, a higher ionic strength should lead to less neptunium uptake through competition of Na^+ and NpO_2^+ for the available sorption sites in the acidic region.

The experimental results are presented in Figure 5.5; unfortunately, showing no effect they do not well support the expectation. Taking K_d -data modelled with Visual MINTEQ (Gustafsson, 2007, see Section 5.1.5 below) the experiment at 0.1 M NaClO_4 could largely be reproduced. The uptake at 0.01 M NaClO_4 , however, was expected to equal ca. 35 % in the acidic region from pH 3.5 to 5.5, and the maximum to reach about 75 %. Here barely 10 % were measured at low pH and 35 % at maximum in the first batch (lower pale pink curve). Thus, this experiment at 0.01 M NaClO_4 yielded results that were uniformly too low by about 25-30 % sorption, corresponding to $\sim 0.7 \log K_d$ -units. The reason for this deviation between experimental and theoretical data could not precisely

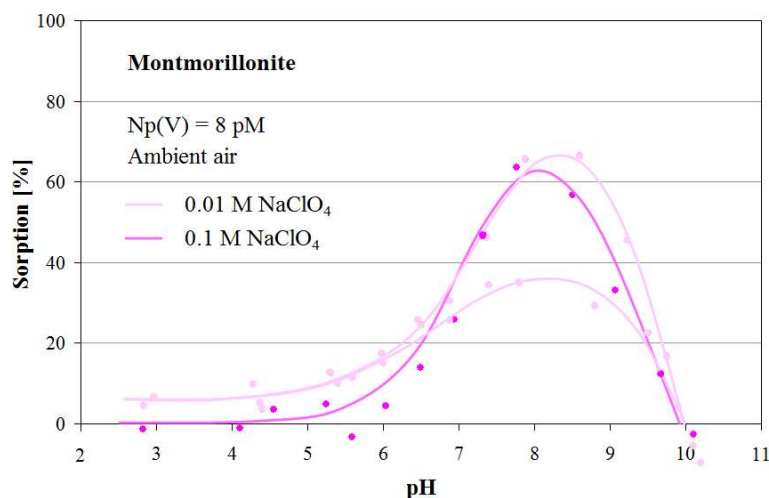


Figure 5.5: The influence of ionic strength on the sorption of neptunium on montmorillonite. The experiment at 0.01 M NaClO_4 yielding overall low sorption (lower pale curve) was repeated and provided reasonable results for the maximum (higher pale curve), while the sorption regime of the ion exchange region, i.e. below $\text{pH} \sim 6$, was the same in both batches.

be identified. Assuming an experimental error, a repetition – also shown in Figure 5.5 (higher pale pink curve) – gave the anticipated maximum sorption around that of the 0.1 M NaClO₄ batch, but still stayed unexpectedly low in the acidic region.

The selectivity coefficient for the exchange of two monovalent cations on montmorillonite should be around unity. Consultation of literature, however, showed that deviations from this value for neptunyl cation exchange with sodium have been observed before. Bradbury and Baeyens (2005), for example, summarise that in 0.1 M Na⁺-solution sorption coefficients of 0.8 and 1.0 were observed, but that at lower ionic strength (0.025 M) a value of only 0.4 was derived; unfortunately, the authors provide no explanation. In the present case, together with the – in comparison to γ -Al₂O₃ – marked scattering of the data, the unexpected low neptunium sorption at 0.01 M NaClO₄ might result from the constant solid-to-liquid ratio bearing only small differences between initial and final neptunium concentration, which in combination with the total trace (picomolar) amount constituted the source of analytical imprecision.

The only direct hint from literature that could explain the observations of this study was found in Del Nero et al. (2004): In their experiments with amorphous alumino-silicates (so-called allophanes) at 0.01 M NaClO₄ they observed a slight increase of the ionic strength with decreasing pH of acidic solutions due to the pH-dependent ad- and desorption of Na⁺, ClO₄⁻, and Cl⁻. With the ionic strength in this way becoming higher than desired, the electrostatic sorption would decrease by the corresponding amount.

5.1.3 Isotherms

The use of the two radioisotopes ²³⁷Np and ²³⁹Np, which have identical chemical behaviour but different specific activities, enables sorption studies over a wide range of neptunium concentrations. As pointed out above, a similar tendency towards lower sorption for higher neptunium-to-solid ratios is observed in all cases. The more neptunium is offered the lower percentage is sorbed to the mineral surface. This effect is also illustrated – more or less clearly – by a decreasing slope of the long-range isotherms, as will be demonstrated in this section.

As the data shown in Figure 5.6 indicate, under ambient air conditions precipitation of neptunium is observed at ca. 3·10⁻⁵ M, while it stays dissolved above this concentration when CO₂ is absent. This finding agrees with the solubility limit of neptunium carbonate complexes of 3·10⁻⁵ M at pH 8.5 measured by Neck, Runde, Kim and Kanellakopulos (1994). Below this concentration, there is no significant difference on the magnitude of sorption at pH 8.5 between the

two types of atmospheres examined for $\gamma\text{-Al}_2\text{O}_3$. At pH 9 already the influence of neptunium carbonate complexation becomes obvious, though (Figure 5.7, top): over the whole concentration range sorption is evenly smaller by a factor of about 2 in the experiment conducted under ambient air. This finding agrees well with the sorption maxima determined in the batch studies discussed above. Under ambient air, the absolute value of sorption is approximately equal at pH 8 and 9 (Figure 5.7, bottom); the slightly different slopes of the isotherms are regarded insignificant, originating from imprecision of the experiments and corresponding scattering of the data rather than from different chemical behaviour.

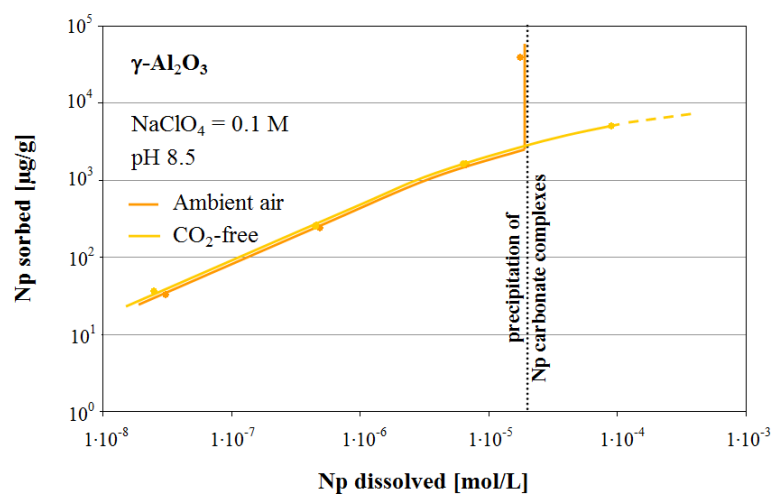


Figure 5.6: Comparison of isotherms on $\gamma\text{-Al}_2\text{O}_3$ for ambient air and CO_2 -free conditions. For the former precipitation of neptunium carbonate complexes above their solubility limit of $\sim 3 \cdot 10^{-5}$ M at pH 8.5 is observed.

All isotherms follow a closely linear Freundlich-type (compare Section 4.3.7) with a slope of ~ 1 . In the case of $\gamma\text{-Al}_2\text{O}_3$, this slope slightly decreases at higher neptunium concentrations (to ~ 0.75 around 10^{-5} M Np(V), cf. Figure 5.9), which could indicate the saturation of available binding sites in the 0.5 g/L suspension. Because of the linearity of the isotherm for montmorillonite (Figure 5.7), measured at 4 g/L, a saturation of its binding sites can be excluded for the applied neptunium concentrations. Nevertheless, for clay minerals, too, a nonlinear trend in the isotherm at high radionuclide supply may be observed under certain conditions. The presence of many dissolved ions would potentially lead to the formation of polynuclear aqueous complexes when the sorbate concentrations are increased beyond the capacity of sorption sites (Turner et al., 2006). At the very dilute concentrations applied in this study, however, the number of avail-

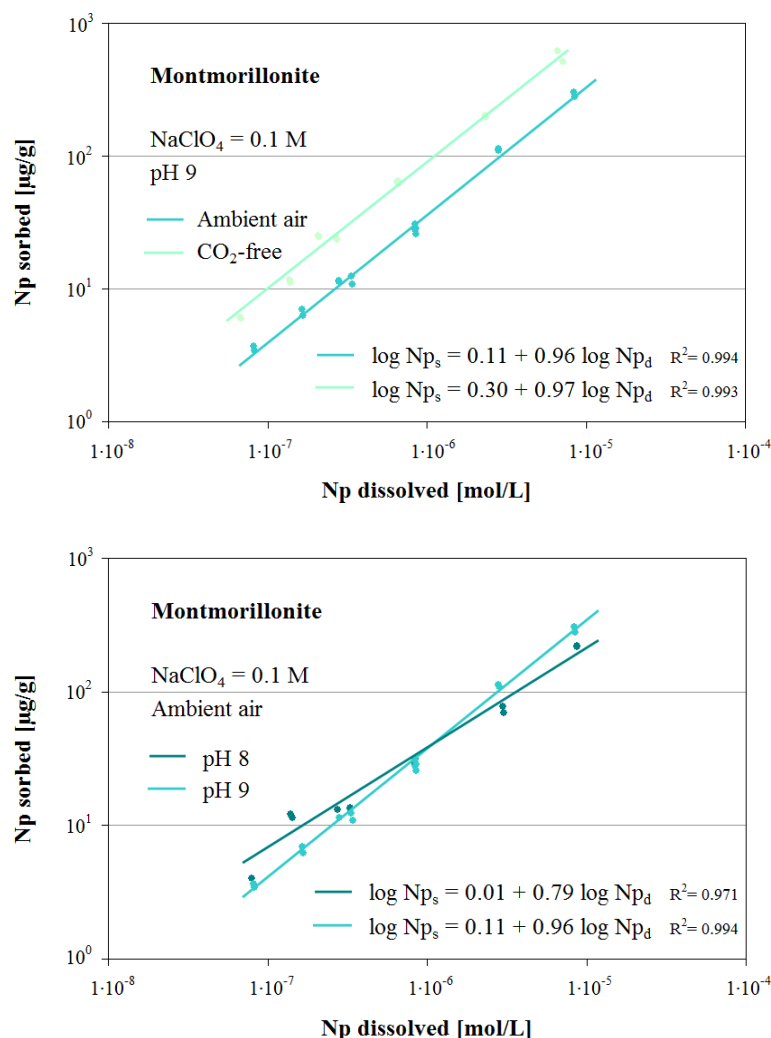


Figure 5.7: Top: Influence of CO₂ on the absolute sorption at pH 9. – Bottom: No influence of pH on sorption; the slightly different slopes are attributed to analytical inaccuracy, particularly at low neptunium concentration.

able sites (3.376 meq/L,⁵ accommodating 3.376 mM/L singly charged cations) is far in excess of the number of neptunium ions, so that such reactions have at best little, if any, effect on the sorption behaviour observed here.

The linearised Freundlich equations given in Figure 5.7 yield the constants n (slope) and K_F (intercept) as discussed before. The latter represents no reliable value, though, because the relatively short isotherms of two orders of magnitude had to be extrapolated quite far up to 10⁰ M Np(V) to identify the intercept.

⁵calculated from the CEC of 84.4 meq/100 g (cf. Table 4.1, page 91) for the solid-to-liquid ratio of 4 g/L

In spite of the significantly different sorption capacities for γ -Al₂O₃ and montmorillonite as recognisable from their K_d -values (see Section 5.1.5 below for details) the isotherms, viewed over the whole concentration range, show only little disparity. This is visualised in Figures 5.8 and 5.9. The difference on the log scale reflects the considerably lower number of sorption sites per gram for Np(V) on montmorillonite compared to γ -Al₂O₃ (e.g. 20 vs. 300 $\mu\text{g/g}$ at 10^{-6} M Np(V)).

Through the joint activities of the working group, a comparison of the isotherms of neptunium sorption on montmorillonite with that on kaolinite was possible. As presented in Figure 5.8, both clay minerals behave largely similar. Neptunium uptake by kaolinite is higher than by montmorillonite, since the relevant aluminol binding sites are accessible not only at the mineral edges like on montmorillonite, but also on one plane side of the octahedral sheet. The effect contributes by a factor of almost 2.

Similarly, the γ -Al₂O₃ data were compared to gibbsite, α -Al(OH)₃, for which an equally extended isotherm was measured; the results are shown in Figure 5.9. Like kaolinite, this experiment supports the precipitation of neptunium carbonate complexes at $\sim 3 \cdot 10^{-5}$ M Np(V) as well as a steady onset of saturation of the available binding sites. A considerably lower sorption on gibbsite compared to γ -Al₂O₃ by a factor of about 25 is observed, which agrees well with the significantly smaller surface area of 1.22 m²/g in respect to ~ 100 m²/g.

Literature data of sorption isotherms is rather scarce. A fairly small range of neptunium concentrations from 0.1 to $3.0 \cdot 10^{-5}$ M Np(V) was covered by Li

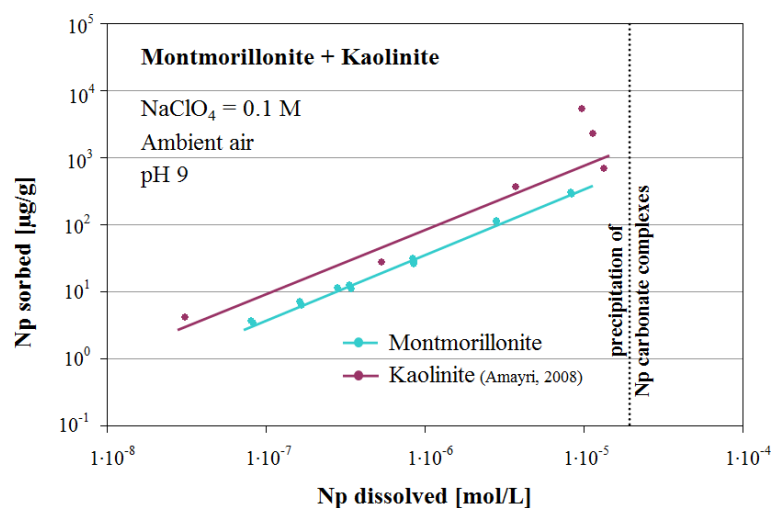


Figure 5.8: Neptunium sorption on two different clay minerals, the triple-layered montmorillonite and the double-layered kaolinite (experiment and data processing by Amayri, 2008).

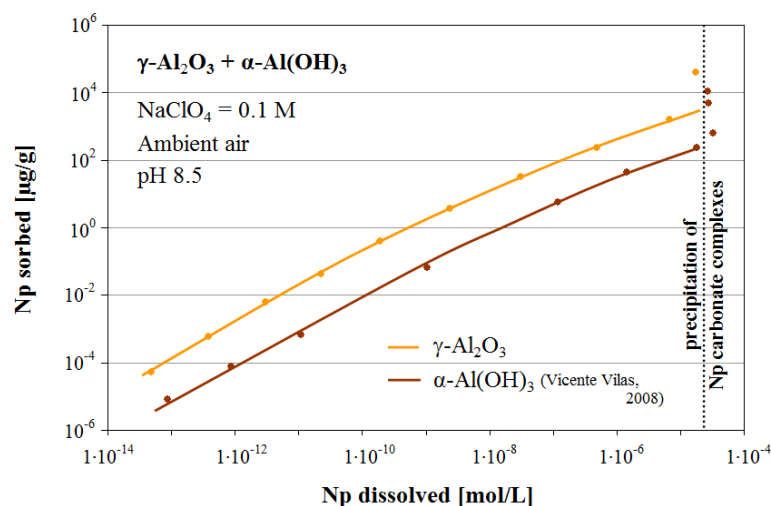


Figure 5.9: Neptunium sorption on aluminium oxide ($\gamma\text{-Al}_2\text{O}_3$) and aluminium hydroxide ($\alpha\text{-Al(OH)}_3$, gibbsite, studied by Vicente Vilas, 2008). The decreasing slope indicates the saturation of the available neptunium sorption sites.

and Tao (2003) for $\gamma\text{-Al}_2\text{O}_3$ at $\text{pH} \sim 4.5$. They observed a slope marginally above 1. Nagasaki and Tanaka (2000) measured an isotherm with 0.08 g/L montmorillonite at $\text{pH} 6$. Like in the present case, the slope equals 1 and is linear for 10^{-8} to 10^{-5} M neptunium.

As with the batch experiments, a direct, numerical comparison of different studies is only possible via the distribution coefficients. For example, the absolute sorption measured by Li and Tao (2003) around $1 \cdot 10^{-5}$ M Np(V) at $\text{pH} 4.5$, i.e. below the sorption edge, is more than 1.5 log units, respectively a factor of 30, higher than reported here for the same neptunium equilibrium concentration at $\text{pH} 8.5$, which is beyond the sorption edge. That might result from a larger surface area of their $\gamma\text{-Al}_2\text{O}_3$ compared to that used in this study, but it might also – instead or additionally – have been caused by the high solid-to-liquid ratio of 10 g/L. Only normalisation of the experimental conditions to K_d could provide the required mutual basis for the assessment, whether both experiments are comparable. The distribution coefficient can be calculated according to Equation 4.3.5, page 101, by inserting the amount of neptunium sorbed to the substrate and the dissolved equilibrium concentration, which are both given in the isotherm plot. Their relation must simply be multiplied by the respective liquid-to-solid ratio. The K_d calculated from the data by Li and Tao (2003) equals 1.4 for $\text{pH} 4.5$ and around $1 \cdot 10^{-5}$ M Np(V), as opposite to a K_d of 2.9 determined in the present study for the same neptunium equilibrium concentration but at $\text{pH} 8.5$. Compared to the batch results presented in Figure 5.15, page 138, the sorption determined by Li and Tao (2003) is well within the range of this work.

5.1.4 Neptunium Complexation by Carbonates

Some of the observations made during the batch experiments and isotherm studies provided strong hints that the dissolved neptunium is influenced by carbonate ligands originating from aerial CO_2 . The formation of soluble complexes was already mentioned in the discussion of the results above. The present section briefly summarises these indications and reflects on supportive studies on this topic published in literature.

At higher pH, i.e. above pH 8.5-9.0, the percentage of Np(V) sorbed decreases significantly under ambient air conditions (cf. Figure 5.1, page 121). Generally, the mineral surface becomes increasingly negative with pH, which would result in steadily more neptunyl cations being sorbed, as observed under exclusion of CO_2 . The prominent effect for the ambient air studies can be attributed to the formation of negatively charged aqueous neptunyl-carbonate complexes, which are repelled from the mineral surface. Precisely, the decrease in sorption results both from competition between surface groups and aqueous carbonate anions for cations in solution, as well as from competition for the sorption sites by carbon species (CO_3^{2-} , HCO_3^-) and aqueous neptunium species, as Turner et al. (2006) conclude from their extensive literature review.

A comparison of the sorption behaviour with the theoretical aqueous speciation of neptunium is shown in Figure 5.10 to aid the identification of likely surface species. From this calculation, the aqueous phase is dominated by the neptunyl ion over the whole acidic pH-range, but from around pH 7 on hydrolysis becomes progressively significant. While the share of the hydroxy species increases continuously under CO_2 -free conditions but remains rather insignificant even up to pH ~ 11 , the stability of the neutral species $\text{NpO}_2\text{OH}_{aq}$ reaches a maximum near pH 8.5 under ambient atmosphere. This apparently correlates with the observed sorption maximum giving rise to the hypothesis that the neptunium carbonate species formed progressively beyond this pH barely sorb to the mineral surface.

When comparing the different batches a discrepancy of sorption in the high pH-range becomes apparent. This is evident e.g. in Figure 5.2, page 122. With 0.1 M NaClO_4 , for example, still 30 % (μM), respectively 65 % (pM Np(V) concentration) of the total neptunium is sorbed on $\gamma\text{-Al}_2\text{O}_3$ at pH 10, while far less Np(V), i.e. 0 %, respectively 15 %, is taken up by montmorillonite at this pH. The higher sorption in case of the former, observed in the very early experiments, is ascribed to a smaller amount of $\text{HCO}_3^-/\text{CO}_3^{2-}$ in the suspension. This was applied due to the neglect of ionic-strength effects in the initial calculation with Visual MINTEQ. In the experiments with on $\gamma\text{-Al}_2\text{O}_3$ only 250 μL NaHCO_3 were added at pH 10, while in those with montmorillonite this was increased to

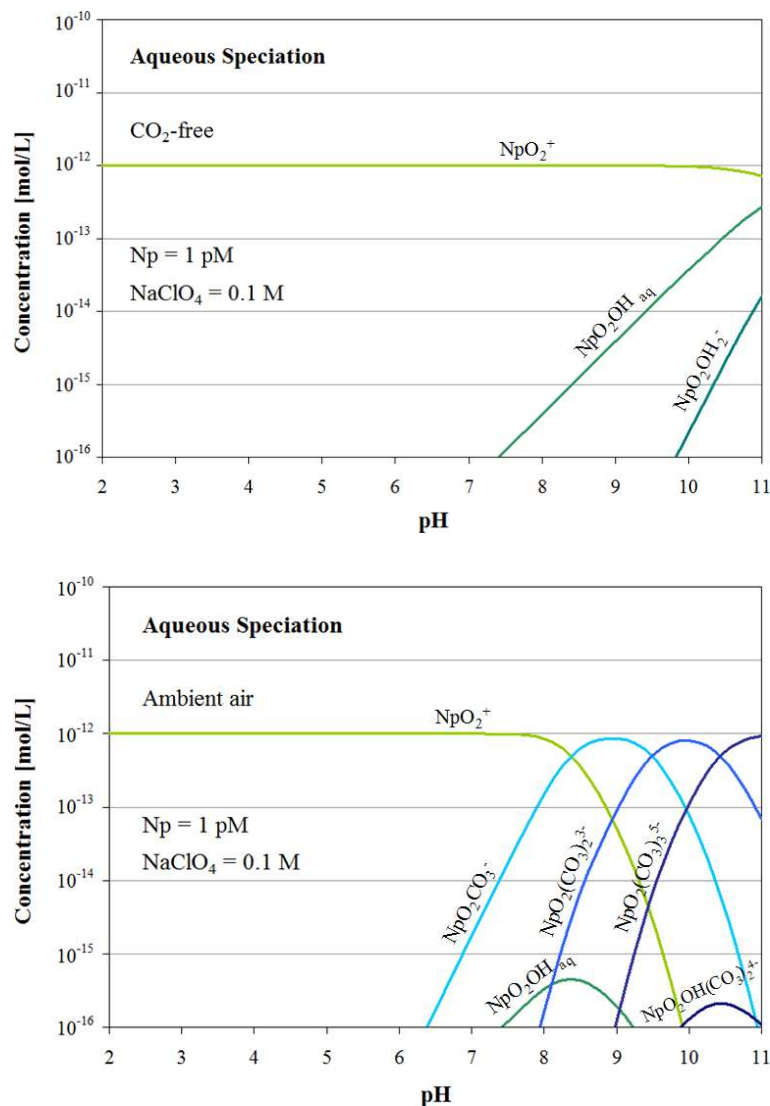


Figure 5.10: Aqueous speciation of neptunium in 0.1 M NaClO_4 in the absence and presence of ambient CO_2 , calculated with Visual MINTEQ.

$898.3 \mu\text{L NaHCO}_3$ plus additionally $2527 \mu\text{L Na}_2\text{CO}_3$. With the more appropriate amounts as applied in the later experiments, i.e. with montmorillonite, the sorption of Np(V) on $\gamma\text{-Al}_2\text{O}_3$ above $\text{pH} \sim 9.5$ is also expected to drop to zero like in the case of montmorillonite, indicated by the dashed line in Figure 5.2.

In the isotherm experiments, which were conducted at $\text{pH} 8.0, 8.5,$ and 9.0 , precipitation of neptunium was observed under ambient air conditions above $2\text{-}3 \cdot 10^{-5} \text{ M}$, giving rise to the assumption that it coprecipitated with the dissolved carbonate. Consultation of corresponding literature supports this hy-

pothesis: The maximum solubility of the sodium neptunium carbonate complex determined by Neck et al. (1994), displayed in Figure 5.11, matches the observed value.

In a workshop discussion the question was raised, whether variations of the CO_2 concentration in the laboratory air (due to e.g. different numbers of persons present or varying seasonal airing habits) could cause experimental errors. Although an effect cannot be precluded, the changeability of the ambient CO_2 is regarded largely neglectable, because it is much smaller than the influence of (variable) ambient CO_2 compared to a CO_2 -free atmosphere. Only a markedly increased CO_2 concentration enhances the aqueous neptunium fraction at high pH beyond the sorption maximum, but it does not influence the location of the sorption edge (Turner et al., 2006). However, the experimental conditions specified in the previous chapters should be more correctly worded “ambient air conditions of $\geq 10^{-3.5}$ bar CO_2 ”.

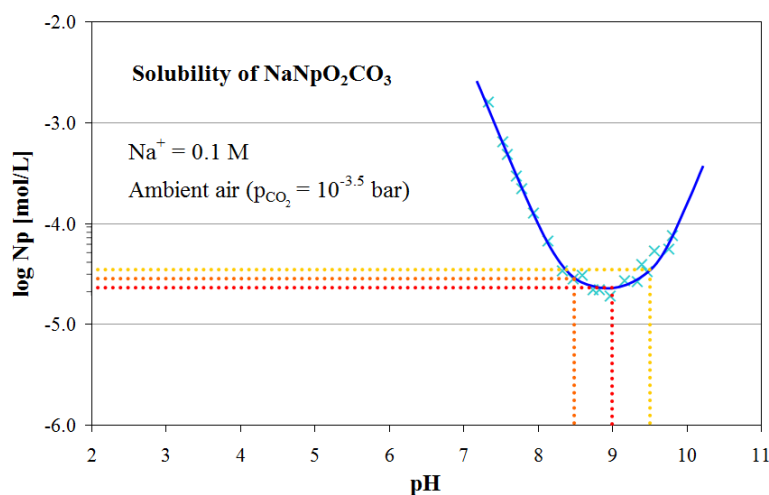


Figure 5.11: Solubility of solid $\text{NaNpO}_2\text{CO}_3$ in 0.1 M NaClO_4 as a function of pH; it increases with decreasing ionic strength (Neck et al., 1994). Around pH 9 aqueous neptunium carbonate complexes precipitate above $\sim 2 \cdot 10^{-5}$ M Np. The dotted lines mark the pH values of the isotherms measured in this study and their corresponding precipitation limits, which are depicted in their respective plots.

5.1.5 Distribution Coefficients

For validation of the present experiments on the basis of other studies the results of neptunium sorption were converted into K_d -values as described in Section 4.3.5. So far, published data of neptunium sorption on $\gamma\text{-Al}_2\text{O}_3$ are quite

scarce in literature, for montmorillonite it even proved difficult to identify any studies of at least comparable experimental conditions. The ones encountered are, nevertheless, presented here and collated to the findings of this study.

Figure 5.12 compiles the experimental results together with the modelled⁶ data for montmorillonite in ambient air. Again in both experimental series – as already pointed out in Section 5.1.2 – the effect of changes in ionic strength at $\text{pH} < 6$ should show up more pronounced in the experimental data. A difference of one decimal power in the NaClO_4 concentration should be reflected by an increase of ca. one $\log K_d$ unit in the acidic pH -range, where ion exchange processes dominate, as demonstrated by Bradbury and Baeyens (2006a). Only about one third to half of this value was determined in the present study below $\text{pH} 6$. This deviation is ascribed to the generally observed too low sorption values for the ionic strength of 0.01 M NaClO_4 .

Above $\text{pH} \sim 6$ neptunium sorption on montmorillonite met the expectations: The position as well as the height of the maximum sorption in this study largely correspond with the literature data. Typical $\log K_d$ values measured under exclusion of CO_2 range from -0.7 at $\text{pH} 2.6$ to ~ 3.8 at $\text{pH} 11.8$ (Ohe et al., 1993, cited in Turner, Pabalan and Bertetti, 1998). The distribution coefficients for CO_2 -free conditions determined in this study are very similar to those observed by scientists from the PSI (e.g. Bradbury and Baeyens, 2005, or Bradbury and Baeyens, 2006a). Researchers at Los Alamos, USA, published the only set of

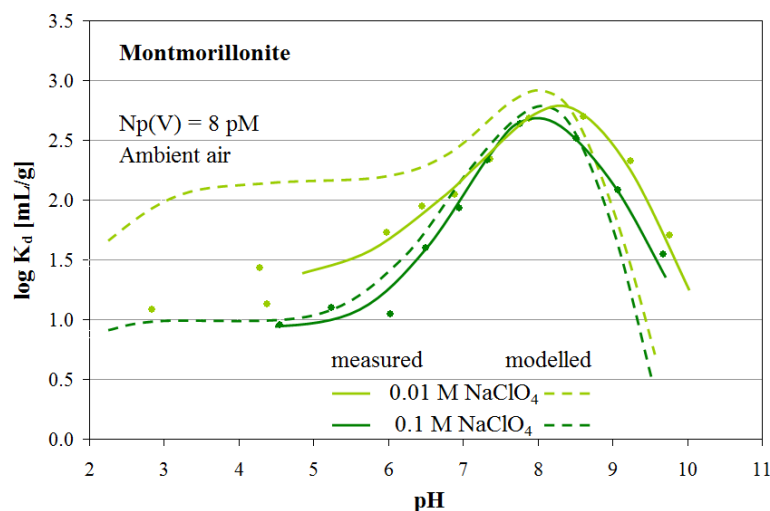


Figure 5.12: Measured (points and solid line) and modelled (dashed line) data for the sorption of picomolar neptunium on montmorillonite.

⁶Details on the modelling procedure and further calculations are presented in the third part of this chapter in Section 5.3 (page 158 ff).

experimental data under ambient air available in literature together with results from CO₂-free conditions. Data were taken in the micromolar concentration range at $9 \cdot 10^{-7}$ M neptunium in 0.1 M NaNO₃ and can be compared to the corresponding results of this work, as shown in Figure 5.13: The sorption maximum in ambient air observed by Bertetti, Pabalan, Turner and Almendarez (1996)⁷ amounts to a log K_d of approximately 2 and occurs at pH 8 to 8.5. Below pH 5.5 their distribution coefficients level off around 1. Thus, the American study is in reasonable agreement with the PSI data as well as with the present work.

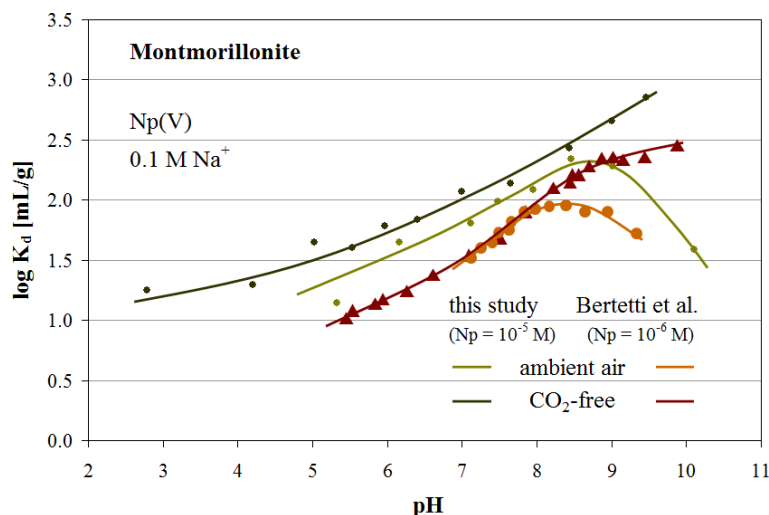


Figure 5.13: Distribution coefficients of micromolar neptunium sorption on montmorillonite for ambient air and CO₂-free conditions provided by Turner et al., 1998, respectively Bertetti et al., 1998, Los Alamos, USA, compared to this study.

An alternative for the assessment of the distribution coefficients is possible via sorption isotherms. Again, few studies on the influence of sorbate concentration have been published: The isotherm at pH 6 measured by Nagasaki and Tanaka (2000) for montmorillonite reveals values that are higher by ca. 0.7 in log K_d compared to the distribution coefficients determined in this work at maximum sorption (pH 8 and 9). The authors report that their values were one to three orders of magnitude larger than data published elsewhere (reference to batch experiments with smectite). The log K_d calculated from their data ($m/V = 0.08$ g/L) is ~ 4.4 corresponding to ~ 1.7 measured for pH 6 in this study, further supporting that the present data meet the literature.

⁷This data was also published in Turner, Pabalan and Bertetti (1998) and Bertetti, Pabalan and Almendarez (1998).

With maximum values around 3 and 4 for $\log K_d$ at micro- and picomolar neptunium concentration, respectively, the distribution coefficients measured for $\gamma\text{-Al}_2\text{O}_3$ are accordingly larger than those for montmorillonite, reflecting the results from the batch experiments discussed before. This is also in accordance with the sorption isotherm, from which the distribution coefficients of the picomolar batch should exceed those of the micromolar experiments. For visualisation of this relationship, the corresponding graph has been calculated in terms of K_d as function of neptunium equilibrium concentration; it is presented in Figure 5.14 showing a quite smooth curve. Due to progressive saturation of the sorption sites the K_d decreases from ca. 10^{-10} M on with increasing neptunium concentration.

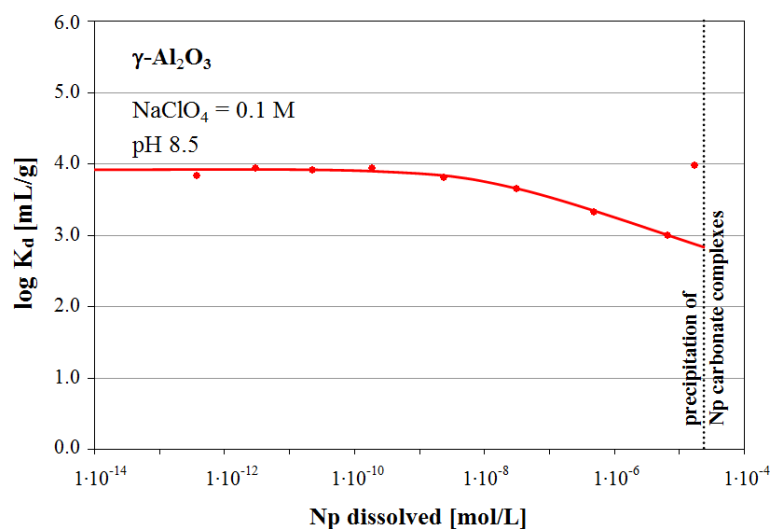


Figure 5.14: Distribution coefficient calculated for the $\gamma\text{-Al}_2\text{O}_3$ sorption isotherm.

Like for montmorillonite data of neptunium sorption on $\gamma\text{-Al}_2\text{O}_3$ is rare. Furthermore, most of the experiments reported are not directly comparable to this study. Only in few cases it was possible to convert the data to K_d values, when the required additional parameters were given; a comparison of these is presented in Figure 5.15. Righetto, Bidoglio, Marcandalli and Bellobono (1988), for example, present their results as percentage. This at least facilitates the determination of the sorption edge, which occurs at pH 7.3 in their experiments using $1 \cdot 10^{-14}$ M Np(V) and 0.2 g/L $\gamma\text{-Al}_2\text{O}_3$ ($130 \text{ m}^2/\text{g}$) at 0.1 M NaClO_4 . Calculated from the experimental parameters given in their paper this would correspond to a $\log K_d$ of 3.4 at pH 7.3. The maximum of 95 % sorption is reported there at pH 8.5 being equivalent to a $\log K_d$ of 3.7. This is very similar to the coefficients determined in this study, where a value of 3.6 can be extrapolated

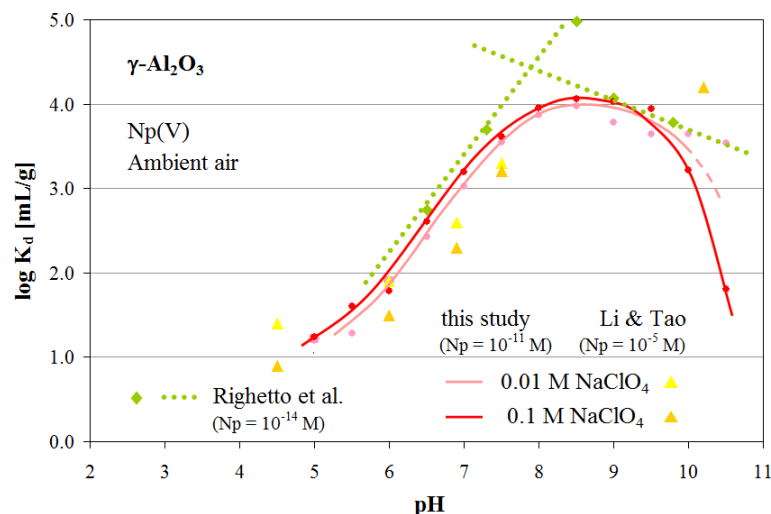


Figure 5.15: The distribution coefficients for $\gamma\text{-Al}_2\text{O}_3$ of this work in comparison with the studies by Li and Tao, 2003, and Righetto et al., 1988. The latter published two linear relations representing their experimental results.

from the measured isotherm (Figure 5.14) to the value of $1 \cdot 10^{-14}$ M Np(V). Additionally, the authors provide equations for their proposed linear relations of $\log N_{p_s}$ versus pH. Transferred to $\log K_d$ applying their solid-to-liquid ratio, the two lines intersect at ~ 4.5 at $\text{pH} 7.9$, which is in agreement with the findings of this study yielding maxima of ~ 4.0 for picomolar and ~ 3.0 for micromolar neptunium concentrations at slightly higher pH.

Li and Tao (2003), in contrast, found much higher distribution coefficients than expected from Figure 5.14 and no discrete maximum at $\text{pH} \sim 8.5$ (for Np(V) = $1 \cdot 10^{-5}$ M, $\text{NaNO}_3 = 0.01$ and 0.1 M). This could indicate that their $\gamma\text{-Al}_2\text{O}_3$ was not affected by saturation even at the high neptunium concentration applied – but similarly, this finding might be attributed to shortcomings of their experimental procedure; they remark, for example, that colloids were not removed from the equilibrium solution. This surmise would rather explain the large discrepancy between their and all other studies at high pH. Yet, the average $\log K_d$ -values of their isotherms at $\text{pH} 4.5$ and 4.6 (not shown) are 1.3 and 1.4 , respectively, which is within the range of variation of this work.

A further study by Yamaguchi, Nakayama and Yoshida (2004) must be considered with caution. They measured ambient air distribution coefficients for $\text{pH} 11.3\text{-}13.6$ and a neptunium concentration of $1 \cdot 10^{-6}$ M. Although the precipitation limit of neptunium carbonate complexes is clearly beyond this concentration in the pH-range applied (see Figure 5.11, page 134), their $\log K_d$ values of up to 5.1 are mysteriously high. Since these data are rather questionable and

since the pH is far outside the range addressed in this study, this publication is not used for reference.

Surface Normalisation

Sometimes it is helpful to relate the distribution coefficient to the surface area of the substrate to generate K_a [mL/m²], especially when comparing materials of largely different grain size. Thereby, not only experiments which use the same sorbent can be compared, but also those measuring the sorption of a sorbate on different solids: In general, the sorption process reveals no direct dependence on the surface characteristics of the sorbent such as point of zero charge, pH_{PZC} ⁸, or surface area, as Misaelides and Godelitsas (1999) state in their literature review. Thus, relating the distribution coefficients obtained from metal sorption on different minerals to their respective surface areas – i.e. calculating the K_a – indicates a similar site density among them (Turner et al., 2006).

As already pointed out, sorption primarily occurs on the mineral edges of montmorillonite (see Section 2.4.1), which make up about 10 % of the specific surface area (Turner et al., 2006), and $\gamma\text{-Al}_2\text{O}_3$ was chosen to represent the $\equiv\text{SOH}$ functional groups encountered there. Neptunium sorption, expressed as a mass-per-mass ratio, was expected to be significantly higher on the reference substance $\gamma\text{-Al}_2\text{O}_3$ than on montmorillonite, because in the former such sites are accessible all over the surface of the oxide. This hypothesis was confirmed within the present study, becoming obvious when comparing the different K_d values.

Due to inconsistencies of manufacturer information and own BET measurements, unfortunately no definite surface area could be determined for $\gamma\text{-Al}_2\text{O}_3$ (cf. Section 4.2.2). Hence, surface normalised data were only calculated and compared to literature for montmorillonite. The interpretation of results within the scope of this study, however, focusses on K_d values in order to ensure inclusion of all experiments and comparability among $\gamma\text{-Al}_2\text{O}_3$ and montmorillonite.

However, converting the K_d into K_a values (using 100 m²/g for $\gamma\text{-Al}_2\text{O}_3$ relying more on the manufacturer analyses for material characterisation than on the singular BET measurement) as shown in Figure 5.16, just for a brief impression, it becomes obvious that the density of sorption sites is – as expected – much higher on $\gamma\text{-Al}_2\text{O}_3$ than on montmorillonite. If only 10 % of the surface area specified for montmorillonite are considered, though, the corresponding

⁸This point describes the condition when the electrical charge density on a surface is zero. Below the PZC, the water donates more protons than hydroxide groups, and so the surface is positively charged attracting anions. Conversely, above this point, the surface is negatively charged attracting cations.

K_a increases by two orders of magnitude approaching 1.7 and 1.8 at picomolar neptunium concentration for 0.1 and 0.01 M NaClO_4 , respectively. This finding confirms the hypothesis that only $\sim 10\%$ of the surface of montmorillonite is accessed by neptunium. A complete coincidence of the curves occurs when assuming 5% of the surface area. The micromolar graphs, in contrast, should not be compared directly because of saturation effects on $\gamma\text{-Al}_2\text{O}_3$ at this high neptunium concentration indicated by the decreasing isotherm as presented and discussed above.

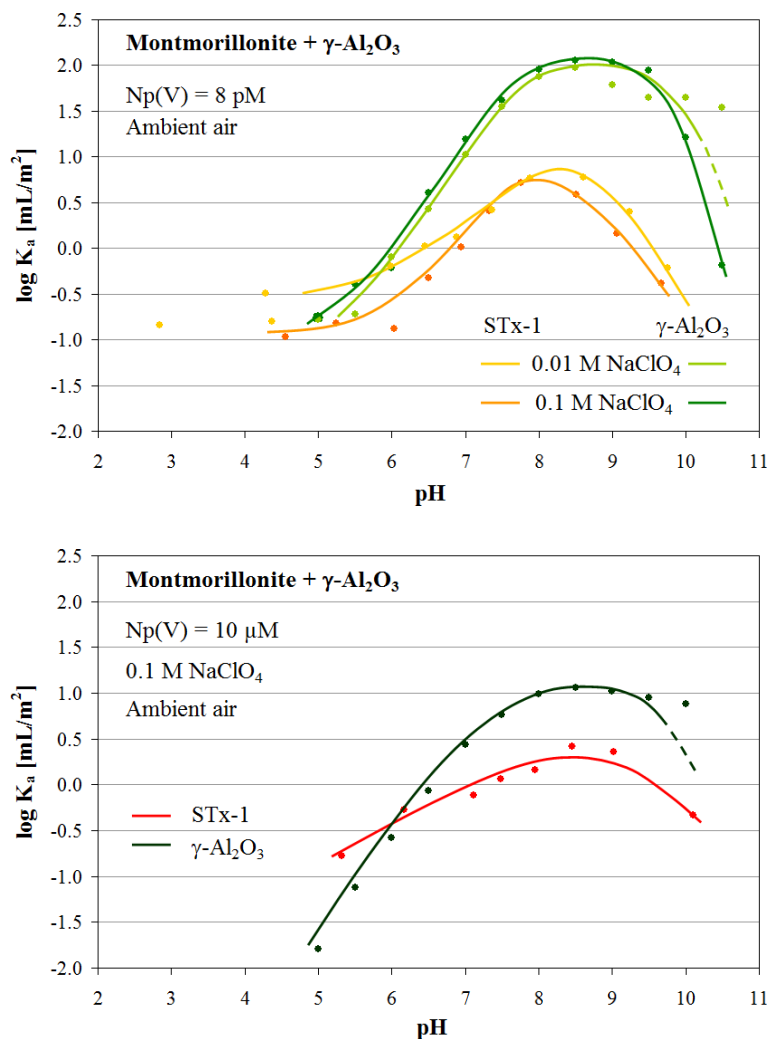


Figure 5.16: Surface normalised distribution coefficients K_a obtained in this study at picomolar (top) and micromolar (bottom) neptunium concentration, comparing sorption on montmorillonite and $\gamma\text{-Al}_2\text{O}_3$ in both cases.

5.2 Speciation

The identification of the neptunium species formed by sorption at the surface is everything but straightforward. Analyses of the molecules via EXAFS spectroscopy necessarily require some idea of the expected structure of the complex. Therefore, the information that can be deduced from theory as well as from the observed sorption behaviour are resumed first, before the experimental results are presented. Two suitable models for data analysis, accounting for sorption to a surface and for complexation by carbonate, respectively, were defined in advance based on the anticipated neptunium compounds.

5.2.1 Theoretical Implications

Based on the theoretical knowledge about the general sorption phenomena (Section 2.5.2) and the structure of the solids (Sections 2.4.1 and 2.4.2), different mechanisms are expected to govern neptunium sorption on montmorillonite and its reference substance $\gamma\text{-Al}_2\text{O}_3$. In both cases, surface aluminol groups facilitate chemical sorption, creating inner-sphere complexes. This process of specific sorption occurs above the point of zero charge (pH_{PZC}), when the NpO_2^+ ion can approach the surface and bind to the deprotonated $\equiv\text{SO}^-$ -groups. The pH_{PZC} is around pH 7.3 for conditioned Na-montmorillonite (according to titration measurements by Bradbury and Baeyens, 1995) and at pH 8.5 for $\gamma\text{-Al}_2\text{O}_3$ (Parks, 1965, cited in Brown et al., 1999). Thus, above the sorption edge, inner-sphere complexes should be present with the neptunyl ion retaining its inherent structure and the surface atoms should be visible in the EXAFS spectra. In the interlayer space of montmorillonite ion exchange processes are expected to occur, resulting in the formation of relatively loosely bound outer-sphere complexes independent of pH. They should constitute the only species in the acidic region and proportionally contribute to the overall signal at neutral to alkaline pH.

Inner- and outer-sphere complexes are distinguishable from each other by their different bond lengths of the equatorial oxygen atoms. While in the aquoion these are part of water molecules and form strongly ionic bonds with the neptunyl ion, they progressively become deprotonated with pH (see Figure 5.10). This results in a significant decrease in bond length, because by losing a proton the negative charge of the oxygen atom increases causing stronger attraction towards the positively charged neptunium atom. Similarly, inner-spherical sorption involving oxygen surface atoms yields shorter distances than typical for the aquoion. Experiments with U(VI), for example, revealed bond lengths of 2.41-2.43 Å at low pH and 2.34-2.38 Å at higher pH, which were attributed to the

formation of outer-sphere and inner-sphere complexes, respectively (Antonio and Soderholm, 2006).

Carbonate complexation, in return, results in lengthening of the equatorial bonds, since a chelate ring formed between neptunium, carbon, and the two shared oxygen atoms causes steric repulsion. Often a splitting of the coordination sphere is observed with inner-sphere sorption and/or carbonate complexation indicated by large values for σ^2 . – Since uranium and neptunium are known to behave analogously, the experimental findings for uranyl ions can be transferred to this study.

5.2.2 Indications from the Sorption Behaviour

The theoretical expectations are vividly reflected in the sorption curves of the batch studies presented above. For both substrates, specific sorption starts with the sorption edge. While below pH ~ 5 sorption is zero on γ -Al₂O₃, neptunium is sorbed on montmorillonite to a certain extent depending on the ionic strength. With EXAFS samples being chosen appropriately, this difference should be visible in the analyses, on the basis of distinctive bond lengths alterations and identity of neighbouring atoms.

A comparison of the sorption isotherms shows that site saturation becomes apparent on γ -Al₂O₃. This finding implies that also weak sites should be engaged – in contrast to montmorillonite, on which only strong sites are involved in neptunium sorption, according to literature (Bradbury and Baeyens, 2006a). A weaker sorption of neptunium on γ -Al₂O₃ than on montmorillonite would result in the neptunyl ion staying more contracted, thus being more similar to the aquoion compared to a strongly sorbed molecule. Depending on the ratio of binding to strong and weak sites, differences in the Np-O_{ax} and Np-O_{eq} bond lengths should be detectable by EXAFS.

5.2.3 EXAFS-data and Curve-fitting

To further investigate the role of the aluminol groups for the sorption of Np(V), the possible surface complexes formed on montmorillonite and γ -Al₂O₃ were examined by EXAFS spectroscopy. Via the provision of complementary information about the molecular environment of the sorbed neptunium, these studies should allow for the differentiation between possible inner- and outer-sphere sorption complexes.

To obtain the EXAFS spectra, five to 26 (depending on sample quality and beamline parameters) separate scans were averaged and processed. It was taken

care to treat all sets as similar as possible to ensure maximum comparability of the fitted bond distances. Determined by the intercept points of EXAFS curve and abscissa, k_{min} was chosen at 2.50-3.00 \AA^{-1} and k_{max} at 9.45-9.75 \AA^{-1} . Taking the neptunyl ion as basis, the number of axial oxygen atoms was fixed at 2 and that of equatorial ones at 5. In certain cases (e.g. with the carbon and the second aluminium sphere), the quantity σ^2 of the Debye-Waller-factor had to be fixed (at 0.003 \AA^2) to achieve a proper termination of the iterations.

Figure 5.17 provides an overview of the major EXAFS results obtained within this study. EXAFS spectra of neptunium sorption samples on montmorillonite prepared at different pH under CO_2 -free conditions (left) are compared to the corresponding samples prepared under ambient air (right). A progressive alteration of their shape as function of pH becomes apparent in the latter case, but is not observed in the former. This finding is ascribed to the formation of neptunium carbonate complexes. These must be sorbed to the mineral surface, even though surface atoms could not be identified in the spectra, as will be discussed below. The explanation for this statement is the following: The samples were prepared as wet pastes containing 22.4 % solid phase (cf. Section 4.4.1) with either at least 70 ppm neptunium sorbed (at pH 7, see Table 4.4 on page 106) or alternatively a minimum of 5 % sorption from the initial neptunium concentration (at pH 5, see Figure 5.1, top, page 121) of $1 \cdot 10^{-5}$ M at most. Hence, numerical calculation gives that the neptunium sorbed to the mineral surface

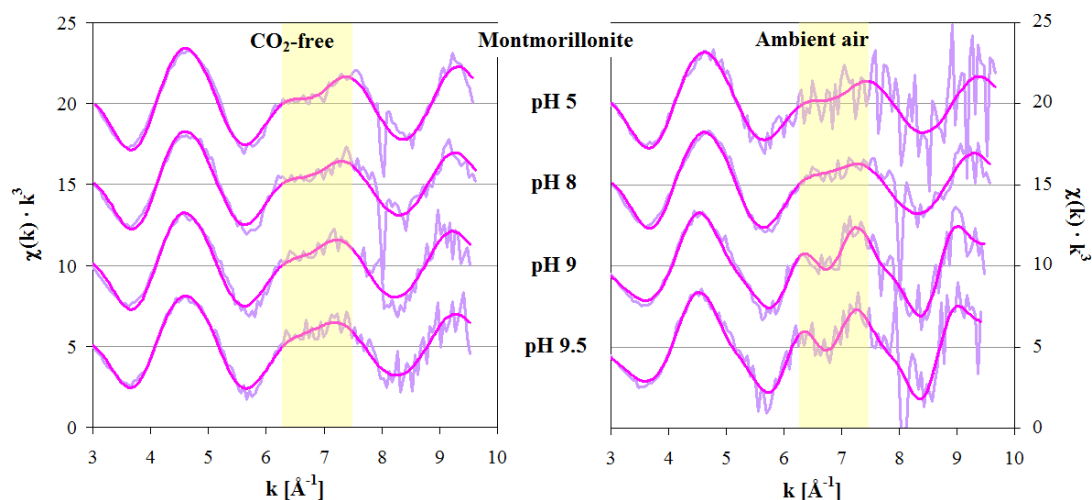


Figure 5.17: EXAFS raw data and fits of neptunium sorption samples on montmorillonite prepared as wet pastes in the absence and presence of ambient CO_2 . The range indicated in yellow denotes the region seemingly influenced by atmospheric CO_2 . At 8 \AA^{-1} a strong monochromator glitch is visible as experimental artefact.

within the wet paste sample is at least nine times in excess of that present in the liquid portion. In the region relevant to the influence of CO_2 at $\text{pH} > 8$, however, sorption amounts to ~ 140 ppm and 40 %, respectively, yielding almost 30 times more neptunium bound to the solid phase than dissolved in the surrounding solution. Since the EXAFS signal is an average over all species of the absorbing atom present in the sample (Reich, 2005), any well distinguishable alteration in the EXAFS spectra under the influence of atmospheric CO_2 , thus, must be ascribed to the sorbed portion, i.e. the formation of ternary surface neptunyl carbonate complexes. So far, such complexes have already been found for uranium sorption on montmorillonite (e.g. Catalano and Brown, 2005) or neptunium sorption on hematite (Arai et al., 2007), but no study investigating such neptunium complexes on montmorillonite has been published yet.

A neptunyl-carbonate model⁹ (Volkov et al., 1981) was applied to calculate the number of neighbouring atoms and the corresponding distances iteratively towards best fit. The Fourier transformations of the data presented in Figure 5.17 are shown in Figure 5.18. It reveals in all cases two distinctive peaks at 1.83 ± 2 and $2.53 \pm 3 \text{ \AA}^{10}$, that can be attributed to the two axial and five equatorial oxygen atoms. These coordination numbers were predefined by the chemical structure of the assumed linear actinyl unit and corresponding theoretical calculations (e.g. Tsushima and Suzuki, 2000) of the energetically most likely equatorial configuration.

For the ambient air data at $\text{pH} 9$ and 9.5 a significantly different structure to the other plots is observed around values of $(R + \Delta) = 2.4$ to 4 \AA . An inclusion of 2, respectively 2.3 carbon atoms at $\sim 3.00 \text{ \AA}$ in the fit was tested together with the consideration of a distal oxygen atom of the carbonate group at $\sim 4.24 \text{ \AA}$. In this way a quite perfect approximation of the structure was obtained. This interpretation of the experimental observation as a structural change in the sorbed species only at relatively high pH is supported by literature: Atmospheric levels of CO_2 revealed no influence on neptunium sorption on clays at $\text{pH} < 8$ (Turner, Pabalan and Bertetti, 1998).

The compilation of the EXAFS spectra and the suitable reproduction by the fit routine using very reasonable assumptions strongly confirm that the neptunium retains its fifth oxidation state. Under all chosen conditions the Np-O_{ax} bond length stays constant, reflecting the similar oxidation state of the metal. In the hexavalent neptunyl ion, for example, it would be $\sim 0.14 \text{ \AA}$ shorter than in the pentavalent NpO_2^+ (Burns and Musikas, 1977, cited in Gutowski et al.,

⁹The model parameters for which the corresponding *feff* input files were calculated are O_{ax} 1.79 \AA , O_{eq} 2.55 \AA , C 2.92 \AA , and O_{dist} 4.20 \AA .

¹⁰The precise distance can not be extracted from the graph directly, since it includes the phase shift of $\sim 0.5 \text{ \AA}$ (see Section 3.2.3).

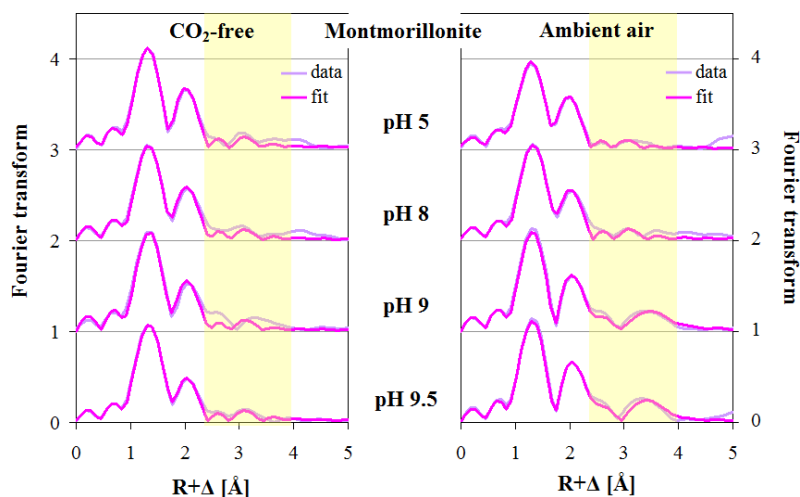


Figure 5.18: Fourier transforms of the samples shown in the previous figure (phase shift $\Delta \approx 0.5 \text{ \AA}$). The influence of CO_2 becomes visible through the broad peak between 3 and 4 \AA (yellow shaded) in the ambient air samples at pH 9 and 9.5, which can be attributed to the distal oxygen atom.

2006). Somewhat in contradiction to the findings of the present study Sabodina et al. (2006) report that on the surface of bentonite, which also contains other (reducing) minerals than montmorillonite, neptunium solely sorbed as Np(IV) , while in the pore water Np(V) was present, too.

A synoptic view of the determined bond distances and the corresponding fit parameters is provided in Table 5.1. Unfortunately, a low signal-to-noise ratio hampered the determination of the distance between neptunium and the surface atoms – i.e. Al – in most cases. Nevertheless, the structure of the neptunyl ion itself provides certain indications of how it is bound to the surface. Apparently, at pH 5 the sorbed complex is slightly more contracted – similar to the neptunium aquoion – than at higher pH, which points towards outer-spherical sorption at low pH developing into predominantly inner-spherical sorption beyond the sorption edge.

The bond distances determined by theoretical calculations (e.g. Balasubramanian and Cao, 2007, or Gagliardi and Roos, 2002) are given in Table 5.2; they are complemented by experimental literature data. The two calculated values for the distances of the two axial oxygen atoms in the neptunyl aquoion are 1.77 and 1.81 \AA . The corresponding experimental data vary from 1.80 to 1.85 \AA . For the equatorial oxygen atoms only one theoretical value is available in literature, namely 2.52 \AA . The respective experimental distances appear shorter with 2.44 to 2.51 \AA . In three of the four experiments, five equatorial oxygen atoms were fit to the data, while in the fourth only 3.6 atoms were determined, for

Table 5.1: Bond distances [\AA], ΔE_0 [eV], and χ^2 determined for the montmorillonite EXAFS samples (Np loading in [ppm]). The inaccuracy of O_{ax} is 0.01\AA , of O_{eq} and C 0.02\AA , and of O_{dist} 0.03\AA . The number of C-atoms, N_C , varies by 0.5 and 0.8. $N_{O_{ax}}$ is fixed at 2, $N_{O_{eq}}$ at 5, and $N_{O_{dist}}$ is linked to N_C . The σ^2 of the Debye-Waller-factor ranges from 0.002 to 0.005\AA^2 for O_{ax} , from 0.011 to 0.016\AA^2 for O_{eq} , from 0.003 to 0.006\AA^2 for O_{dist} , and is fixed at 0.003\AA^2 for C.

pH	CO ₂	Np	O _{ax}	O _{eq}	C	N _C	O _{dist}	ΔE_0	χ^2
5.0	no	408	1.83	2.52				-7.6	0.27
	yes	81	1.81	2.50				-8.7	1.76
8.0	no	165	1.84	2.53				-6.1	0.38
	yes	139	1.84	2.51				-7.0	0.49
9.0	no	314	1.85	2.54				-5.7	0.34
	yes	166	1.84	2.55	3.00	2.0	4.23	-8.0	0.42
9.5	no	416	1.84	2.51				-7.4	0.32
	yes	139	1.84	2.55	3.00	2.3*	4.24	-8.5	0.99

* The fact that N_C is not an integer reflects the overlapping of two or more species at this pH, as indicated in Figure 5.20.

which the authors could provide no explanation. The three neptunium carbonate complexes – mono-, bi-, and tri-carbonate – were theoretically calculated in two studies and synthesised for experimental analysis once. While the distances of the axial oxygen atoms agree reasonably well, the variations in the equatorial bond lengths are considerably larger, e.g. from 2.40 to 2.49\AA in the mono-carbonate complex. In the theoretical data, the distances of the oxygen atoms in the equatorial plane increases with the number of bound CO₃-groups, while this relation is somewhat less pronounced in the experimental data. Their number $N_{O_{eq}}$ increases from mono- via bi- to tri- carbonate from 5 to 6-7. The bond lengths of the carbon and the distal oxygen atoms do not allow for the determination of any systematic behaviour. Instead their position seems to be influenced by the overall structure of the molecule in question.

Estimation of Fit Quality

The quality of the fit is described by the reduced error parameter χ^2 . In EXAFS-PAK this is calculated as the squared differences of the ratio of deviation Δ , squared, between the experimental and the fitted values divided by the squares

Table 5.2: Literature data on bond distances [\AA] of the neptunyl aquoion and carbonate complexes comparing theoretical calculations and experimental values. $N_{O_{ax}}$ was always fixed at 2.

Molecule	O_{ax}	O_{eq}	$N_{O_{eq}}$	C	N_C	O_{dist}	$N_{O_{dist}}$	Source
NpO_2^{+*}	1.77	†	5					Gagliardi and Roos, 2002
NpO_2^{+*}	1.81	2.52	5					Tsushima and Suzuki, 2000
NpO_2^{\dagger}	1.85	2.50	5±1					Allen et al., 1997
NpO_2^{\dagger}	1.80	2.44	5					Antonio et al., 2001
$\text{NpO}_2^{+\diamond}$	1.85	2.51	~5					Combes et al., 1992
NpO_2^{\dagger}	1.82	2.49	3.6					Reich et al., 2000
$\text{NpO}_2(\text{CO}_3)^{-*}$	1.83	2.40-2.41	5	2.84	1	4.10	1	Balasubramanian and Cao, 2007
$\text{NpO}_2(\text{CO}_3)_2^{3-*}$	1.84	2.43-2.56 [#]	5	2.89	2	4.16	2	
$\text{NpO}_2(\text{CO}_3)_3^{5-*}$	1.86	2.50-2.55	6	2.96-2.98	3	4.24-4.26	3	
$\text{NpO}_2(\text{CO}_3)^{-*}$	1.86	2.46	5	2.95	1	4.22	1	Gagliardi and Roos, 2002
$\text{NpO}_2(\text{CO}_3)_2^{3-*}$	1.85	2.55	6	2.89	2	4.24	2	
$\text{NpO}_2(\text{CO}_3)_3^{5-*}$	1.88	2.60	6	2.97	3	4.36	3	
$\text{NpO}_2(\text{CO}_3)^{-}$	1.84	2.49	4-5	2.94	<2	4.24	n/a	Clark et al., 1996
$\text{NpO}_2(\text{CO}_3)_2^{3-}$	1.85	2.48	6-7	2.93	<2.5	4.18	1.5	
$\text{NpO}_2(\text{CO}_3)_3^{5-}$	1.86	2.53	6-7	2.98	2.7	4.18	3	

* theoretical calculation; † value not given; \diamond sorbed on goethite; # smallest distance for O connected to C, largest for hydrated O.

of the experimental values and the degrees of freedom (i.e. the number of data points minus the number of adjustable variables):

$$\chi^2 = \frac{\sqrt{\sum k^6 (\chi_{ex} - \chi_{th})^2 / \sum k^6 \chi_{ex}^2}}{n - v} \quad (5.1)$$

where χ_{ex} and χ_{th} are the experimental and the theoretical values of the EXAFS, n is the number of data points, and v the number of adjusted variables. These values are indicated in all tables presenting the fit results of this study, e.g. in Table 5.1. This definition of χ^2 , as given in George and Pickering (1995), deviates significantly from the traditional χ^2 expression, where Δ^2 is divided by the errors:

$$\chi^2 = \sum_{i=1}^k \frac{(x_i - \mu_i)^2}{\sigma_i^2} \quad (5.2)$$

with x_i being the observed and μ_i the expected value, and σ_i the experimental error of the i^{th} data point. While with purely statistical errors χ^2 should ideally approach unity (Vlaic and Olivi, 2004), a considerably lower value well below one is obtained in EXAFSPAK, since fit and experimental data may produce values even below unity after division by the number of degrees of freedom. Thus, the minimal achievable ‘ideal’ χ^2 value from the program used here (EXAFSPAK, subroutine OPT) depends on the experimental conditions and cannot absolutely be quantified mathematically. Practically, χ^2 should just approach a lowest possible value with the presently applied conditions.

Nevertheless, the value of χ^2 generated by EXAFSPAK still gives a reasonable measure for the quality of the fit. Comparing the individual values of Table 5.1, for example, primarily the fit for the ambient air sample of montmorillonite at pH 5 yields a high χ^2 – which does not necessarily mean that the fit is rather poor, but can clearly be attributed to the low neptunium load of only 81 ppm resulting in a correspondingly low signal-to-noise ratio. However, also a wrong calculation of standard deviations has an impact on the χ^2 .

Recently, research on error analysis and interpretation in X-ray absorption spectroscopy has been intensified. The interested reader is, for example, referred to the LASE software, written by Curis (2006). Its application in the context of this study, however, had to be abandoned, because the Windows version is still under constructions, and the documentation is presently available in French only.

5.2.4 Structure of the Neptunium Carbonate Surface Complexes

The EXAFS analyses yield a bidentate coordination of the carbonate ion with NpO_2^+ at high pH as shown in Figure 5.19. The corresponding Np-C distance is given by Clark, Conradson, Ekberg, Hess, Neu, Palmer, Runde and Tait (1996) as 2.93 to 2.98 Å for CO_3 -ligands. In the samples studied in this work the carbonate complexes formed at pH 9 and 9.5 have 2 to 2.3 CO_3 -ligands with Np-C distances of 3.00 Å, while all other samples contain no carbon and are similar to the Np(V)-aquoion (cf. Tables 5.1 and 5.2).

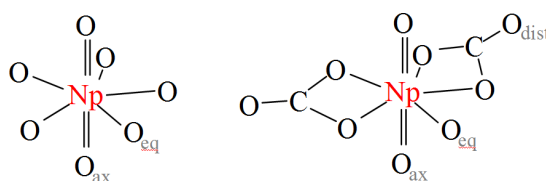


Figure 5.19: Molecular structure of the neptunyl aquoion (left) and bicarbonate (right). O_{ax} – axial oxygen (double bond), O_{eq} – equatorial oxygen (single bond), C – carbon, O_{dist} – distal oxygen of the carbonate group.

The number of carbon atoms present in the identified complexes should reflect the aqueous neptunium speciation shown in Figure 5.20. The only sample, for which that expectation properly applies is the one at pH 8.0 with $N_C = 0$, while those at pH 9.0 and 9.5 exhibit higher coordination numbers of $N_C = 2.0$ and 2.3 than predicted by the diagram giving 0.15, 1.05, and 1.5 carbon atoms, respectively. This finding could be attributed to the still doubtful thermodynamic data (see Section 3.3) or still inaccurate, i.e. too high, additions of $\text{NaHCO}_3/\text{Na}_2\text{CO}_3$ (cf. Sections 4.2.5 and 5.1.4). Equally, an elevated CO_2 concentration in the laboratory air could have somewhat altered the aqueous speciation like exemplified in Figure 5.21: When the CO_2 partial pressure increases, the carbonate equilibrium is shifted towards lower pH. Thus, e.g. at pH 8.5 already more than 60% of the neptunium are present as monocarbonate complex and 10% are even bound by two carbonate ligands, when the CO_2 partial pressure is doubled.

Nevertheless, the existence of ternary neptunyl carbonate surface complexes is unequivocally demonstrated, even though the applied model does not provide for the analysis of aluminium surface atoms to prove the chemical bond directly. An evidence of neptunium carbonates present in the wet paste sample, however, strongly implies the existence of such surface complexes, because the fraction of neptunium sorbed is in great excess of the dissolved fraction, as discussed above.

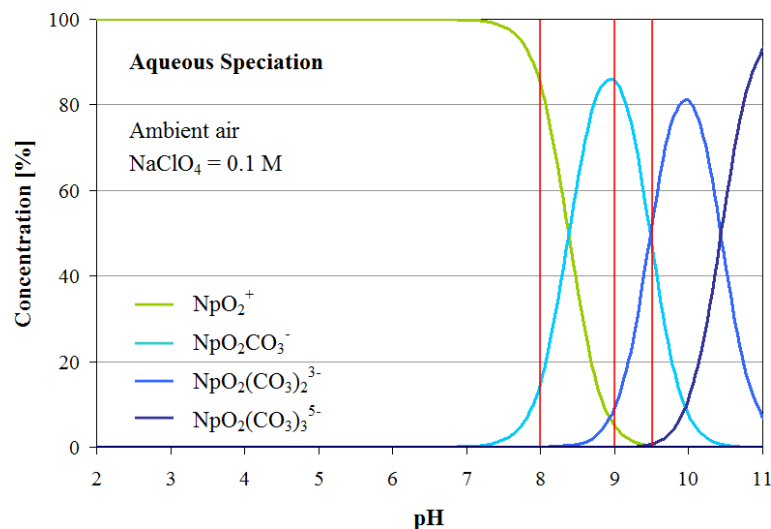


Figure 5.20: Aqueous neptunium speciation under ambient air conditions. The red lines mark the pH-values of the EXAFS samples. At pH 8.0 only 15 % of the neptunium should be present as monocarbonate complex. At pH 9.0 this makes up 85 %, while 10 % form bicarbonate complexes. At pH 9.5 both complexes constitute 50 % each. The tricarbonate complex becomes relevant only beyond pH 9.5.

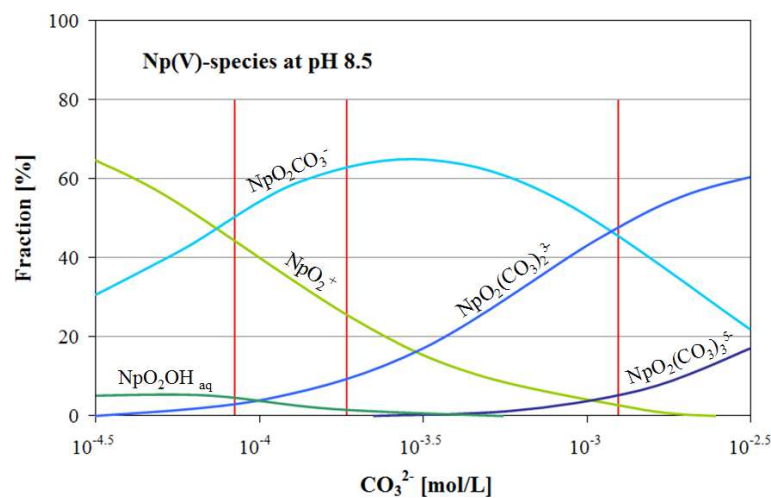


Figure 5.21: Influence of the carbonate concentration on the aqueous neptunium speciation under ambient-air conditions at pH 8.5 and 0.2 M NaClO₄ according to Bidoglio et al., 1985. The left red line indicates the CO₃²⁻-concentration under ambient air of 10^{-3.5} bar CO₂, calculated with Visual MINTEQ. The middle line denotes the dissolved CO₃²⁻-concentration under twice this partial pressure, and the third line marks the value for 0.5 % CO₂, which is the maximum allowable concentration at a workplace.

5.2.5 Insights into the Sorption Mechanism

Although inner-spherical sorption can definitely be anticipated from the batch experiments as well as from the molecular structure of the neptunyl unit, no Np-Al interaction could be identified in the EXAFS data of the montmorillonite samples. The structural parameters obtained, however, do not contradict a monodentate bonding of Np(V) to aluminol (or silanol) surface groups; merely, the atomic distance would be too large to be identified in the data, which are rather noisy beyond $\sim 4 \text{ \AA}$. To overcome this problem a larger set of data and/or preciser measurements would be necessary.

5.2.6 EXAFS on $\gamma\text{-Al}_2\text{O}_3$ – Reliability Test of the Results

The reproducibility of the experimental and analytical method was assessed through the independent preparation of two times three alike samples of $\gamma\text{-Al}_2\text{O}_3$ prepared at pH 8.5 under ambient air or CO_2 -free conditions, respectively, and investigated during different beamtimes in November 2006, March 2007, and May 2007. The outcome of this test is presented in Figure 5.22 and Table 5.3. Apparently, the CO_2 -free sample measured in November 2006¹¹ does not agree with all others. Most striking is the very different energy shift of 1.5 eV compared to -13.0 to -18.1 eV of the other samples. Therefore, it was attempted to fix this value at the average of 16.1 eV, but with this limitation the program yielded no sensible results. O_{ax} levelled off at 1.80 \AA matching its ambient air counterpart. However, the experimental curve could roughly be reproduced only with O_{eq} also fixed, e.g. at 2.44 \AA , but in this way χ^2 increased to 2.97. Due to these complications the first approach with free floating ΔE_0 -value during the iteration process was given preference.

Apart from the first CO_2 -free sample, all five other EXAFS spectra are largely similar at least up to $k = 6.5 \text{ \AA}^{-1}$. Still, the extracted bond distances scatter notably. Disregarding the first CO_2 -free sample, O_{ax} of the two others agrees well with 1.83 and 1.82 \AA from the central neptunium atom. O_{eq} by contrast varies somewhat more, yielding 2.41 vs. 2.45 \AA . Among the ambient air samples the first one proves dissimilar to its analogues, too. While the latter reveal both atomic distances of 1.85 \AA for the distance of O_{ax} and 2.45, respectively 2.48 \AA for O_{eq} , the bond lengths of the first sample are with 1.80 and 1.41 \AA shorter by approximately 0.05 \AA . The discrepancies of the two samples

¹¹When this sample was measured the synchrotron beam current was very low due to technical problems, which resulted in a strongly impaired signal. The ambient air sample of the same date was affected as well, but less severely; it just becomes very noisy above $k \approx 8.5 \text{ \AA}^{-1}$, respectively at $R > 3 \text{ \AA}$.

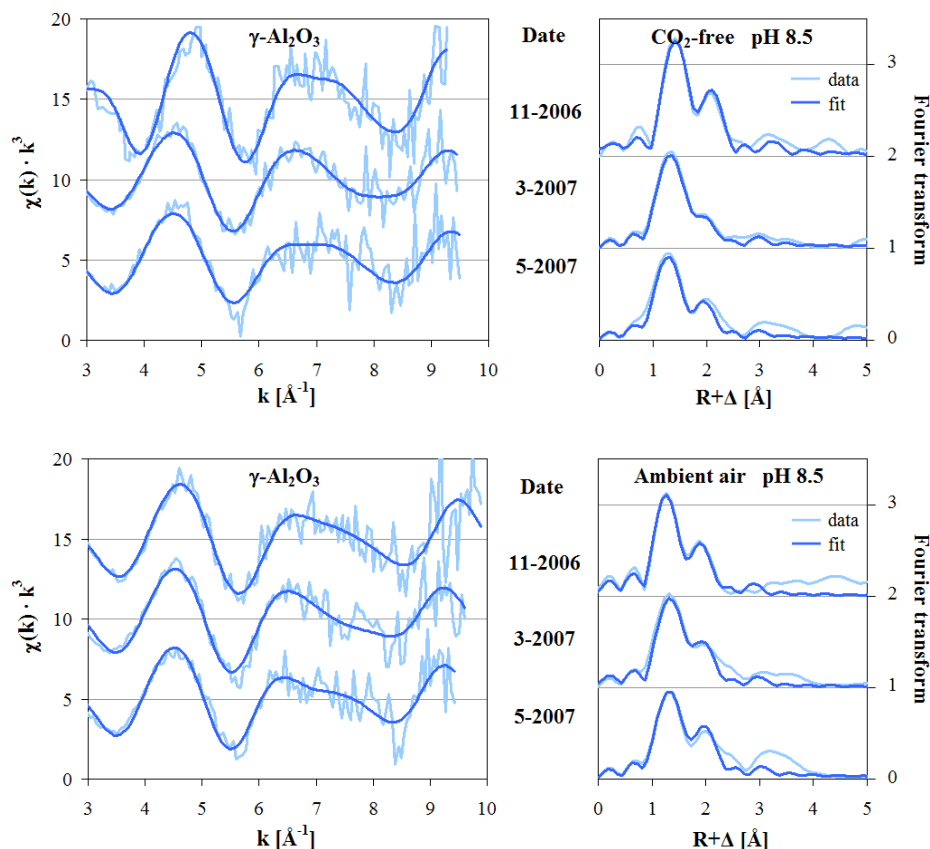


Figure 5.22: EXAFS raw data and fit (left) with their corresponding Fourier transforms (right) of three different $\gamma\text{-Al}_2\text{O}_3$ samples prepared at pH 8.5 under exclusion of CO_2 (top) compared to the same samples prepared under ambient air conditions (bottom).

measured in 2006 are ascribed to facility malfunction, corresponding to very low and unstable beam current. Since no such technical difficulties were encountered with all other samples, these latter data are regarded reliable within the errors given.

With respect to the Fourier transforms, a larger discrepancy in the R -range above ca. 3.8\AA can be generally noticed among the ambient air samples compared to those of CO_2 -free constitution. Within the former, the last sample differs from the two others in that it shows a broad peak between 3 and 4\AA similar to those, which have been interpreted as distal oxygen atoms of the carbonate groups in the montmorillonite samples (see above). At pH 8.5 the formation of neptunyl carbonate complexes is possible as already discussed and shown in Figure 5.21. Additional consideration of C (2.94\AA , $N_C = 1.4$) and O_{dist} (2.94\AA) improved the χ^2 of the fit by -0.08 .

Table 5.3: Reproducibility test of the EXAFS analysis. Bond distances [\AA], ΔE_0 [eV], and χ^2 were measured in identical $\gamma\text{-Al}_2\text{O}_3$ samples at pH 8.5 and 0.1 M NaClO_4 (Np loading in [ppm]), which were prepared and analysed independently. The inaccuracy of O_{ax} is 0.01\AA and of O_{eq} 0.02\AA . σ^2 of the Debye-Waller-factor ranges from 0.003 to 0.008\AA^2 for O_{ax} and from 0.009 to 0.013\AA^2 for O_{eq} .

Date	CO ₂	Np	O _{ax}	O _{eq}	ΔE_0	χ^2
Nov '06	no	314	1.87	2.51	1.5	1.30
Mar '07	no	437	1.83	2.41	-18.1	0.56
May '07	no	418	1.82	2.45	-16.3	1.04
Nov '06	yes	408	1.80	2.41	-16.3	1.57
Mar '07	yes	382	1.85	2.45	-13.9	0.72
May '07	yes	407	1.85	2.48	-13.0	0.83

Alternative Model for the Fit Procedure

Further samples were prepared at pH 9.5 to obtain a clearer information of the impact of CO₂ on the Np(V)- $\gamma\text{-Al}_2\text{O}_3$ system and, of course, to produce a reference for the EXAFS spectroscopy on montmorillonite. A comparison of the extracted bond lengths for pH 8.5 and 9.5, in both cases under ambient air and CO₂-free conditions, is provided in Table 5.4. In the ambient air sample, 1.7 carbon atoms could be fitted at a distance of 2.97\AA . The assumed distal oxygen atoms, however, already appear in a distance of $3.81 \pm 0.02 \text{\AA}$ from the neptunium atom. Since this is much closer than the model expectation (4.20\AA), such a value for the coordination sphere rather suggests a different complex. The soddyite¹² model based on Demartin et al. (1992), for example, comprises two silicon spheres – exchangeable against aluminium owing to similar Z – at 3.16 and 3.80 , and the O_{eq} distance is shorter here (2.31\AA) compared to the carbonate model (2.55\AA). The inclusion of these spheres changed the Np-O_{ax} and Np-O_{eq} distances by not more than 0.03\AA . The complete analysis of the data using this model is presented in Table 5.5.

The best fit of these data could be obtained assuming 0.5 and 1 aluminium atoms, respectively, while one sample yielded an optimum χ^2 with coordination numbers of 1 and 1.5. A visual comparison of the two models is given in Figure 5.23 exhibiting a rather similarly good reproduction of the experimental

¹²(UO₂)₂(SiO₄)·2(H₂O); the molecular structure is transferable to a neptunium-aluminium oxide compound.

Table 5.4: Bond distances [\AA], ΔE_0 [eV], and χ^2 measured in the $\gamma\text{-Al}_2\text{O}_3$ EXAFS samples (Np loading in [ppm]) using the carbonate model. The inaccuracy of O_{ax} amounts to 0.01\AA , of O_{eq} and C to 0.01\AA , of O_{dist} to 0.02\AA , and of the number of C-atoms, N_C , to 0.2. Again, $N_{O_{ax}}$ is fixed at 2, $N_{O_{eq}}$ at 5, and $N_{O_{dist}}$ is linked to N_C . σ^2 ranges from 0.001 to 0.003\AA^2 for O_{ax} , from 0.010 to 0.012\AA^2 for O_{eq} , is 0.015\AA^2 for O_{dist} , and fixed at 0.003\AA^2 for C.

pH	CO ₂	Np	O_{ax}	O_{eq}	C	N_C	O_{dist}	ΔE_0	χ^2
8.5	no	437	1.83	2.41				-18.1	0.56
	yes	382	1.85	2.45				-13.9	0.72
9.5	no	638	1.86	2.47				-13.7	0.15
	yes	583	1.86	2.51	2.97	1.7	3.81	-13.3	0.18

Table 5.5: Fit parameter for the soddyite model to the $\gamma\text{-Al}_2\text{O}_3$ EXAFS samples (Np loading in [ppm]). The inaccuracy of O_{ax} amounts to 0.01\AA , of O_{eq} to 0.02\AA , of Al-1 to 0.02\AA (1^{st} sample 0.1), of Al-2 and Np to 0.05\AA . $N_{O_{ax}}$ is fixed at 2, $N_{O_{eq}}$ at 5, and N_{Al} and N_{Np} are fixed at the numbers shown. σ^2 ranges from 0.002 to 0.004\AA^2 for O_{ax} , from 0.009 to 0.012\AA^2 for O_{eq} , and from 0.001 to 0.014\AA^2 for the other atoms; σ^2 of Al-2 is fixed at 0.003\AA^2 for the first three samples.

pH	CO ₂	Np	O_{ax}	O_{eq}	Al-1	N_{Al-1}	Al-2	N_{Al-2}	Np	N_{Np}	ΔE_0	χ^2
8.5	no	437	1.82	2.41	3.05	0.5	3.85	1	3.87	1	-15.3	0.53
	yes	382	1.82	2.42	3.12	1	3.78	1.5	3.99	2	-15.0	0.57
9.5	no	638	1.85	2.48	3.11	0.5	3.88	1	3.92	1	-11.1	0.16
	yes	583	1.85	2.51	3.19	0.5	3.80	1			-11.3	0.13

data. This impression is supported by the almost identical χ^2 values obtained for each curve.

In three of the four samples, however, the fit could further be significantly improved by allowing for a Np-Np interaction around 3.94\AA . This is somewhat surprising, since precipitation of neptunium should not be observed at the concentration applied in this study. The saturation indices for Np_2O_5 , however, turn positive at high neptunium concentrations and pH values, as shown in Figure 5.24. To rule out the eventuality of precipitation, identical montmorillonite samples with different neptunium loadings were prepared and analysed; their

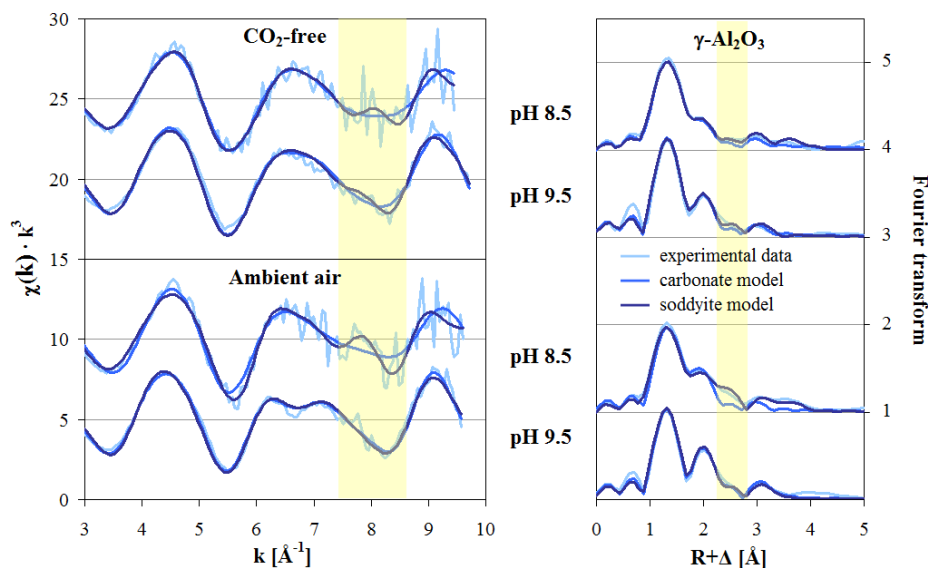


Figure 5.23: Fit of two different models on the EXAFS data of $\gamma\text{-Al}_2\text{O}_3$ samples (at pH 8.5; data from March 2007 because of the least noise among all samples). The zone highlighted in yellow marks the area in question.

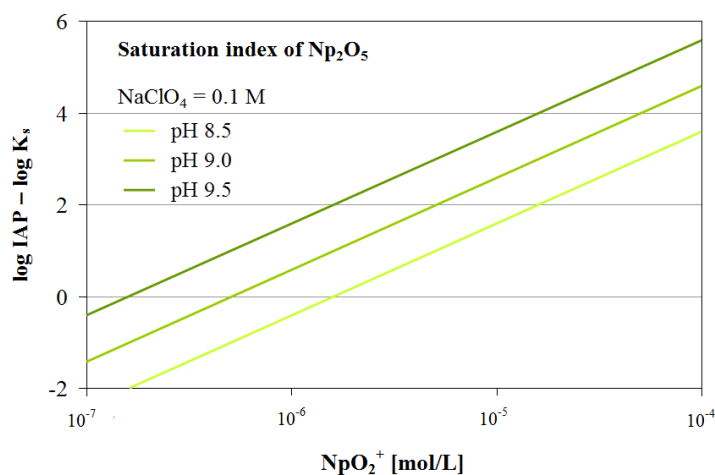


Figure 5.24: Saturation indices for Np_2O_5 as function of NpO_2^+ concentration at different pH. Although it becomes positive already under the experimental conditions applied in this study, precipitation does not occur according to calculations with Visual MINTEQ (IAP – ion activity product).

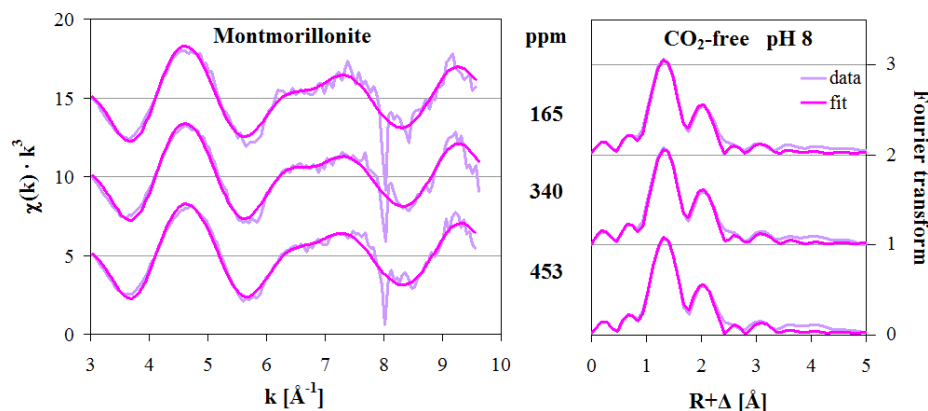


Figure 5.25: Different neptunium loading in the EXAFS spectra. No influence is observed.

spectra are presented in Figure 5.25. Variations from 165 to 453 ppm, however, gave no indication of structural changes with increasing neptunium concentration, i.e. no onset of dimerisation was observed. This negative finding once again reflects the difficulties and shortcomings of the EXAFS data processing. As pointed out above (Section 3.2.3), the fitting procedure requires as input already some concept about the likely chemical structure of the compound in question. In the present case, there is no clear indication of which model provides a better representation of the experimental data. Possibly a still more suitable interpretation might be found, but its assignment and understanding will need the study of further samples and the systematic variation of numerous parameters under the relevant conditions, which could not be performed within the present study.

Since one of the underlying models was derived from soddyite comprising two UO_2 units, which could be identified as dimeric structure, processes of dimerisation demand consideration also in the present case. A dimeric structure of ternary actinyl carbonate surface complexes was also observed for uranium sorption on hematite, $\alpha\text{-Fe}_2\text{O}_3$ (Bargar, Reitmeyer, Lenhart and Davis, 2000). For neptunium, instead, dimerisation seems rather unlikely. Below 0.2 mol/L, Np(V) was shown to exist only monomeric and the $(\text{NpO}_2)_2^{2+}$ dimer was found barely in solutions of higher concentration, while beyond 2 mol/L, even polynuclear species form (Grégoire-Kappenstein, Moisy and Blanc, 2003).

The interaction between two cations may occur linearly involving an axial and an equatorial bond as well as parallel via bridging solvent molecules, i.e. two equatorial oxygen atoms, as depicted in Figure 5.26. The chemical modification of the cation from mono- to dimer is small; in the EXAFS spectra the second neptunium atom appears in a peak around 3.9 \AA , from which a distance of

4.20 and 4.00 Å, respectively, for the linear and parallel molecules ($O_{ax} = 1.83$ Å; $O_{eq} = 2.54$ Å) is extracted (Den Auwer, Grégoire-Kappenstein and Moisy, 2003). In further studies, the parallel mode – which also forms in the solid – proved more likely, and the corresponding stability constant was determined to be 0.74 (Skanthakumar, Antonio and Soderholm, 2008).

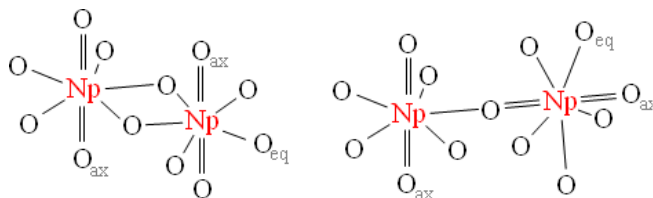


Figure 5.26: Two possible binding modes of Np(V)-dimers: Parallel (left) and linear structure (right) (after Den Auwer et al., 2003, modified).

Shilov and Yusov (1999), however, detected neptunium dimerisation under the influence of UV irradiation, whereby an excited ion reacts with a ground state ion. To what extent the structure of the neptunium in the present samples might have been influenced by the synchrotron light during the EXAFS measurements is not clear. Since no information on such interactions could be found in literature, the neptunium coordination sphere at ~ 3.9 Å may equally be an artefact of some other – i.e. the truly realised, but not yet derived – structure.

5.2.7 Compilation of Speciation Results

Finally, a visual synopsis of all fit data is provided in Figure 5.27. Here, some general differences between Np(V) sorption on montmorillonite and γ -Al₂O₃ are apparent from the bond lengths of equatorial and axial oxygen, carbon, and distal oxygen, or, respectively, aluminium and neptunium atoms. Altogether, the distances between neptunium and the equatorial oxygen atoms are slightly longer in the former compared to its reference substance by about 0.05 Å. This could be interpreted as a hint at a somewhat different mechanism involved in neptunium sorption on these two substrates. Probably the neptunium is not only sorbed to the surface as inner-spherical complex, but also as aquoion bound in the interlayer space of the clay minerals. Hence, the distances measured for montmorillonite could be the average between both neptunium species present in the sample. However, while ternary neptunyl carbonate surface complexes could clearly be attested for montmorillonite, this was not conclusive for γ -Al₂O₃. There instead, an interaction of neptunium with the surface atoms seems feasible. A model combining both aspects would be necessary to draw a final conclusion from the experimental data.

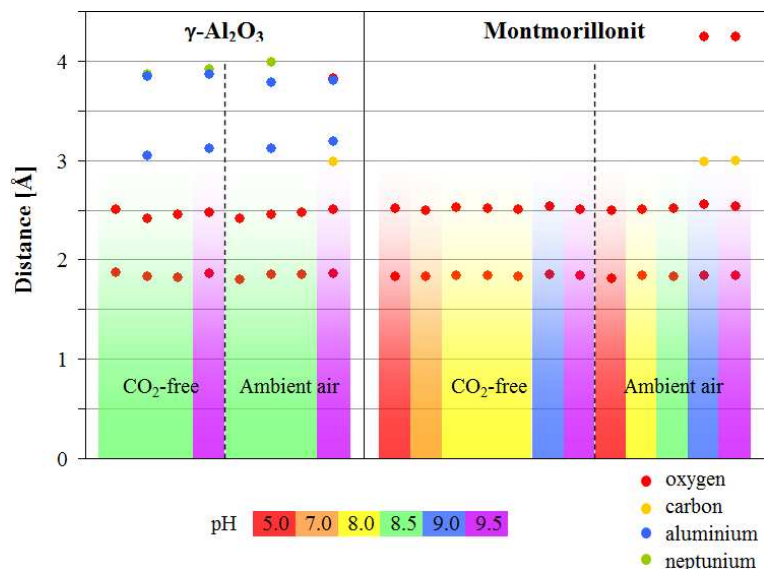


Figure 5.27: Visualisation of the atomic distances of neighbouring atoms to the central absorbing neptunium atom for all samples analysed in this study. Note: The fit of aluminium was tentatively attempted only in the four samples shown; this does not imply that it would fail in the others!

5.3 Modelling Np(V) Sorption on Montmorillonite and $\gamma\text{-Al}_2\text{O}_3$

To complete the experimental approach of this study, the empirical data obtained were attempted to be modelled with the 2SPNE SC/CE model, presented before, using Visual MINTEQ Version 2.53 (Gustafsson, 2007). This simulation involved both fixed programme parameters as well as adjustable constants to reproduce, respectively predict, the sorption of Np(V) on montmorillonite and $\gamma\text{-Al}_2\text{O}_3$.

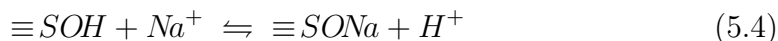
5.3.1 Fixed Programme Parameters

For the cation exchange part, the sorption model selected in the surface complexation menu was that of fixed charge sites specifying only one type of surface. Here, several parameters had to be entered into the programme that were fixed during the modelling process. The site concentration was calculated from the cation exchange capacity of 84.4 meq/100 g (cf. Table 4.1, page 91) and the solid-to-liquid ratio of 4 g/L equalling 3.376 mmol/L. The selectivity coefficient $\frac{Na}{Np}K_C$

for the counterion accumulation was set via definition of two separate selectivity coefficients for the partial reactions



and



which were varied during the modelling procedure.

For the non-electrostatic surface complexation part, the Langmuir isotherm was chosen in the specific sorption menu according to the considerations discussed earlier in this work. Assuming that the low neptunium concentrations applied involve only the strong sorption sites $\equiv S^S OH$, just one type of sites was specified with $Q_{max} = 0.008$ mmol/L calculated for 4 g/L from a site capacity of $2 \cdot 10^{-3}$ mmol/g (Bradbury and Baeyens, 1997). The constants (here named $\log K_L$) for the protolysis reactions were fixed during the programme run at 4.5 and -7.9, respectively (Table 3.1, page 84), while those for the surface complexation of NpO_2^+ and NpO_2OH , ${}^S K_0$ and ${}^S K_1$, were varied to obtain the best fit to the data.

In the modelling of neptunium sorption under ambient air conditions, the equilibrium atmospheric pressure of CO₂ was fixed at 0.00038 atm, which is the programme default.

5.3.2 Adjusted Constants

As a first approach, the adjustable parameters $\frac{Na}{Np} K_C$, ${}^S K_0$, and ${}^S K_1$ were taken from Bradbury and Baeyens (2006a), who modelled Np(V) sorption on montmorillonite under CO₂-free conditions; the corresponding modelling results are shown in Figure 5.28 together with the experimental data of this study¹³. Obviously, the curves match not perfectly with the data points, while the overall magnitude and the trend is nevertheless in reasonable agreement, especially for the CO₂-free data. Here, the reduced error χ^2 was calculated to be 4.1, while values of 16.2 and 27.2 were computed for the ambient air conditions at 0.1 and 0.01 M NaClO₄, respectively. Therefore, the coefficients were adjusted for a better representation of the sorption peak¹⁴. The region from pH 5 to 6.5 proved very difficult to be modelled, and it was entirely impossible to correctly reproduce the cation exchange at the two different ionic strengths with the same selectivity coefficient. Both data sets should be representable by one selectivity

¹³In the figures showing the modelling results the curves split above the sorption maximum depending on whether ambient CO₂ was included in the calculation. The colours were chosen the same to stress the fact that no other parameter was varied.

¹⁴Due to the few data and their relatively large scattering at low pH, the acidic region was regarded with lower significance.

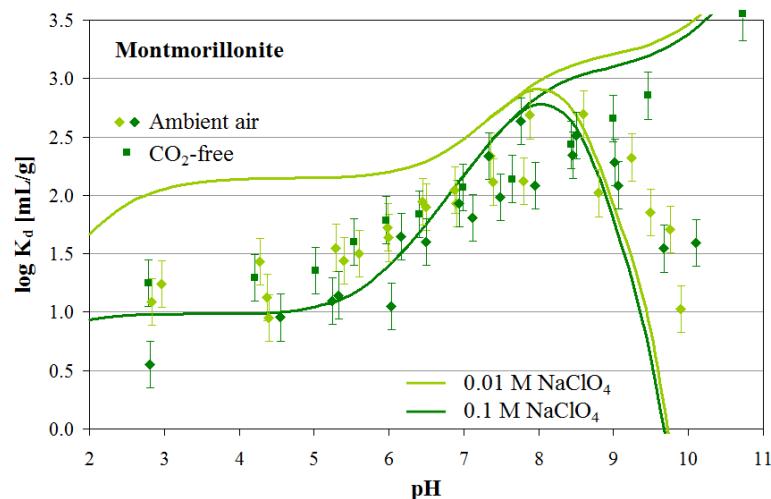


Figure 5.28: Modelled Np(V) sorption on montmorillonite using the parameters published by Bradbury and Baeyens (2006a) (${}_{Np}^{Na}K_C = 1.1$; $\log {}^S K_0 = -2$; $\log {}^S K_1 = -12$) and the experimental data of this study. The error bars represent the uncertainty of $\pm 0.2 \log K_d$ units determined by those authors (Baeyens and Bradbury, 1995b and 2006a).

coefficient, which reflects the ion exchange ability of the sorbent tested here at two different conditions, because all experimental parameters except for the ionic strength were the same. The finding that this could not be achieved may be interpreted as experimental deficiency in this pH region. To proceed with the modelling, two different values had to be chosen for ${}_{Np}^{Na}K_C$, namely 1.6 for 0.1 M and 0.2 for 0.01 M NaClO₄.

Unfortunately, the visual improvement achieved that way yielded no clear enhancement in χ^2 , though. Especially the ambient air data at pH >9 could not be covered with the two surface complexation processes that had been specified in the programme. Also the model developed by Turner et al. (2006), which accounts for aqueous neptunyl-carbonate species but neither includes the formation of such surface complexes nor competition for available sorption sites by CO₃²⁻ or HCO₃⁻, also tends to underpredict neptunium sorption at high pH. From this the authors suggest the possibility of a neptunyl-carbonate surface complex. Thus, for consideration of this effect, a third surface species was defined and included, namely a ternary carbonate complex ($\equiv \text{SONp}_2\text{CO}_3^{2-}$). In this way, χ^2 could be successfully reduced from values beyond 20 down to 2.7 and 1.9 for the ambient air data at 0.1 and 0.01 M NaClO₄ using surface complexation constants of -2.4, -12.2 and 1.9 for $\log {}^S K_0$, $\log {}^S K_1$, and $\log {}^S K_{\text{CO}_3}$, respectively. This agreement, nicely visualised in Figure 5.29, is interpreted as a confirmation of this assumption.

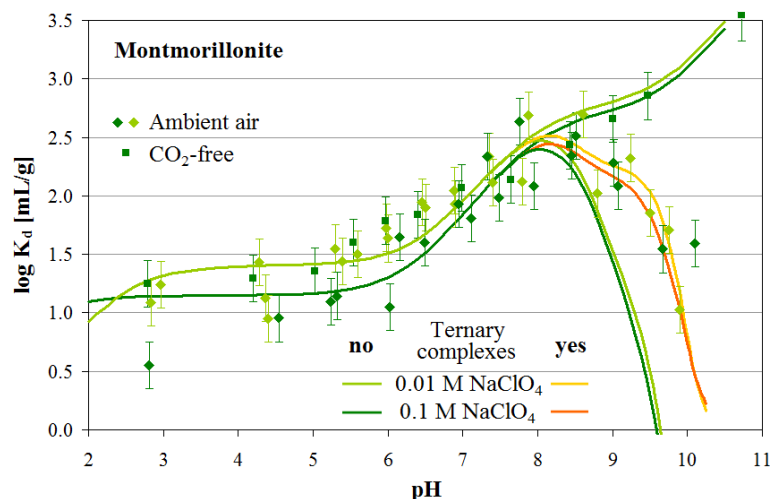


Figure 5.29: The sorption of Np(V) on montmorillonite modelled with parameters chosen to best represent the experimental data of this study ($\frac{N_a}{N_p}K_C = 1.6$ and 0.2; $\log^S K_0 = -2.4$; $\log^S K_1 = -12.2$; $\log^S K_{CO_3} = 1.9$).

Due to the rather few measurements of maximally two batches, a determination of a suitable experimental error in the present study was not straightforward. Baeyens and Bradbury (1995b) extracted a mean error of ± 1.6 mL/g, equalling $\pm 0.2 \log K_d$ units, from their numerous data of cation sorption on montmorillonite; this value was adapted for the respective experiments of the present work (e.g. in Figures 5.28 and 5.29). For γ -Al₂O₃, however, no such value could be found in literature. Lacking sufficient representative data, instead the range of the two averaged batches is shown in Figures 5.30 and 5.31. Alternatively, a similar error as for montmorillonite could be assumed, too, extending the plotted bars by 0.2 units into either direction. Still another problem arose from the fact that sorption on γ -Al₂O₃ is zero at acidic pH. Following experimental imprecision, however, the measured data scatters around the true value, resulting in slightly positive or slightly negative values in this pH region. In the latter case no meaningful logarithm could be taken of the resulting $K_d \leq 0$. Therefore, the mean was calculated replacing negative numbers by zero, assuming that sorption can logically not be less, and the K_d values were averaged first before the logarithm was taken. In these cases, the error bars shown in the graphs amount to three times the average error of the respective batch.

The modelling of neptunium sorption on γ -Al₂O₃ differed from that on montmorillonite in that no cation exchange processes were considered, since these are exclusively subject to clay minerals, which provide a permanent charge and interlayer space. Hence, the CE part of the 2SPNE SC/CE model was omitted. The required sorption site density was estimated as explained in Sec-

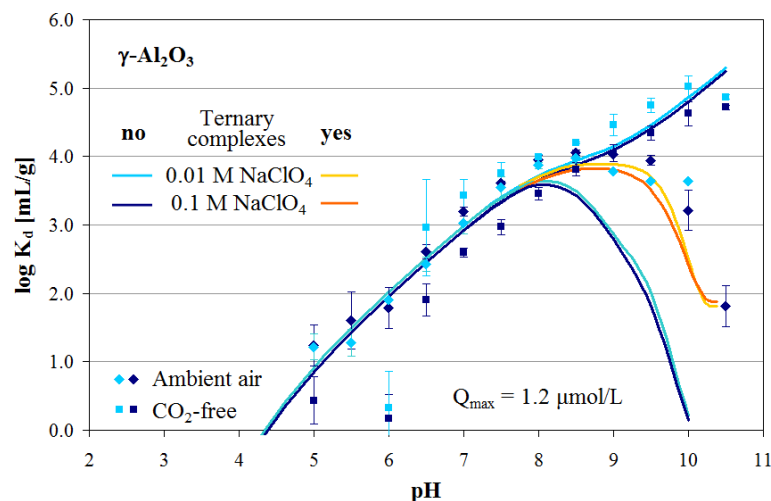


Figure 5.30: Np(V) sorption on $\gamma\text{-Al}_2\text{O}_3$ with model parameters from Table 5.6 ($\log^S K_0 = -1.3$; $\log^S K_1 = -10.4$; $\log^S K_{CO_3} = 3.5$). The error bars give the range of two independent batches each and the data point represents their average.

tion 4.5 and adapted to the applied solid-to-liquid ratio of 0.5 g/L for $Q_{max} = 1.2 \cdot 10^{-3}$ mmol/L. Correspondingly, all complexation constants had to be altered substantially from those determined for montmorillonite; the assigned values are provided in Table 5.6. The curves, which are depicted in Figure 5.30, however, could be reasonably well fitted to the data with χ^2 values of 11.8 and 12.2 (0.1 and 0.01 M NaClO₄, respectively) for CO₂-free and 3.6 and 4.4 for ambient air experiments.

Since a great similarity between the sorption sites on montmorillonite and those on $\gamma\text{-Al}_2\text{O}_3$ has been assumed throughout this whole study, a second ap-

Table 5.6: Derived model parameters for the sorption of neptunium on montmorillonite ($Q_{max} = 8 \mu\text{mol/L}$ for a solid-to-liquid ratio of 4 g/L) and on $\gamma\text{-Al}_2\text{O}_3$.

	STx-1		$\gamma\text{-Al}_2\text{O}_3$	
	literature*	this work	$1.2 \mu\text{mol/L}^\ddagger$	$25 \mu\text{mol/L}^\ddagger$
$\frac{Na}{Np} K_C$	1.1	1.6/0.2 [#]		
$\log^S K_0$	-2	-2.4	-1.3	-2.6
$\log^S K_1$	-12	-12.2	-10.4	-11.6
$\log^S K_{CO_3}$		1.9	3.5	2.3

* Bradbury and Baeyens, 2006a; [‡] site capacity Q_{max} in a 0.5 g/L suspension; [#] for 0.1 and 0.01 M NaClO₄, respectively (see text)

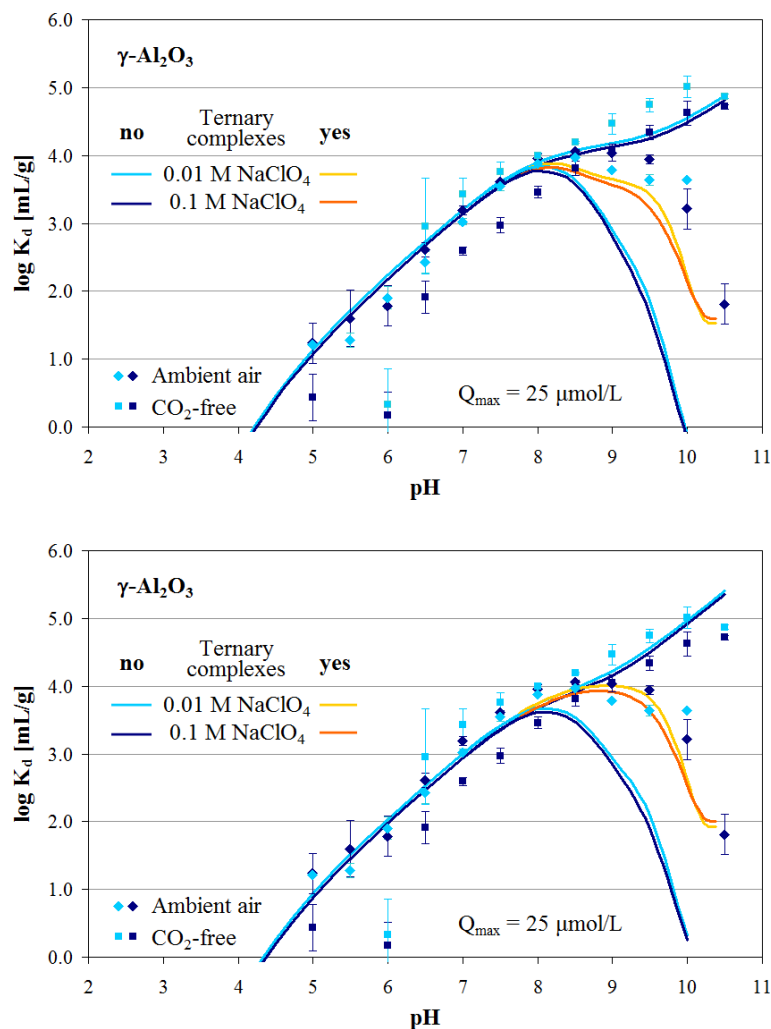


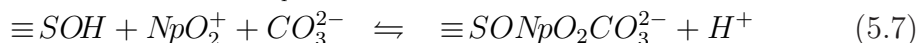
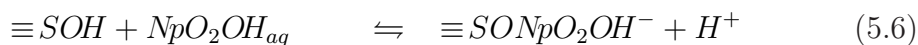
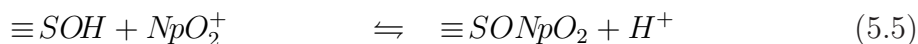
Figure 5.31: Second approach to the modelling of Np(V) sorption on $\gamma\text{-Al}_2\text{O}_3$: Assuming similarity of the sorption sites, the constants determined for montmorillonite are fixed and Q_{max} is adjusted to the best fit first (top), before ${}^S K_0$, ${}^S K_1$, and ${}^S K_{CO_3}$ are fine-tuned (bottom).

proach to modelling the latter was attempted for comparison: All complexation constants were set as determined for montmorillonite and Q_{max} was varied until the best fit to the data was achieved (Figure 5.31, top). Interestingly, this yielded a surface site capacity of 20 times that of montmorillonite, which perfectly matches the surface normalised distribution coefficients of picomolar neptunium sorption as illustrated in Figure 5.16, top, on page 140 ($\Delta \log K_a \approx 1.3 \text{ mL/m}^2$). Keeping this – by a factor of 20 higher – site capacity, ${}^S K_0$, ${}^S K_1$, and ${}^S K_{CO_3}$ were then fine-tuned to optimise the modelling (Figure 5.31,

bottom). With values of -2.6, -11.6, and 2.3, respectively, these quantities were much closer to those determined for montmorillonite than before (see Table 5.6). The reduced errors for 0.1 and 0.01 M NaClO₄ were 12.8 and 12.1 for the CO₂-free data and 2.5 and 3.8 for the ambient air data, which confirms a reasonable reproduction.

The final decision which of the two approaches followed here to model neptunium sorption on γ -Al₂O₃ is more adequate, cannot be taken without additionally conducting titration experiments like described in Baeyens and Bradbury (1995a) to determine the true sorption site capacity. Such a study was beyond the scope of this work, so that here only the two indirect approaches to this unknown parameter necessary for the modelling of Np(V) sorption on γ -Al₂O₃ as discussed before could be attempted. The site capacity estimated in the latter way ($5 \cdot 10^{-5}$ mol/g), however, comes close to the total number of $\equiv S^S OH$ and $\equiv S^W OH$ determined for montmorillonite, $8.2 \cdot 10^{-5}$ mol/g (Table 3.1, page 84), but does not fully reproduce the value. This finding suggests that in the sorption of neptunium on γ -Al₂O₃ not only strong, but also weak sites are involved, which is already indicated by the corresponding isotherms (cf. Section 5.1.3).

Unfortunately, the modelling results presented here could not be related to further literature data, because up to now only Bradbury and Baeyens have published corresponding studies employing the 2 SPNE SC/CE model. All other articles available, which deal with modelling neptunium sorption on either montmorillonite or γ -Al₂O₃, use different models. Hence, their constants are not comparable to the ones presented here. Nevertheless, the necessity of a neptunyl carbonate surface complex in neptunium sorption modelling has been stated before, although it was not included in those studies (Turner et al., 2006; Wang, Anderko and Turner, 2001). In the present work, instead, a ternary surface complex was considered and the following three surface complexation reactions were identified to occur on the external amphoteric edge sites:



whereby the latter applies to ambient air conditions only. On montmorillonite these processes were accomplished by cation exchange on the fixed-charge, basal-plane interlayer sites. These four reactions were sufficient to properly represent the experimental data of Np(V) sorption on montmorillonite and γ -Al₂O₃, respectively.

5.4 Consolidation of Results

The combination of experiments designed to complement each other in the sorption and speciation studies of Np(V) fulfilled this purpose well. The implicit information on the behaviour of neptunium obtained from the batch experiments allowed for the identification of regions of different sorption regimes. Furthermore, the influence of carbonate on the extent of neptunium sorption became obvious. In detail, the findings of this part of the present work are the following:

- For montmorillonite outer- and inner-sphere complex formation could be assigned to the ranges of low and high pH, respectively, through an markedly increased neptunium uptake above the sorption edge;
- With montmorillonite, ion exchange was observed in the acidic region, indicated by dependence of the sorption on ionic strength;
- On γ -Al₂O₃ no sorption occurred at low pH and no influence of ionic strength was visible hinting at the formation of inner-sphere complexes only;
- A decrease in slope of the sorption isotherms of γ -Al₂O₃ pointed towards saturation of the available sorption sites;
- The formation of aqueous complexes with carbonate ions was obvious beyond pH \sim 8, expressed by a decrease in sorption under ambient air conditions with both substrates.

EXAFS analyses of samples chosen on the basis of these findings provided further insight into the molecular structure of the surface complexes. They could confirm, respectively complement the above stated facts. In particular, the following conjectures could be deduced from the identified neighbouring atoms and their corresponding bond lengths:

- Outer-spherical sorption was ascertained in the low pH region, because the atomic distances were similar to those of the neptunyl aquoion. At high pH, in contrast, the bond lengths of the equatorial oxygen atoms were slightly shorter, pointing towards direct binding to atoms of the mineral surface;
- An interaction of neptunium and surface atoms could be identified explicitly only in some cases, due to the low signal-to-noise ratio as well as due to the lack of a suitable theoretical model for data analysis;

- Systematic variations between the complexes formed on montmorillonite and those on $\gamma\text{-Al}_2\text{O}_3$ hint at different sorption mechanisms, which require further investigation beyond the present study;
- Carbonate, bound in a bidentate manner, was detected in the ambient air samples prepared at $\text{pH} > 8.5$. The coordination number roughly reflected the aqueous speciation of CO_2 .

The 2 SPNE SC/CE model was extended and refined by the experimental findings of this study. Not only the conception of CO_2 -containing conditions was rendered possible, but also additional information was achieved on the properties of the binding sites involved in Np(V) sorption on $\gamma\text{-Al}_2\text{O}_3$.

- While the definition of two types of neptunium surface complexes was sufficient for CO_2 -free conditions, a third one – namely a neptunium carbonate complex – was necessary to properly match the ambient air sorption data of montmorillonite as well as $\gamma\text{-Al}_2\text{O}_3$;
- The ion exchange of montmorillonite could not be modelled satisfactorily because of limited data quality and quantity. Thus, it was not possible to determine a corresponding single selectivity coefficient representative for the whole data set. Instead two different coefficients had to be assigned to the CO_2 -free and ambient air experiments, respectively;
- The 2 SPNE SC/CE model was adapted to $\gamma\text{-Al}_2\text{O}_3$ by leaving out the ion exchange part. The sorption site density required as input proved difficult to assess. The approach followed here indicates the involvement of not only strong sites, but also in addition one type of weak sites, which is in agreement with the sorption isotherms and might explain the differences to montmorillonite observed by EXAFS.

Within this work existing knowledge about the general sorption behaviour of Np(V) on montmorillonite was confirmed, while the usage of $\gamma\text{-Al}_2\text{O}_3$ as reference material provided valuable complementary insight into the peculiarities of neptunium binding to aluminol sites. The occurrence and significance of ternary neptunium carbonate surface complexes could be demonstrated, even though their sorption could not be proven directly. The refined 2 SPNE SC/CE model could be used to include the binding of ternary neptunium carbonate complexes to the mineral surface. In return, the modelling process revealed that Np(V) sorption to surface sites of $\gamma\text{-Al}_2\text{O}_3$ must not be regarded identical to that on montmorillonite, which was already indicated by variations in the respective isotherms. Hence, this substance should be considered as a suitable

reference for clay minerals in phenomenological batch sorption studies at low sorbate concentration only, but not be seen as an analogon on molecular scale. The analysis of the differences of reactions on montmorillonite and $\gamma\text{-Al}_2\text{O}_3$ surface sites, however, require additional research.

Altogether, the present work comprises substantial contributions to the understanding of neptunium sorption as function of pH, Np(V) concentration, ionic strength, and presence, respectively absence, of aerial CO_2 . Furthermore, through EXAFS certain insight could be gained into the molecular processes involved. Jointly, the knowledge obtained will stimulate and facilitate future studies on related topics as well as fortify repository safety assessments based on theoretical models.

6

Conclusion and Outlook

This study on sorption and direct speciation of neptunium is located in the field of nuclear safety research. It was designed to aid the assessment of final repositories by providing new and further information on the environmental behaviour of neptunium, whose long-lived isotope ^{237}Np is regarded a radionuclide of major concern in nuclear waste. Within this broad context, the present work concentrated on the interaction between Np(V) and the clay mineral montmorillonite, which is the main component of many host rock formations selected for final disposal as well as of backfill materials regarded suitable for sealing the caverns. Thereby, not only the qualitative and quantitative sorption behaviour was focussed on, but also the surface species formed under different conditions – pH, Np(V) concentration, ambient vs. CO_2 -free atmosphere, varying ionic strengths – were identified via EXAFS analyses to elucidate the sorption process on a molecular level. As a simplified approach, $\gamma\text{-Al}_2\text{O}_3$ served as a reference substance for montmorillonite, since neptunium binds preferably to the aluminol surface groups of the clay. It was attempted to reproduce the experimental results by the 2SPNE SC/CE model. This contributes to the development of a theoretical background from which the effects of physical and chemical variability on neptunium sorption can be simulated, allowing for extrapolation beyond experimental conditions. The collected results will add to founding a scientific basis for the risk assessment of clay-based nuclear waste repositories.

With the progress of this study, the choice, design, and configuration of materials and experiments proved well suitable to achieve the intended aim. In spite of their different structures, both substrates addressed, $\gamma\text{-Al}_2\text{O}_3$ and montmorillonite, reveal a widely similar sorption behaviour. This emphasises the dominance of the aluminol groups for neptunium sorption on montmorillonite over the silanol surface groups. Additionally, it could be shown that $\gamma\text{-Al}_2\text{O}_3$ can also serve as a reference substance for bi-layered clay minerals such as kaolinite for studying the sorption of Np(V) as a function of pH in the presence and

absence of ambient CO_2 . On molecular level, however, the mechanisms of neptunium sorption on $\gamma\text{-Al}_2\text{O}_3$ seem to be somewhat different than on clay minerals. Details on this peculiarity require further investigations, though.

Regarding the general behaviour of neptunium sorption on $\gamma\text{-Al}_2\text{O}_3$ and montmorillonite, the trend established from literature could be affirmed. Sorption occurs merely at relatively high pH resulting in a quite pronounced mobility under the assumed environmental conditions at final disposal sites. These characteristics support the classification of neptunium as an actinide of major concern regarding the safety of nuclear repositories. With montmorillonite being the main component of host rock and/or backfill material its physical properties such as swelling (hence sealing) ability and poor water permeability are rather of importance for neptunium retardation than its particular sorption properties, as long as the pH of the pore water is in the acidic to neutral region.

In general, this work attempts to provide valuable information and suitable input data for modelling studies and release simulations. Especially the finding that ternary neptunium carbonate complexes form on the surface renders mobility predictions at high pH more realistic compared to current hypotheses. Their existence does not only affect models of the strongly simplified system Np(V)-montmorillonite, but also all kinds of estimations involving these two components, particularly release scenarios of mixtures of various radionuclides and other heavy metals in an aqueous clay or soil environment.

6.1 Summary of the Experiments

The experiments conducted in this study were chosen and designed to give complementary insight into the processes, which are involved in the sorption of Np(V) on the clay mineral montmorillonite and – as a model substance for the surface sites – on $\gamma\text{-Al}_2\text{O}_3$. This objective included the identification of the surface species formed.

6.1.1 Sorption Processes

The first part of this study was devoted to the sorption behaviour of neptunium on the two substrates under different conditions, such as variable ionic strength, sorbate concentration, and presence or absence of airborne CO_2 .

The sorption batch experiments revealed that on both substrates neptunium binds to amphoteric surface sites, which is apparent from the clear sorption edges forming and, under exclusion of CO_2 , the continuous increase of sorption with

pH. Only in the case of montmorillonite and in the low pH region ($\text{pH} < \sim 5$), variations in ionic strength are reflected in the sorption behaviour. This points towards ion exchange processes, which take place at interlayer sites, while the pH dependent sorption occurs at the crystal edges. The influence of ambient air, i.e. CO_2 , is such that the sorption curve traverses a maximum at pH 8-9 and, beyond pH ~ 9 , decreases to zero around pH ~ 10 , which indicates the formation of aqueous neptunium carbonate complexes. Furthermore, the sorption isotherms show that neptunium carbonate complexes precipitate at Np(V) concentrations above $2 \cdot 10^{-5} \text{ M}$ around pH 9.

6.1.2 Surface Species

EXAFS speciation studies, carried out to support the analyses on a microscopic, phenomenological scale, aimed at the detection and characterisation of the Np(V) complexes formed on the mineral surface.

The predominant occurrence of the fifth oxidation state of neptunium and its neptunyl form were confirmed. Precipitation could be ruled out for the sorbate concentrations applied, although the data allows for the conjecture of neptunium dimerisation. The molecular structure measured supports the theory of outer-spherical sorption in the low pH region as opposed to inner-spherical sorption at higher pH. Unfortunately, due to the relatively low signal-to-noise ratio, not in all samples an explicit Np-Al interaction could be identified to support this deduction. Beyond the sorption maximum, CO_3 -structures could be fit to the experimental data providing evidence for the formation of ternary neptunium carbonate surface complexes of bidentate ligand coordination. The number of carbonate groups roughly reflects the aqueous speciation of neptunium under ambient air conditions.

For modelling the data of neptunium sorption on montmorillonite the approach of Bradbury and Baeyens was adopted employing their 2 SPNE SC/CE model. Unfortunately, quantity and quality of the experimental data was not sufficient in the acidic pH region to properly confirm the expected influence of the ionic strength on cation exchange prevailing there. Consequently, no singular selectivity constant could be defined for this study. The published surface complexation constants had to be varied only marginally to obtain satisfactory compliance with the CO_2 -free experiments, while the ambient air curve could only be fit by incorporation of a third species, a ternary neptunium carbonate surface complex. Similarly, the consideration of a sorbed neptunium carbonate complex was required to adequately match the experimental data of neptunium sorption on $\gamma\text{-Al}_2\text{O}_3$. In contrast to montmorillonite, modelling of the $\gamma\text{-Al}_2\text{O}_3$ sorption data yielded some hints at the involvement of weak sorption sites. This

anticipation would explain the smaller inner-molecular atomic distances of the neptunyl ion measured by EXAFS for γ -Al₂O₃ compared to those of Np(V) bound to montmorillonite (cf. Tables 5.1 and 5.4 on pages 146 and 154, respectively), assuming a certain share of outer-spherical sorption on these sites.

So far, the formation of ternary surface neptunyl carbonate complexes has been suggested at high carbonate concentrations only (Kohler et al., 1999, cited in Del Nero et al., 2004). The present study now provides evidence for such structures under neptunium trace concentrations, too.

6.2 Evaluation and Usability of the Results

Under all circumstances, certain general restrictions on the comprehensibility of a natural system must still be realised. Despite of numerous approaches, it is impossible to entirely characterise a natural system, because the identification and quantification of all variables involved is by far beyond the existing analytical capabilities.

Although many constraints are not foreseeable precisely, generalised considerations may indicate a tendency for interpretation of the present results. The temperature in the vicinity of a nuclear repository, for example, will be increased due to radioactive decay. Since sorption increases with temperature (Lu et al., 2000), the results presented here could be seen as conservative upper limits for neptunium mobility. Equally, other factors are not ascertainable at all. Natural systems contain variable amounts of organics as well as micro- and macroscopic concentrations of various inorganic species that can compete with, complex or react with actinides via hydrolysis, complexation, redox reactions, and colloid formation. Without determining their final concentration the natural environmental chemistry is inevitably different from the ordinary solution chemistry studies in the laboratory. Even basic parameters such as the solid-to-liquid ratio raise difficulties when transferred to nature. During the present experiments it was fixed at 0.5 or 4 g/L, respectively, while in a natural system of porous media, this parameter is everything but well constrained.

In a possible scenario of radionuclide release from a repository, the varying conditions close to the source as well as further away must be considered. In spent nuclear fuel most actinides are present in low oxidation states. Microbial activity or corroding iron may maintain these, keeping soluble concentrations low. Anyway, as soon as oxidising waters infiltrate the system, the actinides, including neptunium, will convert into their more soluble higher oxidation states. This process is much more critical for the resulting hazard and, therefore, usually treated with greater emphasis in environmental impact assessment.

Still the present approach is the only possibility to refine the understanding of the processes determining the behaviour of natural systems including the fate of contaminants. This work is an approach towards further insight into a few relevant details, which – together with many more others – will lead to a more conclusive representation of the real conditions.

6.3 Future Progression

Even though precise and immediate implications for repository design are not directly derivable from this study, it supports the general safety assessment by providing experimental data on one actinide of primary concern, namely ^{237}Np . The studies on Np(V) also enhance the understanding of analogous pentavalent actinides like Am(V) or Pu(V) , which can be investigated only with considerable experimental effort. The environmental impact of civil and military usage of nuclear technology becomes more conceivable in this way.

Besides critical confirmation of already existing knowledge like on the general sorption behaviour of actinides, future research on this topic should also concentrate on the investigation of basic details such as the molecular processes involved. It is widely accepted that still “[...] much more understanding of the behaviour [of the actinides] in the environment is needed to allow proper and reliable modelling [...]” (Choppin, 2007), while “[...] advances in actinide chemistry will continue to be increasingly important in the foreseeable future. These advances must necessarily be accompanied by more complex structural analyses that will achieve a more thorough understanding of the chemical behaviour of the actinides” (Gutowski et al., 2006).

Within this context, recommendations can be made for scientific research to follow three different pathways: First, speciation studies should be improved and extended; second, the experimental design of sorption studies should advance towards more realistic conditions, e.g. by considering real backfill material such as Opalinus clay as well as influences from humic substances and microorganisms, by including competing radionuclides and other heavy metals, by utilisation of natural pore water compositions, etc.; third, modelling and simulation studies should try to estimate various scenarios of radionuclide release from different types of final repositories. Thereby, all these scientific efforts should generally be motivated by the ambition to ensure maximum safety of our current corporate activities for future generations.

Bibliography

- Albright, D. and Barbour, L. (1999). Troubles tomorrow? Separated Neptunium²³⁷ and Americium, *in* D. Albright and K. O'Neill (eds), *The Challenges of Fissile Material Control*, Institute for Science and International Security Press, Washington, D.C., chapter 5, pp. 85–96. ISBN 0-9669467-0-7, LCCN 98-75828, <http://www.isis-online.org/publications/fmct/book/>.
- Albright, D. and Kramer, K. (2005). Neptunium 237 and americium: World inventories and proliferation concerns, *Global stocks of nuclear explosive material*, Institute for Science and International Security (ISIS), Washington, D.C., chapter 10. http://www.isis-online.org/global_stocks/end2003/tableofcontents.html.
- Alekseyev, V. A. (2007). Equations for the dissolution reaction rates of montmorillonite, illite, and chlorite, *Geochemistry International* **45**(8): 770–780.
- Allard, B., Olufsson, U. and Torstenfelt, B. (1984). Environmental actinide chemistry, *Inorganica Chimica Acta* **94**: 205–221.
- Allen, P. G., Bucher, J. J., Shuh, D. K., Edelstein, N. M. and Reich, T. (1997). Investigation of aquo and chloro complexes of UO_2^{2+} , NpO_2^+ , Np^{4+} , and Pu^{3+} by X-ray absorption fine structure spectroscopy, *Inorganic Chemistry* **36**: 4676–4683.
- Amayri, S. (2008). private communication.
- Amayri, S., Jermolajev, A. and Reich, T. (2005). Influence of ionic strength on neptunium(V) sorption onto kaolinite in the presence and absence of CO_2 , *Annual report C4*, Institute for Nuclear Chemistry, University of Mainz.
- ANKA (2009). Homepage of the Synchrotron Light Source at the Research Centre Karlsruhe, http://ankaweb.fzk.de/instrumentation_at_anka/beam_lines.php?id=9.

- Antonio, M. R. and Soderholm, L. (2006). X-ray absorption spectroscopy of the actinides, in L. R. Morss, N. M. Edelstein and J. Fuger (eds), *The Chemistry of the Actinide and Transactinide Elements, Third Edition*, Springer, chapter 28, pp. 3086–3198.
- Antonio, M. R., Soderholm, L., Williams, C. W., Blaudeau, J.-P. and Bursten, B. E. (2001). Neptunium redox speciation, *Radiochimica Acta* **89**: 17–25.
- Appelo, C. A. J. and Postma, D. (2005). *Geochemistry, Groundwater and Pollution*, 2nd edn, A. A. Balkema Publishers.
- Arai, Y., Moran, P. B., Honeyman, B. D. and Davis, J. A. (2007). In situ spectroscopic evidence for neptunium(V)-carbonate inner-sphere and outer-sphere ternary surface complexes in hematite surfaces, *Environmental Science and Technology* **41**: 3940–3944.
- Argonne National Laboratory (2005). Neptunium, *Human Health Fact Sheet, August 2005*, Environmental Science Division (EVS). <http://www.ead.anl.gov/pub/doc/neptunium.pdf>.
- Baeyens, B. and Bradbury, M. H. (1995a). A quantitative mechanistic description of Ni, Zn and Ca sorption on Na-montmorillonite. Part I: Physico-chemical characterisation and titration measurements, *PSI Report No. 95-10, Nagra NTB 95-04*, Paul Scherrer Institut, Villigen PSI, Switzerland.
- Baeyens, B. and Bradbury, M. H. (1995b). A quantitative mechanistic description of Ni, Zn and Ca sorption on Na-montmorillonite. Part II: Sorption measurements, *PSI Report No. 95-11, Nagra NTB 95-05*, Paul Scherrer Institut, Villigen PSI, Switzerland.
- Baeyens, B. and Bradbury, M. H. (1997). A mechanistic description of Ni and Zn sorption on Na-montmorillonite. Part I: Titration and sorption measurements, *Journal of Contaminant Hydrology* **27**(3-4): 199–222.
- Balasubramanian, K. and Cao, Z. (2007). Theoretical studies on structures of neptunyl carbonates: $\text{NpO}_2(\text{CO}_3)_m(\text{H}_2\text{O})_n^{q-}$ ($m = 1-3$, $n = 0-3$) in aqueous solution, *Inorganic Chemistry* **46**: 10510–10519.
- Bargar, J. R., Reitmeier, R., Lenhart, J. J. and Davis, J. A. (2000). Characterisation of U(VI)-carbonate ternary complexes on hematite: EXAFS and electrophoretic mobility measurements, *Geochimica et Cosmochimica Acta* **64**(16): 2737–2749.

- Bertetti, E. P., Pabalan, R. T. and Almendarez, M. G. (1998). Studies of neptunium(V) sorption on quartz, clinoptilolite, montmorillonite, and α -alumina, in E. A. Jenne (ed.), *Adsorption of Metals by Geomedia – Variables, Mechanisms, and Model Applications*, Academic Press, chapter 4, pp. 131–148.
- Bertetti, E. P., Pabalan, R. T., Turner, D. R. and Almendarez, M. G. (1996). Studies of neptunium(V) sorption on clinoptilolite, quartz, and montmorillonite, in W. M. Murphy and D. A. Knecht (eds), *Materials Research Society Symposium Proceedings – Scientific Basis for Nuclear Waste Management XIX, Vol. 412*, pp. 631–638.
- Bradbury, M. H. and Baeyens, B. (1995). A quantitative mechanistic description of Ni, Zn and Ca sorption on Na-montmorillonite. Part III: Modelling, *PSI Report No. 95-12, Nagra NTB 95-06*, Paul Scherrer Institut, Villigen PSI, Switzerland.
- Bradbury, M. H. and Baeyens, B. (1997). A mechanistic description of Ni and Zn sorption on Na-montmorillonite. Part II: modelling, *Journal of Contaminant Hydrology* **27**(3-4): 223–248.
- Bradbury, M. H. and Baeyens, B. (2003). Porewater chemistry in compacted re-saturated MX-80 bentonite, *Journal of Contaminant Hydrology* **61**: 329–338.
- Bradbury, M. H. and Baeyens, B. (2005). Modelling the sorption of Mn(II), Co(II), Ni(II), Zn(II), Cd(II), Eu(III), Am(III), Sn(IV), Th(IV), Np(V) and U(VI) on montmorillonite: Linear free energy relationships and estimates of surface binding constants for some selected heavy metals and actinides, *Geochimica et Cosmochimica Acta* **69**(4): 875–892.
- Bradbury, M. H. and Baeyens, B. (2006a). Modelling sorption data for the actinides Am(III), Np(V) and Pa(V) on montmorillonite, *Radiochimica Acta* **94**: 619–625.
- Bradbury, M. H. and Baeyens, B. (2006b). A quasi-mechanistic non-electrostatic modelling approach to metal sorption on clay minerals, in J. Lützenkirchen (ed.), *Surface Complexation Modelling*, Elsevier Ltd., chapter 19, pp. 518–538.
- Brown, Jr., G. E., Henrich, V. E., Casey, W. H., Clark, D. L., Eggleston, C., Felmy, A., Goodman, D. W., Grätzel, M., Maciel, G., McCarthy, M. I., Nealon, K. H., Sverjensky, D. A., Toney, M. F. and Zachara, J. M. (1999). Metal oxide surfaces and their interactions with aqueous solutions and microbial organisms, *Chemical Reviews* **99**: 77–174.

- Bundesamt für Strahlenschutz (2002). Auswertung von Langzeitsicherheitsanalysen hinsichtlich Kriterien für die Auswahl von Endlagerstandorten, *Schlussbericht NPB 01-31*, Arbeitsgemeinschaft Nationale Genossenschaft für die Lagerung radioaktiver Abfälle (Nagra), Colenco Power Engineering AG und Gesellschaft für Anlagen- und Reaktorsicherheit (GRS) mbH. PSP-Nr. WS 0008 / BfS-Bestell-Nr. 8391-0.
- Bunker, G. (1997). Elements of XAFS, <http://gbxafs.iit.edu/training/xafs/overview.pdf>, Physics Department, Illinois Institute of Technology, Chicago, IL.
- Canberra Industries, Inc. (2007). GenieTM 2000 Gamma Analysis Software, <http://www.canberra.com/products/835.asp>.
- Catalano, J. G. and Brown, Jr., G. E. (2005). Uranyl adsorption onto montmorillonite: Evaluation of binding sites and carbonate complexation, *Geochimica et Cosmochimica Acta* **69**(12): 2995–3005.
- Choppin, G. R. (2005). Actinide science: fundamental and environmental aspects, *Journal of Nuclear and Radiochemical Sciences* **6**(1): 1–5.
- Choppin, G. R. (2006a). Actinide speciation in aquatic systems, *Marine Chemistry* **99**: 83–92.
- Choppin, G. R. (2006b). Environmental behaviour of actinides, *Czechoslovak Journal of Physics* **56**: D13–D21.
- Choppin, G. R. (2007). Actinide speciation in the environment, *Journal of Radioanalytical and Nuclear Chemistry* **273**(3): 695–703.
- Choppin, G. R. and Jensen, M. P. (2006). Actinides in solution: Complexation and kinetics, in L. R. Morss, N. M. Edelstein and J. Fuger (eds), *The Chemistry of the Actinide and Transactinide Elements, Third Edition*, Springer, chapter 23, pp. 2524–2621.
- Choppin, G. R. and Wong, P. J. (1996). Current status of radioactive waste disposal, *Journal of Radioanalytical and Nuclear Chemistry* **203**(2): 575–590.
- Choppin, G. R. and Wong, P. J. (1998). The chemistry of actinide behaviour in marine systems, *Aquatic Geochemistry* **4**: 77–101.
- Clark, D. L., Conradson, S. D., Ekberg, S. A., Hess, N. J., Neu, M. P., Palmer, P. D., Runde, W. and Tait, C. D. (1996). EXAFS studies of pentavalent neptunium carbonato complexes. Structural elucidation of the principal

-
- constituents of neptunium in groundwater environments, *Journal of the American Chemical Society* **118**: 2089–2090.
- Clark, D. L., Hobart, D. E. and Neu, M. P. (1995). Actinide carbonate complexes and their importance in actinide environmental chemistry, *Chemical Reviews* **95**: 25–48.
- Combes, J.-M., Chisholm-Brause, C. J., Gordon E. Brown, J. and Parks, G. A. (1992). EXAFS spectroscopic study of neptunium(V) sorption at the α -FeOOH/water interface, *Environmental Science and Technology* **26**: 376–382.
- Curis, E. (2006). Logiciel d'analyse des spectres EXAFS (LASE), <http://xlase.free.fr>.
- Davis, J. A. and Kent, D. B. (1990). Surface complexation modeling in aqueous geochemistry, *Reviews in Mineralogy and Geochemistry* **23**: 117–260.
- Del Nero, M., Assada, A., Madé, B., Barillon, R. and Duplâtre, G. (2004). Surface charges and Np(V) sorption on amorphous Al and Fe silicates, *Chemical Geology* **211**: 15–45.
- Demartin, F., Gramaccioli, C. M. and Pilati, T. (1992). The importance of accurate crystal structure determination of uranium minerals. II. Soddyite $(\text{UO}_2)_2(\text{SiO}_4) \cdot 2\text{H}_2\text{O}$, *Acta Crystallographica Section C: Crystal Structure Communications* **48**: 1–4.
- Den Auwer, C., Grégoire-Kappenstein, A. C. and Moisy, P. (2003). Np(V) cation–cation interactions. A new contribution from EXAFS spectroscopy?, *Radiochimica Acta Rapid Communication* **91**: 773–776.
- Denecke, M. A., Rothe, J., Dardenne, K., Blank, H. and Hormes, J. (2005). The INE-beamline for actinide research at ANKA, *Physica Scripta* **T115**: 1001–1003.
- Dierking, S., Vicente Vilas, V., Baeyens, B. and Reich, T. (2006). Sorption experiments with neptunium on conditioned Na-montmorillonite [in German], *Annual report C7*, Institute for Nuclear Chemistry, University of Mainz.
- DOE (2003). The history of nuclear energy, *Technical Report DOE/NE-0088*, U.S. Department of Energy, Office of Nuclear Energy, Science, and Technology, Washington, D.C. 20585.

- Dozol, M. and Hagemann, R. (1993). Radionuclide migration in groundwaters: Review of the behaviour of actinides (Technical Report), International Union of Pure and Applied Chemistry, Analytical Chemistry Division, Commission on Radiochemistry and Nuclear Techniques, *Pure and Applied Radiochemistry* **65**(5): 1081–1102.
- Eberhardt, K. and Kronenberg, A. (2000). The research reactor TRIGA Mainz – A neutron source for versatile applications in research and education, *Kerntechnik* **65**: 269–274.
- Eckhardt, R. C. (2000). Yucca Mountain – Looking ten thousand years into the future, *Los Alamos Science* (26): 464–489.
- Ekström, L. P. and Firestone, R. B. (2004). WWW Table of Radioactive Isotopes, Version 2.1, <http://ie.lbl.gov/toi/index.htm>. LBNL Isotopes Project - LUNDS Universitet.
- ESRF (2009). Homepage of the Rossendorf Beamline at the European Synchrotron Radiation Facility, <http://www.esrf.eu/UsersAndScience/Experiments/CRG/BM20/>.
- Fanghänel, T. and Neck, V. (2002). Aquatic chemistry and solubility phenomena of actinide oxides/hydroxides, *Pure and Applied Chemistry* **74**(10): 1895–1907.
- FEFF Project (2002). FEFF8 (Version 8.20), Department of Physics, University of Washington, Seattle, WA, <http://leonardo.phys.washington.edu/feff/>.
- Filges, U. (2002). Neptunium und Americium – Kernbrennstoffe aus nuklearem Abfall, *Technical report*, Fraunhofer-Institut für Naturwissenschaftlich-Technische Trendanalysen (INT).
- Firestone, R. B. (2003). Overview of nuclear data, *Lecture given at the Workshop on Nuclear Data for Science and Technology: Material Analysis, Trieste, 19-30 May*, Lawrence Berkeley National Laboratory.
- FZD (2009). Homepage of the Research Centre Dresden-Rossendorf, <http://www.fzd.de/pls/rois/Cms?pNid=247>.
- Gagliardi, L. and Roos, B. O. (2002). Coordination of the neptunyl ion with carbonate ions and water: A theoretical study, *Inorganic Chemistry* **41**: 1315–1319.
- George, G. N. and Pickering, I. J. (1995). EXAFSPAK – A suite of computer programs for analysis of X-ray absorption spectra, SSRL Stanford CA, USA, <http://www-ssrl.slac.stanford.edu/exafspak.html>.

- Gmelin Institute, F. K. (1997). Retrieve 2.01 – ICSD Inorganic Crystal Structure Database, CD-ROM.
- Goldberg, S., Davis, J. A. and Hem, J. D. (1996). The surface chemistry of aluminum oxides and hydroxides, *in* G. Sposito (ed.), *The Environmental Chemistry of Aluminum*, Lewis Publishers, chapter 7, pp. 271–331.
- Grégoire-Kappenstein, A. C., Moisy, P. and Blanc, P. (2003). Dimerization of Np(V) and media effects in concentrated solutions, *Radiochimica Acta* **91**: 665–672.
- Guillaumont, R., Fanghänel, T., Fuger, J., Grenthe, I., Neck, V., Palmer, D. and Rand, M. H. (2003). *Update on the Chemical Thermodynamics of Uranium, Neptunium, Plutonium, Americium, and Technetium*, Vol. 5 of *Chemical Thermodynamics Series*, Elsevier, OECD Nuclear Energy Agency.
- Gustafsson, J. P. (2007). Visual MINTEQ (Version 2.53), Department of Land and Water Resources Engineering, Royal Institute of Technology (KTH), Stockholm, <http://www.lwr.kth.se/English/OurSoftware/vminteq/>.
- Gutiérrez, G., Taga, A. and Johansson, B. (2001). Theoretical structure determination of γ -Al₂O₃, *Physical Review B* **65**(012101): 1–4.
- Gutowski, K. E., Bridges, N. J. and Rogers, R. D. (2006). Actinide structural chemistry, *in* L. R. Morss, N. M. Edelstein and J. Fuger (eds), *The Chemistry of the Actinide and Transactinide Elements, Third Edition*, Springer, chapter 22, pp. 2380–2523.
- Holleman, A. F. and Wiberg, E. (2007). Die Actinoide, *Lehrbuch der Anorganischen Chemie*, de Gruyter, chapter 36, pp. 1948–1976.
- Horst, J. and Höll, W. H. (1997). Application of the surface complex formation model to ion exchange equilibria – Part VI: Amphoteric sorption onto γ -aluminium oxide, *Journal of Colloid and Interface Science* **195**: 250–260.
- IAEA Safety Standards (1989). Safety Series No. 99 – Safety principles and technical criteria for the underground disposal of high level radioactive wastes, *Technical report*, International Atomic Energy Agency, Vienna.
- IEA Energy Technology Essentials (2007). Nuclear power, *Technical Report ETE04*, International Energy Agency.
- International Union of Pure and Applied Chemistry (IUPAC) (2008). IUPAC Compendium of Chemical Terminology (Gold Book), Electronic Version, <http://goldbook.iupac.org>. Release 2.0.2.

- Jermolajev, A., Kasbohm, J. R., Amayri, S. and Reich, T. (2005). Sorption of neptunium on kaolinite under environmental conditions, *Annual report C5*, Institute for Nuclear Chemistry, University of Mainz.
- Köhler, S. J., Dufaud, F. and Oelkers, E. H. (2003). An experimental study of illite dissolution kinetics as a function of pH from 1.4 to 12.4 and temperature from 5 to 50°C, *Geochimica et Cosmochimica Acta* **67**(19): 3583–3594.
- Konings, R. J. M., Morss, L. R. and Fuger, J. (2006). Thermodynamic properties of actinides and actinide compounds, in L. R. Morss, N. M. Edelstein and J. Fuger (eds), *The Chemistry of the Actinide and Transactinide Elements, Third Edition*, Springer, chapter 19, pp. 2113–2224.
- Koningsberger, D. C. and Prins, R. (1988). *X-ray Absorption: Principles, Applications, Techniques of EXAFS, SEXAFS and XANES*, Vol. 92 of *Chemical Analysis*, John Wiley & Sons, Inc.
- Köster, H. M. and Schwertmann, U. (1993). Beschreibung einzelner Tonminerale, in K. Jasmund and G. Lagaly (eds), *Tonminerale und Tone – Struktur, Eigenschaften, Anwendungen und Einsatz in Industrie und Umwelt*, Steinkopff Verlag, chapter 2, pp. 33–88.
- Lagaly, G. and Köster, H. M. (1993). Tone und Tonminerale, in K. Jasmund and G. Lagaly (eds), *Tonminerale und Tone – Struktur, Eigenschaften, Anwendungen und Einsatz in Industrie und Umwelt*, Steinkopff Verlag, chapter 1, pp. 1–32.
- Langmuir, D. (1997). *Aqueous Environmental Geochemistry*, Prentice-Hall, Inc.
- Laverov, N. P., Yudinsev, S. V., Stefanovsky, S. V., Omel'yanenko, B. I. and Nikonov, B. (2006). Murataite as a universal matrix for immobilization of actinides, *Geology of Ore Deposits* **48**(5): 335–356.
- Lawrence Berkeley National Laboratory (2000). Radioactivity in the natural environment, <http://www.lbl.gov/abc/wallchart/chapters/15/3.html>.
- Lefèvre, G., Duc, M., Lepeut, P., Caplain, R. and Fédoroff, M. (2002). Hydration of γ -alumina in water and its effects on surface reactivity, *Langmuir* **18**: 7530–7537.
- Lemire, R. J., Fuger, J., Nitsche, H., Potter, P., Rand, M. H., Rydberg, J., Spahiu, K., Sullivan, J. C., Ullman, W. J., Vitorge, P. and Wanner, H. (2001). *Chemical Thermodynamics of Neptunium and Plutonium*, Vol. 4 of *Chemical Thermodynamics Series*, Elsevier, OECD Nuclear Energy Agency.

- Li, W. and Tao, Z. (2003). Comparative study on Np(V) sorption on oxides of aluminium and silicon: Effects of humic substance and carbonate in solution, *Journal of Colloid and Interface Science* **267**: 25–31.
- Lieser, K. H. (2001). *Nuclear and Radiochemistry – Fundamentals and Applications*, second, revised edn, Wiley-VCH.
- Lieser, K. H. and Mühlenweg, U. (1988). Neptunium in the hydrosphere and in the geosphere, *Radiochimica Acta* **43**: 27–35.
- Loveland, W. D., Morrissey, D. J. and Seaborg, G. T. (2006). *Modern Nuclear Chemistry*, John Wiley & Sons Inc.
- Lu, N., Conca, J., Parker, G. R., Leonard, P. A., Moore, B., Strietelmeier, B. and Triay, I. R. (2000). Adsorption of actinides onto colloids as a function of time, temperature, ionic strength, and colloid concentration, *Waste Form Colloids Report for Yucca Mountain Program LA-UR-00-5121*, Los Alamos National Laboratory.
- Magill, J. and Galy, J. (2005). *Radioactivity, Radionuclides, Radiation*, Springer-Verlag.
- Manceau, A., Marcus, M. A. and Tamura, N. (2002). Quantitative speciation of heavy metals in soils and sediments by synchrotron X-ray techniques, *Reviews in Mineralogy and Geochemistry* **49**(1): 341–428.
- McMillan, E. M. (1940). The seven-day uranium activity, *Physical Review* **58**: 178.
- McMillan, E. M. (1951). The transuranium elements: Early history, Nobel Lecture, December 12.
- McMillan, E. M. and Abelson, P. H. (1940). Radioactive element 93, *Physical Review* **57**: 1185–1186.
- Meinrath, G. (1994). Np(V) carbonates in solid state and aqueous solution, *Journal of Radioanalytical and Nuclear Chemistry, Letters* **186**(3): 257–272.
- Misaelides, P. and Godelitsas, A. (1999). Interaction of actinides with natural microporous materials: A review, *Czechoslovak Journal of Physics* **49**: 167–174.
- Nagasaki, S. and Tanaka, S. (2000). Sorption equilibrium and kinetics of NpO_2^+ on dispersed particles of Na-montmorillonite, *Radiochimica Acta* **88**: 705–709.

- Nagasaki, S., Tanaka, S. and Suzuki, A. (1997). Interfacial behavior of actinides with colloides in the geosphere, *Journal of Nuclear Materials* **248**: 323–327.
- Neck, V., Runde, W., Kim, J. I. and Kanellakopulos, B. (1994). Solid-liquid equilibrium reaction of neptunium(V) in carbonate solution at different ionic strength, *Radiochimica Acta* **65**: 29–37.
- Newville, M. (2004a). Fundamentals of X-ray absorption fine structure, *Technical report*, Consortium for Advanced Radiation Sources, University of Chicago, IL. Version 1.6.1.
- Newville, M. (2004b). Fundamentals of XAFS, *Technical report*, Consortium for Advanced Radiation Sources, University of Chicago, IL.
- Nitsche, H. (1991). Solubility studies of transuranium elements for nuclear waste disposal: Principles and overview, *Radiochimica Acta* **52/53**: 3–8.
- Nuclear Energy Institute (2000). Nuclear technology milestones 1942-2000, http://scienceclub.nei.org/scienceclub/4yourclassproject/4ycp_timeline.html. Washington, DC.
- van Olphen, H. and Fripiat, J. J. (1979). *Data Handbook for Clay Materials and Non-metallic Minerals*, Pergamon Press.
- Omel'yanenko, B. I., Livshits, T. S., Yudintsev, S. V. and Nikonov, B. S. (2007). Natural and artificial minerals as matrices for immobilization of actinides, *Geology of Ore Deposits* **49**(3): 173–193.
- ORACLE'ThinkQuest Education Foundation (–). Chemystery – interactive guide to understanding chemistry: Electron configurations, <http://library.thinkquest.org/3659/structures/electronconfig.html>.
- Paglia, G., Rohl, A. L., Buckley, C. E. and Gale, J. D. (2005). Determination of the structure of γ -alumina from interatomic potential and first-principle calculations: The requirement of significant numbers of nonspinel positions to achieve an accurate structural model, *Physical Review B* **71**(224115): 1–16.
- Pfennig, G., Klewe-Nebenius, H. and Seelmann-Eggebert, W. (1998). Karlsruher Nuklidkarte – Chart of the Nuclides, Forschungszentrum Karlsruhe.
- Pinto, H. P., Nieminen, R. M. and Elliot, S. D. (2004). *Ab initio* study of γ -Al₂O₃ surfaces, *Physical Review B* **70**(125402): 1–11.

- Radiation Safety Information Computational Center (RSICC), Oak Ridge National Laboratory and Grove Engineering (2006). World Information Service on Energy (WISE) Uranium Project, Universal Decay Calculator (Vers. B), <http://www.wise-uranium.org/rccb.html>. Last updated 21 March 2006.
- Ravel, B. (2000). Introduction to EXAFS experiments and theory, <http://cars9.uchicago.edu/~ravel/talks/course/basics.pdf>. Version 0.02.
- Ravel, B. (2001). Introduction to EXAFS analysis using theoretical standards, <http://feff.phys.washington.edu/~ravel/course/basics/IEAUTS/annotation/annotation.ps>, Naval Research Laboratory, Washington, DC.
- Ravel, B. (2008). Advanced topics in EXAFS analysis, http://xafs.org/Workshops/APS2008?action=AttachFile&do=get&target=Ravel_Advanced.pdf. APS XAFS Summer School August 5-8, 2008.
- Reed, D. T., Sherman, C. and Hermes, A. (2000). Speciation of neptunium in spent fuel, *Annual Report Appendix 4*, Nuclear Energy Research Initiative (NERI).
- Rehr, J. J. and Albers, R. C. (2000). Theoretical approaches to X-ray absorption fine structure, *Reviews of Modern Physics* **72**(3): 621–654.
- Reich, T. (2005). Speciation analysis with synchrotron radiation, *Analytical and Bioanalytical Chemistry* **383**(1): 10–11.
- Reich, T., Bernhard, G., Geipel, G., Funke, H., Hennig, C., Rossberg, A., Matz, W., Schell, N. and Nitsche, H. (2000). The Rossendorf Beam Line ROBL – a dedicated experimental station for XAFS measurements of actinides and other radionuclides, *Radiochimica Acta* **88**: 633–637.
- Righetto, L., Bidoglio, G., Marcandalli, B. and Bellobono, I. R. (1988). Surface interactions of actinides with alumina colloids, *Radiochimica Acta* **44/45**: 73–75.
- RÖMPP Online (2007a). RD-14-01945: Nukleare Endlagerung, <http://www.roempp.com>. Version 3.1.
- RÖMPP Online (2007b). RD-18-00068: Radioaktive Abfälle, <http://www.roempp.com>. Version 3.1.
- Rudolph, S. (2004). Übersicht über die Systematik der Tonminerale bzw. Schichtsilicate, <http://www.a-m.de/deutsch/lexikon/ton-tafell.htm>. Büro für angewandte Mineralogie, Tönisvorst.

- Runde, W. (2000). The chemical interactions of actinides in the environment, *Los Alamos Science* **26**: 392–411.
- Sabodina, M. N., Kalmykov, S. N., Artem'eva, K. A., Zakharova, E. V. and Sapozhnikov, Y. A. (2006). Behavior of Cs, Np(V), Pu(IV), and U(VI) in pore water of bentonite, *Radiochemistry* **48**: 488–492.
- Sayers, D. E., Stern, E. A. and Lytle, F. W. (1971). New technique for investigating noncrystalline structures: Fourier analysis of the extended X-ray-absorption fine structure, *Physical Review Letters* **27**(18): 1204–1207.
- Scheffer, F., Schachtschabel, P. and Blume, H.-P. (2002). *Lehrbuch der Bodenkunde*, Spektrum-Lehrbuch, 15th edn, Spektrum Akademischer Verlag.
- Schwertmann, U. (1993). Oxide und Hydroxide, in K. Jasmund and G. Lagaly (eds), *Tonminerale und Tone – Struktur, Eigenschaften, Anwendungen und Einsatz in Industrie und Umwelt*, Steinkopff Verlag, chapter 2.6, pp. 68–88.
- Seibert, A., Mansel, A., Marquardt, C. M., Keller, H., Kratz, J. V. and Trautmann, N. (2001). Complexation behaviour of neptunium with humic acid, *Radiochimica Acta* **89**: 505–510.
- Shilov, V. P. and Yusov, A. B. (1999). Dimers in photochemistry and chemistry of *f* elements, *Radiochemistry* **41**(5): 441–444.
- Shilov, V. P. and Yusov, A. B. (2001). Photochemical reactions of neptunium ions in aqueous carbonate solutions, *Radiochemistry* **43**(4): 371–378.
- Siegel, M. D. and Bryan, C. R. (2003). Environmental geochemistry of radioactive contamination, *Sandia Report SAND2003-2063*, Sandia National Laboratory, Albuquerque, NM, and Livermore, CA, USA.
- Sigg, L. and Stumm, W. (1996). *Aquatische Chemie – eine Einführung in die Chemie wässriger Lösungen und natürlicher Gewässer*, 4th edn, B.G. Teubner.
- Skanthakumar, S., Antonio, M. R. and Soderholm, L. (2008). A comparison of neptunyl(V) and neptunyl(VI) solution coordination: The stability of cation–cation interactions, *Inorganic Chemistry* **47**: 4591–4595.
- Sohlberg, K., Pennycook, S. J. and Pantelides, S. T. (1999). Hydrogen and the structure of the transition aluminas, *Journal of the American Chemical Society* **121**: 7493–7499.

- Störr, M. (1993). Lagerstätten von Tonrohstoffen, *in* K. Jasmund and G. Lagaly (eds), *Tonminerale und Tone – Struktur, Eigenschaften, Anwendungen und Einsatz in Industrie und Umwelt*, Steinkopff Verlag, chapter 5, pp. 193–211.
- Stumm, W. (1992). *Chemistry of the Solid-Water Interface – Processes at the Mineral-Water and Particle-Water Interface in Natural Systems*, John Wiley & Sons, Inc.
- Szabó, Z., Toraiishi, T., Vallet, V. and Grenthe, I. (2006). Solution coordination chemistry of actinides: Thermodynamics, structure and reaction mechanisms, *Coordination Chemistry Reviews* **250**: 784–815.
- Tadjerpisheh, N. and Kohler, E. E. (1998). Tone und Tonminerale – eine Übersicht, *in* W. Hiltmann and B. Stribrny (eds), *Handbuch zur Erkundung des Untergrundes von Deponien und Altlasten – Band 5: Tonmineralogie und Bodenphysik*, Springer-Verlag, chapter 1.1, pp. 1–5.
- Takeno, N. (2005). Atlas of Eh-pH diagrams – Intercomparison of thermodynamic databases, *Geological Survey of Japan Open File Report No. 419*, National Institute of Advanced Industrial Science and Technology, Research Center for Deep Geological Environments.
- Teo, B. K. (1986). *EXAFS: Basic Principles and Data Analysis*, Springer-Verlag.
- Thompson, R. C. (1982). Neptunium - the neglected actinide: A review of the biological and environmental literature, *Radiation Research* **90**: 1–32.
- Tochiyama, O., Yamazaki, H. and Mikami, T. (1996). Sorption of Neptunium(V) on various aluminium oxides and hydrous aluminium oxides, *Radiochimica Acta* **73**: 191–198.
- Tsushima, S. and Suzuki, A. (2000). Hydration numbers of pentavalent and hexavalent uranyl, neptunyl, and plutonyl, *Journal of Molecular Structure* **529**: 21–25.
- Tuli, J. K. (2005). *Nuclear Wallet Cards*, 7th edn, National Nuclear Data Center, Brookhaven National Laboratory, Upton, N.Y. <http://www.nndc.bnl.gov>.
- Turner, D. R., Bertetti, F. P. and Pabalan, R. T. (2006). Applying surface complexation modelling to radionuclide sorption, *in* J. Lützenkirchen (ed.), *Surface Complexation Modelling*, Elsevier Ltd., chapter 21, pp. 553–604.
- Turner, D. R., Pabalan, R. T. and Bertetti, F. P. (1998). Neptunium(V) sorption on montmorillonite: An experimental and surface complexation modeling study, *Clays and Clay Minerals* **46**(3): 256–269.

- Vantelon, D., Montarges-Pelletier, E., Michot, L. J., Briois, V., Pelletier, M. and Thomas, F. (2003). Iron distribution in the octahedral sheet of dioctahedral smectites. An Fe K-edge X-ray absorption spectroscopy study, *Physics and Chemistry of Minerals* **30**: 44–53.
- Vicente Vilas, V. (2008). private communication.
- Vlaic, G. and Olivi, L. (2004). EXAFS spectroscopy: a brief introduction, *Croatica Chemica Acta* **77**(3): 427–433.
- Volkov, Y. F., Visyashcheva, G. I., Tomilin, S. V., Kapshukov, I. I. and Rykov, A. G. (1981). Study of carbonate compounds of pentavalent actinides with alkali metal cations. IX. Determination of the crystal structure of $M_3AnO_2(CO_3)_2 \cdot n H_2O$ compounds, *Radiokhimiya Radka* **23**(2): 243–247.
- Wang, P., Anderko, A. and Turner, D. R. (2001). Thermodynamic modeling of the adsorption of radionuclides on selected minerals. i: Cations, *Industrial and Engineering Chemical Research* **40**: 4428–4443.
- World Nuclear Association (2008). World nuclear power reactors 2007-08 and uranium requirements, <http://www.world-nuclear.org>.
- xtimeline by Famento, Inc. (2007-2008). History of nuclear power, <http://www.xtimeline.com/timeline/History-of-Nuclear-Power>.
- Yamaguchi, T., Nakayama, S. and Yoshida, T. (2004). Interactions between anionic complex species of actinides and negatively charged mineral surfaces, *Radiochimica Acta* **92**: 677–682.
- Yoshida, Z., Johnson, S. G., Kimura, T. and Krsul, J. R. (2006). Neptunium, in L. R. Morss, N. M. Edelstein and J. Fuger (eds), *The Chemistry of the Actinide and Transactinide Elements, Third Edition*, Springer, chapter 6, pp. 699–812.
- Yusov, A. B., Fedoseev, A. M., Isakova, O. V. and Delegard, C. H. (2005). Complexation of Np(V) with silicate ions, *Radiochemistry* **47**(1): 39–44.
- Zysset, M. and Schindler, P. W. (1996). The proton promoted dissolution kinetics of K-montmorillonite, *Geochimica et Cosmochimica Acta* **60**(6): 921–931.

APPENDIX



Chronology of Nuclear Research and Development

Sources: U.S. Department of Energy DOE (2003), Nuclear Energy Institute, Washington, DC (2000), and xtimeline (2007-2008).

The 1940's

1942 December 2. The first self-sustaining nuclear chain reaction is brought into criticality and operation at the University of Chicago by Enrico Fermi.

1945 July 16. The U.S. Army's Manhattan Engineer District (MED) tests the first atomic bomb at Alamogordo, New Mexico, under the code name Manhattan Project.

1945 August 6. The atomic bomb nicknamed Little Boy is dropped on Hiroshima, Japan. Three days later, another bomb, Fat Man, is dropped on Nagasaki, Japan. Japan surrenders on August 15, ending World War II.

1946 August 1. The Atomic Energy Act of 1946 creates the Atomic Energy Commission (AEC) to control nuclear energy development and explore peaceful uses of nuclear energy.

1947 October 6. The AEC first investigates the possibility of peaceful uses of atomic energy, issuing a report the following year.

1949 March 1. The AEC announces the selection of a site in Idaho for the National Reactor Testing Station.

The 1950's

1951 December 20. In Arco, Idaho, Experimental Breeder Reactor I produces the first electric power from nuclear energy, lighting four light bulbs.

1952 June 14. Keel for the Navy's first nuclear submarine, Nautilus, is laid at Groton, Connecticut.

1953 March 30. Nautilus starts its nuclear power units for the first time.

1953 December 8. President Eisenhower delivers his 'Atoms for Peace' speech before the United Nations. He calls for greater international cooperation in the development of atomic energy for peaceful purposes.

1954 August 30. President Eisenhower signs the Atomic Energy Act of 1954, the first major amendment of the original Atomic Energy Act, giving the civilian nuclear power program further access to nuclear technology.

1955 January 10. The AEC announces the Power Demonstration Reactor Program. Under the program, AEC and industry will cooperate in constructing and operating experimental nuclear power reactors.

1955 July 17. Arco, Idaho, population 1 000, becomes the first town powered by a nuclear powerplant, the experimental boiling water reactor BORAX III.

1955 August 8-20. Geneva, Switzerland, hosts the first United Nations International Conference on the Peaceful Uses of Atomic Energy.

1957 July 12. The first power from a civilian nuclear unit is generated by the Sodium Reactor Experiment at Santa Susana, California. The unit provided power until 1966.

1957 September 2. The Price-Anderson Act provides financial protection to the public and AEC licensees and contractors if a major accident occurs at a nuclear powerplant.

1957 October 1. The United Nations creates the International Atomic Energy Agency (IAEA) in Vienna, Austria, to promote the peaceful use of nuclear energy and prevent the spread of nuclear weapons around the world.

1957 December 2. The world's first large-scale nuclear powerplant begins operation in Shippingport, Pennsylvania. The plant reaches full power three weeks later and supplies electricity to the Pittsburgh area.

1958 May 22. Construction begins on the world's first nuclear-powered merchant ship, the N.S. Savannah, in Camden, New Jersey. The ship is launched July 21, 1959.

1959 October 15. Dresden-1 Nuclear Power Station in Illinois, the first U.S. nuclear plant built entirely without government funding, achieves a self-sustaining nuclear reaction.

The 1960's

1960 August 19. The third U.S. nuclear powerplant, Yankee Rowe Nuclear Power Station, achieves a self-sustaining nuclear reaction.

Early 1960's. Small nuclear-power generators are first used in remote areas to power weather stations and to light buoys for sea navigation.

1961 November 22. The U.S. Navy commissions the world's largest ship, the U.S.S. Enterprise. It is a nuclear-powered aircraft carrier with the ability to operate at speeds up to 30 knots for distances up to 400 000 miles (740 800 kilometres) without refuelling.

1963 December 12. Jersey Central Power and Light Company announces its commitment for the Oyster Creek nuclear powerplant, the first time a nuclear plant is ordered as an economic alternative to a fossil-fuel plant.

1964 August 26. President Lyndon B. Johnson signs the Private Ownership of Special Nuclear Materials Act, which allows the nuclear power industry to own the fuel for its units. After June 30, 1973, private ownership of the uranium fuel is mandatory.

1964 October 3. Three nuclear-powered surface ships, the Enterprise, Long Beach, and Bainbridge, complete 'Operation Sea Orbit', an around-the-world cruise.

1965 April 3. The first nuclear reactor in space (SNAP-10A) is launched by the United States. SNAP stands for Systems for Nuclear Auxiliary Power.

The 1970's

1970 March 5. The United States, United Kingdom, Soviet Union, and 45 other nations ratify the Treaty for Non-Proliferation of Nuclear Weapons.

1971. Twenty-two commercial nuclear powerplants are in full operation in the United States. They produce 2.4 percent of U.S. electricity at this time.

1973. U.S. utilities order 41 nuclear powerplants, a one-year record.

1974. The first 1 000-megawatt-electric nuclear powerplant goes into service – Commonwealth Edison's Zion 1 Plant.

1974 October 11. The Energy Reorganization Act of 1974 divides AEC functions between two new agencies – the Energy Research and Development Administration (ERDA), to carry out research and development, and the Nuclear Regulatory Commission (NRC), to regulate nuclear power.

1977 April 7. President Jimmy Carter announces the United States will defer indefinitely plans for reprocessing spent nuclear fuel.

1977 August 4. President Carter signs the Department of Energy Organization Act, which transfers ERDA functions to the new Department of Energy (DOE).

1977 October 1. DOE begins operations.

1979 March 28. The worst accident in U.S. commercial reactor history occurs at the Three Mile Island nuclear power station near Harrisburg, Pennsylvania. The accident is caused by a loss of coolant from the reactor core due to a combination of mechanical malfunction and human error. No one is injured, and no overexposure to radiation results from the accident. Later in the year, the NRC imposes stricter reactor safety regulations and more rigid inspection procedures to improve the safety of reactor operations.

1979. Seventy-two licensed reactors generate 12 percent of the electricity produced commercially in the United States.

The 1980's

1980 March 26. DOE initiates the Three Mile Island research and development program to develop technology for disassembling and de-fuelling the damaged reactor. The program will continue for 10 years and make significant advances in developing new nuclear safety technology.

1982 October 1. After 25 years of service, the Shippingport Power Station is shut down. Decommissioning would be completed in 1989.

1983 January 7. The Nuclear Waste Policy Act (NWPA) establishes a program to site a repository for the disposal of high-level radioactive waste, including spent fuel from nuclear powerplants. It also establishes fees for owners and generators of radioactive waste and spent fuel, who pay the costs of the program.

1983. Nuclear power generates more electricity than natural gas.

1984. The atom overtakes hydropower to become the second largest source of electricity, after coal. Eighty-three nuclear power reactors provide about 14 percent of the electricity produced in the United States.

1985. The Institute of Nuclear Power Operations forms a national academy to accredit every nuclear powerplant's training program.

1986. The Perry Power Plant in Ohio becomes the 100th U.S. nuclear powerplant in operation.

1986 April 26. Operator error causes two explosions at the Chernobyl No. 4 nuclear powerplant in the former Soviet Union. The reactor has an inadequate

containment building, and large amounts of radiation escape. A plant of such design would not be licensed in the United States nor in any Western country.

1987 December 22. The Nuclear Waste Policy Act (NWPA) is amended. Congress directs DOE to study only the potential of the Yucca Mountain, Nevada, site for disposal of high-level radioactive waste.

1988. U.S. electricity demand is 50 percent higher than in 1973.

1989. One hundred and nine nuclear powerplants provide 19 percent of the electricity used in the U.S.; 46 units have entered service during the decade.

1989 April 18. The NRC proposes a plan for reactor design certification, early site permits, and combined construction and operating licenses.

The 1990's

1990 March. DOE launches a joint initiative to improve operational safety practices at civilian nuclear powerplants in the former Soviet Union.

1990. America's 110 nuclear powerplants set a record for the amount of electricity generated, surpassing all fuel sources combined in 1956.

1990 April 19. The final shipment of damaged fuel from the Three Mile Island nuclear plant arrives at a DOE facility in Idaho for research and interim storage. This ends DOE's 10-year Three Mile Island research and development program.

1991. One hundred and eleven nuclear powerplants operate in the United States with a combined capacity of 99 673 megawatts. They produce almost 22 percent of the electricity generated commercially in the United States.

1992 February 26. DOE signs a cooperative agreement with the nuclear industry to co-fund the development of standard designs for advanced lightwater reactors.

1992 October 24. The Energy Policy Act of 1992 is signed into law. The Act makes several important changes in the licensing process for nuclear powerplants.

1992 December 2. The 50th anniversary of the historic Fermi experiment is celebrated worldwide.

1993 March 30. The U.S. nuclear utility consortium, the Advanced Reactor Corporation (ARC), signs a contract with Westinghouse Electric Corporation to perform engineering work for an advanced, standardised 600-megawatt pressurised-water reactor. Funding for this next-generation plant comes from ARC, Westinghouse, and DOE.

1993 September 6. The U.S. nuclear utility consortium, ARC, signs a contract with General Electric Company for cost-shared, detailed engineering of a

standardised design for a large, advanced nuclear powerplant. The engineering is being funded under a joint program among utilities, General Electric, and DOE.

1993 December. In 1993, two decades after the first oil embargo, the 109 nuclear power plants operating in the United States generate 610 billion kilowatt-hours of net electricity, providing about one-fifth of the nation's electricity.

1994 January 14. More than a half century after President Eisenhower stood before the United Nations and urged the countries of the world to take nuclear materials 'out of the hands of the soldiers...[and place them] into the hands of those who will...adapt [them] to the arts of peace', the U.S. again leads the world in promoting the peaceful uses of nuclear technology by signing a contract to buy uranium from the Russian Federation that could be blended down into power plant fuel, ensuring it will never again be used for warheads.

1994 July. The Nuclear Regulatory Commission issues final design approval for the first two of four advanced nuclear power plant designs – General Electric's Advanced Boiling Water Reactor (ABWR) and ABB Combustion Engineering's System 80+. The approval means that all major design and safety issues have been resolved to the satisfaction of the NRC staff and the Advisory Committee on Reactor Safeguards. The two plants are the first to obtain final design approval under the NRC's new regulations for licensing standardised plant designs. The NRC will now prepare a rulemaking, which will include public comment, to codify the designs.

1995 April 7. The NRC publishes proposed design certification rules for General Electric's Advanced Boiling Water Reactor (ABWR) and ABB Combustion Engineering's System 80+ plant designs. These rulemakings will codify the ABWR and System 80+ final design approvals issued in 1994. Certification is expected in 1996.

1996 February 9. The NRC grants the Tennessee Valley Authority (TVA) a full-power license for its Watts Bar 1 nuclear power plant, bringing the number of operating nuclear units in the United States to 110.

1996 September 30. First-of-a-kind engineering design is completed for the GE Advanced Boiling Water Reactor.

1996 November 7. Kashiwazaki-Kariwa 6, the world's first Advanced Boiling Water Reactor, begins commercial service in Japan – ahead of schedule and under budget.

1997 May 12. The NRC issues design certification for the General Electric Advanced Boiling Water Reactor. It is valid for the next 15 years.

1997 May 20. The NRC issues design certification for the ABB Combustion Engineering System 80+. It is valid for the next 15 years.

1998 January 12. President Clinton certifies that China supports international nuclear nonproliferation efforts, paving the way for the sale of U.S. nuclear technology to that country.

1998 April 10. Baltimore Gas and Electric Co. submits an application to the NRC to renew the license of its two-unit Calvert Cliffs nuclear power plant – the first U.S. company to apply for a 20-year extension of its 40-year license.

1998 July 7. Duke Power Co. submits an application to the NRC to renew the license of its three-unit Oconee nuclear power plant.

1999 July 13. Entergy Nuclear closes on its purchase of the Pilgrim Station from Boston Edison Co., the first completed nuclear plant sale in the nation.

The 2000's First Decade

2000 March 23. The NRC issues the first-ever license renewal to Constellation Energy's Calvert Cliffs Nuclear Power Plant, allowing an additional 20 years of operation.

2000 May 23. The NRC approves a 20-year extension to the operating license of Duke Energy's three-unit Oconee Nuclear Station.

2002 December 20. The Bulgarian Council of Ministers votes to restart construction of the Belene Nuclear Power Plant.

2004. In the U.S., three consortia responded in 2004 to the U.S. Department of Energy's solicitation under the Nuclear Power 2010 Program and were awarded matching funds – the Energy Policy Act of 2005 authorised loan guarantees for up to six new reactors, and authorised the DOE to build a reactor based on the Generation IV Very-High-Temperature Reactor concept to produce both electricity and hydrogen. As of the early 21st century, nuclear power is of particular interest to both China and India to serve their rapidly growing economies – both are developing fast breeder reactors.

2005. Since the late 1980's capacity has risen much more slowly, reaching 366 GW in 2005. Between around 1970 and 1990, more than 50 GW of capacity was under construction (peaking at over 150 GW in the late 70's and early 80's) – in 2005, around 25 GW of new capacity was planned. More than two-thirds of all nuclear plants ordered after January 1970 were eventually cancelled. Many countries remain active in developing nuclear power, including Japan, China and India, all actively developing both fast and thermal technology, South Korea and the United States, developing thermal technology only, and South Africa and China, developing versions of the Pebble Bed Modular Reactor (PBMR). Finland, France and Rumania actively pursue nuclear programs (the only three

countries in the EU to do so); Finland has a new European Pressurised Reactor under construction by Areva, which is currently two years behind schedule. Japan has an active nuclear construction program with new units brought on-line in 2005.

A large 2005 study of powerplant accidents found that the death toll includes the 50 workers who died of acute radiation syndrome, nine children who died from thyroid cancer, and an estimated 4000 excess cancer deaths in the future. This accident occurred due to several critical design flaws in the Soviet RBMK reactors, such as lack of a containment building which would have stopped radioactive emissions from that accident, and that security in the remaining RBMK reactors have greatly improved. As such, the Chernobyl accident, involving a badly designed RBMK reactor in the Soviet Union, operated dangerously in an unauthorised way by untrained personnel, has absolutely no relevance to the question of the use of nuclear energy in the Western world today.

2005 September 22. Two sites in the U.S. are selected to receive new power reactors (exclusive of the new power reactor scheduled for INL).

2005 December. Russia plans to build another breeder reactor, BN-800, at Beloyarsk nuclear power plant – at this date the only unit producing power is BN-600 in Beloyarsk, Russia, with an electricity output of 600 MW. Breeder technology has been used in several reactors, but the high cost of reprocessing fuel safely requires prices of more than 200 USD/kg before becoming justified economically. Also, Japan's Monju reactor is planned for restart (having been shut down since 1995), and both China and India intend to build breeder reactors.

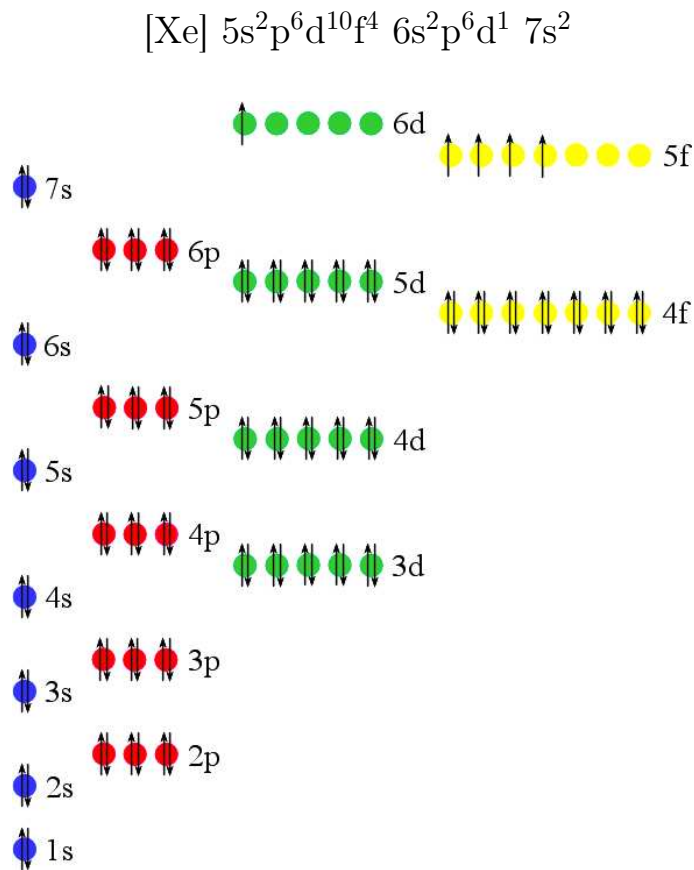
2007 August. TVA is approved to restart construction of Watts Bar 2. The reactor is scheduled to be completed and come online in 2013.

2007 October. Two new plants are scheduled to build in Texas. They should be online by 2014.

B

Nuclear Properties of Np

B.1 Electronic Configuration of ${}_{93}\text{Np}$



(source: ORACLE ThinkQuest Education Foundation, modified)

B.2 Isotopes and Decay Modes

Nuclear Wallet Cards

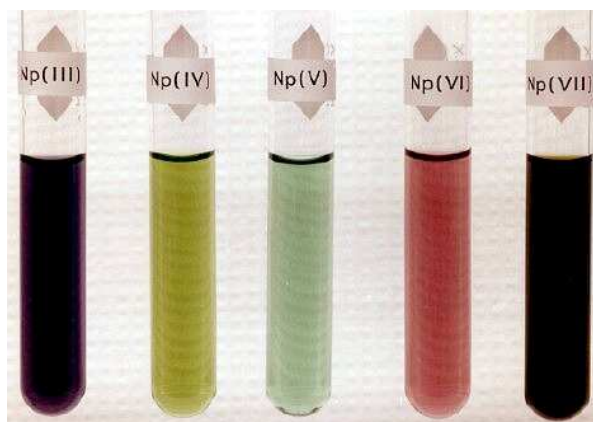
Nuclide		Δ	$T_{1/2}$, Γ , or	
Z	El A	(MeV)	Abundance	Decay Mode
93 Np	225	(9/2-)	31.59	>2 μ s α
	226		32.74s	35 ms 10 α
	227		32.56	0.51 s 6 α
	228		33.7s	61.4 s 14 ϵ 60%, α 40%
	229		33.78	4.0 m 4 α 68%, ϵ 32%
	230		35.24	4.6 m 3 ϵ \leq 97%, α \geq 3%
	231	(5/2)	35.63	48.8 m 2 ϵ 98%, α 2%
	232	(4+)	37.4s	14.7 m 3 ϵ
	233	(5/2+)	37.95	36.2 m 1 ϵ , α \leq $1.0 \times 10^{-3}\%$
	234	(0+)	39.957	4.4 d 1 ϵ
	235	5/2+	41.045	396.1 d 12 ϵ , α $2.6 \times 10^{-3}\%$
	236	(6-)	43.38	154×10^3 y 6 ϵ 87.3%, β - 12.5%, α 0.16%
	236m	1	43.44	22.5 h 4 ϵ 52%, β - 48%
	237	5/2+	44.873	2.144×10^6 y 7 α , SF \leq $2 \times 10^{-10}\%$
	238	2+	47.456	2.117 d 2 β -
	239	5/2+	49.312	2.356 d 3 β -
	240	(5+)	52.31	61.9 m 2 β -
	240m	(1+)	52.31	7.22 m 2 β - 99.88%, IT 0.12%
	241	(5/2+)	54.26	13.9 m 2 β -
	242	(1+)	57.4	2.2 m 2 β -
	242m	(6+)	57.4	5.5 m 1 β -
	243	(5/2-)	59.88s	1.85 m 15 β -
	244	(7-)	63.2s	2.29 m 16 β -

for explanation see: National Nuclear Data Center (Tuli, 2005)

B.3 Colour of Np-Ions in Aqueous Solution

	Ion	Colour	Solid	Colour
III	Np^{3+}	crimson-violet		
IV	Np^{4+}	yellow-green	$\text{NpO}_3 \cdot \text{H}_2\text{O}$	black
V	NpO_2^+	green	Np_2O_5	dark brown
VI	NpO_2^{2+}	pink-red	NpO_2	brown
VII	NpO_2^{3+}	deep green		

(Holleman and Wiberg, 2007)



(source: http://www.chemie-master.de/pse/Np_ox_st_.jpg)

C

Radioactivity

C.1 Types of Radioactive Decay

Alpha (α)	Heavy, proton rich nuclides emit an alpha particle (${}^4_2\text{He}$) – the daughter nuclide contains two protons (Z) and two neutrons (N) less than the parent: ${}^A_Z X^N \rightarrow \alpha + {}^{A-4}_{Z-2} Y^{N-2}$;
Beta-minus (β^-)	In neutron rich nuclides, a neutron decays to a proton – thereby an electron (β^-) is emitted together with an anti-neutrino ($\bar{\nu}$): $n \rightarrow p + e^- + \bar{\nu}$. Z increases by one and N decreases by one: ${}^A_Z X^N \rightarrow e^- + \bar{\nu} + {}^A_{Z+1} Y^{N-1}$;
Beta-plus (β^+)	In proton rich nuclides, a proton in the nucleus changes to a neutron – thereby a positron (β^+) is emitted together with a neutrino (ν): $p \rightarrow n + e^+ + \nu$. Z decreases by one and N increases by one: ${}^A_Z X^N \rightarrow e^+ + \nu + {}^A_{Z-1} Y^{N+1}$;
Electron capture (ε or ec)	An orbital electron is ‘captured’ by the nucleus resulting in a proton being converted to a neutron and a neutrino (ν). The daughter nucleus is usually left in an excited state. The changes in Z and N are the same as for β^+ decay; commonly, nuclides with neutron deficiency can proceed by either mechanism;

Gamma (γ)	A nucleus in an excited state decays through the emission of a photon; there is no change in Z or N . After each of the previously discussed decay modes α , β^- , β^+ , and ε the nuclide is most often left in an excited state and decays to the ground state by emission of one or more consecutive γ rays (isomeric transition). If there is a significant delay between these processes, the γ emission is considered a separate event;
Internal conversion (IC)	A nucleus decays from an excited state through emission of an orbital electron (usually from the K-shell);
Proton (p)	A proton is ejected from the nucleus;
Neutron (n)	A neutron is ejected from the nucleus;
Spontaneous fission (SF)	The parent nucleus splits into two daughter nuclei (D_H , D_L) with mass and charge in the region of about half that of the parent. Several neutrons (νn) are emitted additionally;
Special beta-decay processes (β^-n , $\beta^+\alpha$, β^+p)	Particle (neutron, alpha, proton) emission immediately following beta decay;
Heavy-ion radioactivity	A heavy parent decays by emission of a light ion.

(Magill and Galy, 2005; Siegel and Bryan, 2003)

C.2 Nuclear Data Sources

Information on nuclear structure and decay data are available in various forms. Firestone (2003) provides a brief but extensive overview about the different sources of printed media, websites, the internet, software, and databases.

C.3 Decay Series

²³⁸ U decay series			²³⁵ U decay series			²³² Th decay series			²³⁷ Np decay series		
²³⁸ U	4.47·10 ⁹ y	α	²³⁵ U	7.04·10 ⁸ y	α	²³² Th	1.40·10 ¹⁰ y	α	²³⁷ Np	2.14·10 ⁶ y	α
²³⁴ Th	24.1 d	β ⁻	²³¹ Th	1.06 d	β ⁻	²²⁸ Ra	5.76 y	β ⁻	²³³ Pa	27.0 d	β ⁻
²³⁴ Pa	1.17 m	β ⁻	²³¹ Pa	3.28·10 ⁴ y	α	²²⁸ Ac	6.15 h	β ⁻	²³³ U	1.59·10 ⁵ y	α
²³⁴ U	2.46·10 ⁵ y	α	²²⁷ Ac	21.8 y	β ⁻	²²⁸ Th	1.91 y	α	²²⁹ Th	7.30·10 ³ y	α
²³⁰ Th	7.54·10 ⁴ y	α	²²⁷ Th	18.7 d	α	²²⁴ Ra	3.66 d	α	²²⁵ Ra	14.9 d	β ⁻
²²⁶ Ra	1.6·10 ³ y	α	²²³ Ra	11.4 d	α	²²⁰ Rn	55.6 s	α	²²⁵ Ac	10.0 d	α
²²² Rn	3.82 d	α	²¹⁹ Rn	4.0 s	α	²¹⁶ Po	0.15 s	α	²²¹ Fr	4.8 m	α
²¹⁸ Po	3.10 m	α	²¹⁵ Po	1.78·10 ⁻³ s	α	²¹² Pb	10.6 h	β ⁻	²¹⁷ At	32 ms	α
²¹⁴ Pb	27.0 m	β ⁻	²¹¹ Pb	36.1 m	β ⁻	²¹² Bi	60.6 m	β ⁻	²¹³ Bi	45.6 m	β ⁻
²¹⁴ Bi	19.9 m	β ⁻	²¹¹ Bi	2.14 m	α	²¹² Po	45 s	α	²¹³ Po	4 μs	α
²¹⁴ Po	1.64·10 ⁻⁴ s	α	²⁰⁷ Tl	4.78 m	β ⁻	²⁰⁸ Pb	Stable		²⁰⁹ Pb	3.25 h	β ⁻
²¹⁰ Pb	22.6 y	β ⁻	²⁰⁷ Pb	Stable					²⁰⁹ Bi	Stable	
²¹⁰ Bi	5.01 d	β ⁻									
²¹⁰ Po	138 d	α									
²⁰⁶ Pb	Stable										

²³⁹ Pu decay series		²³⁸ Pu decay series		²⁴¹ Am decay series				
²³⁹ Pu	2.44·10 ⁴ y	α	²³⁸ Pu	87.7 y	α	²⁴¹ Am	433 y	α
²³⁵ U	Follows ²³⁵ U series		²³⁴ U	As in ²³⁸ U series		²³⁷ Np	Follows ²³⁷ Np series	

Figure C.1: Major decay paths for several important actinides (Parrington et al., 1996, cited in Siegel and Bryan, 2003).

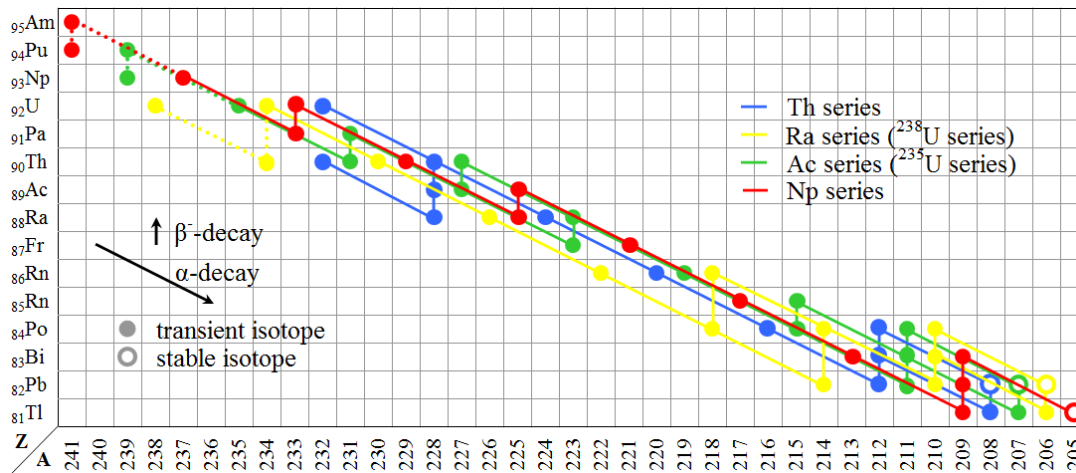


Figure C.2: Illustration of the decay chains (source: http://commons.wikimedia.org/wiki/File:Radioactive_decay_chains_diagram.svg, modified).

D

Disposal of Radioactive Material

D.1 Treatment of Nuclear Waste

The IAEA identified two overlying principles of underground disposal of radioactive waste, namely its isolation from the human environment without relying on future generations to maintain the integrity of the repository, and insuring long-term protection of humans as well as the environment in accordance with current internationally agreed principles (IAEA Safety Standards, 1989). Under these maxims, a multibarrier concept has been developed comprising the following components:

1. Calcination: Destruction of the nitrates from, e.g., reprocessing and conversion of the radionuclides to their metal oxide.
2. Vitrification: Incorporation of the calcined product into a glass matrix, which has, owing to its amorphous nature, a greater mechanical, structural, and thermal strength as well as better radiation resistance compared to a crystalline state. The calcined fission products are mixed with the components of the borosilicate glass (ca. 1:4) and melted together at 1 000-2 000 °C.¹
3. Stainless steel or copper containers: Dimensions and packing are linked to the thermal load of the content in that the container surface should not extend 200 °C. For reinforcement against environmental pressures, the canisters may be backfilled with lead.

The efficiency of this procedure is approximately 1 t of spent fuel condensed into 200 kg vitrified glass and the expected conditions are 150-200°C in the near field and 100-300 bar at 500-1 000 m depth.

(Loveland et al., 2006; Choppin and Wong, 1996)

¹Germany utilises phosphate glass, which is incorporated into a metal alloy matrix; the calcination step is omitted due to the denitration with phosphoric acid.

Liquid wastes are evaporated, precipitated, sedimented, filtered, centrifuged, etc. and solidified in borosilicate or phosphate glasses, asphalt, bitumen-salt-mixtures, concrete, ceramic matrices, or synthetic rocks. With the so-called PUREX process, $\sim 90\%$ of the fission products can be eliminated from the solutions. Flammable waste materials can be burned in a way that all radioactivity remains in the ashes, which is treated like described above (RÖMPP Online, 2007b).



Figure D.1: Swiss transport and storage container for highly radioactive waste (Visitors Centre psi forum, Paul Scherrer Intitut, Villigen, Switzerland).

International information on all parts of the nuclear fuel cycle are supplied by the World Nuclear Association (WNA) on the Internet under the address

<http://www.world-nuclear.org>.

The treatment and conditioning of nuclear wastes as well as storage and disposal options considered worldwide are presented in Appendices 1 and 2 of the information paper 'Waste Management in the Nuclear Fuel Cycle' accessible via the main menu. A thorough and comprehensive view of the German situation is provided by the Gesellschaft für Nuklear-Service mbH (GNS) under

<http://www.endlagerung.de>,

which is available in German as well as in English. The basics of long-term safety assessment for different host rock formations and the guidelines of various countries (with emphasis on Germany) for the selection of final repository sites are summarised in Bundesamt für Strahlenschutz (2002; in German).

E

Definition and Classification of Clay Minerals

E.1 Definition by Particle Size

Soil separates of the fine earth

Diameter [mm]	Main separate	Sub-separate	Abbreviation
<0.002	Clay		T
<0.0002		fine clay	fT
0.0002-0.0006		medium clay	mT
0.0006-0.002		coarse clay	gT
0.002-0.063	Silt		U
0.002-0.0063		fine silt	fU
0.0063-0.02		medium silt	mU
0.02-0.063		coarse silt	gU
0.063-2	Sand		S
0.0063-0.2		fine sand	fS
0.02-0.63		medium sand	mS
0.63-2		coarse sand	gS

(Scheffer et al., 2002)

E.2 Classification According to Mineral Composition and Structure

Double-layered minerals kaolin-group					
dioctahedral			trioctahedral		
silicate	alumosilicate		silicate	alumosilicate	
·kaolinite			·serpentine	·berthierine	
·dickite			·greenalith	·cronstedtite	
·halloysite			·amesite		
·nakrite					

Triple-layered minerals					
non-swelling glimmer-illite-group			swelling smectite-group		
dioctahedral		trioctahedral		dioctahedral	trioctahedral
silicate	alumosilicate		silicate	alumosilicate	
·pyrophyllite	·muscovite	·talc	·biotite	·montmorillonite	·saponite
	·glaucoie			·beidelite	·hectorite

Quadruple-layered minerals chlorite-group			
dioctahedral		trioctahedral	
di-dioctahedral	di-trioctahedral	tri-dioctahedral	
·donbassite	·sудоite	·soil chlorites	·trioctahedral chlorite
·soil chlorites	·cookeite		

Mixed layers	
even layering	uneven layering
e.g. A-B-A-B (illite-chlorite-illite-chlorite)	trough weathering or alteration

(source: Rudolph, 2004)

F

Instructions for Experimentation

F.1 The $^{237}\text{Np(V)}$ Stock Solution

A solution containing approx. 6 mg Np in 8 M HCl was obtained from partial dissolution of 10 mg NpO_2 and merging with old Np(IV) solutions. Following oxidation with aqua regia and evaporation, NaNO_2 was added to obtain Np(V) and the oxidation state is confirmed by UV/vis spectroscopy. Total volume ca. 6 mL.

γ measurement of the solution yielded 12 000 Bq of Np in 500 μl equalling 3.4 mM. α measurement with a dissolution of 1:20 (max. 2 Bq in 10 μl , efficiency 14%) supported the result.

Separation by Anion-exchange Chromatography

The anion exchange resin is preconditioned and the thermostat set to 55°C.

- The ^{237}Np stock solution is transferred to the Pu-column and the sample tube is washed with $3 \times 1 \text{ mL}$ 8 M HCl. The flow rate should equal 2-3 drops per second.
- $2 \times 10 \text{ mL}$ 8 M HCl are run through the column.
- The column is washed with 10 mL 8 M HCl containing 30 g/L NH_4I : The anion exchange resin turns black in the upper 2 cm. The eluate is discarded.
- Then neptunium is washed from the column using $4 \times 10 \text{ mL}$ 4 M HCl/0.05 M HF and the eluate is collected in a Teflon beaker (the final 2 mL are checked in the γ detector to ensure that no neptunium is left on the column).

- The neptunium concentration is determined in these 40 ml.
- The solution is concentrated in a sand bath under an UV lamp to approx. 1 mL (~2 h).
- The solution is loaded onto the Pa-column and the beaker is washed with $3 \times 1 \text{ mL } 9 \text{ M HCl}$.
- $1 \times 5 \text{ mL } 9 \text{ M HCl}$ are run through the column.
- The neptunium is recovered from the resin using $4 \times 10 \text{ mL } 9 \text{ M HCl}/0.2 \text{ M HF}$ and collected in a Teflon beaker (again the final 2 mL are checked for traces of neptunium).
- The eluate is concentrated in a sand bath under an UV lamp to approx. 1 mL (~2 h) and fumed with $3 \times 10 \text{ mL } 1 \text{ M HClO}_4$ without reaching complete dryness.

Adjustment of Oxidation State and pH

- After boiling the solution, the remains are gathered in 6 mL H_2O and a spatula's edge of NaNO_2 is added to reduce Np(VI) to Np(V) (the colour switches from pink to green).
- The pH (<1) is adjusted to approx. pH 5 using NaOH and, if needed, HClO_4 .
- γ measurement of the solution: 15 645 Bq from Np in 500 μl , total amount in ca. 6 mL ($2.61 \cdot 10^7 \text{ Bq/g}$): $5.06 \cdot 10^{-3} \text{ M}$, resp. 7.19 mg ^{237}Np .

To check the oxidation state purity of the solution, a UV/vis spectrum is measured from a 1 mM ^{237}Np stock solution, which was obtained after $^{237}\text{Np}/^{233}\text{Pa}$ separation and fuming with HClO_4 as described in the previous section. Before adding NaNO_2 , the UV/vis spectrum showed the presence of both Np(V) and Np(VI) . After addition of a tiny amount of NaNO_2 , the absorption of the characteristic Np(V) absorption at 980 nm increased significantly. The total ^{237}Np concentration was determined by γ spectroscopy and liquid scintillation counting. This value agreed with the Np(V) concentration derived from UV/vis spectroscopy.

Cleansing and Conditioning of the Pu-column

- The anion exchange resin is alternately washed with 3×10 mL 4 M HCl containing Na_2SO_3 and 3×10 mL H_2O .
- 3×10 mL hot H_2O are run through the column.
- Finally, it is washed with 3×10 mL 8 M HCl to condition the column for the next use. Approx. 5 mL are left supernatant and the column is sealed with parafilm.

Cleansing and Conditioning of the Pa-column

- The Pa-column is washed alternately with 2×10 mL 9 M HCl and 2×20 mL hot H_2O .
- Then, to transfer the column to the chloride form, 3×10 mL 8 M HCl are run through the resin, of which approx. 5 mL are left supernatant, and the column is sealed with parafilm.

F.2 The $^{239}\text{Np(V)}$ Stock Solution

The isotope ^{239}Np is produced by irradiation of ^{238}U in the Research Reactor TRIGA Mainz. Following the irradiation, ^{239}Np is separated from uranium and its fission products by anion-exchange chromatography at 55°C using a 150×4 mm column filled with Dowex AG 1-X8 (Bio-Rad, chloride form, 200-400 mesh).

Irradiation of ^{238}U

Irradiation takes place two days before the activity is required.

- 30 mg $\text{UO}_2(\text{NO}_3)_2 \cdot 6\text{H}_2\text{O}$ are put into an irradiation tube, 1 mL Millipore water is added. The tube is tightly closed and heat-sealed with two layers of polyethylene foil. The inner package is labelled.
- The sample is irradiated for 6 h at 100 kW reactor power. The irradiated sample can be removed from the reactor the following day.

Separation by Anion-exchange Chromatography

- The thermostat is turned on and the preconditioning is started only after the column has reached a temperature of 55°C.
- The anion-exchange resin is conditioned in the chloride form with 3×5 mL 8 M HCl.
- The irradiated uranium sample is opened and 1 mL 12 M HCl is added to the solution. This U/Np solution (approx. 2 mL) is transferred to the column. The tube is washed with 1 mL 12 M HCl and 3×1 mL 8 M HCl. All the washings are transferred to the column and pushed through using N₂. The pressure should be adjusted to one drop of eluate every 2-3 seconds. The eluate is discarded.
- After the neptunium has been loaded onto the column, the resin is washed with 2×6 mL 8 M HCl. The eluate is discarded.
- After washing the column, the neptunium is stripped from it with 5×5 mL 4 M HCl/0.05 M HF. The eluate is collected in a Teflon beaker.
- The column is washed with 2 mL 4 M HCl/0.05 M HF. The eluate is measured by γ spectroscopy to check whether all ²³⁹Np has been eluted.
- The column is washed with 2×5 mL Millipore water and converted into the chloride form using 3×5 mL 8 M HCl. All eluates are discarded. At the end, 5 mL of 8 M HCl should be left in the top part of the column. The column is sealed with parafilm.

Adjustment of Oxidation State and pH

- Following the collection of the neptunium from the column into a Teflon beaker, the neptunium solution is boiled to dryness using a sand bath (100 W, 250°C) and an infrared lamp.
- The dry residue is transferred to a glass beaker using 5×1 mL 1 M HClO₄. The neptunium solution is boiled and before reaching dryness, 5 mL 1 M HClO₄ are added and boiling continued.
- The boiling is repeated three times using 5 mL 1 M HClO₄ during each step. The solution should never reach dryness.

- After boiling, the solution is transferred to a 15 mL tube using 3×1 mL 0.1 M NaClO_4 . A small amount of NaNO_2 is added (spatula's edge) to reduce Np(VI) to Np(V) . The concentration of the solution can then be determined by γ spectroscopy (see below).
- The pH is adjusted to approx. pH 5 using NaOH and HClO_4 .

Determination of the ^{239}Np Concentration

10 μL of the stock solution is diluted to 2.0 mL with 0.1 M NaClO_4 . Then 50 μL of this solution are transferred to an irradiation tube and measured by γ spectroscopy. The activity of ^{239}Np is calculated using the 103.4 and 106.1 keV γ lines.

F.3 Conditioning of Montmorillonite

1st Day – Preparation

- A 2.5 cm wide dialysis tube is cut into ca. 40 pieces of 40 cm length and doused in ultrapure water (Milli-Q, 18.2 M Ω): approx. 20 for NaClO_4 (one bag per litre), approx. 16 for the clay, and three for the determination of the CEC.
- For equilibrating the ultrapure water with the clay, one shorter piece is cut from a 1.5 cm wide dialysis tube and treated in the same manner as the larger bits.
- Approx. 20 L 1 M NaClO_4 (Fluka puriss. p.a.) are prepared as background electrolyte.

2nd Day – Purification of NaClO_4

- The dialysis tubes are rinsed, closed with a knot at one end, and dried by blowing with pressurised air. Then they are left to dry.
- To scavenge any undesired ions from the 1 M NaClO_4 , 5 g Al_2O_3 (Aldrich 99.99% trace metal basis) are weighed into the large dialysis bags (one bag per litre). They are filled up with 80 mL (for 1 L bottles) or 100 mL (for 2 L bottles) NaClO_4 and, to clean the solution, placed into bottles of NaClO_4 (5 g $_{\text{Al}}$ /L $_{\text{NaClO}_4}$), which are shaken end over end for one day.

Note: The dialysis bags as well as the bottles should contain enough air to facilitate thorough mixing.

- For preparing water (15-20 L) that is in equilibrium with the clay, for each litre 1 mL of an old batch is pipetted into the small dialysis bag and placed into ultrapure water.

3rd Day – Conversion into the Homo-ionic Na-form and Removal of Soluble Salts

- 60 g clay (STx-1, CMS Source Clay Repository) are weighed into 2 L purified NaClO₄.
- The bottle is shaken for three hours. Then, the clay is allowed to settle for one hour and the supernatant is sucked off. The bottle with the clay residue is filled up with NaClO₄ again.
- The previous step is repeated three times and the supernatant discarded.

4th Day – Collection of the Fraction <0.5 μm

- 2 L 1 M NaClO₄ are put into a 20 L canister or bucked.
- The clay suspension is divided among twelve 250 mL centrifuge bottles.
- These are filled up with clay-equilibrated water, mixed thoroughly, and centrifuged for 7 min at 614 *g* (2000 rpm in the Beckman Coulter ultracentrifuge). The supernatant is sucked off into the canister.
- The previous step is repeated ca. 10 times until the water stays clear.
- The canister is filled up with 1 M NaClO₄ (~3 L), and the suspension left to settle over night.

5th Day – Volume Reduction

- The supernatant is sucked off and discarded, and the suspension is concentrated to approx. 5 L. If necessary, more 1 M NaClO₄ is added to force flocculation by increasing the ionic strength.

The suspension can be kept in the dark at 4°C for six months.

6th Day – Purification from Aluminium-hydroxy Complexes

- Half of the stem suspension is brought to pH 3.5 with 1 M HClO₄ for one hour while stirring continuously (magnet).
- Then it is centrifuged at 5 524 g (6 000 rpm) for 7 min and the supernatant discarded.
- The clay is washed into a beaker with ca. 1.5 L 0.1 M NaClO₄.
- The pH is raised to pH 7 with 1 M NaOH.

The suspension can be stored over night.

7th Day – Adjustment of Ionic Strength and Determination of Clay Content

- The suspension is filled into approx. 16 dialysis bags of 100 mL each and placed in bottles containing 0.1 M NaClO₄ (four bags per 2 L bottle). These are shaken end over end.
- The NaClO₄ solution is replaced ca. every 3 h three to five times until the conductivity stays the same (equilibrium); the last solution is kept for further analysis.
- The dialysis bags are emptied into a plastic bottle.
- 3 × 2 mL of the clay suspension and 3 × 10 mL of the equilibrium NaClO₄ solution are pipetted into weighed beakers and dried at 105°C until the weight stays constant (over night).

8th Day – Purity Assurance

- The beakers are weighed and the clay content in the stem solution is calculated.
- To ensure the purity of the stem suspension (e.g. by ICP-OES), the 0.1 M NaClO₄ solution is checked for cations of K, Mg, Ca, Sr, Ba, Al, Si, and Fe; their concentration should be <1 mg/L.

The stem suspension can be kept in the refrigerator for six months.

F.3.1 Adjustment of Ionic Strength from 0.1 to 0.01 M NaClO₄

The same procedure as described above for day 7 is followed using 0.01 M NaClO₄ instead of the 0.1 M solution. The conductivity is correspondingly lower (ca. 1040 μ S).

G

Experimental Overview

Table G.1: Batch experiments conducted within this study. Due to the great temporal effort, unfortunately, not all experiments intended could be realised. It was considered more important to validate some of the results by repetition.

	Atmosphere	Np(V)	NaClO ₄ [M]	No. of batches	
				STx-1	γ -Al ₂ O ₃
Batch experiments	Ambient air	pM	0.01	2	2
			0.1	1	2
		μ M	0.01		
			0.1	1	1
	CO ₂ -free	pM	0.01		2
			0.1		2
		μ M	0.01		
			0.1	1	

Table G.2: pH and neptunium concentration range of the sorption isotherms. The ionic strength was 0.1 M NaClO₄ for all of them.

	Atmosphere	pH	Np(V) [M]	
			STx-1	γ -Al ₂ O ₃
Isotherms	Ambient air	8.0	10 ⁻⁷ –10 ⁻⁵	
		8.5		10 ⁻¹³ –10 ⁻⁵
		9.0	10 ⁻⁷ –10 ⁻⁵	
	CO ₂ -free	8.0	10 ⁻⁷ –10 ⁻⁵	
		8.5		10 ⁻¹³ –10 ⁻⁵

Table G.3: Summary of the EXAFS samples prepared for studies at ANKA and ESRF. A more detailed list is given in the main part of this thesis in Table 4.4 on page 107.

	Atmosphere	pH	NaClO ₄ [M]	No. of samples	
				STx-1	γ -Al ₂ O ₃
EXAFS samples	Ambient air	5.0	0.01	1	
		8.5	0.1	1	4
		9.0	0.1	1	
		9.5	0.1	1	1
	CO ₂ -free	5.0	0.01	1	
		7.0	0.01	1	
		8.0	0.01	4	
		8.5	0.1		4
		9.0	0.1	1	
		9.5	0.1	1	1

H

Periodic Table of the Elements

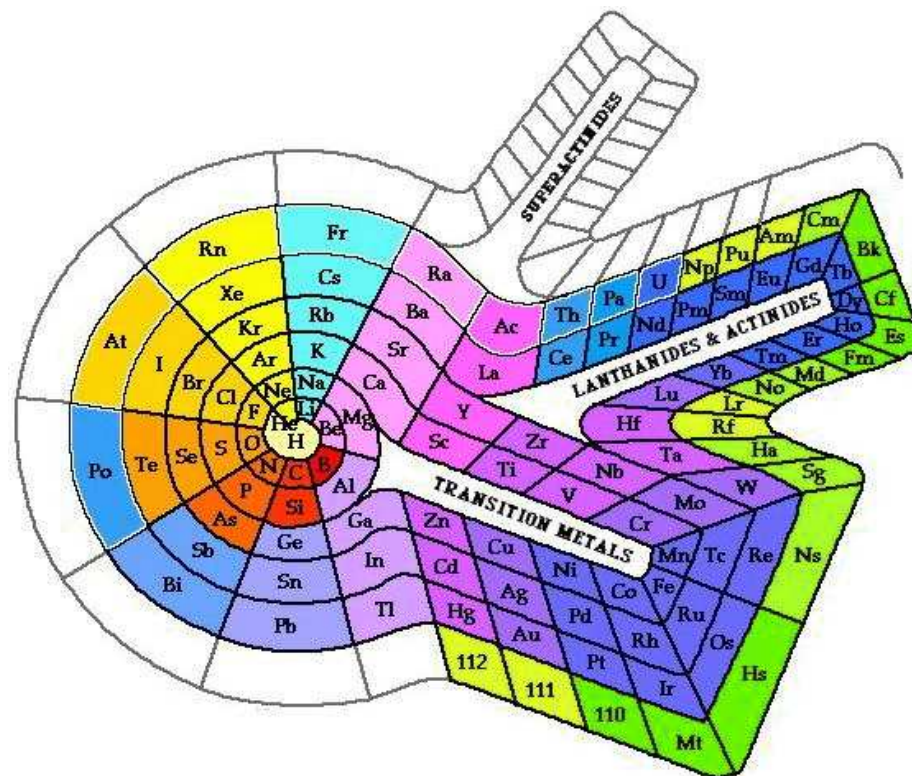


Figure H.1: Alternative periodic table developed by Theodor Benfey 1960. Starting from hydrogen the elements form a two-dimensional spiral, which folds its way around two islands, the transition metals, and lanthanides and actinides. A superactinide island is already indicated.



Curriculum Vitae

Personal data

Name Sonja Wendt, née Dierking
born 1977 in Langenhagen, Germany

Civil status married
one daughter, born 2008

Education

10/2005-09/2009 PhD at the Institute for Nuclear Chemistry, University of Mainz, Germany; fellow of the DFG interdisciplinary Research Training Group 826

10/2001-11/2003 Studies of Geography, University of Hannover, Germany
+10/1997-06/2000 'Diplom-Geographin'

07/2000-06/2001 University of Otago, Dunedin, New Zealand
'Postgraduate Diploma in Science in Geography'

6/1995-07/1997 Highschool at the Gymnasium Mellendorf, Germany
+08/1990-12/1994 'Abitur'

01/1995-05/1995 Highschool in Guymon/Oklahoma, USA

08/1984-07/1990 Elementary school and 'Orientierungsstufe' in Lindwedel and Schwarmstedt, Germany

J

Declaration

I hereby declare that this dissertation has been composed by myself and is based on my own work, unless stated otherwise. Except where reference is made in the text, it contains no material published elsewhere nor extracted in whole or in part from a dissertation presented by me for another degree or diploma. No other person's work has been used without due acknowledgement. This dissertation has not been submitted for the award of any other degree or diploma in any other tertiary institution.